LASER INDUCED PHOTOCATALYTIC CONVERSION OF METHANE INTO METHANOL

BY

ABDUL HAMEED

A Dissertation Presented to the
DEANSHIP OF GRADUATE STUDIES

KING FAHD UNIVERSITY OF PETROLEUM & MINERALS
DHAHRAN, SAUDI ARABIA

In Partial Fulfillment of the
Requirements for the Degree of

DOCTOR OF PHILOSOPHY

In

CHEMISTRY

December, 2003

ProQuest Information and Learning Company
300 North Zeeb Road
P.O. Box 1346
Ann Arbor, MI 48106-1346

KING FAHD UNIVERITY OF PETROLEUM AND MINERALS
DHAHRAN 31261, SAUDI ARABIA

DEANSHIP OF GRADUATE STUDIES

This dissertation, written by **Mr. Abdul Hameed** under the direction of his dissertation advisor and approved by his dissertation committee, has been presented to and accepted by the Dean of Graduate Studies, in partial fulfillment of the requirements for the degree of **DOCTOR OF PHILOSOPHY IN CHEMISTRY**

Dissertation Committee

Prof. Abdulaziz A. Al-Suwaiyan
Dissertation Committee Chairman

M. A. Gondal
Dr. Muhammad Ashraf Gondal
Dissertation Committee Co-Chairman

G. A. Oweimreen
Prof. Ghassan A. Oweimreen
Member

M S Hussain
Prof. Muhammad Sakhawat Hussain
Member

Prof. Uwe. K. A. Klein
Member

Dr. Assad A Al. Thukair
Chairman, Chemistry Department

Prof. Osama A. Jannadi
Dean, College of Graduate Studies

Date: May 2, 2004 ١٣/٣/٢٥هـ

THIS RESEARCH WORK IS DEDICATED TO

MY PARENTS
&
FAMILY

ACKNOWLEDGEMENT

All praises to ALLAH subhana-wa-ta'ala, who granted me strength to complete this work. Peace and blessings of Allah be upon his last Prophet Mohammad (SAW).

Acknowledgement is due to King Fahd University of Petroleum and Minerals for the support and facilities provided for the completion of this dissertation.

I am very grateful to my thesis advisor, **Prof. Abdulaziz A. Al-Suwaiyan**, for his guidance for the completion of this research work. I wish to register my gratitude and appreciation to **Dr. Muhammad Ashraf Gondal** who served as my co-advisor. The success of this work is credited to his tireless support, guidance and precious time. I am very grateful to **Prof. Ghassan A. Oweimreen** for his extended help in thorough reading and correction of the thesis manuscript. My thanks are also due for my committee members **Prof. Muhammad Sakhawat Hussain** and Prof. Uwe. K. A. Klein for their useful suggestions.

I express my gratitude to **Dr. Assad Al-Thukair**, Chairman, Department of Chemistry for his encouragement during the tenure of my Ph.D.

I am thankful for the support of CAPS (RI) for the completion of this dissertation. In this regard, I am grateful to Dr. Hussain M. Masudi (Manager), Dr. A. Al-Arfaj (Current Director) and Dr. Garwan (Ex-Director) for their encouraging attitude.

My special thanks are due for Mr. Farooqi and Saeed Al-Zahrani for helping me in the fabrication of photocatalytic cell.

I am thankful for all the faculty and staff members of chemistry department for their encouragement and support.

I am grateful to Dr. Shakeel Ahmad, Dr. Anwar-Ul-Hamid (RI) and Mr. Saleem (Civil engineering) for their logistic and moral support

I offer my sincere thanks to Dr. Tabet and Mr. Iftikhar (Physics) for helping me in XPS studies and Dr Zain Yamani for useful discussions in solid state physics and lasers.

I would also like to thank my colleagues and friends especially Mr. Tijani, Mr. Yunusa, Mr. Jamil, Dr. Ali El-Rayees, Dr. Waqar Ashraf, Dr. Saeed Ahmed, Dr. Shafique Awan, Mr. Ahsan, Mr. Abdulrahman, Dr. Tahir Mustafa, Mr. Zahid Qamar, Mr. Sohail Akhter, Mr. Sabeer, Mr. Atique, Mr. Mahmood and my friends in Pakistan for their motivation throughout the course of this study.

I am grateful to my parents and family for their moral support, encouragement and prayers without which this work would not have been possible. Thanks to my wife and my daughters, Hadiya and Sarah, for their love and help during this time.

TABLE OF CONTANTS

LIST OF TABLES

LIST OF FIGURES

CHAPTER TWO

CHAPTER THREE

CHAPTER FOUR

CHAPTER FIVE

CHAPTER SIX

ABSTRACT

NAME: **Abdul Hameed**

TITLE: **Laser induced photocatalytic conversion of methane into methanol**

MAJOR FIELD: **Chemistry**

DATE: **30th December, 2003**

The main aim of this dissertation work is the study of the photocatalytic process induced by laser light, for converting methane to methanol and for splitting water to hydrogen and oxygen. The catalysts, WO_3, TiO_2, NiO and α-Fe_2O_3 were investigated; TiO_2, NiO and α-Fe_2O_3 were studied in pure form after pre-treatment whereas WO_3 was studied in its pure as well as the surface modified forms.

The bandgaps of the synthesized photocatalysts were determined by UV-Visible absorption spectroscopy. Scanning electron microscopy (SEM) and electron x-ray dispersive spectroscopy (EDS) was used to study the morphology and composition of synthesized powders. The oxidation states of the doped metals at the surface of host WO_3 were evaluated by x-ray photoelectron spectroscopy (XPS).

A 355 nm UV laser was employed as light source. The progress of the photocatalytic process was monitored by analyzing the yield in gas as well as liquid phase. The photonic efficiencies of all the processes were calculated to estimate photon harvesting. In addition, the effect of the dissolved metal ions on yield was investigated.

The influence of transition metals, as dopants, on the activity of WO_3 was evaluated by comparing the product yield and photonic efficiency of doped WO_3 powders with that of pure WO_3. The variations of pH during the course of reaction were found very useful in explaining the mechanism of photocatalytic processes.

The photonic efficiencies observed for both hydrogen and oxygen production during the photocatalytic splitting of water using laser as light source were found to be much higher than those obtained from conventional light sources. The study indicates a correlation between the photocatalytic splitting of water and conversion of methane in aqueous medium.

DOCTOR OF PHILOSOPHY DEGREE
KING FAHD UNIVERSITY OF PETOLEUM AND MINERALS
DHAHRAN SAUDIARABIA

خلاصة

الإسم: عبد الحميد
العنوان: تحويل الميثان الى الميثانول عن طريق التحفيز الضوئي المحدث بالليزر
التخصص: الكيمياء
التاريخ: 30 / 12 / 2003م

أن هدف بحث هذه الرسالة هو دراسة تحويل الميثان إلى الميثانول وكذلك انقسام الماء إلى هيدروجين وأوكسجين عن طريق التحفيز الضوئي المحدث بالليزر.

لقد تمت دراسة كل من حفازات : α-Fe_2O_3 , NiO , TiO_2 , WO_3 . وقد استعمل الأول في الحالة الخالصة وكذلك كأسطح حاملة لايونات فلزية بينما استعملت المواد الثلاث الأخيرة في الحالة الخالصة فقط بعد معالجة أولية.

لقد تم التوصل إلى فجوة الطاقة الخاصة بالحفازات الضوئية التي تم تصنيعها بواسطة تقنية أطياف الامتصاص المرئية و فوق البنفسجية. وقد استعملت تقنية مجهر المسح الإلكتروني وكذلك أطياف تشتيت أشعة أيكس لدراسة أشكال جسيمات ومكونات المساحيق المصنعة. وتم التوصل إلى تكافؤ تقريبي للفلزات المثبتة على سطح مادة WO_3 المضيفة، بواسطة تقنية أطياف أشعة أيكس للإلكترون الضوئي. و لقد استعملت أشعة ليزر بموجة طولها 355 نانومتر. وتمت مراقبة التفاعلات المحفزة ضوئيا بواسطة تحليل المردود سواء في الحالة الغازية أو السائلة ومن أجل تقدير المردود الضوئي تم حساب الفعالية الضوئية لكل التفاعلات. وتمت كذلك دراسة تأثير أيونات الفلزات المتواجدة في المحاليل.

من أجل دراسة تأثير الفلزات الانتقالية المستعملة لمعالجة مادة WO_3 على نشاط هذه الأخيرة، أجريت مقارنة بين مردود التفاعلات في حالة مادة WO_3 الخالصة مع الحالة المعالجة و تمت كذلك مقارنة الفعالية الضوئية في كلتي الحالتين. وقد مكنت دراسة تغيرات الأس الهيدروجيني للمحاليل أثناء التفاعلات من إيجاد تفسير لآليات هذه التفاعلات. وقد وجد أن قيم الفعاليات الضوئية لعمليات انقسام الماء المحفزة بواسطة الليزر أعلى بكثير من القيم المعروفة لمصادر الضوء التقليدية. و أشارت الدراسات إلى وجود ارتباط بين الانقسام المحفز ضوئيا للماء وتفاعلات الميثان في وسط مائي.

شهادة دكتوراه الفلسفة
جامعة الملك فهد للبترول و المعادن
الظهران – المملكة العربية السعودية

CHAPTER ONE

INTRODUCTION AND OVERVIEW

1.1 Introduction

At present, the major portion of the energy consumed is produced from fossil fuels. Unfortunately, fossil fuel reserves are depleting at a fast rate due to industrial developments and other energy needs. In addition, the use of fossil fuels led to a severe pollution problem. It is generally accepted that CO_2, CH_4 and NO_x, largely contribute to the greenhouse effect, which in turn is responsible for climate change and global worming. In order to avoid an environmental disaster and the depletion of the fossil fuel reserves a growing interest has developed for alternative non-fossil and environmentally friendly energy sources. Hydrogen is considered as the best option, as its combustion leads to the formation of water. The main desire of the scientific community is to use two inexpensive sources such as water and sunlight for the production of hydrogen but this desire is still a dream as no photocatalyst fulfills the prerequisites for complete splitting of water into its components with high efficiencies. Beside this dream, efforts are under way for the production of hydrogen in controlled quantities, with high efficiencies, using water, semiconductors and cheaply available light sources other than sun light.

Another area of interest is the conversion of methane gas into liquid fuels such as methanol and other oxygenates that are much less expensive to transport. The use of light, water, methane and inexpensive semiconductor powders, for the production of alternative fuels, is an attractive approach. Methanol, the initial product of photocatalytic methane oxidation, is a desirable product because it retains much of the original energy of the methane and fulfils the requirements of transportation and storage. In addition, methanol can be used, as fuel, as such or converted to other oxygenated fuels and other valuable products.

Heterogeneous photocatalysis is an emerging advanced oxidation technology (AOT). Like other advanced oxidation technologies, it is based on the generation of highly oxidizing species, such as hydroxyl radicals, at the surface of a semiconductor (also called as "photocatalyst") with the absorption of photons. Fundamental and applied research in this area has been performed extensively during the last two decades. Early research was devoted to photovoltaic conversion and energy storage. Later, with the development and characterization of new wide and short bandgap semiconductor materials, heterogeneous photocatalysis emerged as a potential area of research. The special feature of heterogeneous photocatalysis is the long life of inexpensive photocatalysts and mild temperature conditions used. Nowadays, the focus of photocatalysis research is in the following fields:

- Photocatalytic splitting of water for hydrogen production
- Photocatalytic conversion of light aliphatic hydrocarbons into valuable organic compounds and fuels
- Photocatalytic degradation of contaminants for air purification and waste water treatment

Heterogeneous photocatalysis is still in the developing stage and several aspects of photocatalytic processes are yet to be investigated. The two basic inherited problems associated with the conventional heterogeneous photocatalysis are the long reaction time and low photonic efficiencies. Once these challenges are overcome heterogeneous photocatalysis can be applied as cheap and versatile technique for the synthesis of valuable compounds.

In this dissertation, the above-mentioned problems associated with heterogeneous photocatalytic processes are addressed by modifying the existing conventional setups used to study photocatalytic processes. Instead of using conventional lamp based photocatalytic reactors, a simple reactor free of all logistics, such as heating, cooling and evacuating assemblies, was designed. The availability of commercial lasers at cheap prices triggered the idea of using laser as light source. The focus of these modifications was to enhance the photocatalytic activity of semiconductor photocatalysts. The problem of low spectral response and photonic efficiency by pure WO_3 was overcome by using the surface modification approach and transition metals were employed as surface modifying agents. The impact of dissolved metal ions on the photocatalytic activity of pure photocatalysts such as WO_3, TiO_2, NiO and α-Fe_2O_3, was also studied.

The main aim of this research is to study the activity of various pure and doped photocatalysts for conversion of methane into methanol and for hydrogen production through water splitting. This necessitated the evaluation of the stability of these photocatalysts under a high photon flux illumination.

1.2 Overview of dissertation

The work presented in this dissertation is arranged as follows.

Chapter 2 deals with the theoretical and historical background of heterogeneous photocatalysis and its applications to water splitting and methane conversion. A detailed review of previous work on the role of metal ions and surface modifications in photocatalysis for various processes is discussed in detail in this chapter.

The details of experimental setup, experimental procedure, synthesis and transition metal doped WO_3 and its characterization using various analytical techniques are described in chapter 3.

The experimental results regarding the characterization of the synthesized transition metal-doped WO_3 powders, based on various experimental techniques along with a brief introduction, are discussed in chapter 4.

The experimental results on photocatalytic splitting of water under monochromatic near UV laser irradiation for all the pure and doped catalysts are presented in chapter 5. The experimental results achieved on photocatalytic conversion of methane into methanol over various pure and synthesized catalysts are discussed in chapter 6.

The major conclusions of this work and directions for future work are presented in Chapter 7.

CHAPTER TWO

LITERATURE REVIEW

In this chapter, the theoretical and historical background of heterogeneous photocatalysis along with the selected topics, such as photocatalytic splitting of water, photocatalytic conversion of methane, role of metal ion in photocatalysis and effect of surface modification of photocatalyst on photocatalytic processes, will be reviewed.

2.1 Heterogeneous photocatalysis

Photocatalytic water splitting on TiO_2 was discovered by Fujishima and Honda in 1972 [1]. Since then, it has drawn considerable academic interest as a very attractive for the degradation of organic pollutants [2,3]. However, it has found a very limited degree of commercialization [4]. This trend is primarily due to the low reaction rates exhibited by commonly known photocatalysts. Semiconductors can provide light-induced charges for redox processes due to their electronic configuration [2] and characterized by a filled valence band and empty conduction band [5]. All photocatalysts must possess semiconducting properties in order to be able to perform photo-induced reactions.

Due to the chemical stability and relatively high activity and low price, the most studied and known photocatalyst is TiO_2 [6]. Other transition metal oxides, such as WO_3 [7], Fe_2O_3 [8], Cu_2O [9], Bi_2O_3 [10], In_2O_3 [11], SnO_2 [12], ZnO [13], and ZrO_2 [14,15] as well as a number of mixed oxides were also investigated for photocatalytic water splitting and decontamination of aqueous and gas streams. None of them, however, exhibit sufficient structural stability to photocorrosion in aqueous suspensions. Some of them (WO_3 and Fe_2O_3) show good response to visible light without photocorrosion, but certain modifications of the reaction medium are required. The properties of some selected photocatalysts used, in this study, are given in table 2.1.

Table 2.1: Properties of selected photocatalysts

Photocatalyst	**Bandgap energy (eV)**	**Valance band edge (V)**	**Conduction band edge (V)**	**Density (g/ml)**	**Melting point (°C)**
α-Fe_2O_3	2.2	+2.48	+0.28	5.25	1565
WO_3	2.8	+3.1	+0.4	7.16	1473
TiO_2	3.2	+2.9	-0.3	4.26	1850
NiO	3.5	+3.0	-0.5	6.67	1984

Along with selection of suitable photocatalyst, in photocatalysis, the right choice of light source is also important. The selection of the light source depends upon the band gap of photocatalyst. For a photocatalytic process to be productive, the energy of the incident light should be enough to excite an electron from the valance band to the conduction band of the semiconductor generating electron-hole pair. Normally a linear relationship exists between the electron-hole pair generation and the photon flux or the intensity of the incident light but on the other hand excess photon flux also enhances the rate of electron-hole recombination [2, 5]. Almost in all previous photocatalytic studies, polychromatic conventional broad-spectrum lamps such as xenon arc lamps, mercury vapor lamps and halogen lamps, of various powers and light emitting characteristics were used as light source. In order to obtain the wavelength of interest or to narrow the wavelength range, cut-off filters were used.

The elementary mechanism of photocatalytic transformation includes a number of steps, which have been described in the literature [16]. A semiconductor (SC) is characterized by an electronic band structure in which the highest occupied energy band, called the valence band (VB), and the lowest unoccupied empty band, called conduction band (CB), are separated by an energy gap called band gap (E_g). This bandgap is actually the region of forbidden energies in perfect crystal.

When a photon of energy equal to or greater than the band gap energy is absorbed by the semiconductor particle, an electron from the valance band is promoted to conduction band with a simultaneous generation of a positive entity in the valance band called "hole" (h_{vb}^+). The photoelectrons (e_{cb}^-) and photo-generated holes (h_{vb}^+) can recombine on the surface or in the bulk of the particle in few nanoseconds by dissipating energy as heat or can be trapped in the surface state where they can react with donor (D) or acceptor (A) species adsorbed or close to the surface of the particle. This can initiate anodic and cathodic reactions [2,5,17,18].

The energy level at the bottom of conduction band (CB) is actually the reduction potential of photoelectrons (e_{cb}^-) and the energy level at the top of valance band (VB) determines the oxidizing ability of photo holes (h_{vb}^+). The potential difference that is developed at the SC-Electrolyte interface is called as flat-band potential (V_{fb}). The magnitude of flat-band (V_{fb}) depends on the nature of the photocatalytic material and the system equilibrium. From a thermodynamic point of view, adsorbed species can be reduced by CB electrons if they have the redox potential more positive than the V_{fb} of the CB, and can be oxidized by VB holes if they have the redox potential more negative than V_{fb} of the VB [19].

The efficiency of a photocatalyst depends on the competition of different interface transfer processes involving hole, electrons, and their deactivation by recombination [20-22]. The position of the flat band of a semiconductor depends on the pH of solution, and consequently, the redox chemistry of holes and electrons can be controlled by changes in pH. The general mechanism of photocatalysis along with the graphical representation of the terms discussed above is presented schematically in figure 2.1.

In order to be productive chemically, for the photocatalysis process, electron-hole pair recombination must be suppressed. This can be achieved by trapping either the photogenerated electron or photogenerated hole. Since the recombination of a photogenerated electron-hole pair occurs within a fraction of nanosecond, if efficient conversion of the absorbed photon has to be achieved, the rate of interfacial carrier trapping must be very rapid.

Hole trapping is usually achieved by the use of degradable adsorbates or a sacrificial reagent. The organic species bearing non-bonded electrons or a delocalized π

system e.g. conjugated molecule can act as sacrificial agents. Many polar solvents such as water, methanol, acetonitrile etc. also facilitate hole capture process. In aqueous system, surface bounded hydroxyl radicals particularly at high pH act as hole scavengers [23].

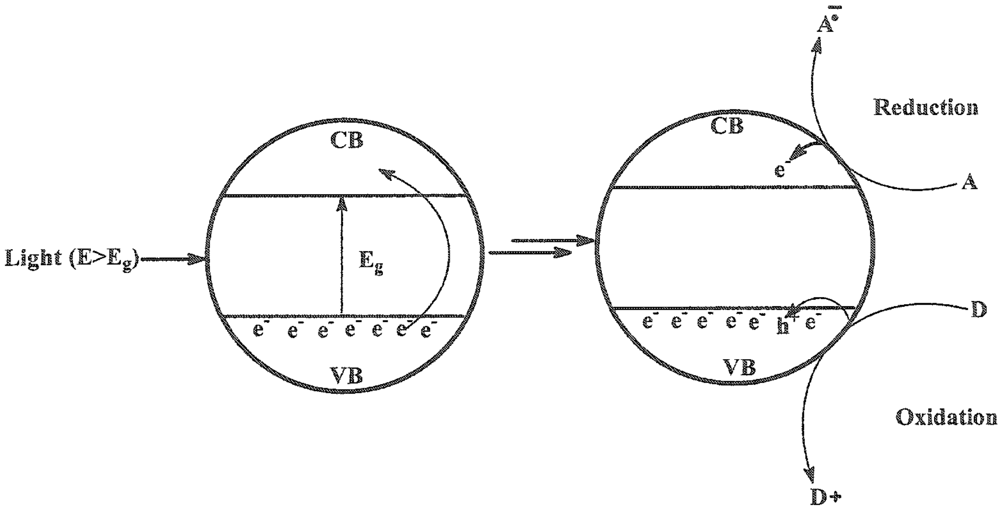

A = Adsorbed acceptor **D = Adsorbed donor**

SEQUENCE OF EVENTS IN AQUEOUS MEDIUM

$$SC + h\nu \longrightarrow SC(e^-_{cb}, h^+) \longrightarrow \text{Recombination}$$

$$SC(h^+) + H_2O_{ads} \longrightarrow SC + H\dot{O} + H^+$$

$$SC(e^-) + H^+ \longrightarrow SC + \dot{H}$$

$$\dot{H} + H\dot{O} \longrightarrow H_2O(\text{Recombination})$$

$$SC(h^+) + D_{ads} \longrightarrow SC + D^+_{ads}$$

$$SC(e^-) + A_{ads} \longrightarrow SC + A^-_{ads}$$

Figure 2.1 Mechanism of photocatalysis process

Similarly electron trapping suppresses electron-hole recombination process. Defect sites in the bulk of the photocatalysts play a very vital role in trapping photogenerated electrons. Trapping of photogenerated electrons with in the semiconductor bulk has been confirmed by EPR experiments [24]. Being isoenergetic with the reduction potential of conduction band of photocatalysts, in inert solvents, dissolved oxygen serves as a trap for photogenerated electrons [25]. It has been observed experimentally that photocatalytic activity is completely suppressed in the absence of dissolved oxygen, possibly because of the back interfacial electron transfer from active species present on photocatalyst surface. A steady state concentration of dissolved oxygen has a profound effect on photocatalytic degradation reactions [26]. In photocatalytic processes, dissolved metal ions are also used to enhance the photocatalytic oxidation by suppressing the unwanted electron hole recombination. Another method to enhance the photocatalytic activity of a photocatalyst, by conduction band electron capture, is the surface modification of the photocatalyst by metals or their respective oxides. The role of dissolved metal ions and the effect of surface modification of the photocatalyst on photocatalytic activity will be discussed separately in detail in the coming sections of this chapter.

The presence of dissolved oxygen, therefore, plays a very vital role in enhancing the efficiency of photocatalytic processes. The precise role of dissolved oxygen is still unambiguous but the rates and efficiencies of photocatalytic degradation processes are sufficiently improved in the presence of oxygen. The molecular oxygen primarily acts as an efficient conduction band electron trap, suppressing electron hole pair recombination. The resulting species, super oxide radical ($O_2^{\cdot-}$), is highly active and can attack either organic molecules or adsorbed intermediates. Also after protonation, it can provide another surface for surface-bound hydroxyl radicals [27]. The attack of $O_2^{-\cdot}$ radical occurs before desorption from the surface since the presence of dissolved super oxide traps in solution does not inhibit photocatalytic oxidative reactivity [28]. In many oxides, the adsorbed oxygen also exchange with the surface oxides but it is difficult to establish the chemical form in which oxygen atoms appear in the oxygenated product.

Numerous studies have discussed the competing role of photogenerated hydroxyl radicals in aqueous suspensions [29]. It has been suggested that in dilute aqueous solutions, phenol is oxidized by homogeneous reaction with hydroxyl radicals, whereas in concentrated solutions, the oxidation is initiated by hole trapping [30]. A surface bound OH radical is treated chemically equivalent to surface trapped hole. The diffused reflectance experiments show that only the activated surface presumes a surface-bound hydroxyl radical since many semiconductors retain an associated water of hydration at the surface even when dispersed in non-aqueous medium. This detection of singly oxidized intermediates indicate that the surface bound OH can act as a hole trap, rather than diffusing to the solution and initiating secondary hydroxylation. In other words, the principal charge trapping event in aqueous solutions is the formation of a surface hydroxyl group, which can initiate primary oxidation of the adsorbed substrate before diffusing into the bulk. On the other hand, contrasting studies in the literature claim that a free hydroxyl radical can diffuse several hundred angstroms from the photocatalyst surface into the bulk solution and establishes oxidation process [31]. If a freely diffusing hydroxyl radical is the sole oxidant in photocatalysis then an increase in the hydroxyl radical concentration (by adding a hydroxyl radical generator such as H_2O_2)

should enhance the efficiency of photooxidation. However, the effect of added quantities of H_2O_2 on photocatalyzed oxidation of chloroethylenes on TiO_2 or ZnO [32] showed no such effect on the efficiency of photooxidation.

Keeping in view, the rapid rate of recombination of photogenerated electrons and holes, it has been suggested that preliminary adsorption is a prerequisite for high efficiency photocatalytic process [33]. In aqueous metal oxide suspensions, the surface adsorbed water molecules serve the role of surface-bound traps for the photogenerated holes forming a surface adsorbed hydroxyl radical. Adsorption of both substrates and oxygen on metal oxide semiconductors are some time enhanced during photolysis [34]. Photo-adsorption can thus dramatically affect the efficiencies of photocatalytic processes.

A common feature of photocatalytic reactions occurring on metal oxides semiconductors in aqueous suspensions is the weak dependence of rate of reaction on the pH of solution. However, the surface charge and band edge positions of semiconductor metal oxides are strongly influenced by pH [35]. The band edge positions of a metal oxide semiconductor can be calculated by using the relation given below.

$$V_{fb} = V_{fb}(pH = 0) - (0.059pH) \qquad 2.1$$

The zero point charge pH (pH_{zpc}) is 6.0 for TiO_2 [36], and positive surface charge is expected at lower pH while a negative surface charge is predicted at higher pH values. Despite the clear evidence for the importance of surface charge on substrate adsorptivity, evidence for higher reaction rates for various photocatalytic conversions at both low pH or at high pH can be found. The rate of photo-production of oxygen in the presence of Ag^+ ions over TiO_2 was affected by the pH of the solution [37]. A decrease in the pH led to the protonation of active surface sites inhibiting the adsorption of positive ions while an increase in pH facilitates the same. The changes in the pH have shown to be significant effect in photoreduction of metals [37].

Generally, photocatalytic reactions are not sensitive to the minor changes in temperature but some specific cases have been reported in the literature showing variable dependence of the rate of reaction on the temperature. The rate of photocatalytic decomposition of aliphatic alcohols was insensitive to temperature [38]. Arrhenius behavior was observed in the photo detoxification of phenol [39]. A linear dependence of reaction rate on temperature was reported in the photocatalyzed decomposition of chloroform [40].

2.2 Photon-assisted splitting of water

Water is abundant in nature and considered to be a cheap feedstock for H_2 production. The splitting of water into hydrogen (H_2) and oxygen (O_2) is an uphill process and requires an energy input of +237.7 kJ/mol. Light-induced photo-oxidation of liquid water to gaseous components using semiconductor catalyst is a possible practical application for H_2 and O_2 generation and it has been extensively studied [41-52]. The photon-assisted generation of H_2 and O_2 from water can be achieved in various ways [45].

2.2.1 Photocatalytic splitting of water

In a photocatalytic system, both excited electrons in the conduction band (CB) and holes in the valence band (VB) directly participate in the water splitting process, in the presence and absence of an external bias respectively [41-44].

For an n-type semiconductor, the semiconductor electrode acts as a photo anode. Accordingly, when an n-type semiconductor electrode is under band gap illumination, photo generated holes in the valance band will oxidize water into O_2, and electrons in the conduction band will move towards the counter electrode to reduce water into H_2.

In the case of a p-type semiconductor, the holes in the valance band are the majority charge carrier and the semiconductor acts as a photocathode. Accordingly, the photo process at p-type semiconductor is just opposite to that of n-type. In order to successfully split water upon irradiation, the valence band of the semiconductor has to be located at a lower energy level than the chemical potential of O_2 evolution (O_2/H_2O) in solution, and the conduction band has to be positioned at a higher energy level than the chemical potential of H_2 evolution (H_2/H^+). If the position of the energy levels of the valence and conduction band is not fulfilled, an external bias (E_{bias}) is required to induce the photo oxidation process. For long-term H_2 and O_2 generation, the electrodes have to be chemically stable and resistant to photo-corrosion. The kinetics and mechanisms behind oxidation of water by photogenerated holes are not clearly understood and vary most probably with interfacial properties of the semiconductor. Four adsorbed photons and two molecules of water are involved to yield one molecule of gaseous O_2 and four protons [44-52].

$$4h\upsilon + SC \rightarrow 4h_{vb}^{+} + 4e_{cb}^{-} \qquad 2.2$$

$$4h_{vb}^{+} + 2H_2O \rightarrow 4H^{+} + O_2 \qquad 2.3$$

This is, by nature, a very complex reaction. The elementary steps in the detailed mechanism are far from known. The heterogeneous rate constant for the hole transfer from the valence band of α-Fe_2O_3 to the hydroxide ion has been reported to be as low as 0.1 to 1 cm/s compared to 103 to 104 cm/s for WO_3 and TiO_2 [53]. However, the kinetics can be improved by surface modification, for instance by surface coating with an efficient catalyst for O_2 evolution, e.g. RuO_2 [54], or increasing the surface area, which facilitate a lower current density, which in turn decrease the over potential [55]. The reduction of water into H_2 is a kinetically simpler process compared to the four-electron redox process to evolve O_2. For any practical applications, an overall efficiency of at least 10% [43] is required to compete with conventional ways of producing H_2. Theoretically, it should be possible to design a device with an overall efficiency of 10% or higher. The peak efficiency would occur for a single bandgap photoconverter in the range 1.4 to 1.6 eV where an efficiency of up to 31% could be achieved [56]. For a tandem device, where two light harvesting electrodes operate in series to cover a broad range of the solar spectrum, the theoretical upper limit is around 41%. However, stability problems, both chemically and low stability towards photocorrosion, as well as low efficiencies have so far prevented the commercial application of photocatalytic device for direct conversion of solar energy to H_2.

After the first successful photoelectrochemical cell by Fujishima and Honda [1], a large number of semiconductor materials e.g. $SrTiO_3$ [57], α-Fe_2O_3 [58,59], WO_3 [60-

64] have been investigated for H_2 and O_2 generation for improving the efficiency of the PEC cell. Heller and co-workers [65] studied the photo-electrolysis of water at p-type semiconductors using InP electrodes. A light to chemical conversion efficiency of 12% was reported for this system, with relatively low stability. Combinations of a photoanode (n-type) and a photocathode (p-type) of doped hematite have also been studied [66]. For these systems external bias was not needed for photo-oxidation of water. However, the conversion efficiency was reported as low as 0.05% [67]. Recently, the most interesting findings in the field of direct solar induced water splitting is the reports by Turner et al [68] and by Grätzel and co-workers [69]. Both groups applied multiple-junction systems, using different materials. Turner and coworker used a highly efficient solid-state photovoltaic cell integrated to a photoelectrochemical device consisting of p-type $GaInP_2$ [68]. Although efficiencies of 12% were obtained but the cost of the system is at present too high to compete with conventional renewable energy techniques. The tandem device described by Grätzel et al [69] was based on nano-crystalline WO_3 biased by dye-sensitized nano-crystalline TiO_2 to absorb transmitted light from WO_3. The overall solar light to chemical conversion efficiency of this device was reported to be 4.5%. Another interesting work is by Licht et al. [70] reported recently. Although their system was not a strict photoelectrochemical one as the photovoltaic system was separated from the water electrolyzer, their study is still of general interest for the water oxidation field. The photovoltaic cell was connected to a water splitter catalyst system of considerably larger area than the solar cell. An overall efficiency of 18.3% was obtained.

Apart from semiconductor based systems, there are other systems designed to photo-evolve oxygen from water. These systems are based upon homogeneous photocatalytic splitting of water [71], sono-photocatalytic decomposition of water [72,73], homogenous oxidation of water using AgCl self-sensitization electrodes [74] and mechano-catalysis for water splitting [75].

2.3 Photocatalytic conversion of methane

Methane has the vast proven geological reserves in the world. In addition, methane may be produced as a by-product of coal gasification. Depending on the gasifier design and operating conditions, up to 18% of the total gaseous product may be methane. Unfortunately most of the methane reserves are located in remote locations and the transportation of methane to consumers is technically difficult and costly. This limits the use of methane at large scale. Research efforts are underway to develop novel methods for conversion of methane to useful, more readily transportable and storable materials. Methanol the initial product of methane oxidation is a desirable product of conversion because it retains much of the original energy of the methane and fulfils the requirements of transportation and storage as existing transportation network can be used for this purpose [76]. Methanol may be used directly as fuel or may be converted to other oxygenated fuels and other valuable products.

It has been reported [77,78], that methane may be photochemically converted to methanol by first passing it through a heated water bath, in order to saturate it with water vapors, and then irradiating it with ultraviolet light at 185 nm in a quartz reactor. This method is purely based upon the free radical generation mechanism i.e. the production of hydroxyl radical through water photolysis, and follows the following reaction scheme.

At λ < 185 nm

$$H_2O + h\upsilon \rightarrow H_2 + \frac{1}{2}O_2 \quad 2.4$$

$$H_2O \rightarrow \frac{1}{2}H_2 + OH^{\bullet} \quad 2.5$$

$$CH_4 + OH^{\bullet} \rightarrow CH_3^{\bullet} + H_2O \quad 2.6$$

$$CH_3^{\bullet} + H_2O \rightarrow CH_3OH + \frac{1}{2}H_2 \quad 2.7$$

The use of photocatalyst like WO_3 allows the reaction to occur in the visible instead of ultraviolet region [79,80]. Catalytic photolysis of water to hydrogen and water occurs during irradiation of liquid water with visible light in the presence of lanthanum (La) doped WO_3 photocatalyst suspended in the solution. The mechanism is also based upon the generation of hydroxyl radical in the presence of doped WO_3 and an electron transfer agent methyl viologen dichloride hydrate. Two hydroxyl radicals couple together to give H_2O_2, which decomposes to give H_2O and O_2.

At λ > 410 nm

$$La/WO_3 + h\upsilon \rightarrow e_{cb}^- + h_{vb}^+ \quad 2.8$$

$$e_{cb}^- + MV^{2+} \rightarrow MV^{+\bullet} \quad 2.9$$

$$h_{vb}^+ + H_2O \rightarrow H^+ + OH^{\bullet} \quad 2.10$$

$$MV^{+\bullet} + H^{+} \rightarrow \frac{1}{2}H_2 + MV^{2+} \qquad 2.11$$

$$2OH^{\bullet} \rightarrow H_2O_2 \rightarrow \frac{1}{2}O_2 + H_2O \qquad 2.12$$

Taylor et. al. reported [76] that in the presence of methane, the hydroxyl radicals produced in solution with the absorption of light by doped WO_3, react with methane to give methyl radical, which react with water again to give methanol at 90°C. The light source used was quartz mercury vapor lamp. The suggested reaction mechanism is as under:

$$La/WO_3 + h\upsilon \rightarrow e^{-}_{cb} + h^{+}_{vb} \qquad 2.13$$

$$e^{-}_{cb} + MV^{2+} \rightarrow MV^{+\bullet} \qquad 2.14$$

$$h^{+}_{vb} + H_2O \rightarrow H^{+} + OH^{\bullet} \qquad 2.15$$

$$MV^{+\bullet} + H^{+} \rightarrow \frac{1}{2}H_2 + MV^{2+} \qquad 2.16$$

$$CH_4 \rightarrow OH^{\bullet} \rightarrow CH_3^{\bullet} + H_2O \qquad 2.17$$

$$CH_3^{\bullet} + H_2O \rightarrow CH_3OH + \frac{1}{2}H_2 \qquad 2.18$$

Gondal et. al. [81] reported the production of methanol over WO_3 using a visible laser at 514 nm as light source and discussed several mechanistic aspects of methane conversion at room temperature.

2.4 Role of metal ions in photocatalysis

In photocatalytic processes, metal ions are used to enhance the efficiency by suppressing the non-productive electron-hole recombination. The metal ions are selected on the basis of redox potentials of the couples or the reduction potentials of the ions involved. The ions, which have the reduction potential more positive than the conduction band potential of the semiconductor, act as electron scavengers and termed as "electron capture agents". The ions, which have the negative reduction potential as compared to the conduction band potential of the semiconductor, cannot capture the conduction band electron directly and are unable to act as electron capture agents. This effect is strongly dependent on the nature and optimal concentration of ion [17].

$$M^{n+} + SC(ye^-_{cb}) \rightarrow M^{(n-y)+} \qquad 2.19$$

It has been proposed that the metal ions can increase the oxidation rate by participating in heterogeneous pathway but also in an alternative homogeneous Fenton-type reaction [82] that produces additional OH radicals.

$$M^{(n-1)+} + H_2O_2 + H^+ \longrightarrow M^{n+} + OH + HO^- \qquad 2.20$$

Not all the metal ions can react through the reaction mentioned in above equation in the absence of H_2O_2 but oxidation rate can be increased by the addition of external H_2O_2. If the metal is deposited on the surface of semiconductor, Fenton-type reactions cannot take place [83]. In the presence of light classical Fenton-type reactions are changed to photo Fenton-type reactions. In classical Fenton-type reaction, the reduced form of ion is consumed gradually and the reaction is stopped while in case of photo-Fenton reaction, regeneration of reduced metal ions through photochemical reduction, takes place i.e.

$$M^{n+} + e^{-} \longrightarrow M^{(n-1)+} \qquad 2.21$$

2.4.1 Effect of high concentrations of metal ions

High concentration of metal ions has a negative effect on the rate of photo-oxidation reactions. The detrimental effect of high concentration of metal ions is mainly due to the following factors [17]:

- High concentration of metal species competes generally with O_2 for conduction band electrons and reduces the generation of OH through cathode pathway.

- Re-oxidation of metal ions by photogenerated holes.

- $M^{(n-1)+} + h_{vb}^{+} \longrightarrow M^{n+}$ 2.22

- Filter effect by the colored metal ions such as Cu^{2+}, Fe^{2+} and Ni^{2+} due to the absorption of UV light.
- The precipitation of dissolved metal ions as hydroxide on the surface of semiconductor can cause a decrease in rate of photooxidation.

2.4.2 Role of metal ions in photocatalytic splitting of water

Metal ions especially the transition metal ions also influence the rate of heterogeneous photocatalytic oxidation of water, which is used to transfer light energy into chemical energy. Derwant and Mills [84] found that the uphill generation of oxygen by water oxidation on WO_3 was possible in the presence of Fe^{3+} ions. Bamwanda et al. [85] studied the photo-oxidation of water in presence of Ce^{4+} ions and observed an increase of 1.3-1.5 times in photo activity.

Bamwenda et al. [86] studied the splitting of water on WO_3 using UV lamps, in the presence of Fe^{3+}/Fe^{2+} redox couple and observed an enhanced rate of photo-oxidation for oxygen production. Bamwenda et al. [87] also studied the photocatalytic oxidation of water to O_2 over CeO_2, and TiO_2 in the presence of Fe^{3+} and Ce^{4+} and observed the increased generation of O_2 in presence of metal ions as compared to pure semiconductor powders demonstrating the electron capture behavior of these ions by suppressing the electron-hole recombination. Wrighton et al. [88] observed oxygen evolution by irradiation of single crystal TiO_2 and $SrTiO_2$ electrodes in Cu^{2+} solutions at pH 7, even without the external bias. The enhancement of the rate of oxygen evolution by illumination of aqueous suspensions of TiO_2, CdS, $SrTiO_2$ and some Platonized semiconductors in the presence of metal ions as electron acceptors such as Ag^+, $PtCl_4^{2-}$,

$PtCl_8^{2-}$ or $FeCl_3$ has been reported in literature [17,18]. The higher quantum yield of oxygen formation in the presence of Ag^+ with respect to Fe^{3+} has been attributed to the irreversibility of photoreaction i.e.

$$4Ag + 2H_2O \xrightarrow{h\upsilon} 4Ag + O_2 + 4H^+ \qquad 2.23$$

Which alters the enhanced oxygen generation until the reduction of silver is complete. Fe^{3+} is less effective because its reduction renders Fe^{2+} that can compete with water for valence band holes. The advantage of Fe^{3+} compared to other electron acceptors (Ga^{3+}, Ca^{2+}, Cr^{3+}, Ni^{2+} and V^{3+}) is that the reaction does not stop by reversible back reactions because Fe^{2+} does not easily adsorb at the surface of the semiconductor and oxidize back to Fe^{3+} thus causing an increase in water oxidation [89].

The role of metal ions in other photocatalytic processes such as photocatalytic degradation, photocatalytic oxidation etc. is reviewed thoroughly in the literature [90-96].

2.5 Surface modification of photocatalysts

One of the most active areas of research in heterogeneous photocatalysis is the use of semiconductor colloids for the development of a photocatalytic system capable of using natural light for synthetic and environment purpose [97]. In general the photocatalytic activity of a particular semiconductor system is measured by the following factors:

- The stability of semiconductor system under illumination

- The efficiency of photocatalytic process
- The selectivity of products of interest
- Wavelength range of response

For example α-Fe_2O_3 and CdS are capable of absorbing energy in the visible region of solar spectrum, but are usually unstable and photo-degraded with time under illumination [18]. On the other hand, TiO_2 and ZnO are quite stable photocatalysts with a band gap of 3.2 and 3.4 eV respectively. Due to large band gap energies these active photocatalysts can absorb only the UV region of solar spectrum, which is less than 10 % of the total solar spectrum [98].

The limitation of a particular semiconductor as a photocatalyst can be compensated by modifying the surface of semiconductor. The major benefits of modifying the surface of a photocatalyst are as under:

- Inhibiting the rate of recombination by increasing charge separation and thereby enhancing the efficiency of photocatalytic process
- Increasing the wavelength response range (excitation of wide band gap semiconductors by visible light)
- Changing the yield or selectivity of a particular product

Several modification techniques have been identified and investigated over the years. The main aim of all types of modifications is to achieve the above mentioned objectives. The major modifications are as follows:

- Metal semiconductor modification
- Surface sensitization
- Impurity sensitization
- Composite sensitization

Metal semiconductor modifications are used primarily to inhibit charge recombination and increase the selectivity of a particular product. Surface sensitization has been extensively used to make the wide band gap semiconductors especially responsive to visible wavelengths. Impurity sensitization is used to alter the n-type or p-type behaviors of the semiconductor by adding or withdrawing a metal dopant. Composite semiconductors employ two or more semiconductors coupled to bring about material characteristics different from the individual semiconductors.

In this study, the surface of WO_3 was modified by using different transition metals and the effect of these modifications was studied towards different photocatalytic activities such as splitting of water and methane conversion for the synthesis of methanol in aqueous suspensions. In this contest, only the metal semiconductor modifications will be discussed in detail.

In photocatalysis, the addition of metals to a semiconductor surface changes the efficiency of a photocatalytic process by changing the surface properties of semiconductor. The contact between a semiconductor and metal generally involves a redistribution of charges and formation of double layer at metal-semiconductor interface. The transfer of mobile charge carriers (i.e. electrons and holes) between the semiconductor and metal produces a space charge layer. For an n-type semiconductor (see for example figure 2.2) due to the immigration of electrons towards the surface interface the surface region becomes negatively charged. To preserve electrical neutrality, a positive space charge layer develops within the semiconductor causing a shift in electrostatic potential and a bending of bands upwards towards the surface. Isolated from each other and electrically neutral, the metal and semiconductor has different Fermi level positions [99]. When two materials are connected electronically, electron migration from the semiconductor to the metal occurs until the two Fermi levels are aligned, forming a space charge layer. The surface of the metal acquires an excess negative charge and because of electron migration away from the barrier region, the semiconductor exhibits all excess positive charge. The bands of the semiconductor bend upward towards the surface and the layer is called as deletion layer. The barrier formed at the metal-semiconductor interface is called as schottky barrier. The schottky barrier formed at the metal-semiconductor interface can serve as efficient electron trap preventing electron-hole recombination a explained in figure 2.2.

The presence of noble metals at semiconductor can enhance the yield of a particular product or the rate of photocatalytic reaction. The enhancement in photocatalytic activity was first observed for the photocatalytic splitting to H_2 and O_2 using Pt/TiO_2 system [100]. Pt changes the surface properties of TiO_2 by changing the electron distribution. The decrease in electron density within the semiconductor also enhances the acidity of surface hydroxyl groups.

The electronic modification of the semiconductor surface via metal deposition can be observed with other metals. Ag has been well studied for surface modification effects

[101]. Taylor et al. [102] modified the surface of WO_3 with La and observed a noticeable increase in the yield of methanol by methane conversion.

Transition metal doping can expand the response of suspended metal oxide particles to the visible range [103]. On such doped materials, enhanced photocatalytic activity for the reduction of CO_2 [104] and N_2 [105] have been reported. Enhancement in the rate of photoreduction upon metal ion loading of a semiconductor can produce a photocatalyst with an improved trapping to recombination ratio [106]. The increase in photocatalytic activity is sensitive to dopant level. For TiO_2, although Fe^{3+} doping increases carrier life time but it sharply reduces the efficiency at higher levels [107]. The effect of transition metal ion dopants is somewhat difficult to generalize for all systems [108].

Some transition metal dopants such as Fe^{3+} and V^{4+} inhibit electron-hole recombination and enhance the rate of photoreduction. On the other hand, sustained water splitting was observed in presence of Cr^{3+} over TiO_2 [18].

In photo-degradation of Phenol, the photocatalytic activity of TiO_2 is not affected by the presence of Cr^{3+} or Fe^{3+} ions. The difference in the activity between the photoreduction of N_2 and photo-oxidation of Phenol has been attributed to the difference in the gas-liquid and liquid-solid interfaces [109]. From a chemical point of view, doping of a semiconductor oxide is equivalent to the introduction of defect sites on the surface.

The difference of photo-reactivity between Fe^{3+}/TiO_2 and Cr^{3+}/TiO_2 is correlated to difference of diffusion length of the infinity carriers. The diffusion length is 1.0μm for pure TiO_2, 0.2μm for Cr^{3+}/TiO_2 and 2.0μm for Fe^{3+}/TiO_2 [110], which suggest the enhanced electron-hole recombination for Cr^{3+}/TiO_2 than Fe^{3+}/TiO_2.

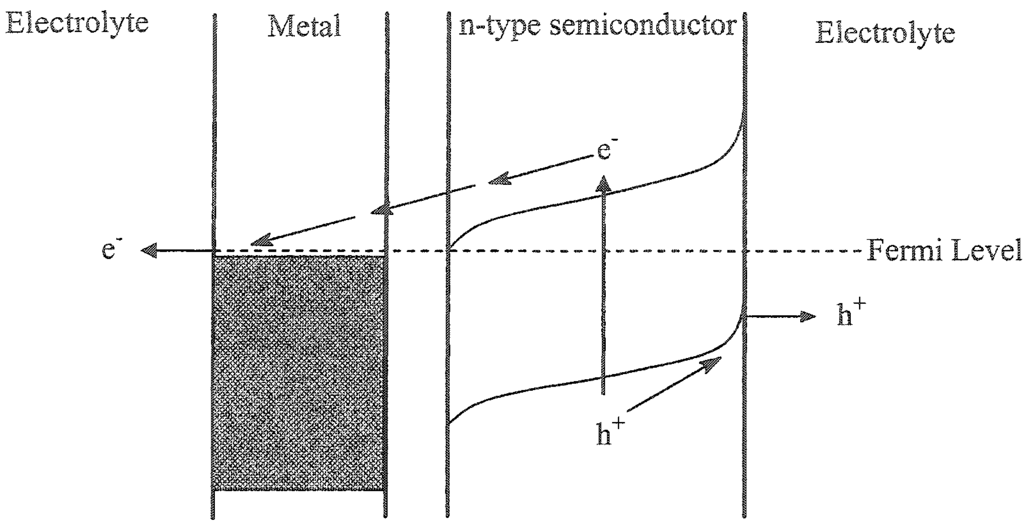

Figure 2.2 Mechanism of electron transfer at semiconductor/metal/electrolyte interface

The polyvalent cation such as Vanadium, Molybdenum, Ga^{3+}, Cr^{3+} and Sb^{5+} affects the photocatalytic activity of TiO_2 negatively [111, 112]. It is postulated that the electrons in the d-orbital of Vanadium and Molybdenum act as donors to quench the photo-generated holes before diffusion to surface. The same was observed for Ga^{3+}, Cr^{3+} and Sb^{5+}. Surface adsorbed Ag^+ ions enhance water oxidation by photo-generated holes through efficient trapping of the photo-generated conduction band electrons [37].

In aqueous semiconductor dispersions of metal-doped semiconductors, metal ions present at the surface in the form of oxides contribute to increase semiconductor photo activity through their interaction with peroxo species produced on the surface of the photocatalyst and in solution [18].

CHAPTER THREE

EXPERIMENTAL DETAILS

The experimental work, in this dissertation, comprises:

- Pre-treatment of pure photocatalysts
- Synthesis & characterization of transition metal doped WO_3 photocatalysts
- Designing & fabrication of photocatalytic reactors
- Experimental setups for various photocatalytic studies

In this chapter, all the experimental details and procedures regarding the above-mentioned tasks along with the observed preliminary changes, with respect to various photocatalysts, during the photocatalytic studies are explained.

3.1 Synthesis of photocatalysts

In this section, the detailed procedure for the synthesis of various catalysts used in this study will be discussed.

3.1.1 Synthesis of WO_3 Photocatalyst

Tungsten oxide (WO_3) was obtained by heating tungstic acid (H_2WO_4) for seven hours at 300°C (after which the sample color became yellow to yellow green) then the temperature was raised to 500°C at a rate of 10°C, kept at 500oC for another seven hours (after which the color became pale yellow) which was considered as an indication for complete removal of water as well as excess oxygen.

3.1.2 Synthesis of Transition Metal-doped WO_3 Photocatalysts

To synthesize of metal-doped WO_3 wet impregnation technique [18], was used. An appropriate amount of respective metal nitrate was dissolved in water and mixed with the required amount of tungstic acid (H_2WO_4). The specifications of the metal nitrates used along with the change in color of WO_3 due to the presence of transition metals at the surface before and after illumination under 355 nm laser photon flux are reported in tables 3.1 and 3.2 respectively. Excess water was removed by heating at $100^{o}C$ with continuous stirring. The slurry was dried at $100^{o}C$ and the nitrates were decomposed by heating at $300^{o}C$. The formation of reddish brown NO_2 gas confirmed the decomposition of nitrates. The dried powder was then transferred to a china crucible and calcined in temperature controlled furnace at $300^{o}C$ for 5 hours for complete removal of nitrates. The powder was than sintered at $500^{o}C$ in air. The heating rate was kept at $10^{o}C$/min. All the steps related to the synthesis of doped catalysts are presented in the figure 3.1.

3.1.3 Pre-treatment of TiO_2, NiO and α-Fe_2O_3 Photocatalysts

Along with WO_3, the other pure photocatalysts used in this study were TiO_2, NiO and Fe_2O_3 of high purity. These photocatalysts were purchased and used after being subjected to the same heat treatment as WO_3 and other doped catalysts. The specifications of these powders along with the changes in their color are presented in table 3.3.

3.2 Characterization of synthesized photocatalysts

The synthesized catalysts were characterized by using the following techniques.

3.2.1 UV-Visible Spectroscopy

UV-Visible spectroscopy was applied to determine the spectral response of the synthesized catalysts. A weight of 10 mg of properly grinded catalyst powder was suspended in 100 cm^3 of deionized water. After shaking it well the suspension was allowed to stabilize for a period of 15 minutes. The sample was transferred to a quartz cell with a path length of 1 cm. De-ionized water was used as blank. The absorbance spectra was recorded by using a SHIMADZU UV-Visible spectrophotometer, Model UV-1601PC, in the wavelength range of 200-800 nm. The measured absorbance spectrum was used to evaluate the maximum spectral response i.e. maximum absorption and relative light harvesting ability of each catalyst. The direct bandgap of each catalyst was calculated by using the procedure reported in the literature [113].

3.2.2 Scanning Electron Microscopy (SEM)

The morphology and the approximate composition of the synthesized powders were studied by scanning electron microscopy (SEM) supplied by JEOL Corporation, Model JSM 5800 LV, and X-ray electron dispersive spectroscopy (EDS). For analysis, the sample was placed on the stub by using a conductive two-sided copper tape. For the analysis of Cu-doped WO_3 samples conductive aluminum tape was used instead of copper tape. For gold coating, the sample was placed in the vacuum chamber at a pressure of $3x10^{-3}$mbars. The sample was gold coated by adjusting the current between 20-25mA. The sample was removed from the vacuum chamber by releasing the pressure slowly. After gold coating the stub was placed in the sample holder of the microscope and photographed by using the attached Polaroid camera. The instrumental parameters, such as magnification and electron beam intensity, were kept constant for all the samples. EDS analysis was also performed simultaneously for each sample.

3.2.3 X-ray photoelectron spectroscopy (XPS)

XP spectra of synthesized powders were recorded by X-ray photoelectron spectroscopy (XPS) supplied by VG Scientific, UK, Model ESCALAB MK-II, using Al K_α radiation. The working pressure was less than $2x10^{-7}$ Nm^{-2}. The spectrometer was calibrated by using the binding energy (BE) of the Au $4f_{7/2}$ line at 83.98 eV, the $Cu2p_{3/2}$ line at 932.67 eV and Cu LMM at 567.96 eV. The C1s peak of hydrocarbon contamination set at 284.8 eV was used as internal reference for absolute binding energies. Detailed scan were recorded for C1s, O1s, W4f and the respective doped metals. The analysis involved non-linear background subtraction, non-linear least-square curve fitting using mixed Gaussian-Lorentzian functions and peak area determination by integration. The precision in the binding energy values of XPS lines was estimated as ±0.15 eV. The quantitative analysis was based on sensitivity factors supplied by the manufacture. All the samples were analyzed as such after being homogenized.

3.3 Designing and fabrication of photocatalytic cells

This section includes the specifications of the cells designed and fabricated to study the evolved gases during the photocatalytic process under 355nm UV laser irradiation. The cell was equipped with a 2.0 cm diameter quartz window and outlets for liquid and gas sampling. The cell is described in detail in figures 3.2. For the measurements of dissolved oxygen and pH changes during the photocatalytic processes, the cell was modified to accommodate the probes of dissolved oxygen and pH meter probes.

3.4 Experimental setup for photocatalytic studies

The details about both the experimental setups i.e. for photocatalytic studies and for pH and dissolved oxygen measurements are given in figures 3.3. The Major difference between the two setups is the photocatalytic cell. Both the cells were designed according to the type of study and measurement of products. To induce the photocatalytic process for water splitting, 355 nm laser radiations were employed. The 355 nm high power laser beam was generated from the third harmonic of a Spectra Physics Nd:YAG laser (Model GCR 250). The pulse width of the laser was ~8 ns with a 10 Hz repetition rate. The beam was directed into the center of the cell window by using mirrors and lenses. The energy of the laser beam required, was adjusted by using a digital power meter. Here it is important to mention that in order to minimize the effects of the focused laser beam itself the laser beam diameter was adjusted at 10mm. For homogeneous distribution of catalyst in aqueous suspension, a Teflon coated magnetic bar and a magnetic stirrer was used. The stirring rate was kept constant for all the experiments. The flow of the purge and feed gases was adjusted by using flow controller.

3.5 Nd:YAG laser GCR 250

The Nd:YAG is the most versatile solid state laser system. It can operate as a cw laser, a pulsed laser with both long pulse (spiking mode) or Q-switched outputs and as a mode-locked laser. The laser consist of a pump source, usually a flash lamp, and a Laser rod contained in an elliptical reflector structure. The laser resonator with components such as Q-switch, polarizer and etalon complete the optical system. The flash lamp is driven by a discharge current that is usually switched from a storage capacitor. The capacitor is charged from a pulse charging power supply. The power supply is completed with a timing circuit, a Q-switch circuit and a water circulation system for cooling the lamps and laser rod.

The Nd:YAG Laser rod consists of a host material which is the YAG crystal (Yttrium aluminum garnet $Y_3Al_{15}O_{12}$) and an active lasing ion which is Nd^{3+} ion. It is a four level laser system.

The laser system (Nd:YAG laser system, Model GCR 250, Spectra Physics) used in this dissertation for photocatalytic studies consists of an oscillator and an amplifier. The oscillator constitutes of a 100% mirror, Q-switch, polarizer, the laser head containing the oscillator rod, etalon and the output mirror. The amplifier consists of the laser head in which the Nd:YAG amplifier rod is housed. The laser head (oscillator and amplifier) is cooled with distilled water, which circulates around the rod to remove excessive heat from the system. Dry nitrogen is used to keep the optical surfaces clean from dust. The oscillator and amplifier output energies increase with increasing flash lamp energy.

Using the harmonic generator, which contains the KDP (potassium dihydrogen phosphate) crystal, the emitted laser 1064nm is frequency tripled to obtain radiation at 355nm. The 355nm radiation is separated from the fundamental wavelength of 1064 nm and a second harmonic wavelength of 532nm by using a dichroic separator. The emitted laser light is in the form of pulses with a pulse width of 10 ns and a pulse repetition rate of 10 Hz. This laser light is within the UV region and thus very useful for the study of photocatalytic processes.

3.6 Experimental procedure for photocatalytic studies

While studying the laser induced photocatalytic processes over WO_3, it was observed that the changes in various parameters i.e. laser energy, laser beam diameter, stirring rate and amount of catalyst greatly affects the products yield. Out of these four parameters, two parameters i.e. beam diameter and stirring rate were kept constant while the other two parameters i.e. amount of catalyst and laser energy were carefully optimized on the basis of dissolved oxygen changes measured by using a dissolved oxygen meter. The following procedure was adopted to optimize the above-mentioned parameters.

3.6.1 Optimization of parameters for photocatalytic studies

To optimize the amount of catalyst, different amounts of the catalyst ranging from 50 mg to 500 mg were suspended in 60 ml of deionized water and illuminated with a laser beam at fixed energy of 100 mJ for a period of 20 minuets. A dissolved oxygen meter (Hanna Model, HI 9143) was used to measure the oxygen produced. This dissolved oxygen meter was calibrated by a routine procedure as prescribed by the manufacturer. A satisfactory reproducibility was observed in successive measurements. The yield of oxygen was then plotted as a function of the amount of catalyst. The amount of the catalyst, for which the maximum yield of oxygen was observed, was taken as the optimum amount of the catalyst and kept constant for rest of the experiments.

For the optimization of the laser energy, the optimized amount of the catalyst obtained from the previous experiment was suspended in 60 ml of deionized water and exposed to laser energy in the range of 20 to 200 mJ for a fixed interval of 20 minutes. The change in the yield of oxygen was recorded by using the dissolved oxygen meter as discussed above. For different energies of laser a fresh suspension of the catalyst was prepared and used. The value of optimized laser energy was calculated by plotting the yield of oxygen versus laser energy. The laser optimized energy in this step was then kept constant for rest of the studies. The photocatalytic cell and detailed experimental setup is presented in figures 3.2 and 3.3 respectively.

3.6.2 Photocatalytic splitting of water

To study the photocatalytic splitting of water using pure and doped photocatalysts, an optimum amount of each photocatalyst (determined from the procedure mentioned earlier) was suspended in 60 cm^3 of distilled water whereas for water splitting studies in the presence of metal ions, the optimized amount of the catalyst was suspended in a 60 cm^3 solution of the respective metal ion. For this purpose, a 10 ppm solution of each metal ion was prepared by dissolving the stoichiometric amount of each metal nitrate in 1000 cm^3 of doubly distilled de-ionized water. To minimize the optical effects i.e. self-absorption of laser light by the metal ion, a 10 ppm solution was used.

An inert atmosphere was produced by purging with argon gas at a high flow rate of 200 ml/min for a period of 15 minutes. The purpose of such a high flow rate was to remove all the dissolved oxygen. The progress of argon purging was studied by analyzing the gas sample from the dead volume of reaction chamber. All the reactions were carried out in argon environment and at room temperature. The other important parameters i.e. the stirring rate and beam diameter were kept constant during all measurements.

A Shimadzu gas chromatograph (GC-17A) equipped with a thermal conductivity detector (TCD) and a 30m molecular sieve 5A "PLOT" column was used to analyze the gaseous products of photocatalytic process. Argon was used as carrier gas in GC as well as a purge gas to remove dissolved oxygen from the photocatalytic reactor. The injector, column and detector temperatures were kept at 50°C, 50°C and 100°C respectively. Because of the high concentration of O_2 in the air, the product gases were analyzed by carefully removing 100μl of the sample from the dead volume of the cell using a gas tight syringe. The amount of produced gases were determined by analyzing against a gases standard, provided by SCOTTY, England, containing 1.0 Mol% of each gas in nitrogen base. Several reproducibility tests were performed over a range of various irradiation times. The uncertainty in the measurement of H_2 and O_2 yield was found to be less than ±3% which was acceptable for the purpose of the present studies.

A pH meter (Hanna Model, 8519) with an option of conductivity measurement was used to measure pH during the coarse of reaction under illumination. Prior to use for pH measurements under illumination, the pH meter was calibrated by using buffers of pH 4, 7 and 10. An acceptable reproducibility in the results was observed as the results achieved in this regard were reproducible over the period of interest.

3.6.3 Photocatalytic conversion of methane into methanol

To study the photocatalytic conversion of methane into methanol, the optimized amount of the catalyst under study (determined by the procedure mentioned earlier), was suspended in 60 ml of water. Instead of purging the catalyst suspension with argon, methane was bubbled through the suspension for 15 minutes at a flow rate of 100 ml/min and the cell was sealed at atmospheric pressure. The suspension was illuminated with 355 nm laser having a beam diameter of 10 mm. The progress of the reaction was studied by measuring the amount of hydrogen produced and change in methanol concentration with time. Separate batch experiments were performed to measure the production of hydrogen and methanol. To measure the produced hydrogen, the sample from the dead volume of reaction cell, was analyzed at regular 15 minutes intervals by using a Shimadzu gas chromatograph (GC-17A) equipped with a thermal conductivity detector and a 30m molecular sieve 5A "PLOT" column. Argon gas was used as carrier at a flow rate of 10 ml/min. To estimate the amount of methanol during the reaction, liquid samples were drawn from the reaction cell at a regular interval of 10 minutes, centrifuged and analyzed by using a gas chromatograph (supplied by Agilent Technologies) equipped with an FID detector and a 2m Chromosorb-101 packed column. Helium gas was used as carrier at a flow rate of 25 ml/min. The injector, column and detector temperatures were set at 250°C, 200°C and 250°C respectively. Both gas chromatographs were calibrated by using external standards prior to sample analysis. The reproducibility of the process was checked by repeating the experiments at regular intervals while the reproducibility of the analysis was estimated by running the standards from time to time.

Table 3.1 The specifications of metal nitrates used in doping of WO_3

Chemical	Chemical form	Manufacturer	Purity
Ferric nitrate	$Fe(NO_3)_3.9H_2O$	Fisher Scientific Co. USA	> 99%
Cobalt nitrate	$Co(NO_3)_2.6H_2O$	Fisher Scientific Co. USA	> 99%
Nickel nitrate	$Ni(NO_3)_2.6H_2O$	Fisher Scientific Co. USA	> 99%
Copper nitrate	$Cu(NO_3)_2.3H_2O$	Fluka Chemie AG. Germany	> 99%
Zinc nitrate	$Zn(NO_3)_2$	Fisher Scientific Co. USA	> 99%
Silver nitrate	$AgNO_3$	Fisher Scientific Co. USA	> 99%

Table 3.2 Color changes in WO_3 after transition metal doping and illumination respectively

Metal-WO_3	**Catalyst**	**Color of catalyst/suspension (before illumination)**	**Color of catalyst/suspension (after illumination)**
Fe-WO_3	0.1% Fe-WO_3	Pale yellow	Green blue
	1.0% Fe-WO_3	Brown yellow	Light green blue
	10% Fe-WO_3	Brown	Black
Co-WO_3	0.1% Co-WO_3	Pale yellow	Green blue
	1.0% Co-WO_3	Grey-yellow	Light green blue
	10% Co-WO_3	Grey	Black/pink
Ni-WO_3	0.1% Ni-WO_3	Pale Yellow	Green blue
	1.0% Ni-WO_3	Green yellow	Black blue
	10% Ni-WO_3	Green-black	black
Cu-WO_3	0.1% Cu-WO_3	Light Yellow	Green blue
	1.0% Cu-WO_3	Yellow	Light green blue
	10% Cu-WO_3	Deep yellow	Light green blue
Zn-WO_3	0.1% Zn-WO_3	Light Yellow	Green blue
	1.0% Zn-WO_3	Light Yellow	Light green blue
	10% Zn-WO_3	Pale-Yellow	Very light blue shade
Ag-WO_3	0.1%Ag-WO_3	Light-yellow	Green blue
	1.0% Ag-WO_3	Yellow	Brown yellow/brown
	10% Ag-WO_3	Deep yellow	Dark brown/dark brown

Table 3.3 Specifications of WO_3, TiO_2, NiO and α-Fe_2O_3 and colors before and after illumination

Chemical	**Chemical form**	**Manufacturer**	**Color Before illumination**	**Color After illumination**
Tungsten oxide	WO_3	Derived from H_2WO_4 at 500°C	Pale-yellow	Green blue
Titanium dioxide	TiO_2	Fisher Scientific Co. USA	White	Grey
Nickel oxide	NiO	Fisher Scientific Co. USA	Green	Black
Iron oxide	Fe_2O_3	Fisher Scientific Co. USA	Red	Black

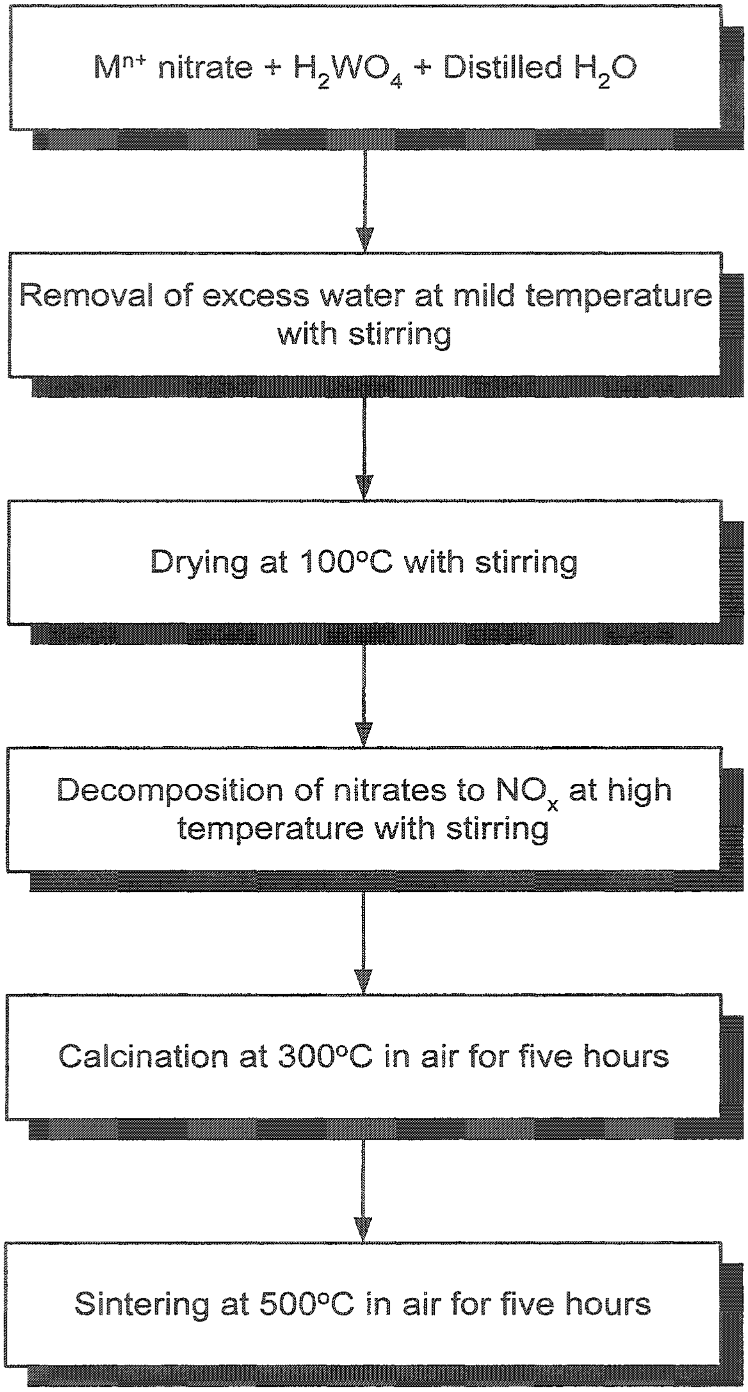

Figure 3.1 Flow diagram for the synthesis of transition metal doped WO_3 photocatalysts

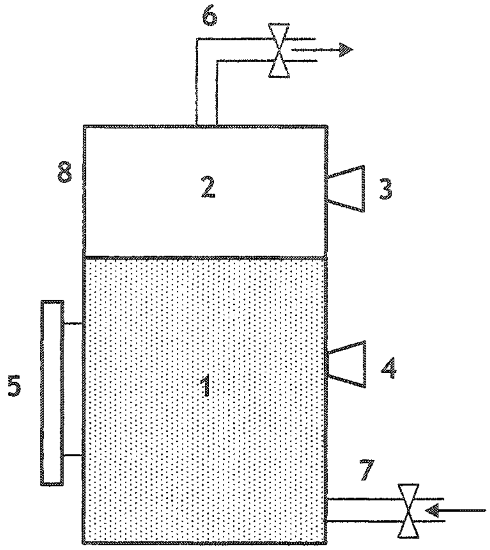

CELL DIMENSIONS

Total volume : 130 cm^3
Quartz window : 2 cm
Diameter : 4.5 cm
Effective Diameter : 4.0 cm

CELL COMPONENTS

1. Effectve volume of cell
2. Dead volume of cell
3. Gas sampling valve
4. Liquid sampling valve
5. Quartz window with 8% reflection
6. Gas outlet
7. Gas inlet
8. Pyrex cell body

Figure 3.2 Photocatalytic cell for measuring evolved gases and liquid products during photocatalytic process

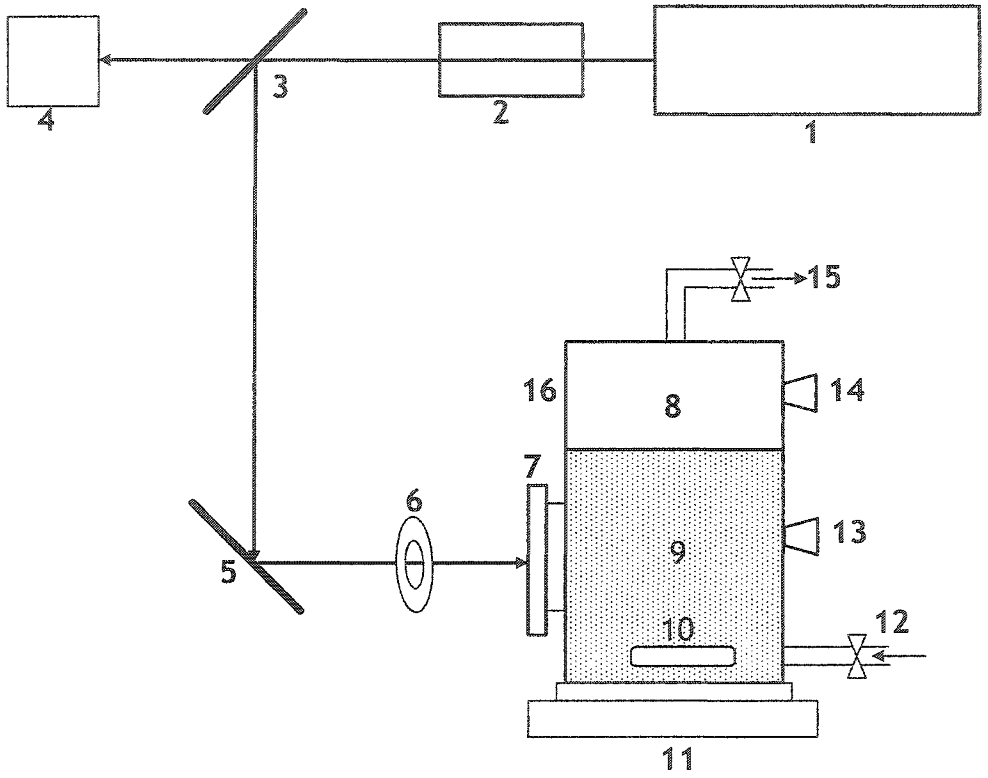

1. Nd:YAG Laser (1060nm)
2. Third harmonic generator (355 nm)
3. Beam splitter
4. Laser energy meter
5. Mirror
6. Beam diameter controller
7. Quartz window
8. Dead volume of cell
9. Effective volume of cell
10. Megnatic stirrer
11. Megnatic plate
12. Gas inlet
13. Liquid sampling valve
14. Gas sampling valve
15. Gas outlet
16. Pyrex cell

Figure 3.3 Setup for measuring evolved gases and liquid products during photocatalytic process

CHAPTER FOUR

ANALYSIS AND CHARECRERIZATION OF SYNTHESIZED CATALYSTS

In this chapter, the characterization of transition metal doped WO_3 are presented and the techniques used to arrive at these characteristics are described.

4.1 UV-Visible spectroscopy

UV–Visible spectroscopy is concerned with the valence electronic transitions between molecular orbitals. These transitions between the electronic levels are located in the range 100-1000 nm. The electronic transitions found in transition metal oxides can be classified as:

- d-d transitions
- Charge transfer (p-d) transitions

The d-d transitions are of lower energy relative to charge transfer transitions and occur in the visible region. Charge transfer transitions are due to electron transfer from an occupied orbital localized on a donor to an unoccupied orbital of an acceptor. The charge-transfer phenomena are of two types, involving an electron transfer in different directions:

(i) From an orbital localized on the transition metal to that localized on the ligand (oxygen) i.e. M-L

(ii) From an orbital localized on the ligand (oxygen) to that localized on the transition metal M i.e. L-M

The energies of these transitions are higher than that for d-d transitions, and accordingly, the absorption occurs in the UV region of the spectra. The energies associated with these electronic 'jumps' are large enough to provoke vibrations of the molecule, and the absorption bands are therefore broadened.

For un-doped WO_3, the basic transition is the transfer of electrons from t_{2g} to e_g i.e. d-d transitions and the transfer of electrons from the HOMO i.e. the 2p orbitals of oxygen to LUMO i.e. the 4f orbitals of W, creating an electron-hole pair i.e. a charge transfer transition. The energy required to carry out the charge transfer transition is termed as bandgap energy, E_g. In terms of UV-Visible absorption spectroscopy, the band gap is defined as the "onset" of absorption. The procedure adopted to determine the bandgaps of synthesized powders will be discussed, in detail, in section 4.1.1.

For doped WO_3, the transition metals present at the surface, contribute to both d-d and charge transfer transitions. In charge transfer transitions, for doped WO_3, the electron from the oxygen 2p orbitals is first transferred to 4f orbitals of tungsten and then to the low lying d-orbital of the doped metal. In addition, the possibility of electron transfer directly from the oxygen to doped metal cannot be ignored. In this study, the absorption spectra of pure and doped WO_3 were recorded in an aqueous environment in the range from 200 nm to 1000 nm. A shift in the absorption maximum towards longer wavelength (red shift) compared to that of 312.5 nm for pure WO_3 was observed for all catalysts except for 10% Zn-WO_3 which was blue shifted. The comparison of absorption spectra of doped WO_3 with that of undoped WO_3 is presented in figure 4.1-4.7. The wavelengths of maximum absorption (λ_{max}) for all powders and their shifts with respect to un-doped WO_3 are summarized in table 4.1.

4.1.1 Bandgap determination

Basically, there are two types of optical transitions that can occur at the fundamental edge of crystalline semiconductors: direct and indirect transitions. Both involve the interaction of an electromagnetic wave with an electron in the valence band, which is raised across the fundamental gap to the conduction band of the semiconductor. However, indirect transitions also involve simultaneous interaction with lattice vibrations [113]. The bandgap is related to the absorption coefficient (α) and the energy of the incident radiation photon as follows:

$$\alpha h \upsilon = (E - E_g)^n \qquad 4.1$$

Where

α = Absorption coefficient

h = planks constant

υ = Frequency of incident light

E = Energy of incident light

E_g = Band gap of semiconductor

Where n = 0.5 for direct allowed transitions and n = 2 for indirect allowed transitions. Due to high density of states (DOS) in solids high values of absorption coefficient, α, in the range of 10^5-10^6 are observed. As the direct evaluation of α in aqueous suspension is usually not exact, the method described by Cassagneau et. al. [114], was used to evaluate it and to determine the bandgap energy of synthesized transition metal doped WO_3. According to this method α is defined as follows:

$$\alpha = (\frac{2.303\rho 1000}{lCM})A(cm^{-1}) \qquad 4.2$$

Where

ρ = Density of powder in g/cm^3

l = Absorption path length in cm

C = Concentration of suspension in mol/cm^3

M = Molecular weight of powder in g/mol

Based on the procedure described by Cassagneau et. al. [114], the bandgap energies of the synthesized catalysts were estimated by plotting $(\alpha h\upsilon)^2$ $(eV/cm)^2$ versus hυ (photon energy in eV). The intercept of the extrapolated straight line on x-axis was taken as bandgap energy.

The calculated bandgap energy of 2.65 eV for pure WO_3 was in agreement with the literature [44-46, 85-87]. With few exceptions a decrease in the bandgap energies was observed for all doped powders. The values of the bandgap energies calculated for WO_3 doped with various concentrations of transition metals are listed in table 4.2. The graphical determination of the bandgap energies for pure and transition metal doped WO_3 is presented in figure 4.8-4.14.

Table 4.1: Wavelengths of maximum absorption (λ_{max}) of WO_3 doped with various concentrations of transition metals and their shifts with respect to un-doped WO_3

DOPANT	**Maximum Absorption wavelength (λ_{max})**		
	0.1 % Dopant/ WO_3	**1.0 % Dopant/WO_3**	**10.0% Dopant/ WO_3**
Fe	330.5 (R)	365.0 (R)	375.0 (R)
Co	319.0 (R)	329.0 (R)	390.0 (R)
Ni	337.0 (R)	388.0 (R)	319.0 (R)
Cu	350.0 (R)	338.0 (R)	334.0 (R)
Zn	352.5 (R)	360.5 (R)	305.0 (B)
Ag^{+1}	359.5 (R)	336.0 (R)	431.5 (R)

R = Red shift with respect to pure WO_3
B = Blue shift with respect to pure WO_3

Table 4.2: Bandgap energies of WO_3 in the presence of various concentrations of dopants

DOPANT	**BANDGAP (eV)**		
	0.1 % Dopant/ WO_3	**1.0 % Dopant/ WO_3**	**10.0% Dopant/ WO_3**
Fe	2.45	2.1	2.09
Co	2.43	2.60	1.9
Ni	2.35	2.35	1.85
Cu	2.29	2.33	2.2
Zn	2.2	2.2	2.4

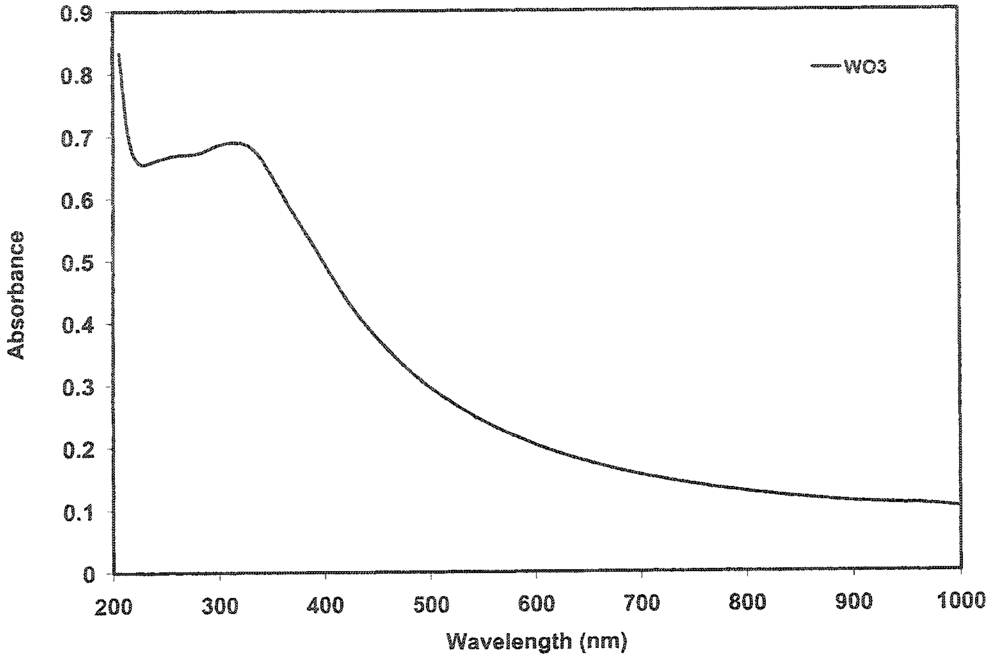

Figure 4.1: Absorption spectra of un-doped WO_3

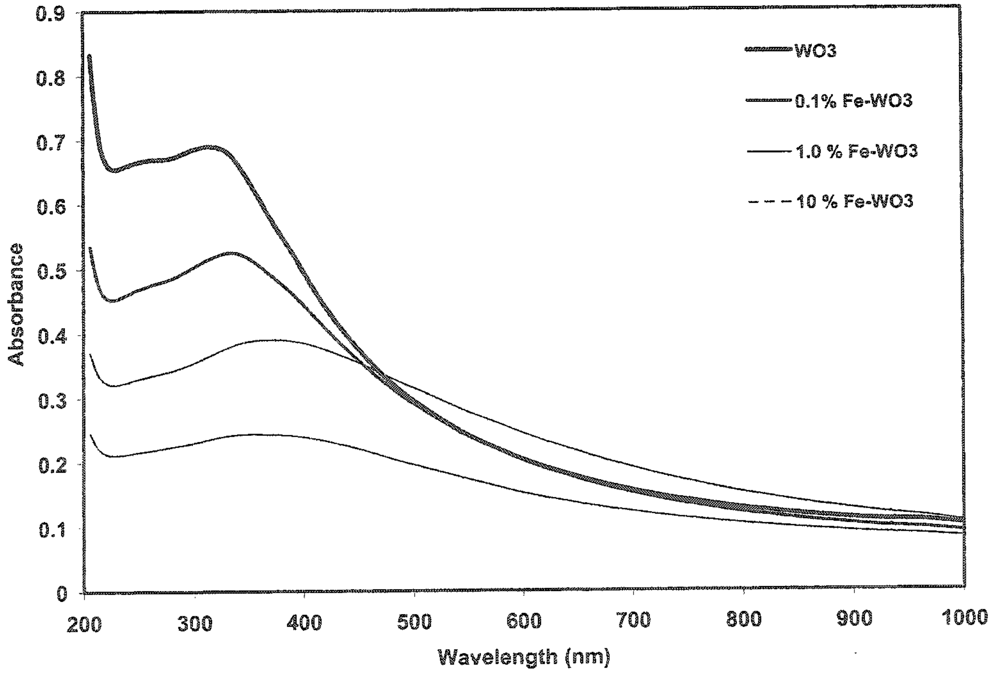

Figure 4.2: Absorption spectra of WO_3 in the presence of various concentrations of Fe as dopant.

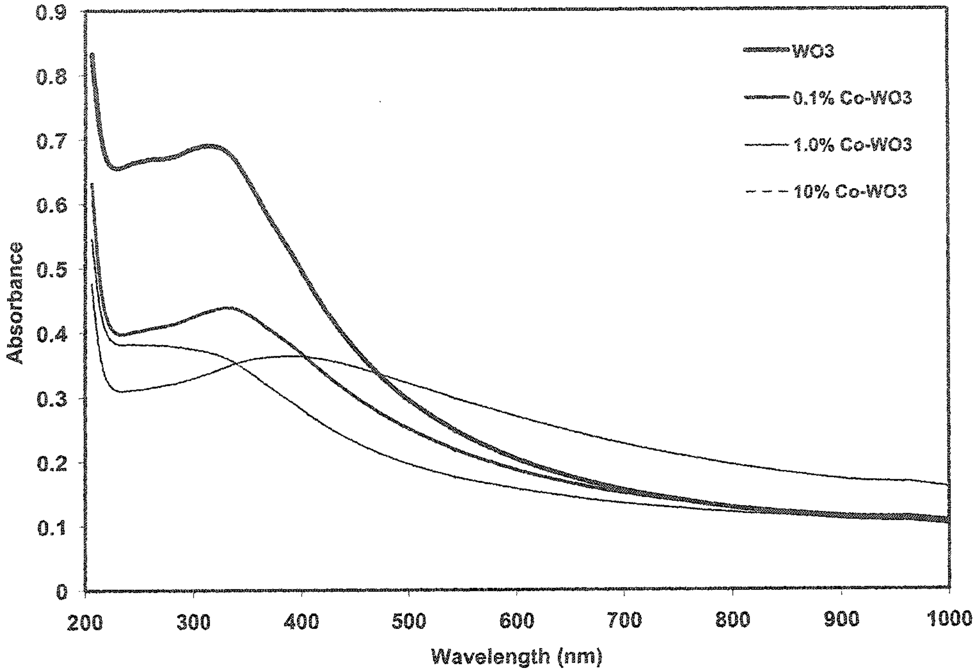

Figure 4.3: Absorption spectra of WO_3 in the presence of various concentrations of Co as dopant.

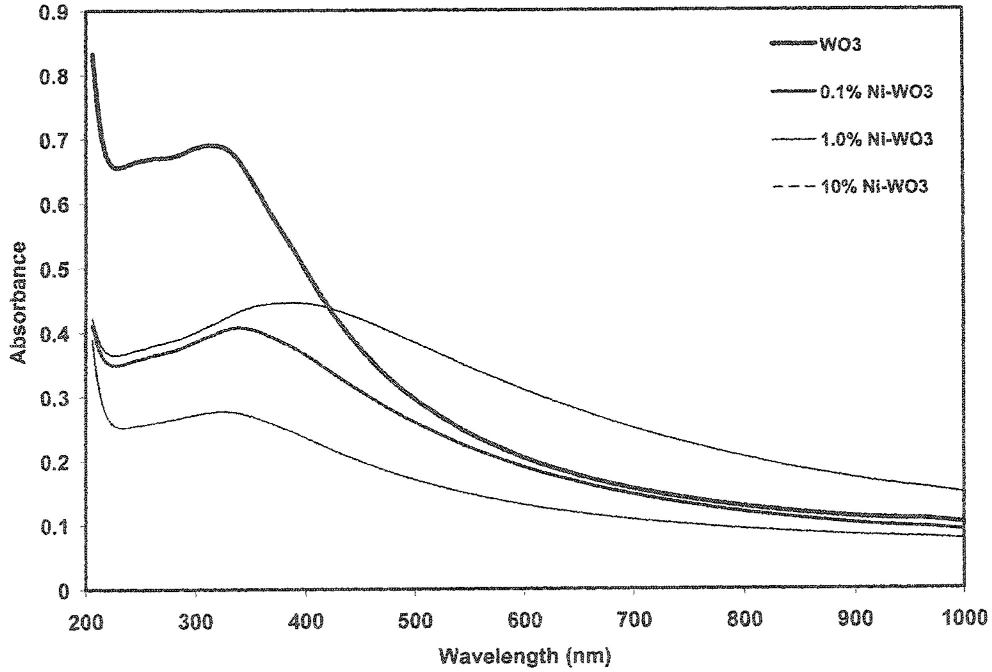

Figure 4.4: Absorption spectra of WO_3 in the presence of various concentrations of Ni as dopant.

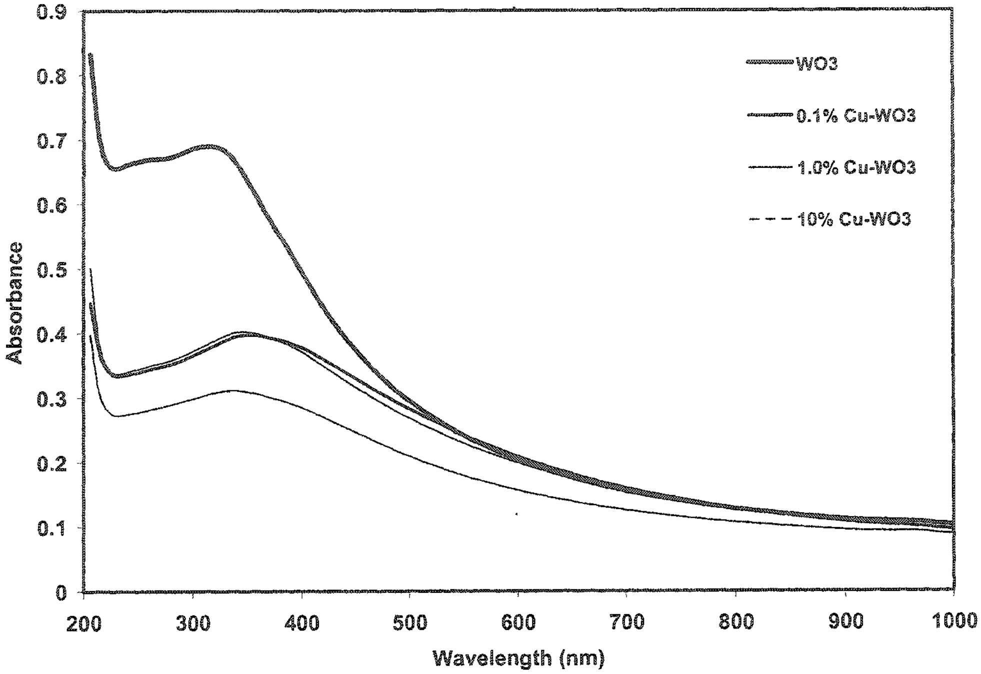

Figure 4.5: Absorption spectra of WO_3 in the presence of various concentrations of Cu as dopant.

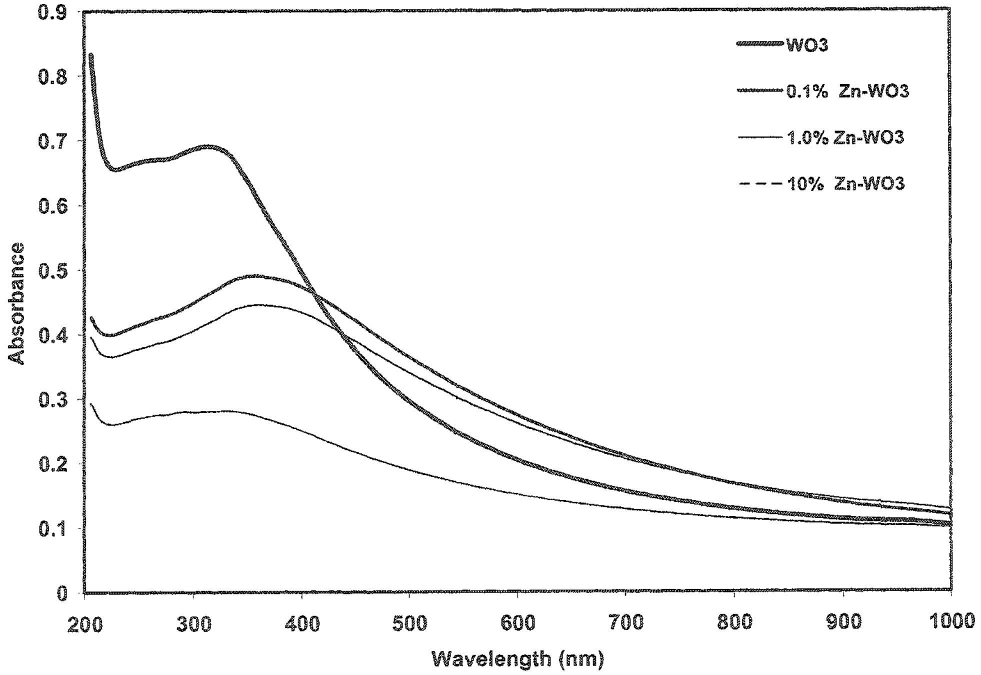

Figure 4.6: Absorption spectra of WO_3 in the presence of various concentrations of Zn as dopant.

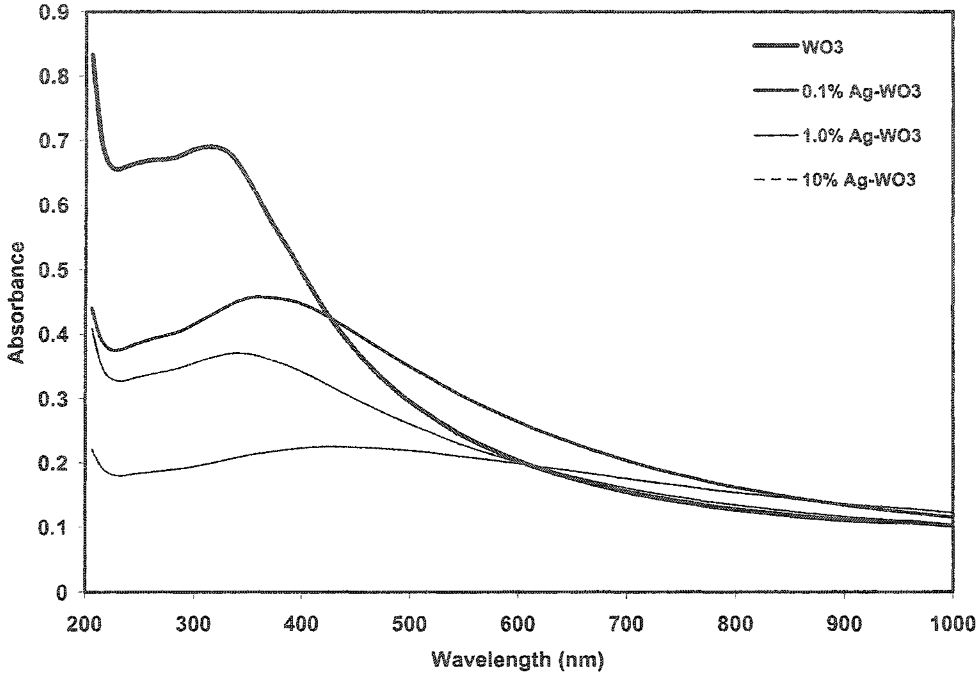

Figure 4.7: Absorption spectra of WO_3 in the presence of various concentrations of Ag as dopant.

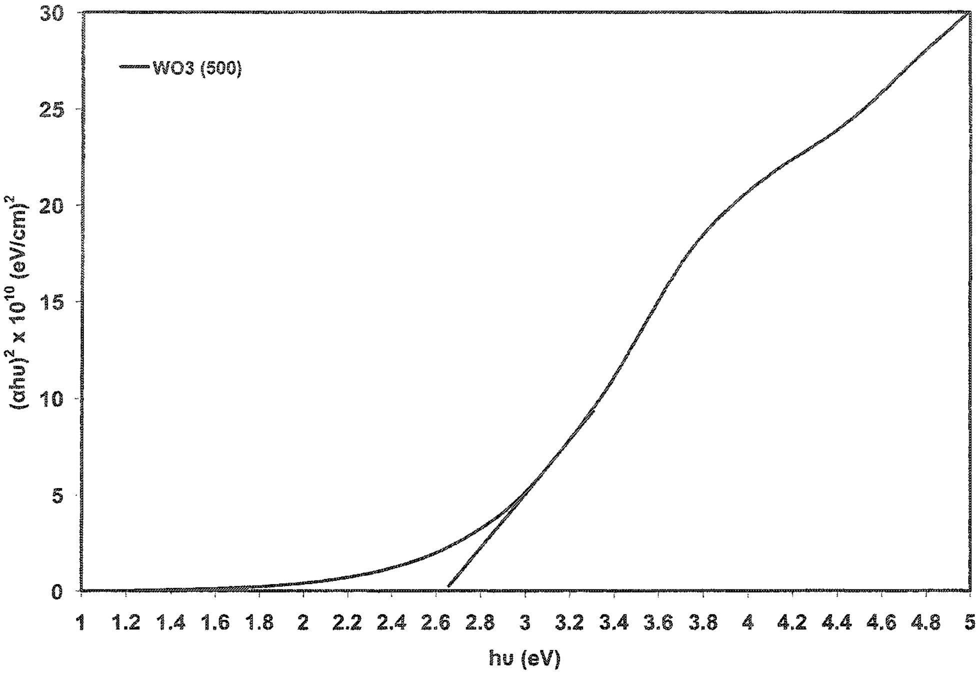

Figure 4.8: Graphical determination of the bandgap of un-doped WO_3

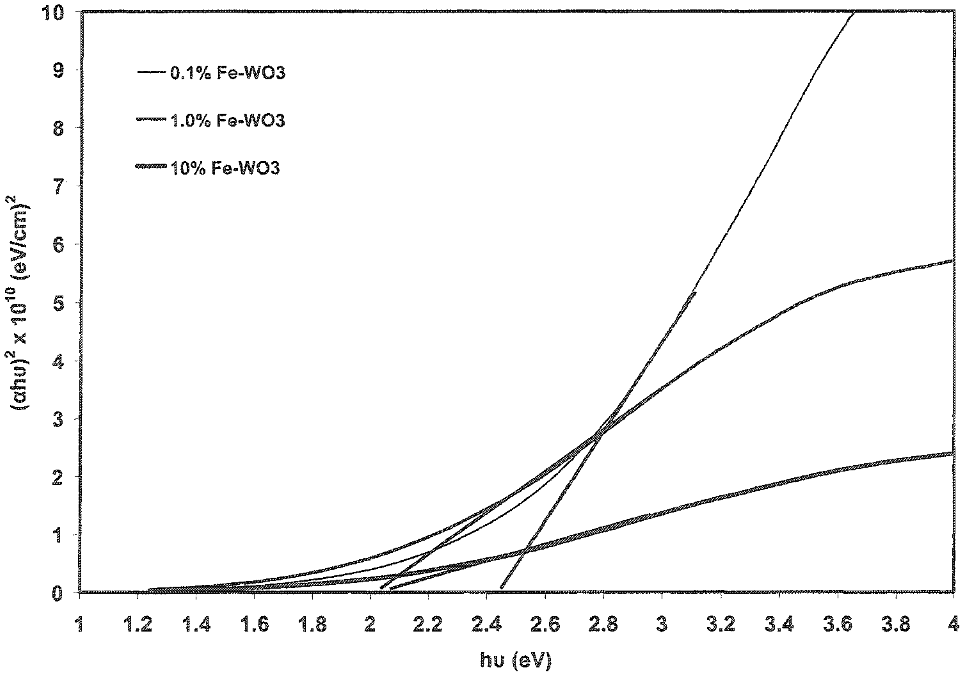

Figure 4.9: Graphical determination of the bandgap of Fe-doped WO_3

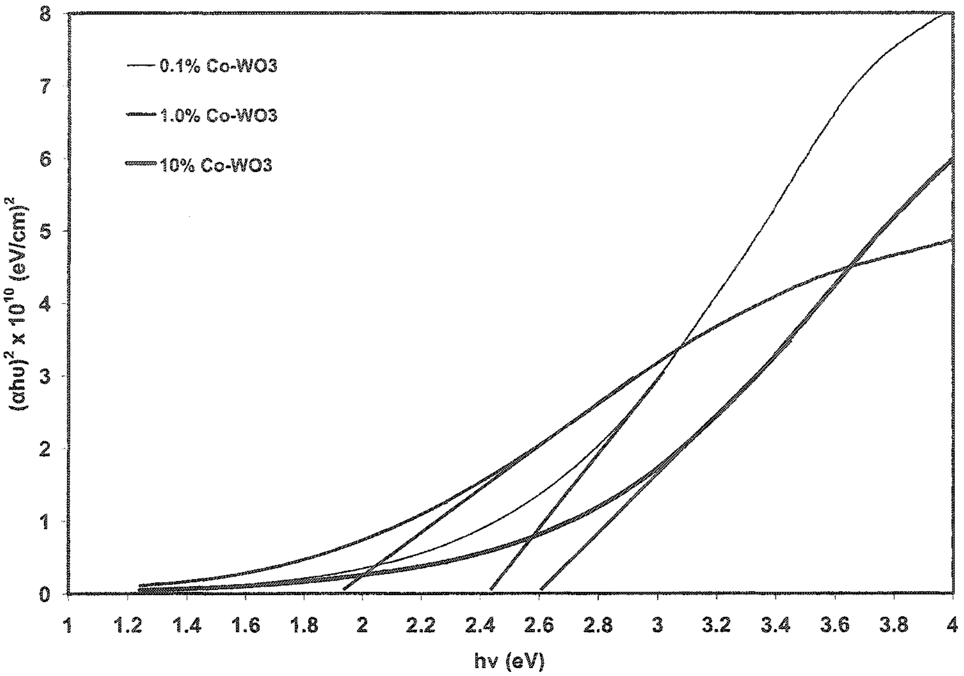

Figure 4.10: Graphical determination of the bandgap of Co-doped WO_3

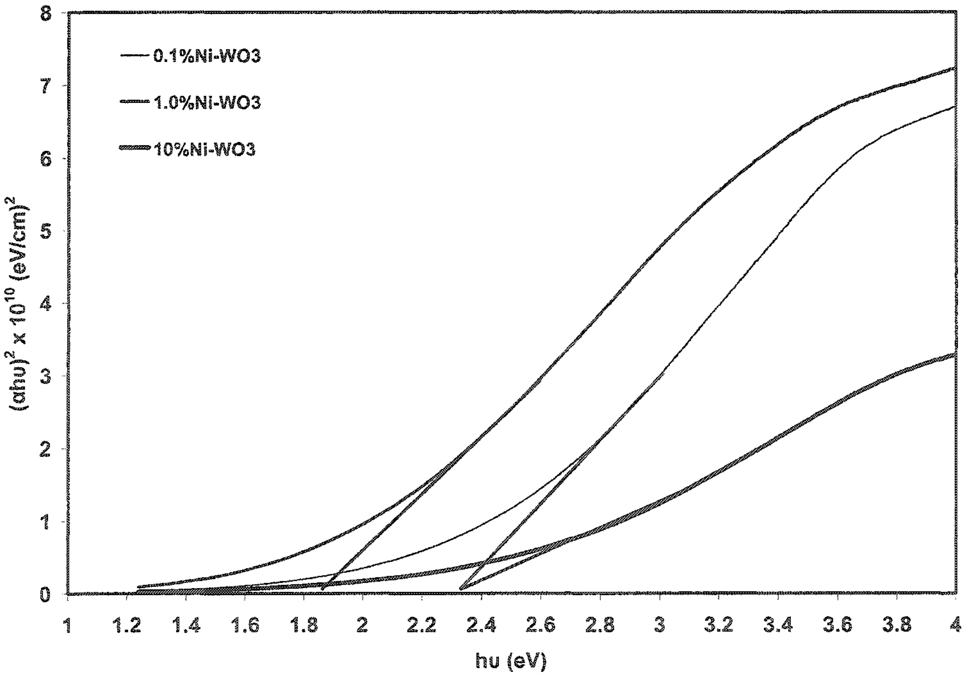

Figure 4.11: Graphical determination of the bandgap of Ni-doped WO_3

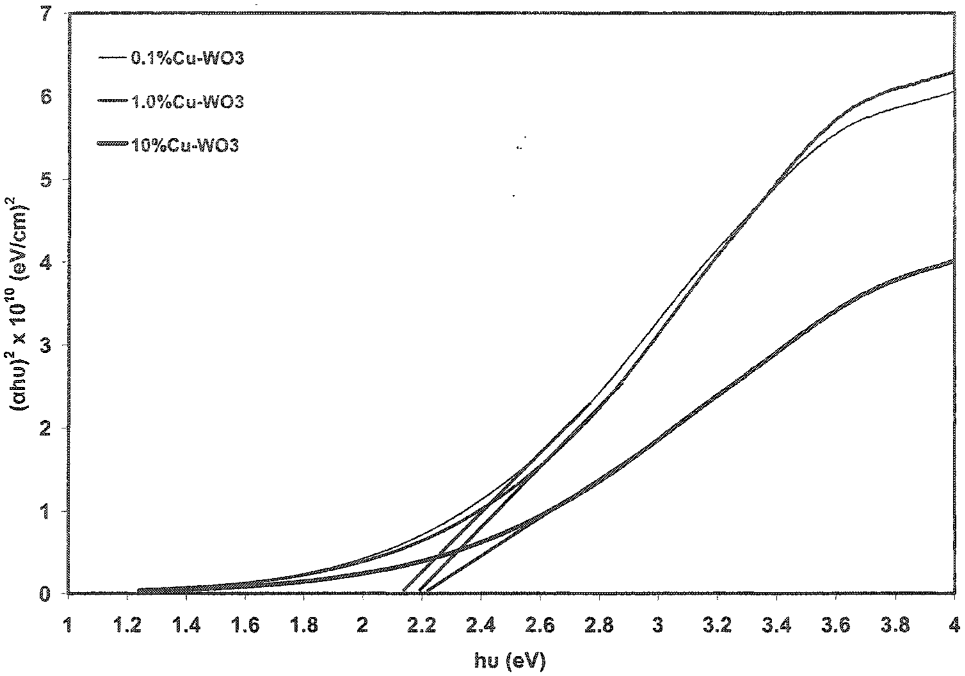

Figure 4.12: Graphical determination of the bandgap of Cu-doped WO_3

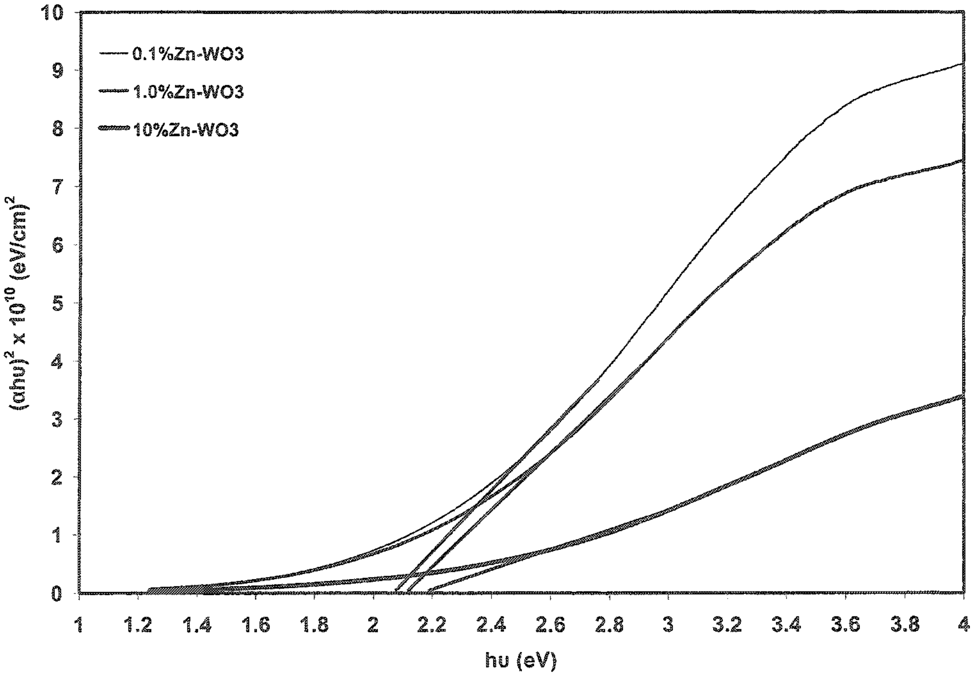

Figure 4.13: Graphical determination of the bandgap of Zn-doped WO_3

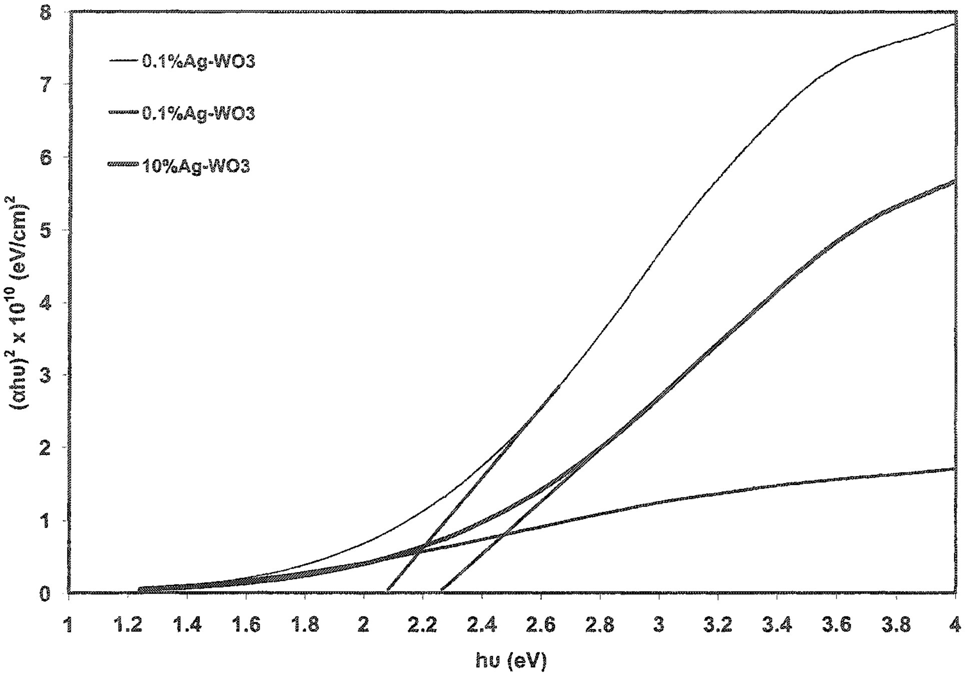

Figure 4.14: Graphical determination of the bandgap of Ag-doped WO_3

4.2 Scanning electron microscopy (SEM)

Scanning electron microscopy (SEM) is a method for high-resolution imaging of surfaces to identify the defects and physical morphology of solids. SEM uses electrons for imaging just as a light microscope uses visible light. The advantages of SEM over light microscopy include much higher magnification (>100,000X) and greater depth of field up to 100 times than that of light microscopy.

SEM generates a beam of incident electrons in an electron column above the sample chamber. The electrons are produced by a thermal emission source, such as a heated tungsten filament, or by a field emission cathode. The energy of the incident electrons can be as low as 100 eV or as high as 30 keV depending on the evaluation objectives. The electrons are focused into a small beam by a series of electromagnetic lenses in the SEM column. Scanning coils near the end of the column direct and position the focused beam onto the sample surface. The electron beam is scanned in a raster pattern over the surface for imaging. The beam can also be focused at a single point or scanned along a line for x-ray analysis. The beam can be focused to a final probe diameter as small as about 10 Å. The incident electrons cause electrons to be emitted from the sample due to elastic and inelastic scattering events within the sample's surface and near-surface material. High-energy electrons that are ejected by an elastic collision of an incident electron, typically with the nucleus of a sample atom, are referred to as backscattered electrons. The energy of backscattered electrons will be comparable to that of the incident electrons. To create an SEM image, the incident electron beam is scanned in a raster pattern across the sample's surface. The emitted electrons are detected for each position in the scanned area by an electron detector.

The intensity of the emitted electron signal is displayed as brightness on a cathode ray tube (CRT). By synchronizing the CRT scan to that of the scan of the incident electron beam, the CRT display represents the morphology of the sample surface area scanned by the beam. Magnification of the CRT image is the ratio of the image display size to the sample area scanned by the electron beam.

Scintillator type detectors are used for secondary electron imaging. This detector is charged with a positive voltage to attract electrons to the detector for improved signal to noise ratio. Detectors for backscattered electrons can be scintillator types or a solid-state detector.

The SEM column and sample chamber are at a moderate vacuum to allow the electrons to travel freely from the electron beam source to the sample and then to the detectors. High-resolution imaging is done with the chamber at higher vacuum, typically from 10^{-5} to 10^{-7} Torr. Imaging of nonconductive, volatile, and vacuum-sensitive samples can be performed at higher pressures.

In this study, Scanning Electron Microscopy (SEM) was used to analyze the pure WO_3 and WO_3 doped with 1.0% and 10% concentrations of various metals. The basic purpose of this study was to observe whether the doped metal is present at the surface of the catalyst or forms its own crystallites away from the surface. The changes in morphology of doped WO_3 compared to that of pure WO_3 were studied by careful analysis of the SEM photographs. Another aspect of this study was to estimate the change in particle size with increase in the concentration of doped metal. The morphology and the particle size of TiO_2, NiO and α-Fe_2O_3 were also studied by SEM. Prior to analysis all the samples were homogenized and coated with gold to reduce the surface repulsion for the electron beam. All the samples were photographed at the magnification of 1000 times (with a scale of 10μm) for particle size measurement.

The SEM photograph of pure WO_3 is presented in figure 4.15, where a broad particle size distribution can be observed. The bigger particles are formed by the aggregation of small particles of various sizes and shapes. The sizes of some of the particles were found to be greater than 10 μm. The shapes of the majority of the particles were irregular with an average particle size distribution of 1-5 μm.

The SEM photographs of pure TiO_2, NiO and α-Fe_2O_3 are presented in figure 4.16-4.18. For TiO_2 the particles of different particle sizes with regular shapes particles and round edges were observed. The larger particles were the aggregates of smaller particles. A non-aggregated particle size distribution 1-10 μm was estimated while for the large aggregates the sizes were higher than 20 μm. Due to the surface charge, even with the gold coating the SEM photographs for α-Fe_2O_3 and NiO are not very clear but serve the purpose. No aggregation of particles was observed for α-Fe_2O_3 while for NiO some aggregates were observed. A submicron regular particle size distribution was observed for both α-Fe_2O_3 and NiO.

The SEM photographs of WO_3 doped with 1.0% and 10% of Fe, Co, Ni, Cu, Zn an Ag are presented in figure 4.19-4.30. The careful comparison of SEM photographs of doped WO_3 with that of bare WO_3 revealed that there was

(i) No significant change in the shapes of the particle

(ii) No individual crystallites of doped metals

(iii) Confirmation of the doped metal at the surface of WO_3

(iv) An increase in the particle size with the increase in the concentration of doped metal

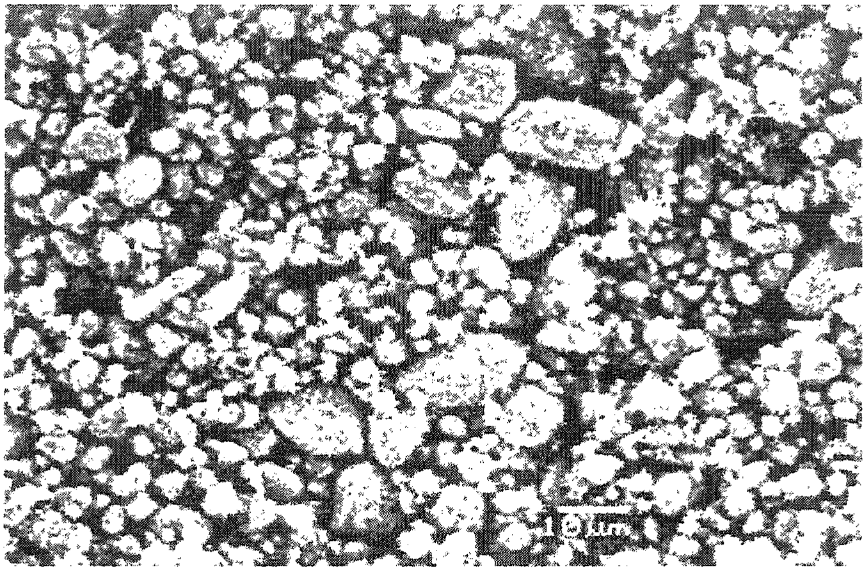

Figure 4.15 SEM photograph of pure WO_3 derived from H_2WO_4 by heat treatment

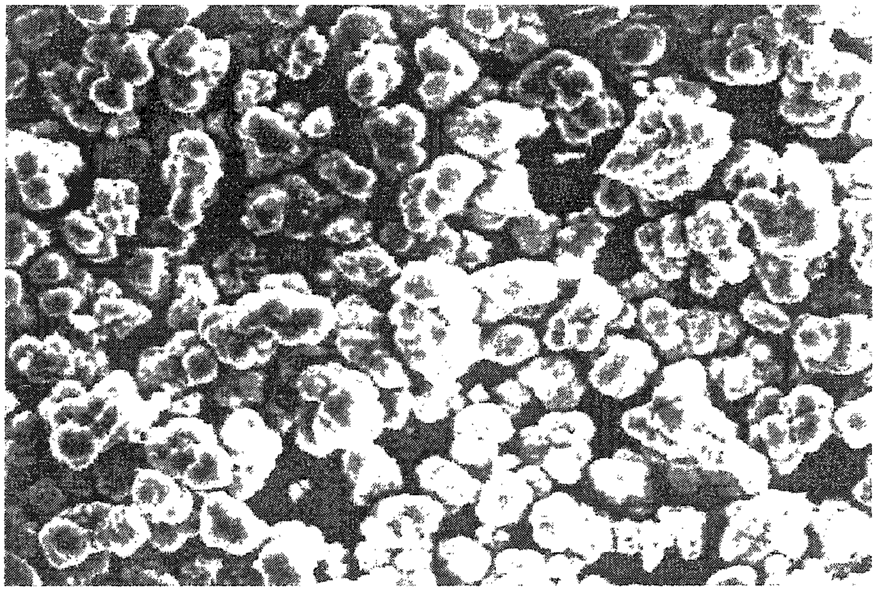

Figure 4.16: SEM photograph of pure TiO_2

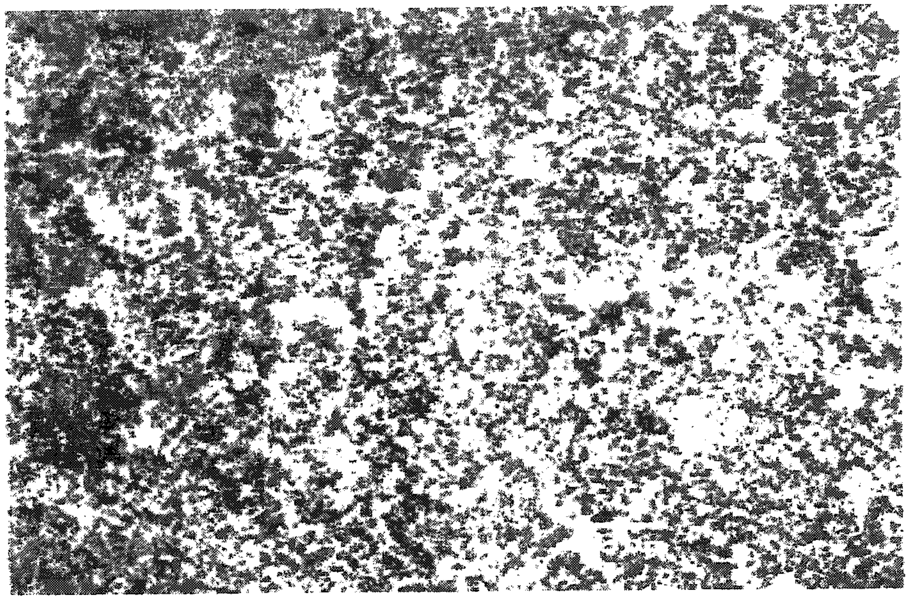

Figure 4.17: SEM photograph of pure α-Fe_2O_3

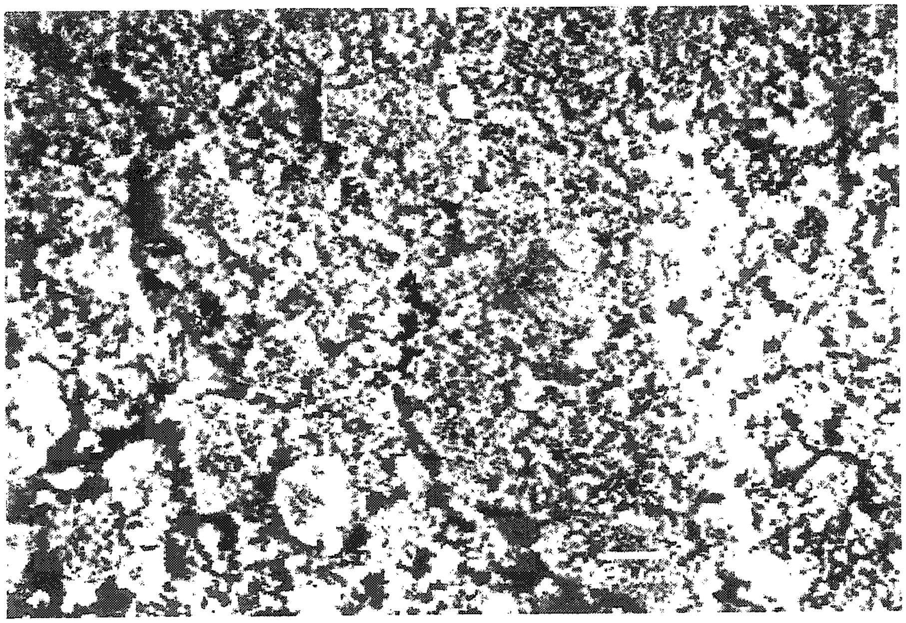

Figure 4.18: SEM photograph of pure NiO

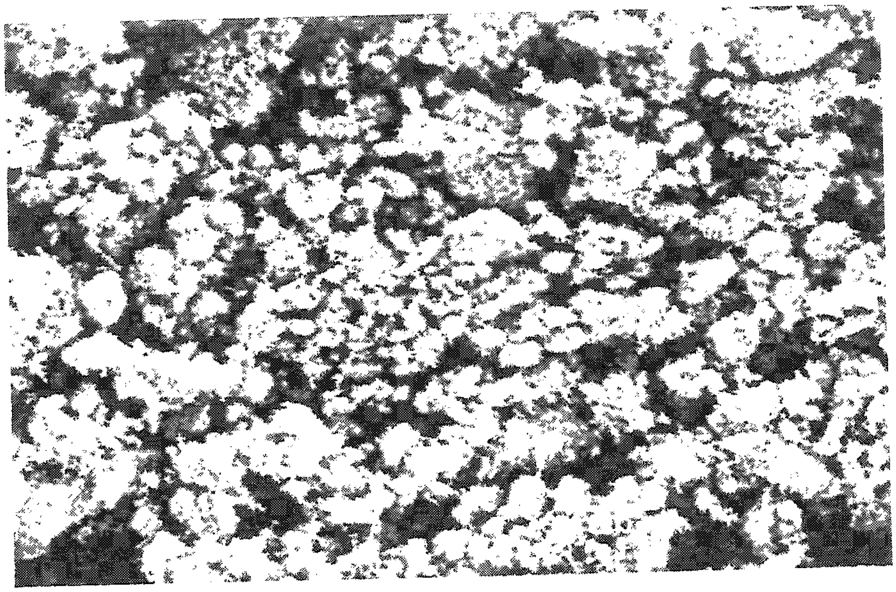

Figure 4.19: SEM photograph of 1.0%Fe-WO_3

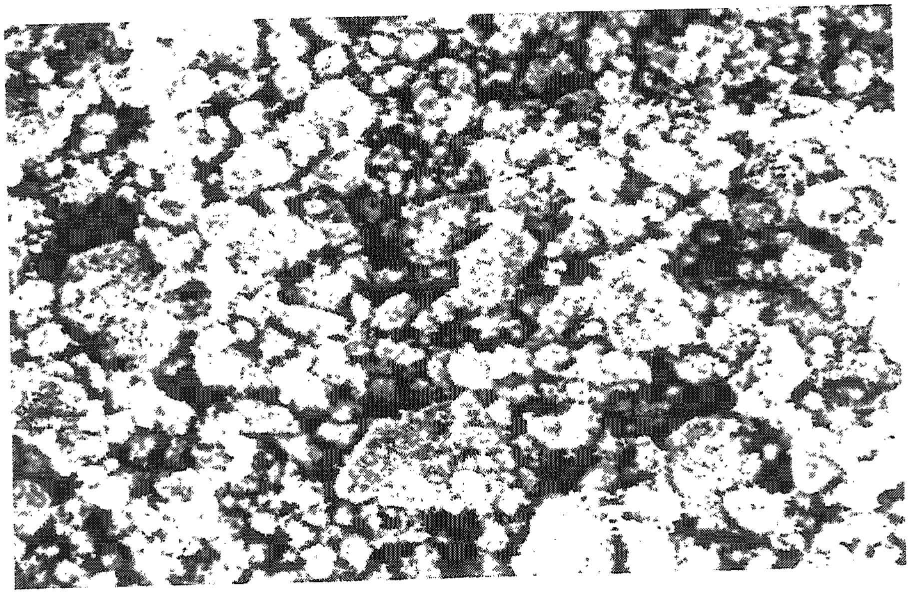

Figure 4.20: SEM picture of 10%Fe-WO_3

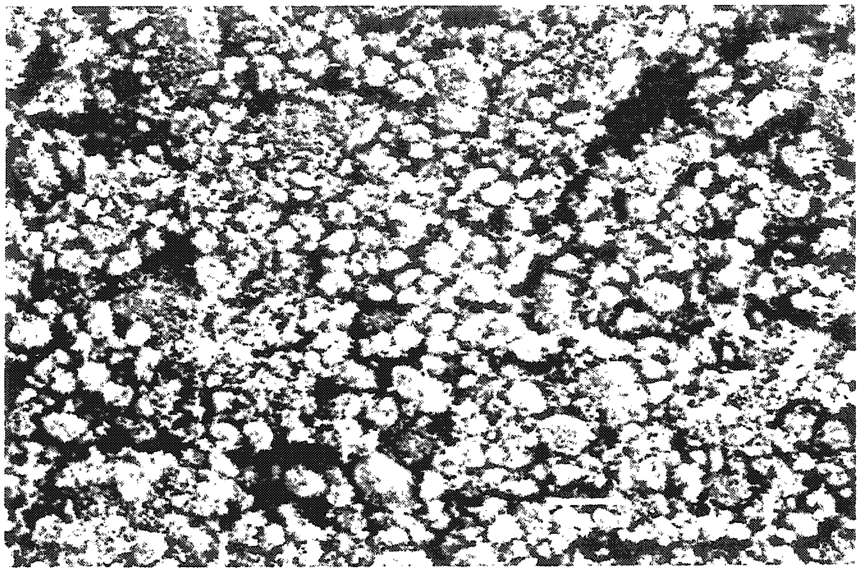

Figure 4.21: SEM photograph of 1.0%Co-WO_3

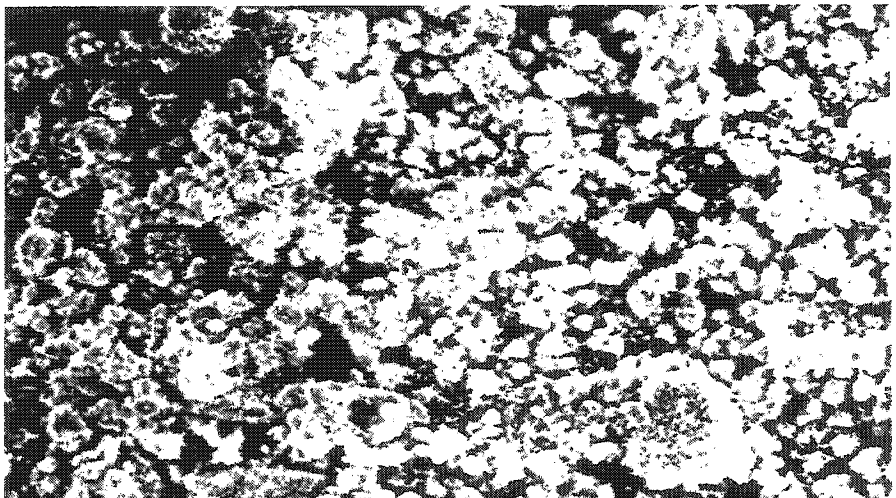

Figure 4.22: SEM photograph of 10% Co-WO_3

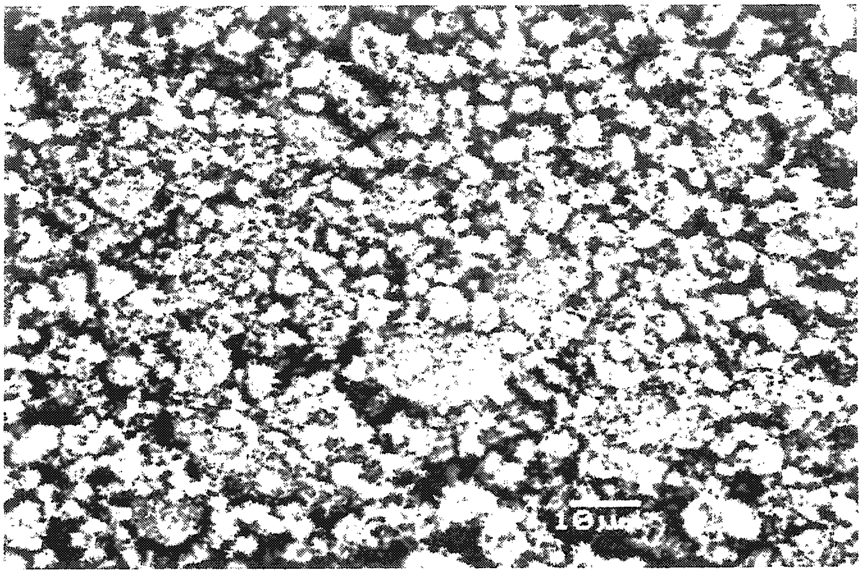

Figure 4.23: SEM photograph of 1.0% Ni-WO_3

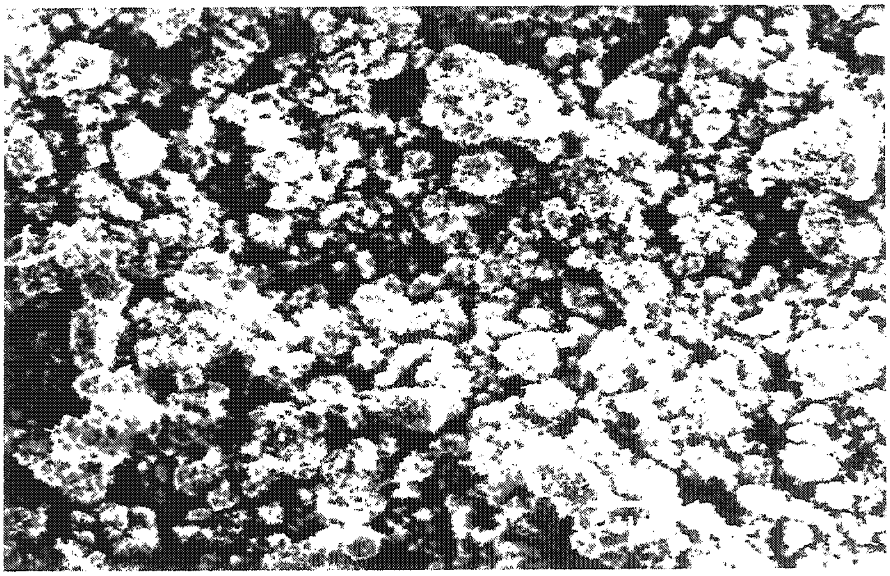

Figure 4.24: SEM photograph of 10% Ni-WO_3

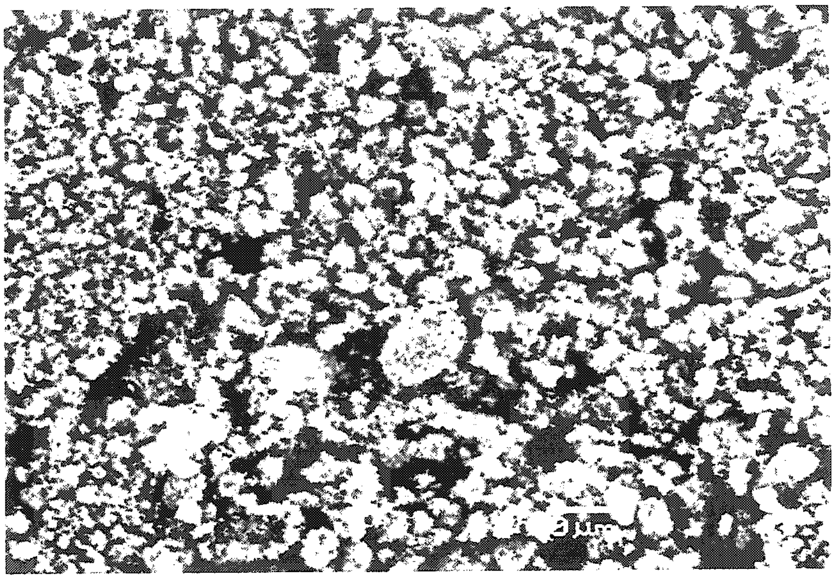

Figure 4.25: SEM photograph of 1.0% Cu-WO_3

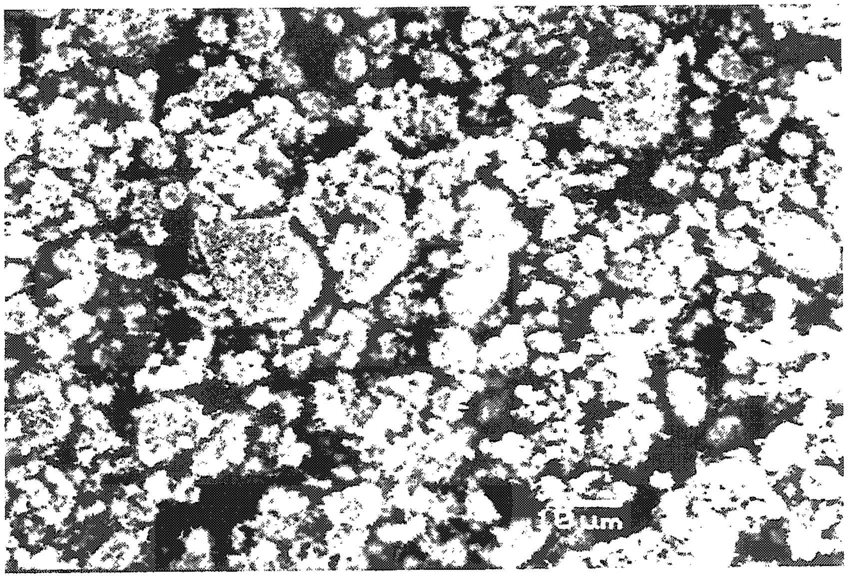

Figure 4.26: SEM photograph of 10% Cu-WO_3

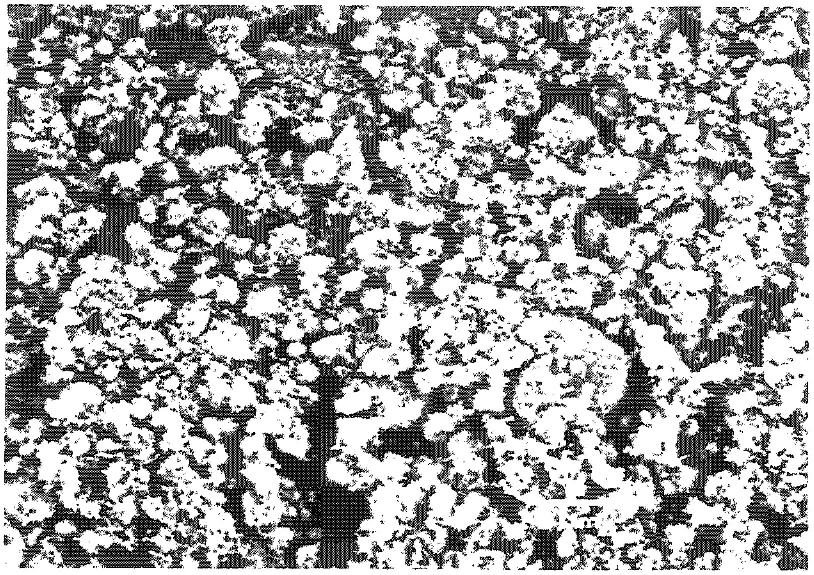

Figure 4.27: SEM photograph of 1.0% Zn-WO_3

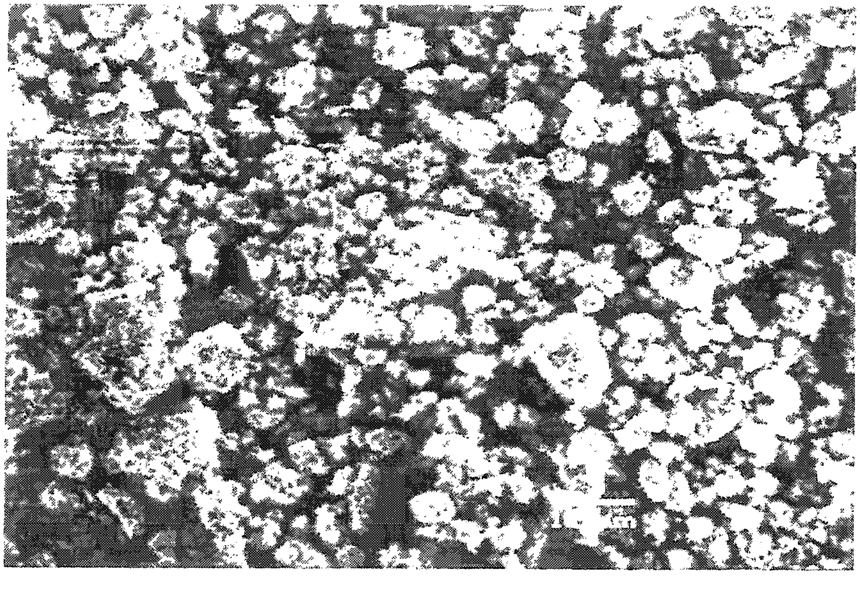

Figure 4.28: SEM photograph of 10% Zn-WO_3

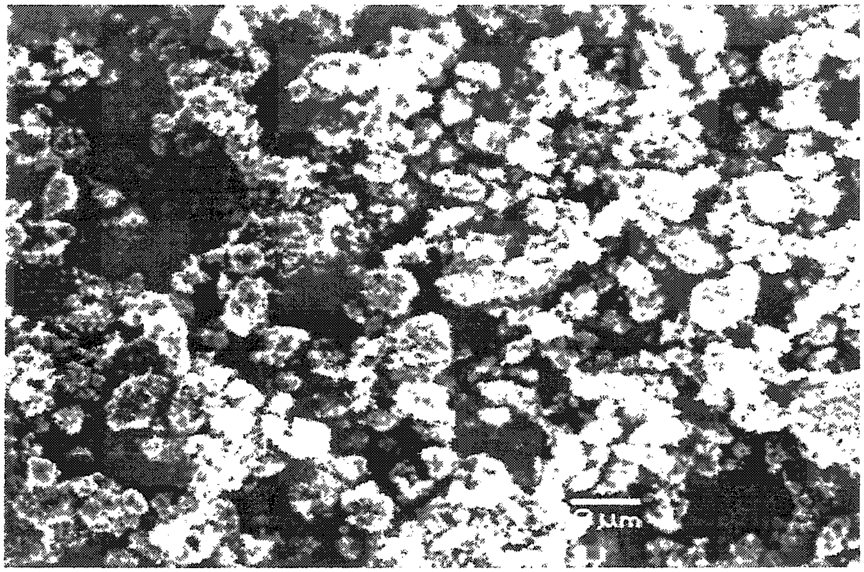

Figure 4.29: SEM photograph of 1.0% Ag-WO_3

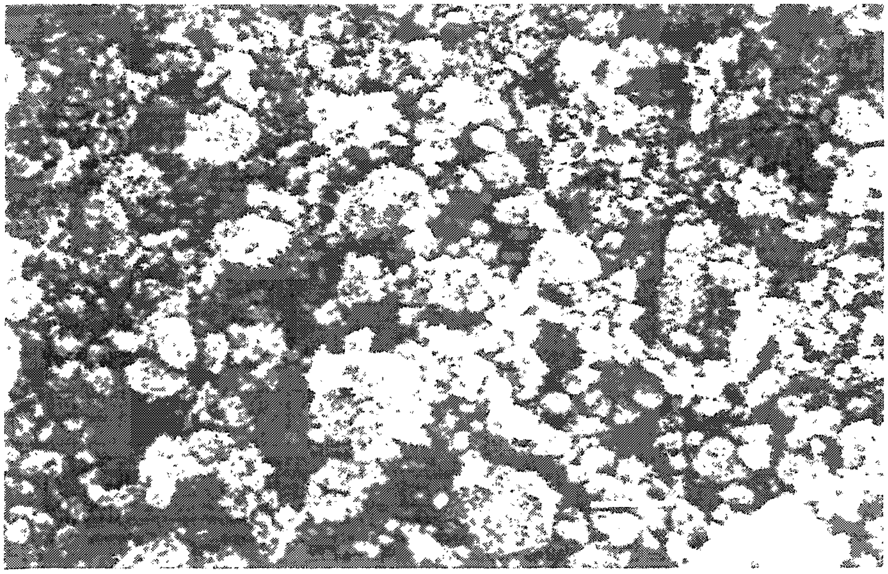

Figure 4.30: SEM photograph of 10% Ag-WO_3

4.3 Energy dispersive x-ray spectroscopy (EDS)

Energy Dispersive X-Ray Spectroscopy (EDS or EDX) is a chemical microanalysis technique used in conjunction with scanning electron microscopy (SEM). The EDS technique detects X-rays emitted from the sample during bombardment by an electron beam to characterize the elemental composition of the analyzed volume. When an electron beam bombards the sample, electrons are ejected from the atoms on the sample's surface. Electrons from a higher state fill the resulting electron vacancies, and an X-ray is emitted to balance the energy difference between the two electronic states. The X-ray energy is characteristic of the element from which it was emitted.

The EDS X-ray detector measures the relative abundance of emitted x-rays versus their energy. The detector is typically a lithium-drifted silicon, solid-state device. When an incident X-ray strikes the detector, it creates a charge pulse that is proportional to the energy of the X-ray. The charge pulse is converted to a voltage pulse (which remains proportional to the X-ray energy) by a charge-sensitive preamplifier. The signal is then sent to a multichannel analyzer where the pulses are sorted by voltage. The energy, as determined from the voltage measurement, for each incident X-ray is sent to a computer for display and further data evaluation. The spectrum of X-ray energy versus counts is evaluated to determine the elemental composition of the sampled volume.

Elements with atomic numbers ranging from that of beryllium to uranium can be detected. The minimum detection limits vary from approximately 0.1 to a few atom percent, depending on the element and the sample matrix. Quantitative results can be obtained from the relative X-ray counts at the characteristic energy levels for the sample constituents.

In this study, EDS analysis was used in conjunction with SEM to evaluate the composition of pure and doped catalysts and found as a useful technique for chemical analysis. The results of the chemical composition obtained from the EDS analysis are reported in table 4.3 and the spectra of pure catalysts and WO_3 doped with various metals are presented in figure 4.31-4.40.

From the values of atomic percentages given in table for WO_3 i.e. 73.15% O and 26.83% W, it can be inferred that at a treatment temperature of $500^{\circ}C$, WO_3 looses its stoichiometry with the loss of lattice oxygen. While metal to oxygen ratio (M:O) in Fe_2O_3, NiO and TiO_2 was observed stoichiometric, as derived from atomic percentages. For transition metal doped WO_3, all the values were found in agreement with that of experimentally doped quantities except for 1.0% Zn-WO_3, 1.0% Ag-WO_3 and 10% Ag-WO_3. For 1.0% Zn-WO_3 and 1.0% Ag-WO_3, instead of 1.0%, the percentages of Zn and Ag were measured as 2.19 and 0.64% while for 10%Ag-WO_3 a percentage of 4.16% was measured by EDS analysis instead of 10%. In EDS analysis, the atomic percentages are measured on the basis of normalized peak area. The overlapping of the peaks is a common source of error especially for those elements whose electron binding energies lie either close to the major component of the doped material or to that of gold, which is used as coating material. These errors can be overcome by the use of carbon as coating material. For 1.0% Zn-WO_3 this discrepancy was due to the overlapping of W and Zn peaks and found more prominent due to the low concentration of Zn. While for 1.0% Ag-WO_3 and 10% Ag-WO_3 the major source of error was the overlapping of Au and Ag peaks.

Table 4.3: Percentage composition of pure and doped catalysts determined by EDS analysis

Sample	Element	Shell	Element %	Atomic %
WO_3	O	K	19.18	73.12
	W	M	80.82	26.83
Fe_2O_3	O	K	37.92	68.07
	Fe	K	62.08	31.93
NiO	O	K	21.67	50.38
	Ni	K	78.33	49.69
TiO_2	O	K	49.21	74.37
	Ti	K	50.79	25.63
1.0 %Fe-WO_3	O	K	18.53	71.53
	Fe	K	1.42	1.57
	W	M	80.05	26.9
10 %Fe-WO_3	O	K	22.95	71.66
	Fe	K	11.88	10.63
	W	M	65.16	17.7
1.0 % Co-WO_3	O	K	16.58	68.87
	Co	K	1.27	1.43
	W	M	82.15	29.7
10 % Co-WO_3	O	K	23.41	72.1
	Co	K	10.56	9.95
	W	M	66.04	17.95
1.0 % Ni-WO_3	O	K	16.25	68.33
	Ni	K	1.32	1.51
	W	M	82.43	30.16

Contd…

Sample	Element	Shell	Element %	Atomic %
10 % Ni-WO_3	O	K	20.03	69.16
	Ni	K	12.93	10.99
	W	M	67.04	19.85
1.0 % Cu-WO_3	O	K	16.96	69.27
	Cu	K	1.81	1.86
	W	M	81.23	28.87
10 % Cu-WO_3	O	K	17.9	66.39
	Cu	K	11.63	10.86
	W	M	70.48	22.75
1.0 % Zn-WO_3	O	K	18.39	71.1
	Zn	K	2.25	2.19
	W	M	79.36	26.7
10 % Zn-WO_3	O	K	20.5	69.14
	Zn	K	12.41	10.46
	W	M	67.09	20.4
1.0 % Ag-WO_3	O	K	18.85	72.14
	Ag	L	1.11	0.64
	W	M	80.36	27.23
10 % Ag-WO_3	O	K	19.85	72.73
	Ag	L	7.63	4.15
	W	M	72.52	23.12

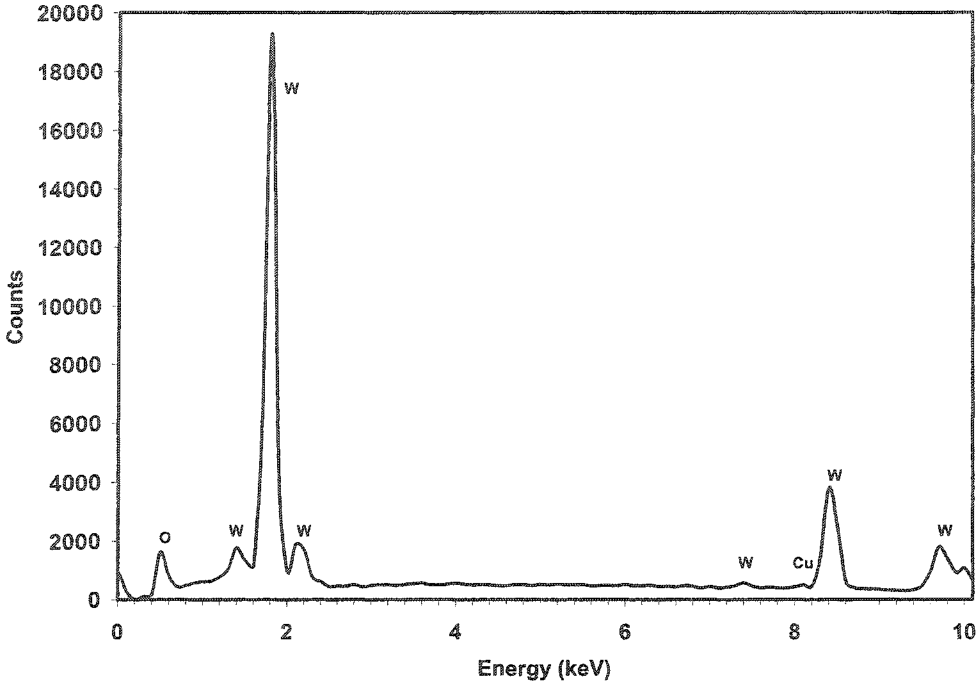

Figure 4.31 EDS spectrum of pure WO_3

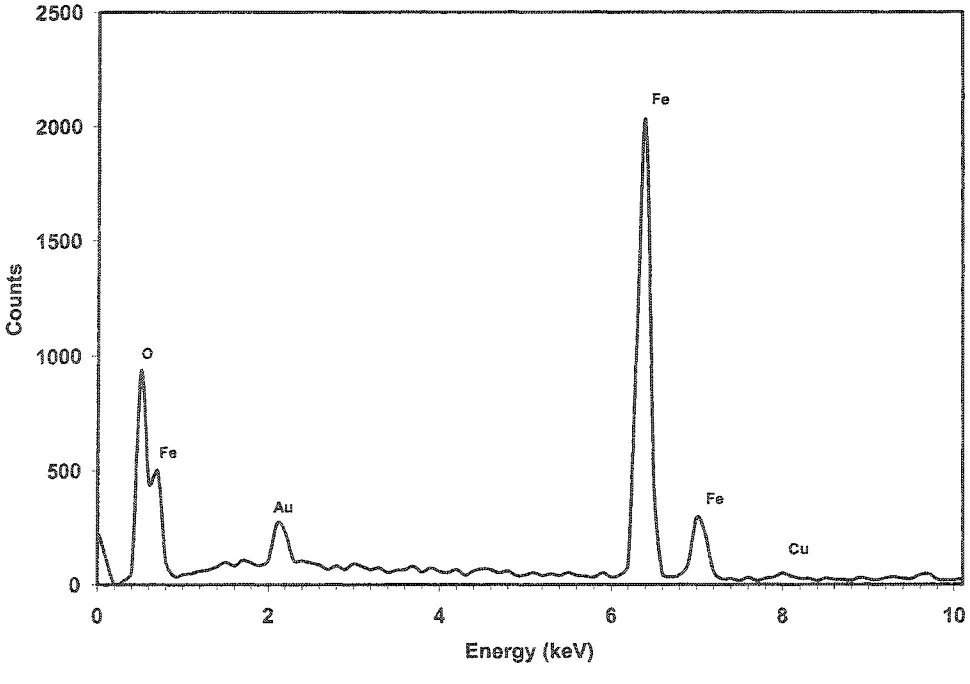

Figure 4.32 EDS spectrum of pure α-Fe_2O_3

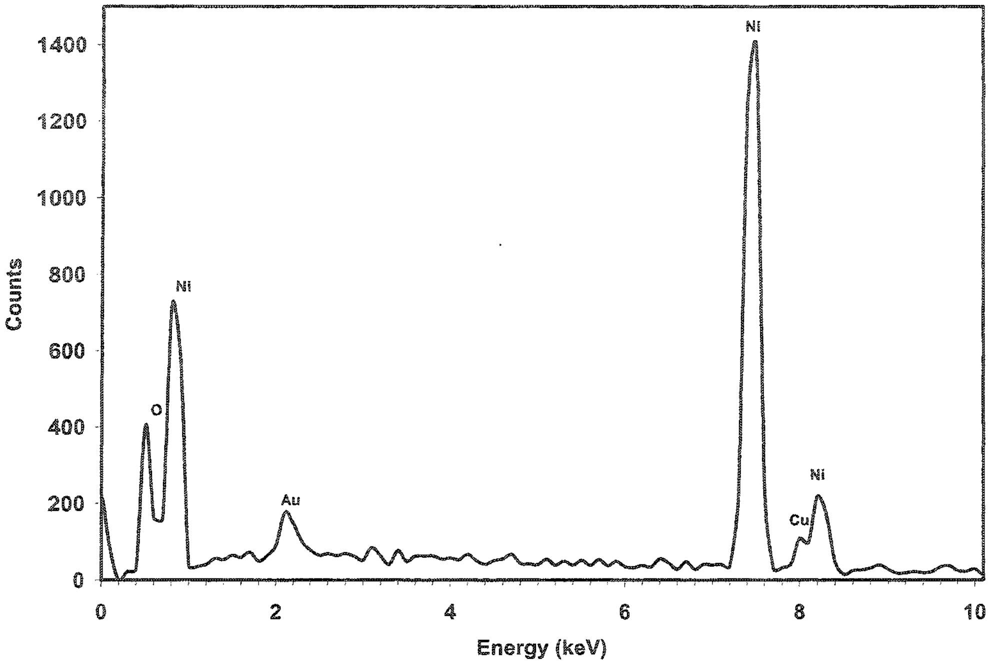

Figure 4.33 EDS spectrum of pure NiO

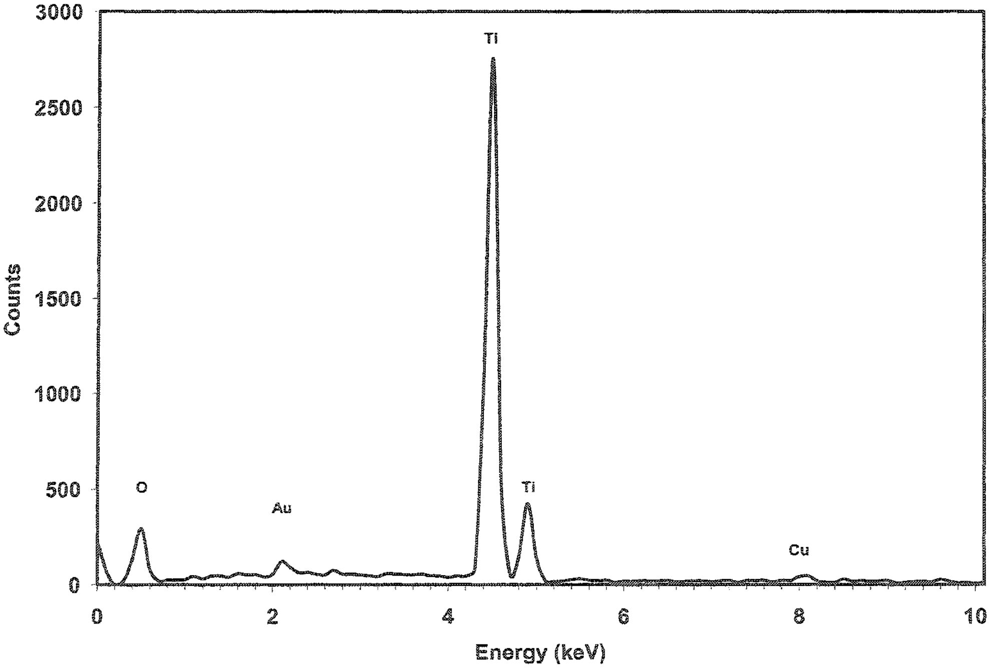

Figure 4.34 EDS spectrum of pure TiO_2

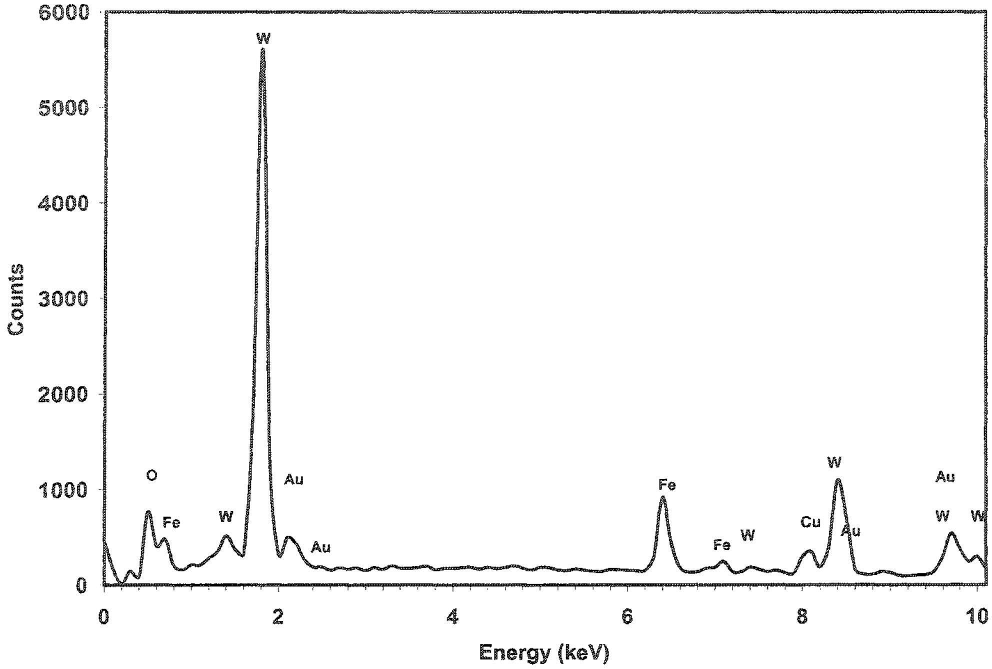

Figure 4.35 EDS spectrum of 10% Fe-WO_3

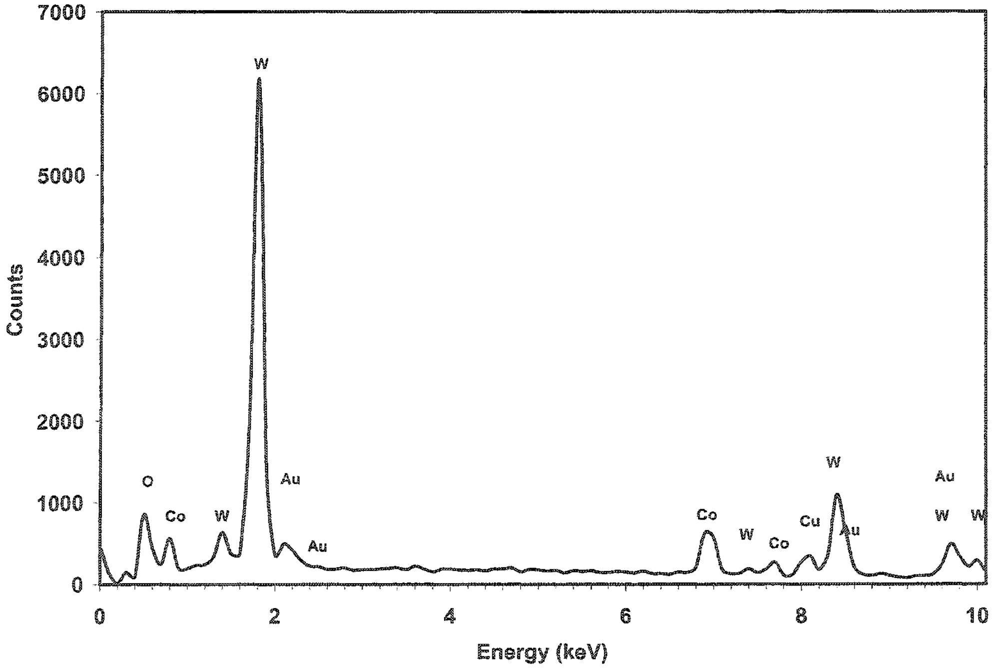

Figure 4.36 EDS spectrum of 10% Co-WO_3

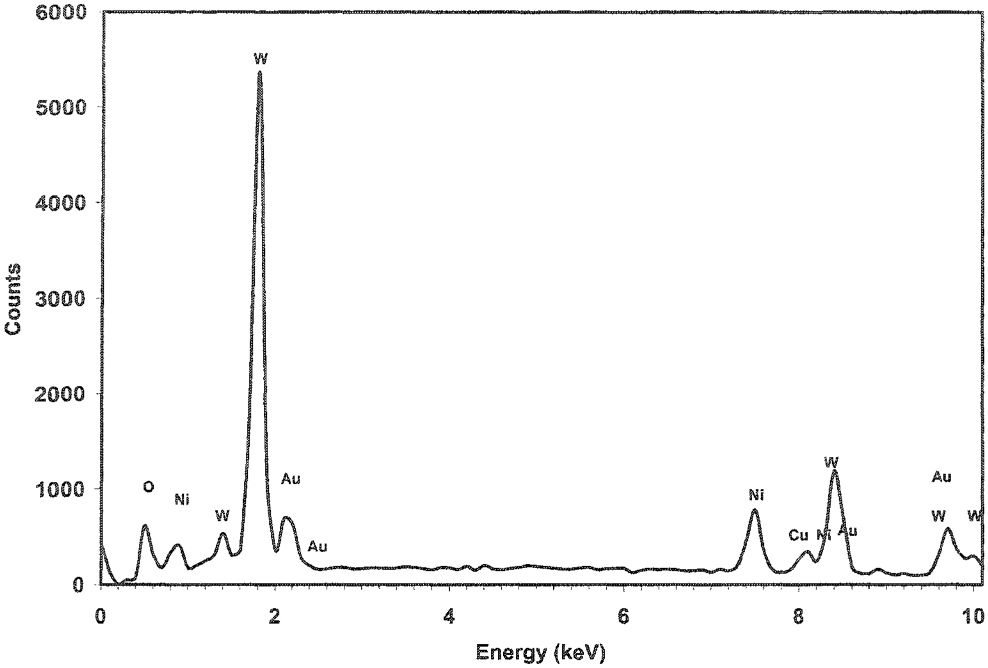

Figure 4.37 EDS spectrum of 10% Ni-WO_3

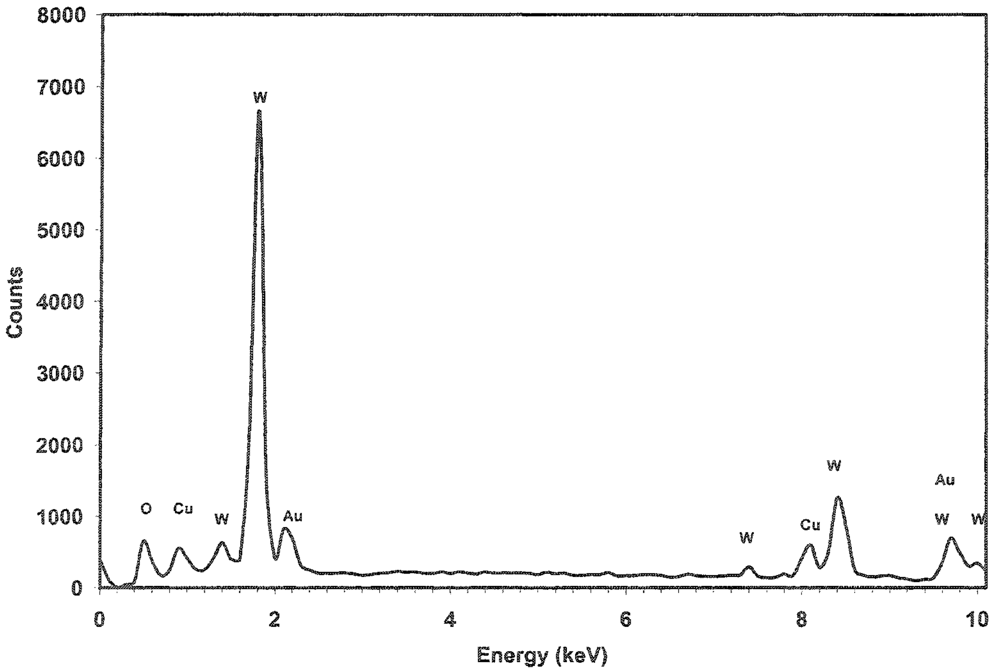

Figure 4.38 EDS spectrum of 10% Cu-WO_3

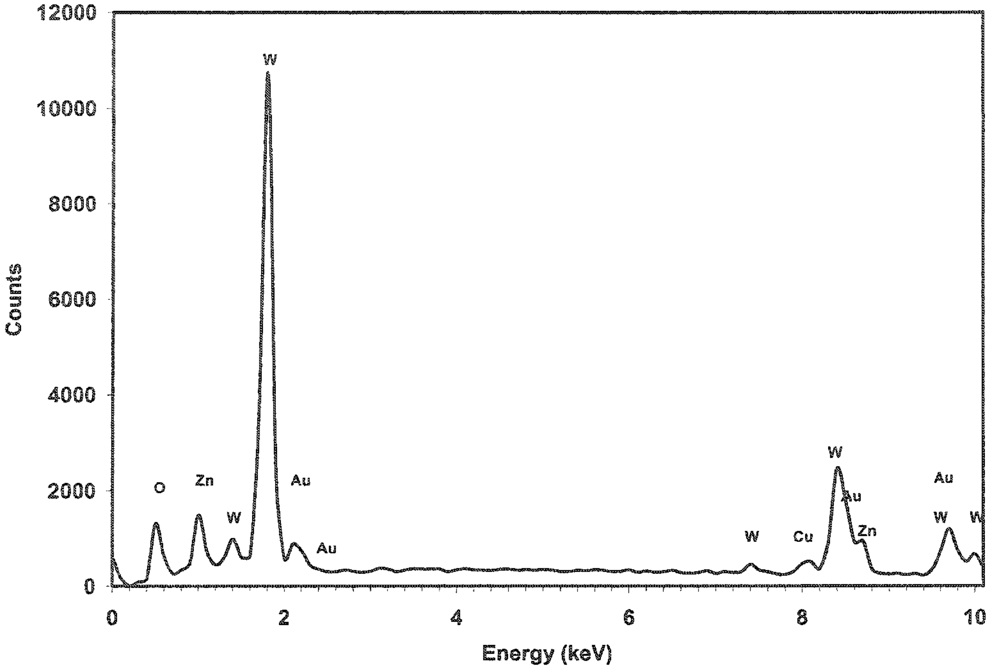

Figure 4.39 EDS spectrum of 10% Zn-WO_3

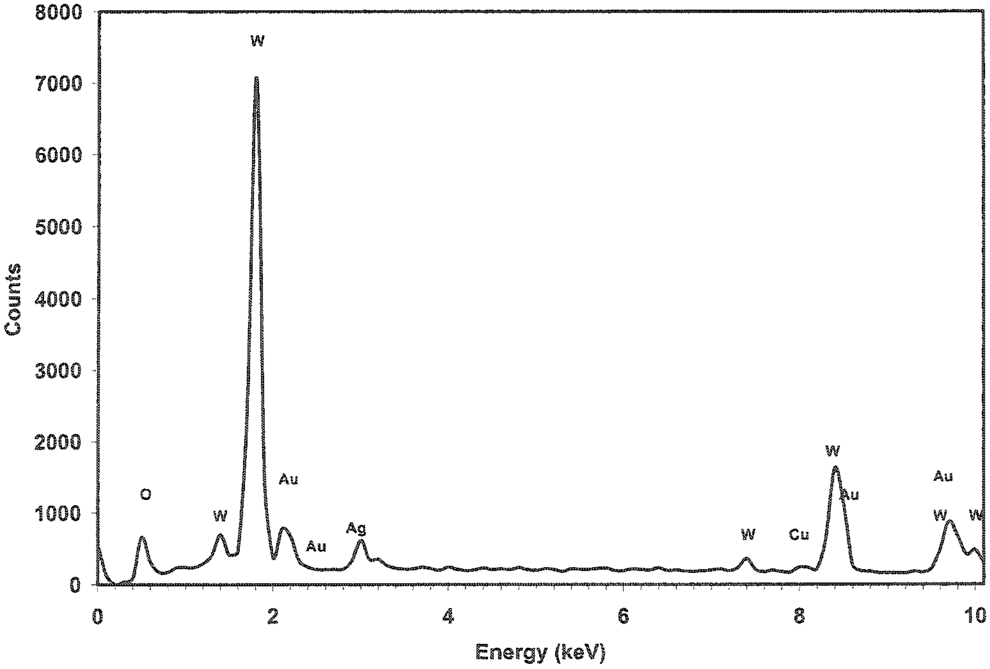

Figure 4.40 EDS spectrum of 10% Ag-WO_3

4.4 X-ray Photoelectron spectroscopy (XPS)

X-Ray Photoelectron Spectroscopy (XPS) is an analysis technique used to obtain chemical information about the surfaces of solid materials. Both the composition and chemical state of surface constituents can be determined by XPS. Insulators and conductors can easily be analyzed in surface areas from a few microns to a few millimeters across.

The sample is placed in an ultrahigh vacuum environment and exposed to a low-energy, monochromatic x-ray source. The incident X-rays cause the ejection of core-level electrons from sample atoms. The energy of a photo-emitted core electron is a function of its binding energy and is characteristic of the element from which it is emitted. Energy analysis of the emitted photoelectrons is the primary data attained from XPS.

An electron energy analyzer detects the photoelectrons emitted from the sample, and their energy is determined as a function of their velocity on entering the detector. By counting the number of photoelectrons as a function of their energy, a spectrum representing the surface composition is obtained. The energy corresponding to each peak is characteristic of an element present in the sampled volume. The area under a peak in the spectrum is a measure of the relative amount of the element represented by that peak. The peak shape and precise position indicates the chemical state for the element.

XPS is a surface sensitive technique because only those electrons generated near the surface escape and are detected. The photoelectrons of interest have relatively low kinetic energy. Due to inelastic collisions within the sample's atomic structure, photoelectrons originating more than 20 to 50 Å below the surface cannot escape with sufficient energy to be detected.

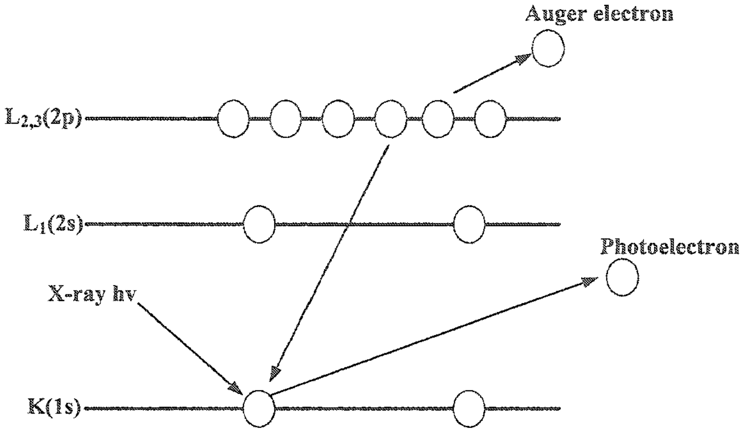

Figure 4. 41: The x-ray photoelectron emission process

Energy peaks in the survey scan identify the elemental composition of the uppermost 20 to 50 Å of the analyzed surface. All elements, except hydrogen and helium, are detected. Detection limits are approximately 0.1 atom percent for most elements.

This technique evaluates the chemical state(s) of each element through its core electron binding energies. Precise determination of binding energies is made with curve-fitting routines applied to the peaks in the multiplex scan. Shifts in the binding energy can result from the atom's oxidation state, chemical bonds, or crystal structure.

The concentrations of the elements identified in the survey scan are determined by integrating the area under a characteristic peak for each element. Sensitivity factors are applied to the peak area values to determine the elemental concentration.

X-ray photoelectron spectroscopy (XPS) is a powerful tool in the study of the electronic structure. XPS provides not only information about the atomic composition, but also the structure and oxidation states present in the sample. The chemical shifts in the core levels provide information on the oxidation state of the different species. Transition metal oxides can be easily identified because their core levels also present distinct satellites. These spectra provide information on the covalent mixing of the different electronic states in the material. In this section, the XPS studies of WO_3 doped with various transition metals will be discussed with emphasis on the oxidation states of the dopant metals. The oxidation states and the chemical forms of the transition metals as estimated by XPS are listed in table 4.4.

4.4.1 XPS analysis of Fe-doped WO_3

The survey scan of 1.0% Fe-WO_3 is given in figure 4.42. The O 1s was observed at the binding energy of 530.41 eV while a splitting was observed for W 4f. The W $4f_{7/2}$ and $W4f_{5/2}$ appeared at the binding energies of 35.42 eV and 37.68 eV respectively. These peaks represent the host WO_3. figure 4.43 shows the Fe 2p XPS spectra of 1.0%Fe-WO_3. The Fe 2p was split by the 2p spin-orbit effect into the $2p_{3/2}$ and $2p_{1/2}$ regions. The Fe $2p_{3/2}$ and Fe$2p_{1/2}$ peaks were observed at the binding energies of 710.18 eV and 724.21 respectively, with a calculated difference of 14.0 eV. The peak positions and the binding energy data in the presence of typical shake-up satellite line at 719.0 eV due to electron transfer processes, confirm the presence of Fe as Fe^{3+} on the surface of WO_3. No significant shift in Fe $2p_{3/2}$ due to the partial transfer of electrons from Fe^{3+} to O_2^- was observed as in case of pure Fe_2O_3 indicating that the concentration of Fe at the surface of WO_3 is not quite enough to show these type of changes. The comparison of the peak position data with the literature [115] was found in good agreement and confirmed the presence of Fe_2O_3 at the surface of WO_3.

4.4.2 XPS analysis of Co-WO_3

In the XPS analysis of 1.0% Co doped WO_3 the O 1s, W $4f_{7/2}$ and W $4f_{5/2}$ states were observed at 530.28 eV, 35.39 eV and 37.60 eV respectively. These values were in agreement with the values reported in the literature for WO_3 confirming the origin of these peaks from the host WO_3. The XPS survey and high-resolution spectra of Co are shown in figure 4.44 and 4.45. The spin-orbit splitting was observed in Co 2p peaks. The peaks due to Co $2p_{3/2}$ and Co $2p_{1/2}$ at 781.20 eV and 797.42 respectively were assigned to Co^{2+}/Co^{3+} species initially. Due to the overlapping of their binding energies, Co^{2+}/Co^{3+} species could not be differentiated. The existence of these species is decided on the basis of the intensity of the shake-up satellites. Forst et al. [116] stated that the high intensity satellite peaks indicated the presence of Co^{2+} species, and less intense satellite structures of Co^{3+} species. Calafat et al. [117] stated that Co as Co^{2+} species can be identified by the presence of high intensity satellite peak at about 6 eV from the $2p_{3/2}$ peak. By the evaluation of Co 2p spectra, an intense satellite at 787.64 eV was observed which confirmed the presence of Co as Co^{2+} in the form of CoO at the surface of WO_3.

4.4.3 XPS analysis of Ni-WO_3

In the XPS analysis of 1.0% Ni doped WO_3, the O1s, W $4f_{7/2}$ and W $4f_{5/2}$ appeared at the binding energies of 530.49 eV, 35.18 eV and 37.42 eV respectively. The survey scan and Ni 2p spectra with the splitting of Ni 2p in $2p_{3/2}$ and $2p_{1/2}$ are presented in figure 4.47 and 4.48. In principle, the XPS technique is ideally suitable to probe the presence of different oxidation states via the chemical shift observed in the XP spectra, but the identification of Ni^{2+} and Ni^{3+} has always been hampered by the intense and complex structure observed in the Ni (2p) spectra from stoichiometric NiO [4]. However, since this satellite structure arises from the interaction of the core photoelectron with electrons in the valence orbitals, it can provide important information about the electronic structure of nickel present at the surface of WO_3. The Splitting of Ni (2p) in $Ni2p_{3/2}$ and $Ni2p_{1/2}$ with binding energies at 856.13 eV and 879.6 eV respectively, due to the spin orbit coupling, was observed. A difference of 23.9eV between the two split peaks with a satellite at 862.1 eV was observed. The presence of a shoulder at 852.8 eV confirmed the presence of Ni^{o} in low concentration and was not included in the quantitation table. The presence of two intense peaks of split Ni 2p at 855.7 eV and 879.6 eV with a difference of 23.9 eV along with a shake-up satellite at 862.1 eV predicted the presence of Ni^{3+} and found in accordance with the values given in literature [115]. The presence of Ni^{2+} as NiO was ruled out in the absence of a Ni $2p_{3/2}$ peak at 854.6 and a satellite centered at around 856.1, which are intrinsic to NiO.

4.4.4 XPS analysis of Cu-WO_3

The binding energies of O1s, W $4f_{7/2}$ and W $4f_{5/2}$ obtained from XPS spectra were 530.15 eV, 35.43 eV and 37.55 eV respectively. All the binding energies were calibrated and corrected based on C 1s binding energy i.e. 284.8 eV, used as a reference for charge correction [3]. The recorded Cu XPS spectra presented in figure 4.48 and 4.49. A splitting in Cu 2p due to spin orbit coupling was observed. The Cu $2p_{3/2}$ and Cu $2p_{1/2}$ peaks at binding energy values of 932.5 eV and 952.02 eV respectively, indicates the presence of Cu^{+} or Cu^{o} species. No shoulder in the Cu peak was evident at 933.7 due to the presence of Cu^{2+}. The oxidation state and the chemical form of Cu was estimated by analyzing the peak pattern, the difference between Cu $2p_{3/2}$ and Cu $2p_{1/2}$ peaks and the presence of a distinct satellite between the two peaks. A difference in the binding energy of 19.7 eV between Cu $2p_{3/2}$ and Cu $2p_{1/2}$ and the presence of a distinct satellite in the region 935-950 eV due to the charge transfer processes indicated in agreement with the literature [115], the presence of Cu in the +1 oxidation state.

4.4.5 XPS analysis of Zn-WO_3

A charge shift value of 10 eV for C 1s was observed for 1.0% Zn doped WO_3. All the binding energies determined by recorded XPS spectra were corrected on the basis of the above mentioned charge shift value. The binding energies of O1s, W $4f_{7/2}$ and W $4f_{5/2}$ obtained from XPS spectra were 530.16 eV, 35.44 eV and 37.56 eV respectively (figure 4.50). For Zn 2p spectra, a splitting due to the spin-orbit coupling was observed. The two Zn 2p i.e. $2p_{3/2}$ and $2p_{1/2}$ were observed at the binding energies of 1021.6 eV and 1044.5 eV respectively as shown in figure 4.51. In the presence of a distinct shake up satellite in the region 1025-1040 eV the above mentioned peaks of Zn 2p were assigned to Zn^{2+} and predicted the presence of Zn as ZnO at the surface of WO_3.

4.4.6 XPS analysis of Ag-WO_3

A charge correction of 3.39 eV was applied to correct the recorded binding energies. The binding energies of O1s, W $4f_{7/2}$ and W $4f_{5/2}$ recorded from XPS spectra were 530.15 eV, 35.15 eV and 37.20 eV respectively as shown in figure 4.52, confirming the host WO_3. The two split 3d levels i.e. $3d_{5/2}$ and $3d_{3/2}$ were observed at the binding energies 367.8 eV and 373.8 eV (Ag 3d, figure 4.53). The binding energy of Ag $3d_{5/2}$ and the difference between the two levels i.e. 6.0 eV confirmed the presence of Ag as Ag^+ at the surface of WO_3. Based on these facts, Ag_2O was predicted as the most likely form.

Table 4.4: Binding energies, oxidation states and chemical form of the transition metals, used as dopants, at the surface of WO_3 as determined by XPS

Sample	**Energy Levels**	**Binding energies (eV)**	**Oxidation state & Chemical form**
WO_3	W $4f_{7/2}$	35.15	+6 WO_3
	W $4f_{5/2}$	37.41	
	O 1s	530.40	
Fe-WO_3	W $4f_{7/2}$	35.42	+3 Fe_2O_3
	W $4f_{5/2}$	37.68	
	O 1s	530.41	
	Fe $2p_{3/2}$	710.18	
	Fe $2p_{1/2}$	724.21	
Co-WO_3	W $4f_{7/2}$	35.39	+2 CoO
	W $4f_{5/2}$	37.60	
	O 1s	530.28	
	Co $2p_{3/2}$	781.20	
	Co $2p_{1/2}$	797.42	
Ni-WO_3	W $4f_{7/2}$	35.18	+3 Ni_2O_3
	W $4f_{5/2}$	37.42	
	O 1s	530.49	
	Ni $2p_{3/2}$	856.13	
	Ni $2p_{1/2}$	879.60	

Contd……

Sample	**Energy Levels**	**Binding energies (eV)**	**Oxidation state & Chemical form**
Cu-WO_3	W $4f_{7/2}$	35.43	+1 Cu_2O
	W $4f_{5/2}$	37.58	
	O 1s	530.15	
	Cu $2p_{3/2}$	932.5	
	Cu $2p_{1/2}$	952.02	
Zn-WO_3	W $4f_{7/2}$	35.44	+2 ZnO
	W $4f_{5/2}$	37.56	
	O 1s	530.16	
	Zn $2p_{3/2}$	1021.6	
	Zn $2p_{1/2}$	1044.5	
Ag-WO_3	W $4f_{7/2}$	35.15	+1 Ag_2O
	W $4f_{5/2}$	37.20	
	O 1s	530.15	
	Ag $3d_{3/2}$	367.80	
	Ag $3d_{5/2}$	373.80	

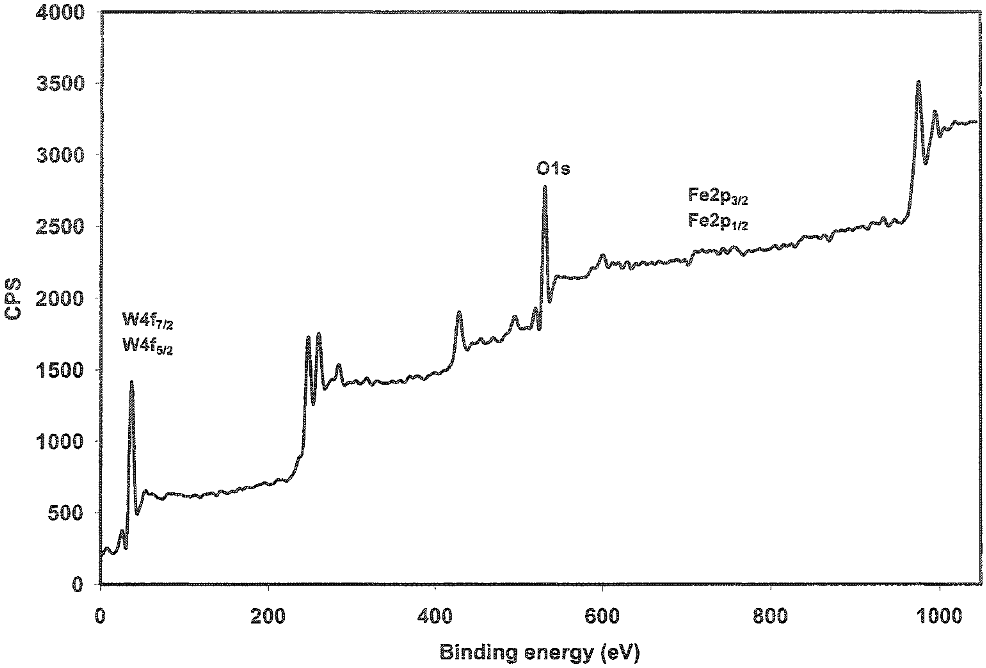

Figure 4.42: XPS survey scan of 1.0% Fe-WO_3.

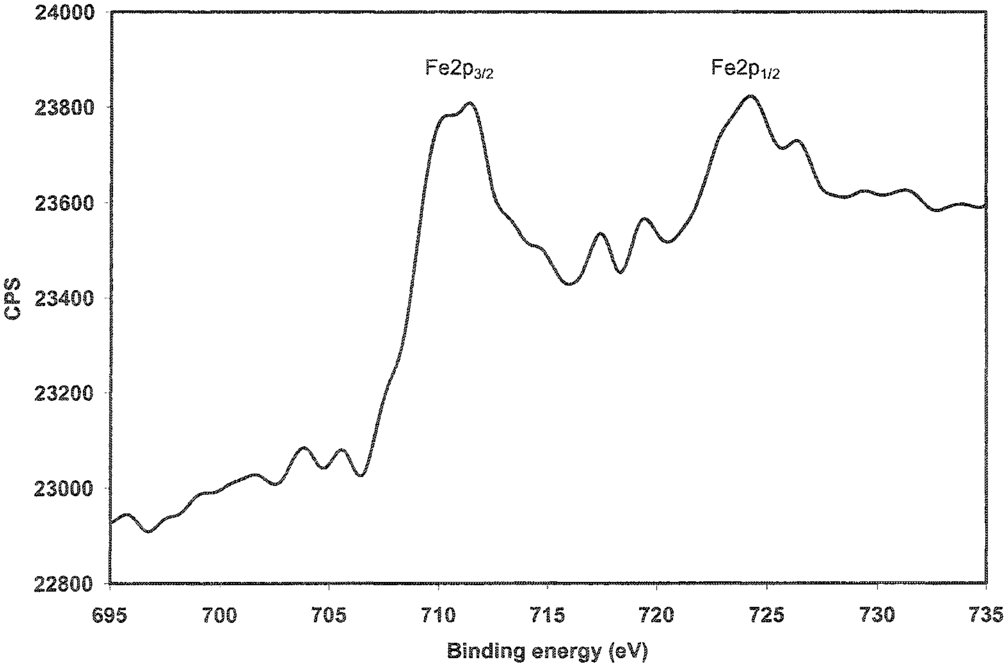

Figure 4.43: XPS spectrum of Fe 2p in 1.0% Fe-WO_3

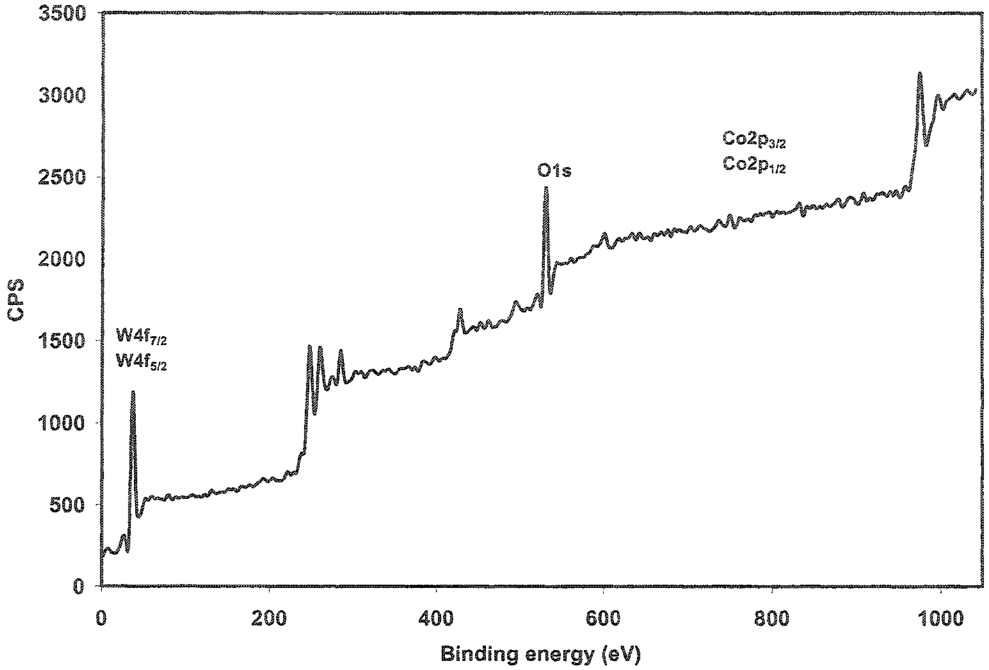

Figure 4.44: XPS survey scan of 1.0% Co-WO_3

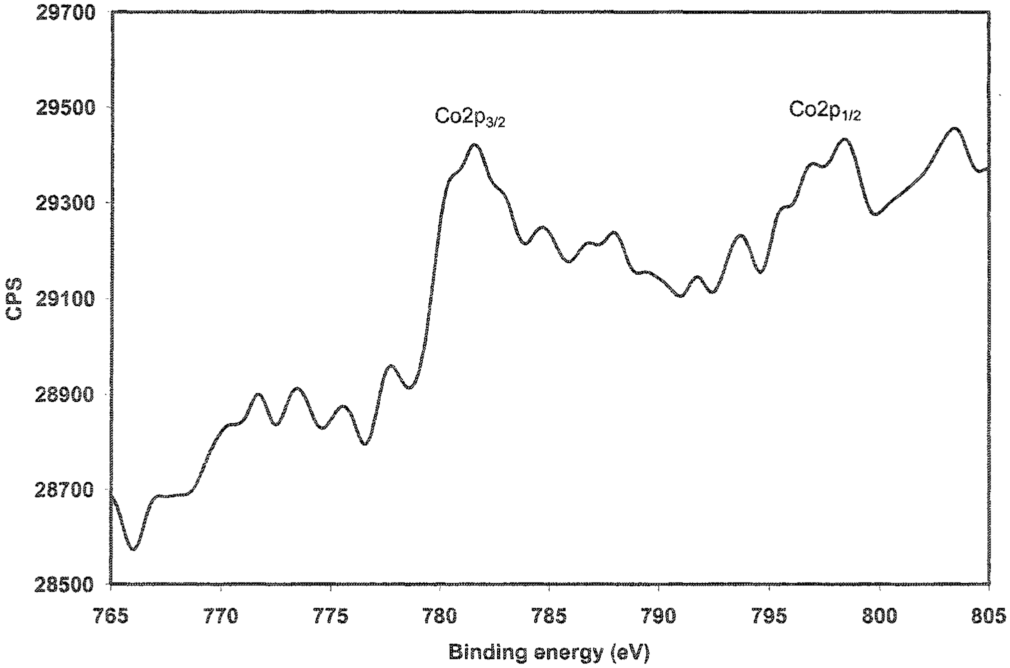

Figure 4.45: XPS spectrum of Co 2p in 1.0% Co-WO_3

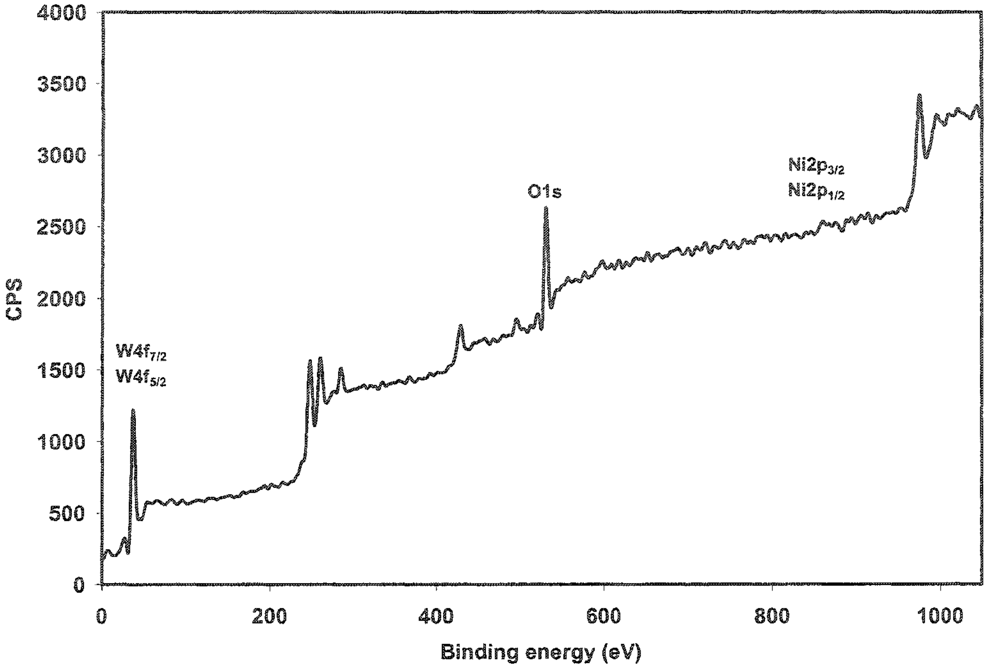

Figure 4.46: XPS survey scan of 1.0% Ni-WO_3

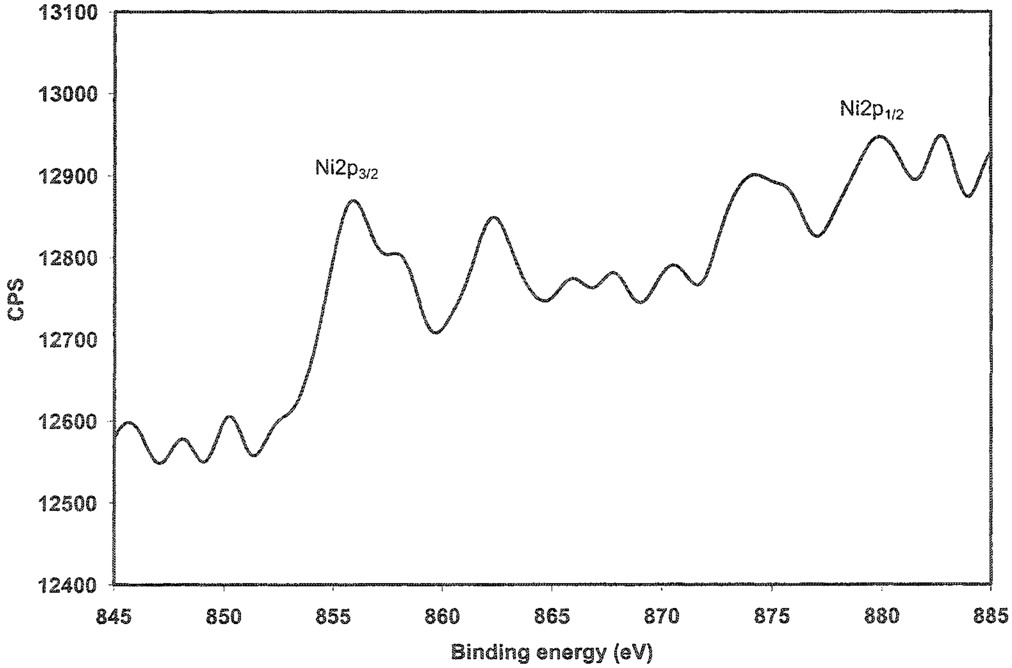

Figure 4.47: XPS spectrum of Ni 2p in 1.0% Ni-WO_3

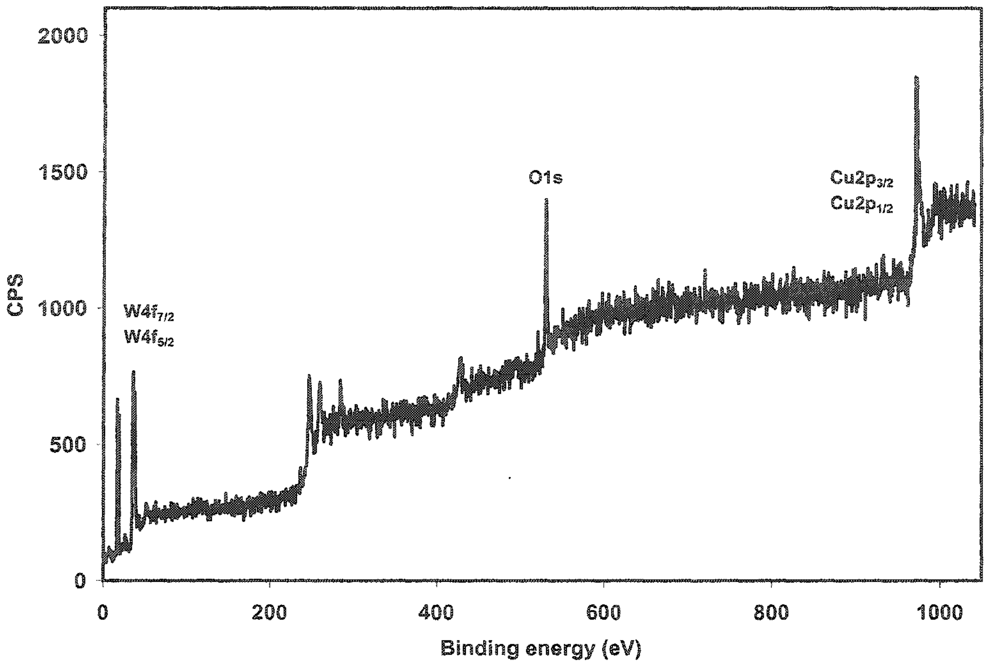

Figure 4.48: XPS survey scan of 1.0% Cu-WO_3

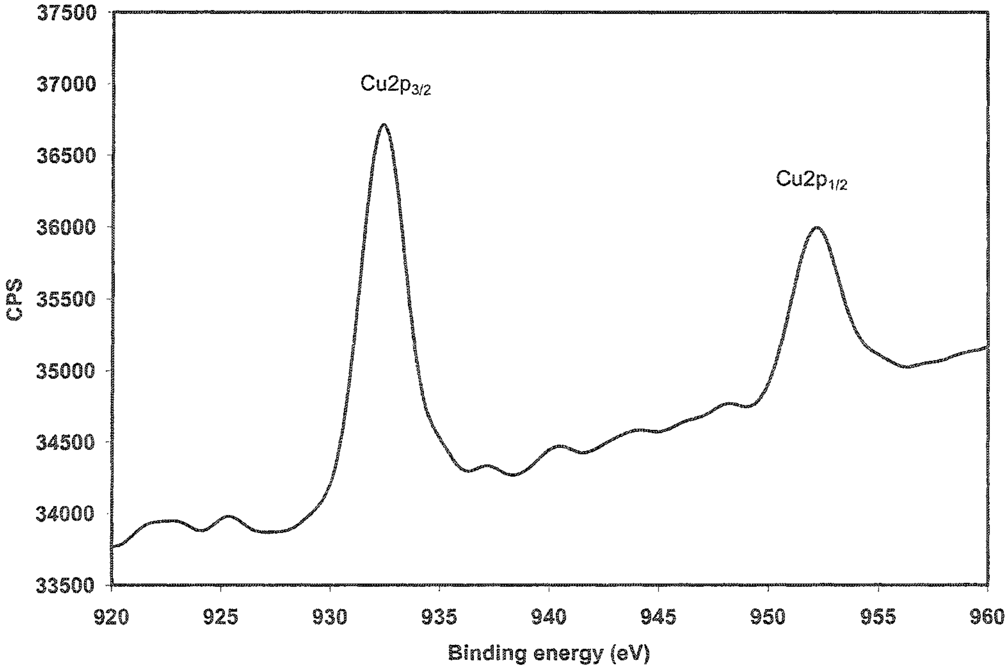

Figure 4.49: XPS spectrum of Ni 2p in 1.0% Cu-WO_3

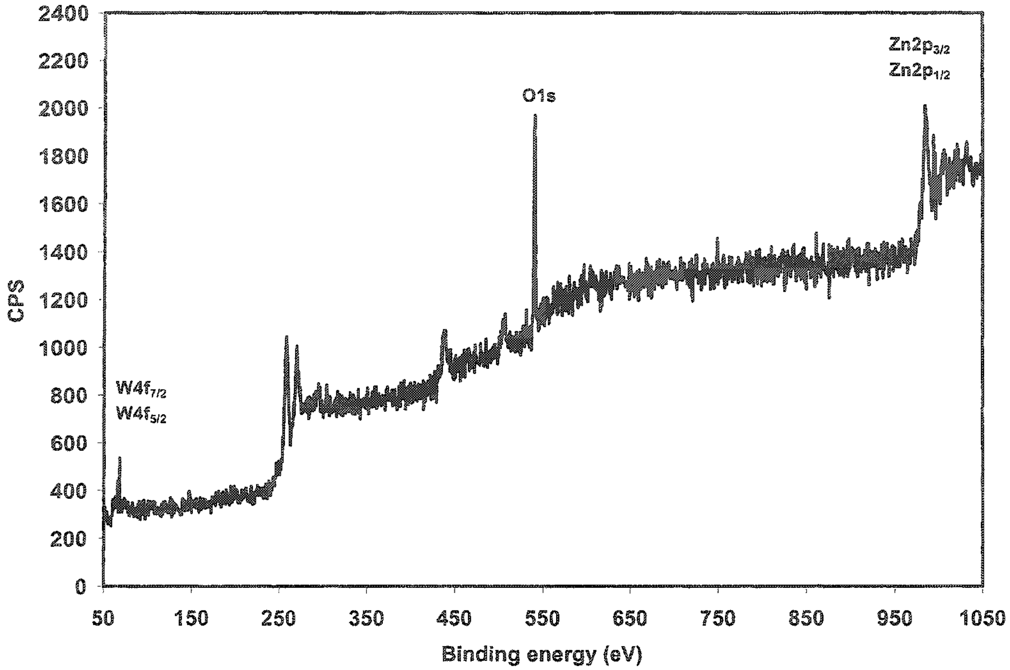

Figure 4.50: XPS survey scan of 1.0% Zn-WO$_3$

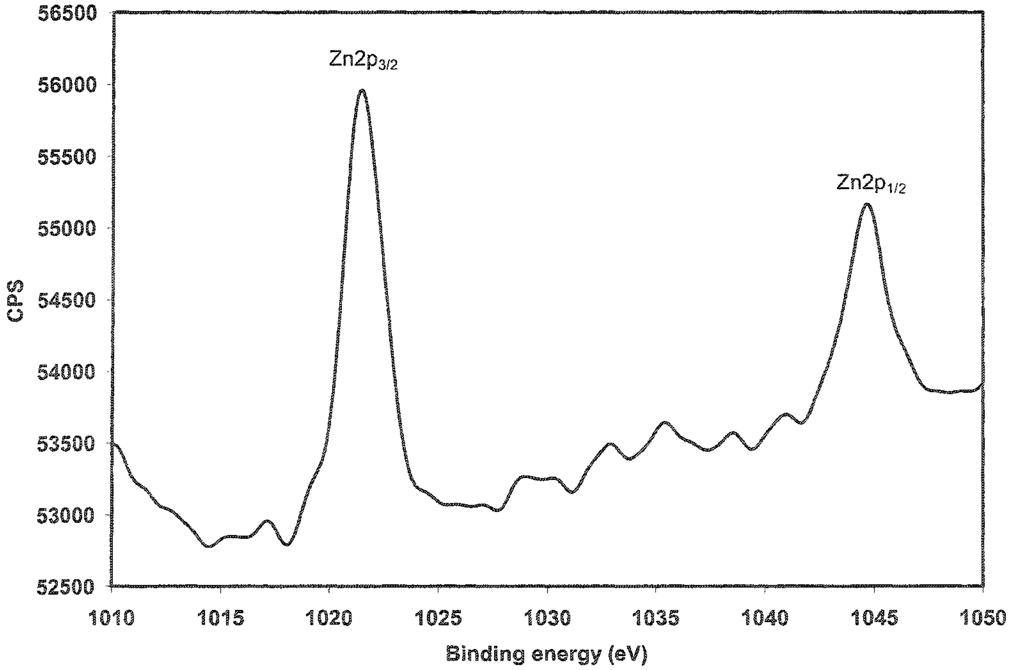

Figure 4.51: XPS spectrum of Zn 2p in 1.0% Zn-WO$_3$

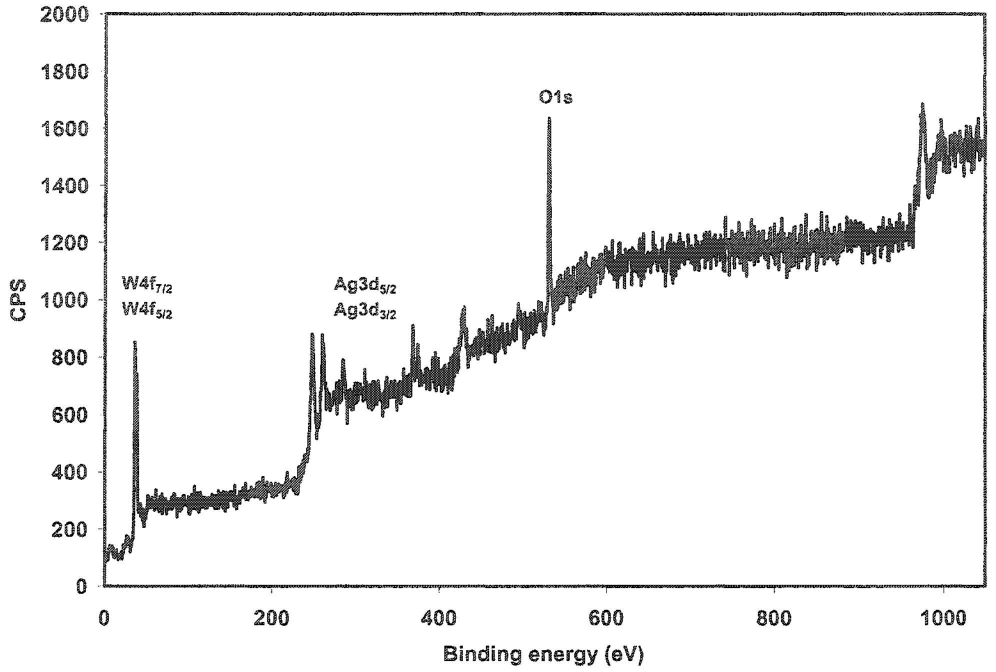

Figure 4.52: XPS survey scan of 1.0% Ag-WO_3

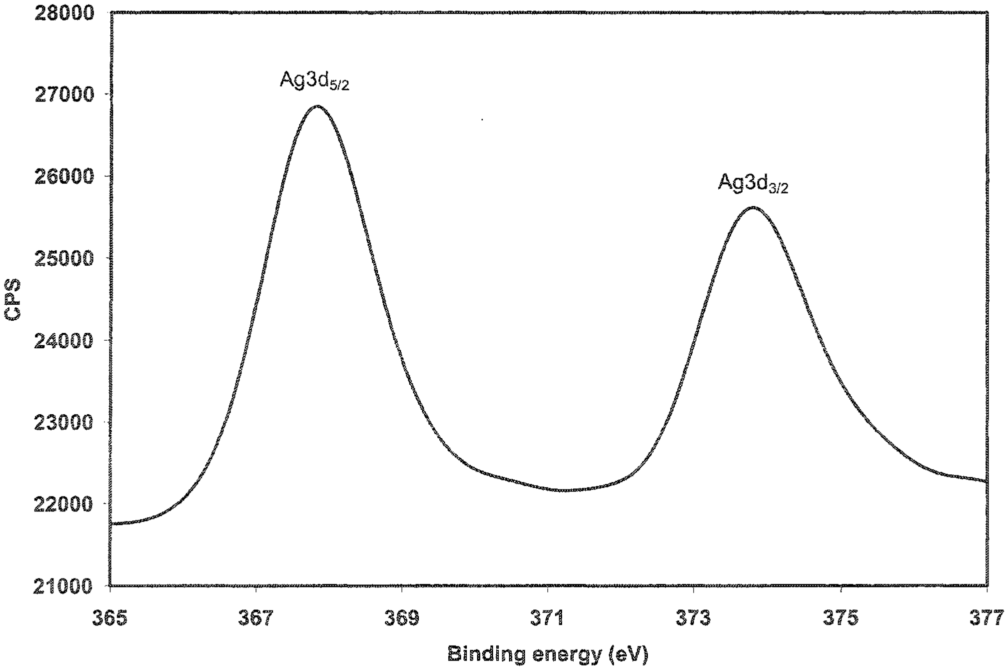

Figure 4.53: XPS spectrum of Ag 3d in 1.0% Ag-WO_3

CHAPTER FIVE

PHOTOCATALYTIC SPLITTING OF WATER

In this chapter, the results obtained for the photocatalytic activity of a number of pure photocatalysts (WO_3, TiO_2, NiO and α-Fe_2O_3), ranging from a narrow bandgap of 2.2 eV to 3.5 eV and transition metal doped WO_3 towards water splitting, using a 355 nm laser as light source are discussed. Prior to the discussion of results a mechanism of photocatalytic water splitting is also discussed briefly.

Photocatalytic splitting of water into oxygen and hydrogen is based upon the formation of hydroxyl radicals ($OH^{\cdot}$) and H^+ ions through water oxidation by the valence band holes produced due to laser irradiation of a semiconductor catalyst in an aqueous suspension. The hydroxyl radicals generate oxygen while H^+ ions form hydrogen by capturing conduction band electrons.

$$SC \xrightarrow{h\upsilon > E_g} SC(h_{vb}^+ + e_{cb}^-) \qquad 5.1$$

$$H_2O + h_{vb}^+ \rightarrow H_2O^+ \rightarrow OH^{\bullet} + H^+ \qquad 5.2$$

$$OH^{\bullet} + OH^{\bullet} \rightarrow H_2O + \tfrac{1}{2}O_2 \qquad 5.3$$

$$H^+ + e_{cb}^- \rightarrow H^{\bullet} + H^{\bullet} \rightarrow H_2 \qquad 5.4$$

The controlling factors in the oxidation of water, formation of hydroxyl radicals and generation of hydrogen at the surface of the catalyst are the redox potentials of various species involved and the potentials of valence and conduction band edges. To oxidize water, the valence band edge of the catalyst should be higher than +1.23 V, the redox potential for the $OH^{\cdot}/H_2O$ reaction, while the potential of conduction band edge should be lower than 0.0 V; the redox potential for hydrogen generation from H^+ ions. By nature, water splitting is a complex reaction due to the possibility of a number of side reactions that occur at the surface of the catalyst and in solution. The effect of these side reactions on oxygen and hydrogen yields for individual catalysts will be discussed in the coming sections. The schematic diagram illustrating the mechanism of water splitting is presented in figure 5.1.

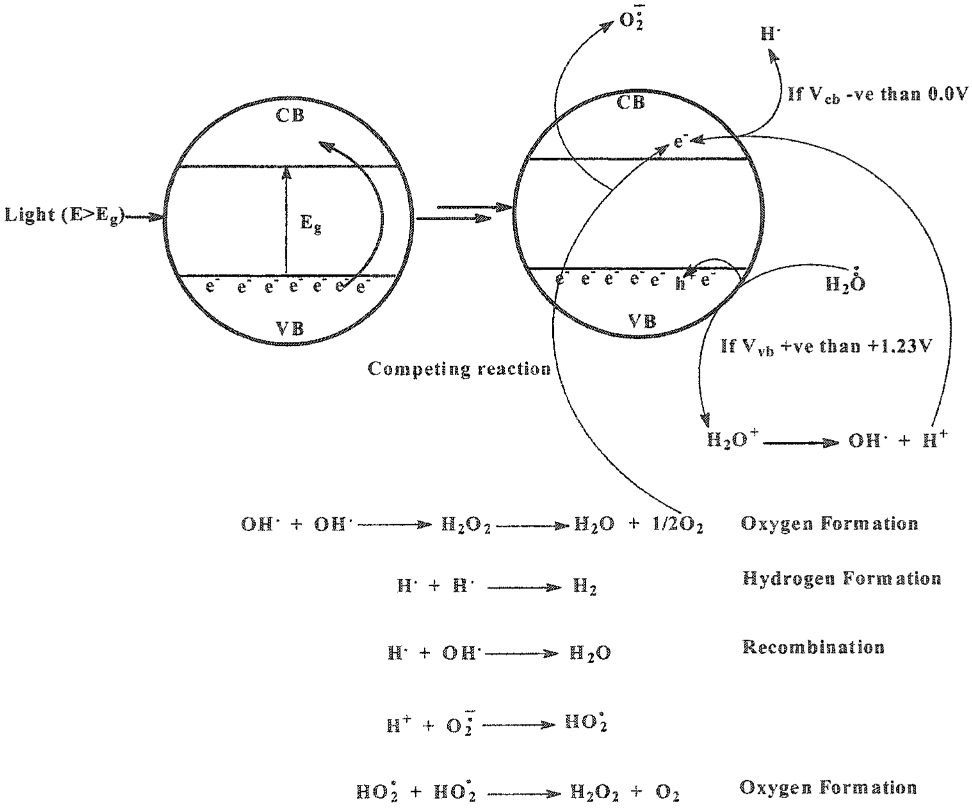

Figure 5.1 General mechanism of photocatalytic water splitting

5.1 Optimization of experimental parameters

While working with the laser as light source, it was observed that the important parameters which affect the production yield and overall photocatalytic process are laser beam diameter, stirring rate, laser energy and the amount of catalyst. The beam diameter and stirring rate were kept constant while the other two parameters i.e. amount of catalyst and laser energy were carefully optimized on the basis of changes in dissolved oxygen measured, as described below, by using a dissolved oxygen meter as described below.

The above-mentioned parameters were optimized for one of the catalyst i.e. WO_3 only and kept constant for all the other transition metal doped and pure photocatalysts. The oxygen yields, for various concentrations of WO_3 suspended in 60 ml of deionized water, were measured for 30 minutes and are plotted in figure 5.2. Where a gradual increase in O_2 yield can be noticed from 50 mg to 400 mg and a decrease in O_2 yield can be observed with further increase in the catalyst amount i.e. 500 mg. This trend indicates the high activity of WO_3 for O_2 production through water oxidation, particularly in 50 mg to 400 mg range but a further increase in particle density causes a decrease in O_2 yield indicating an increase in the extent of non-productive electron- hole recombination. Based on these results experimental results a fixed amount of 400 mg was used for other catalysts and the rest of the experiments.

Figure 5.3 depicts the amount of oxygen formed (yield) plotted versus the laser energy for WO_3 catalysts at 355 nm laser irradiation. During these experiments, the optimized amount of the catalyst from the previous step i.e. 400 mg of the catalyst was suspended in 60 ml of deionized water and the yield of oxygen was measured for different laser energies ranging from 50 to 200 mJ. It can be noticed that the oxygen yield shows strong dependence on the incident photon flux (laser energy). A linear increase in the oxygen yield has been observed in the 50-100 mJ laser energy range. However, the O_2 yield also increases for 100-200 mJ range but the dependence is not linear. The initial increase in oxygen yield with the laser energy could be attributed to the fact that the generation of electron hole pair increases with the incident laser photon flux, which in turn enhances the water oxidation process to generate O_2. Although the process of electron hole generation increases with the increased incident laser photon flux, in the 100-200 mJ laser energy range yet the oxygen yield remains constant. This is due to an increase in the electron hole recombination process, which counteracts with the electron hole generation, resulting in impeding further increase in oxygen yield. Also at constant stirring rate, the total number of catalyst particles exposed per unit area remains the same causing a decrease in O_2 production.

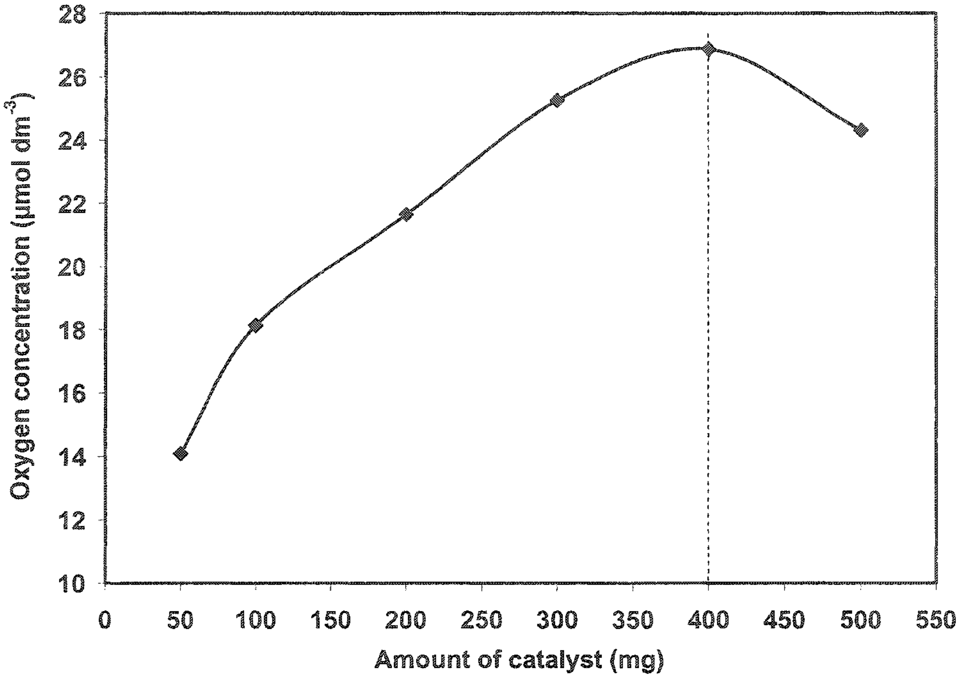

Figure 5.2 Oxygen yield plotted versus the amount of catalyst measured over 30 minutes

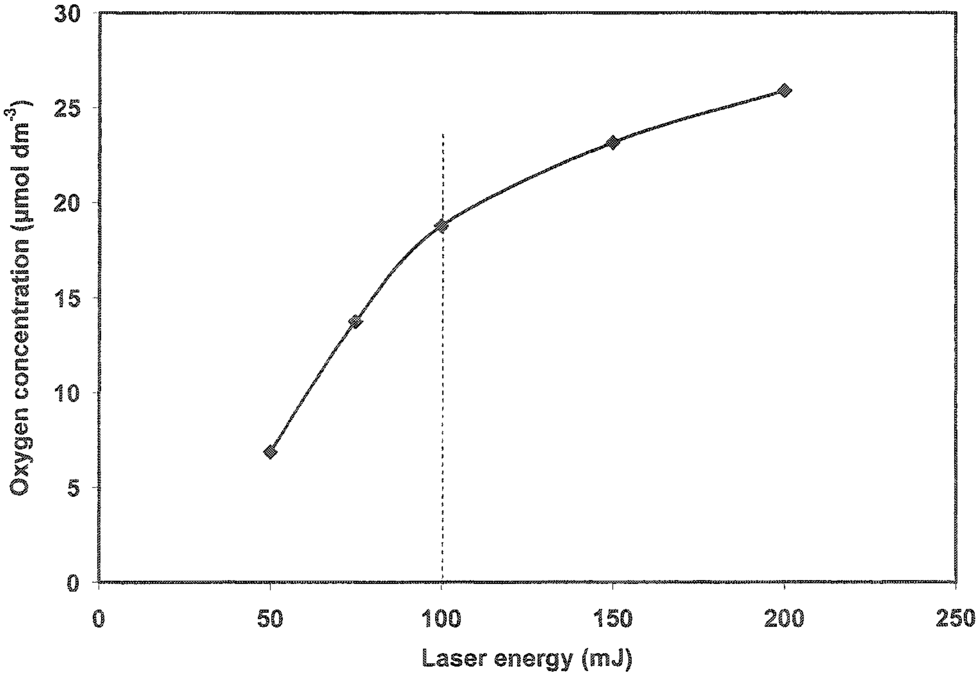

Figure 5.3 Oxygen yield plotted versus the incident laser energy measured over 30 minutes

5.2 Photocatalytic oxidation of water over WO_3

To study the photocatalytic oxidation process as a function of time, a WO_3 suspension was exposed to laser radiation at 355 nm for 90 minutes and yield was recorded at 10 minutes intervals keeping other parameters constant. It was observed that with the increase in laser exposure time the color of the suspension changes from yellow to green-blue indicating the formation of structural defects in WO_3 with the absorption of UV light. In addition to oxygen, the generation of H_2 in non-stoichiometric amounts was also observed. The formation of H_2 was unexpected as the band edge positions i.e. conduction (+0.4 V) and valence bands (+3.1 V) at pH = 0 for WO_3 [85-87] does not support the formation of H_2 gas.

WO_3 regained its yellow color, when the green-blue suspension was kept in the dark for some time. The analysis of the gas sample from the dead volume of the cell placed in the dark confirmed the presence of H_2 gas. To rule out the possibility of H_2 generation by multi photon photolysis, a catalyst free experiment (without WO_3) under the same experimental conditions was performed but no hydrogen or oxygen was observed. This confirmed that the formation of H_2 and the color change of the catalyst are due to the laser irradiation of WO_3 and are interrelated.

The yellow tungsten oxide (WO_3) has slightly distorted monoclinic structure; consisting of WO_6 octahedra, arranged in various corner-sharing or edge-sharing configurations [118,119]. In this configuration, each tungsten atom exists as W^{6+}. Absorption of light causes the transfer of an electron from the valence band of an oxygen atom to the conduction band of a tungsten atom. This weakens the tungsten-oxygen bond, allowing lattice oxygen to be driven out creating a defect site. The additional electron then moves from one tungsten atom to another as illustrated [120].

$$W^{5+}(a) + W^{6+}(b) \rightarrow W^{6+}(a) + W^{5+}(b) \qquad 5.5$$

This process leads to the formation of a hole in the valence band and a trapped electron at the defect site. The hole in the valence band oxidizes the adsorbed water producing O_2 and H^+ ions in the solution as given in equations 5.1-5.4.

The presence of H^+ ions was also confirmed by the pH measurement during the course of the reaction and will be discussed separately. The H^+ ions produced as a result of the photocatalytic oxidation of water are then inserted or intercalated at the defect sites created by the absorption of UV light.

$$xH^+ + xe^- + WO_3 \rightarrow H_xWO_{3-x} \qquad 5.6$$

With this reversible intercalation or insertion, the structural distortion decreases and a blue color is observed [121]. When laser is used as light source, the sample is exposed uni-directionally and the number of WO_3 particles exposed per unit area remains the same if no change in other parameters (laser energy, stirring rate, beam diameter and particle density) takes place. After excitation the WO_3 particles diffuse in the bulk or in the "dark". As the fraction of oxygen produced by the photocatalytic process, remains in the solution due to high solubility in water, it is again inserted into the WO_3 lattice in the dark by displacing the hydrogen in H_xWO_{3-x}.

$$H_xWO_{3-x} + xO_2 \rightarrow WO_3 + x/2\,H_2 \qquad 5.7$$

It is clear from the above-mentioned process that only a small fraction of H^+ ions produced by photocatalytic oxidation can contribute towards H_2 formation. In addition, the produced O_2 competes with H^+ ions for insertion in the defect sites.

To verify the mechanism of color regeneration i.e. from blue to yellow, by the back insertion of produced oxygen and H_2 generation the same reaction was performed in degassed methanol. No regeneration of yellow color was observed, as no oxygen formation occurs in photocatalytic decomposition of methanol. In another experiment, the reduced blue catalyst regained its original yellow color in oxygen saturated de-ionized water in the dark. Therefore, the reversible processes i.e. reduction and re-oxidation of the catalyst are responsible for the production of hydrogen under the influence of a strong laser beam. The yield of evolved gases (mmol) and the rate of production of gases as a function of laser exposure time are presented in figures 5.4 and 5.5, where an initial sharp increase followed by a slow increase in O_2 and H_2 yield, with time, can be observed. The rate of production of both gases decreases with time but the decrease in the rate of oxygen production is relatively sharp compared to that of hydrogen indicating the decrease in the production of hydroxyl radicals with the decrease in the pH of the system. The decrease in the extent of water splitting is mainly due to the shifting of the valence band edge to a more positive value, increasing the magnitude of the over voltage associated. The initial sharp decrease followed by a slow decrease in pH (figure 5.6) during the photocatalytic splitting of water also supports this explanation as is explained in the next section.

5.2.1 pH measurements

The progress of photocatalytic water oxidation was also studied by measuring the pH changes during the course of reaction in an argon environment. The changes in pH as a function of laser exposure time are presented in figure 5.6, where a substantial decrease in pH can be observed in an argon environment because most of the H^+ ions produced as a result of water oxidation remain in the solution and only a small fraction is converted to H_2 by the process described above. The depletion of H^+ ions by super oxide (O_2^{-}) radicals formed by the capture of trapped electrons can be ruled out as the conduction band edge (+0.4 V) of WO_3 does not support their formation. However, the combination of H^+ ions with dissolved oxygen in the presence of aqueous electrons can lead to a decrease in the concentration of H^+ ions in solution.

$$O_{2(ads)} + e_{tr}^{-} \rightarrow O_2^{-\bullet} \tag{5.8}$$

$$H^{+} + O_2 + e_{aq}^{-} \rightarrow HO_2 \tag{5.9}$$

The above-mentioned processes are activated only when the oxygen produced by photocatalytic water oxidation reaches an appreciable quantity. A sharp decease followed by a slow decrease (figure 5.6) suggests that although the conduction band edge of WO_3 is not favorable for the formation of H_2 the probability of H_2 formation through the reversible insertion of H^+ ions increases at high H^+ concentration.

5.2.2 Effect of metal ions

In photocatalytic processes, metal ions are used to enhance the efficiency by suppressing the non-productive electron-hole recombination. The metal ions are selected on the basis of the redox potentials of the couples involved. Ions with reduction potential higher than the conduction band potential of the semiconductor act as electron scavengers and are called as "electron capture agents". Metal ions, with reduction potential lower than the conduction band potential of the semiconductor, do not act as electron capture agents [2,5,17,18]. In this study two metal ions, Fe^{3+} and Ag^+, were selected as electron capture agents since their redox potentials are higher than the conduction band potential of WO_3. Although the redox potential of the Li^+/ Li^o couple is lower than the conduction band potential of WO_3, Li^+ has a comparable reactivity with H^+ ions and is a suitable candidate for insertion in reduced WO_3 lattice to give species like Li_xWO_{3-x}. The reduction potentials of Fe^{3+}/ Fe^{2+}, Ag^+/ Ag^o and Li^+/ Li^o are +0.77 V, +0.80 V and -3.05 V respectively [122].

The effect of these metal ions on H_2 and O_2 yield is presented in figures 5.7 and 5.8 respectively. The expected decrease in H_2 formation (figure 5.7) and increase in O_2 production (figure 5.8) in the presence of Fe^{3+} ions reveals the suitability of the reduction potential for conduction band electron capture before trapping in the surface states and suppresses the formation of hydrogen by producing reduced species such as H_xWO_{3-x} which are basically precursors for H_2 generation. The increase in the O_2 formation also indicates an increase in photocatalytic oxidation of water and decrease in the formation of superoxide radicals through electron capture by the adsorbed oxygen. The sustained increase in O_2 production in the presence of Fe^{3+} suggests the regenerative behavior of Fe^{3+}/Fe^{2+} couple i.e. accepting the conduction electron first and donating it again to valence band hole.

$$Fe^{3+} + e_{cb}^{-} \rightarrow Fe^{2+} \tag{5.10}$$

$$Fe^{2+} + h_{vb}^{+} \rightarrow Fe^{3+} \tag{5.11}$$

Also in the presence of Fe^{2+} ions in the solution, the contribution of homogeneous photo Fenton-type reactions in enhancing the yield of O_2 cannot be neglected [17].

$$Fe^{2+} + H_2O_2 + H^{+} \rightarrow Fe^{3+} + OH^{\bullet} + H_2O \tag{5.12}$$

Ag^{+} has a favorable reduction potential of +0.80 V and qualifies for serving as an electron scavenger. In the presence of Ag^{+} the formation of H_2 is decreased, as shown in figure 5.7, due to the conduction band electron capture but the increase in O_2 yield as presented in figure 5.8, is not comparable to Fe^{3+} suggesting the depletion of Ag^{+} ions with the time. The deposition of Ag^{o} at the surface of the catalyst and the possible formation of Ag_2O in the presence of O_2 [18] is explained below.

$$Ag^{+} + e_{cb}^{-} \rightarrow Ag^{\circ} \tag{5.13}$$

$$2Ag^{+} + 2O_2^{-} \rightarrow Ag_2O \tag{5.14}$$

The reduction potential of Li^+ is much more negative than the potential of conduction band electrons so the probability of capturing conduction band electrons is very low. An increase in the H_2 production in the presence of Li^+ ions was observed in the first 30 minutes (figure 5.7) compared to that of WO_3 indicating the formation of a more reduced site essential for the formation of H_2 and reducing the re-insertion of produced oxygen. A considerable decrease in O_2 production (figure 5.8) indicates the consumption of produced O_2 by Li^+ ions.

The efficiency of a photocatalytic process is measured by its ability to convert the photons to desired products. In this study, we estimated the photonic efficiency for the photo-oxidation of water to H_2 and O_2 over WO_3 in the presence and absence of metal ions. The plots of photonic efficiencies as a function of laser exposure time for H_2 and O_2 are presented in figures 5.9 and 5.10.

It was observed that for pure WO_3 the photonic efficiency for H_2 and O_2 production initially increases rapidly, reaches a maximum value and then starts decreasing gradually. The decrease in photonic efficiency is mainly due to the simultaneous presence of H^+ ions and O_2 in the solution. For Ag^+ and Li^+, the photonic efficiency for H_2 initially increases then decreases very sharply suggesting the depletion of these ions with time. For Fe^{3+}, the photonic efficiency for H_2 production was even lower than WO_3 showing its suitability for conduction band electron capture. For O_2 production, the overall photonic efficiency of 16% was observed for Fe^{3+} and the minimum photonic efficiency of less than 3% was observed for Li^+. A low overall photonic efficiency for both H_2 and O_2 production for pure WO_3 (as given in table 5.1 reveals that the process of water oxidation is rather inefficient over pure WO_3 due to the high over potentials and most of the photons are lost in electron-hole pair recombination. The recombination process can be suppressed by the use of suitable electron capture agents.

Another measure for the efficiency of a photocatalytic water splitting process is O_2:H_2 ratio (figure 5.11). Ideally, this ratio should be 1:2. A maximum overall O_2: H_2 ratio of 1: ~1.6 was observed for Li^+ ions which is due the fact that Li^+ ions increase the production of H_2 by consuming and suppressing the re-insertion of the produced oxygen. For Fe^{3+} and Ag^+ the O_2: H_2 ratio was even lower than pure WO_3, which confirms the electron scavenging nature of these ions.

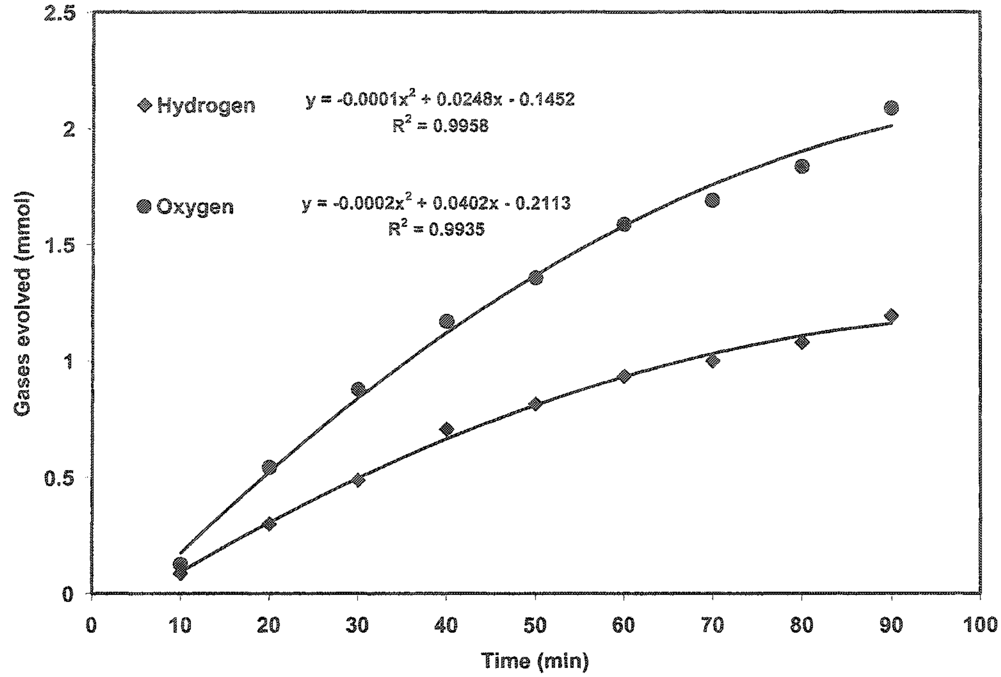

Figure 5.4 Hydrogen and oxygen evolution with time over WO_3

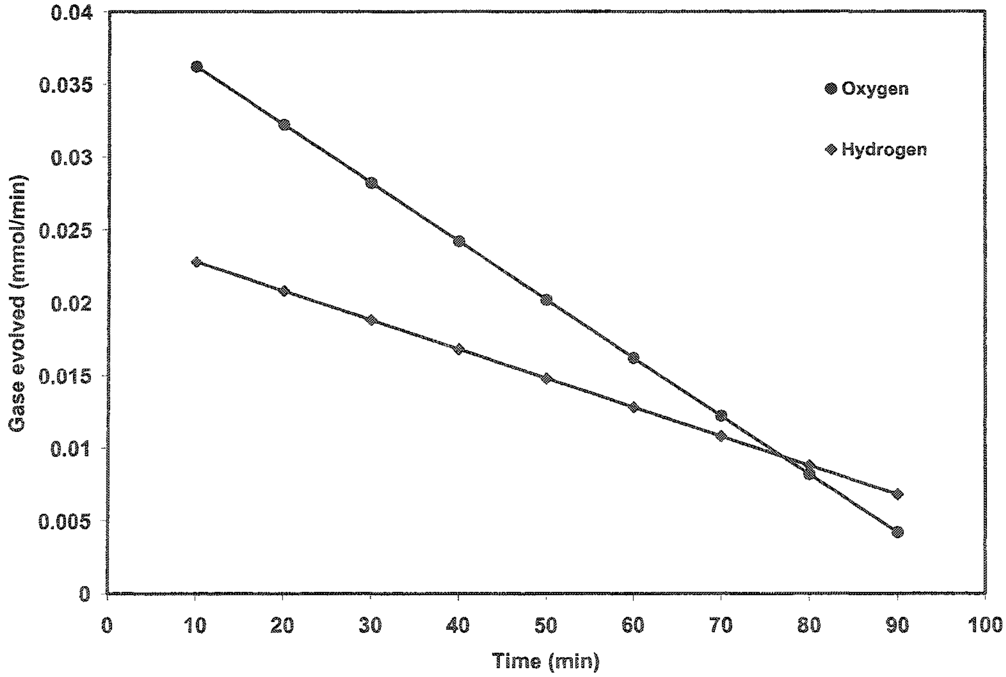

Figure 5.5 Rate of hydrogen and oxygen production over WO_3 plotted as a function of laser exposure time

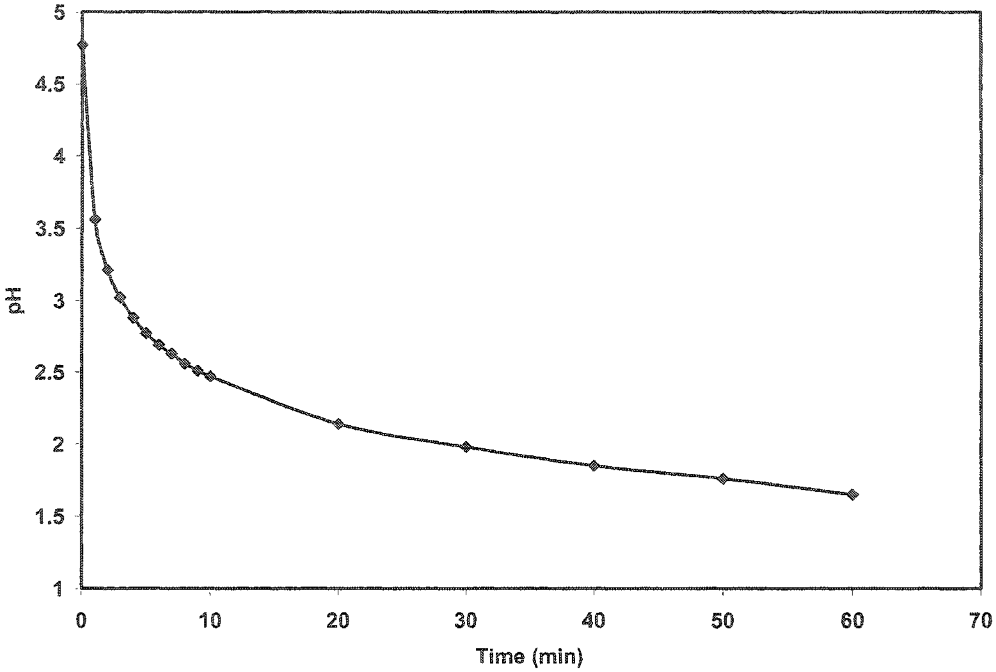

Figure 5.6 pH changes in argon environment during the course of photocatalytic splitting of water over pure WO_3

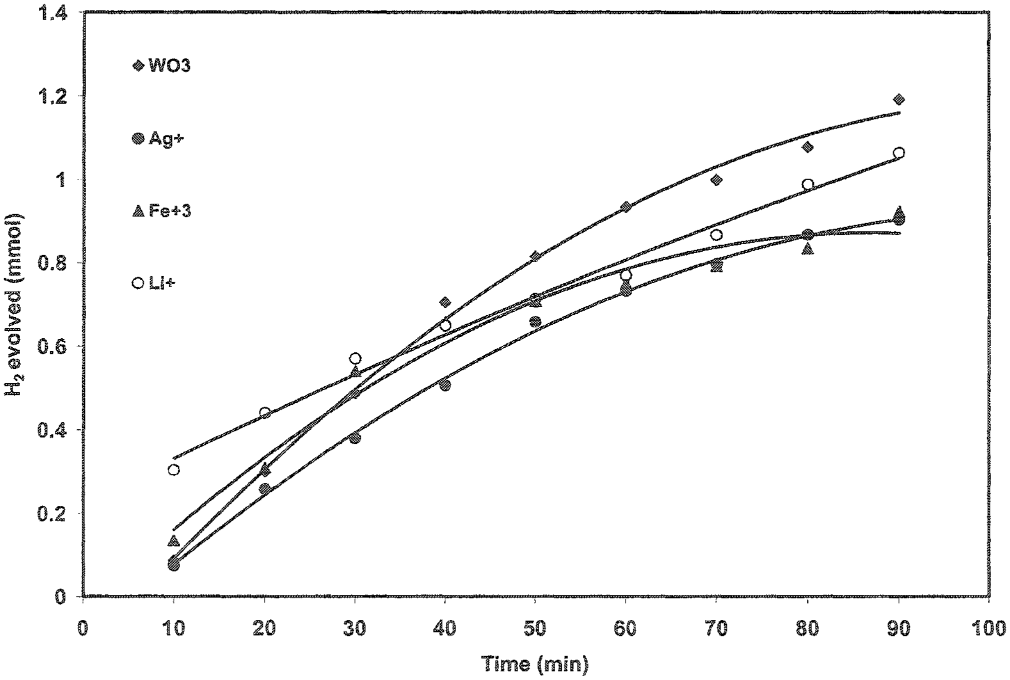

Figure 5.7 Hydrogen production over WO_3 in the presence of metal ions

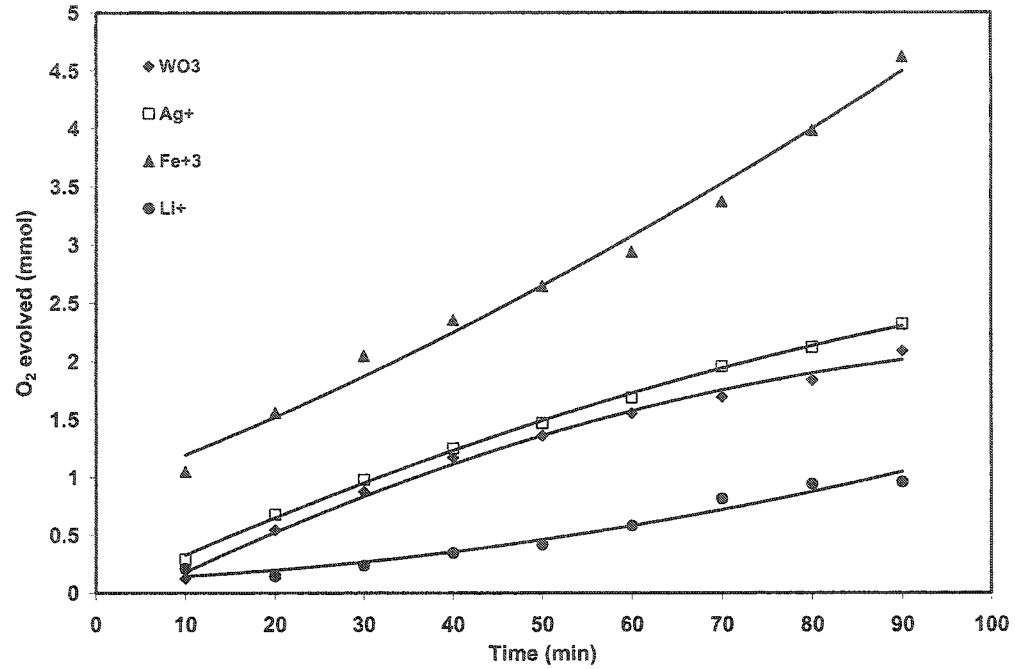

Figure 5.8 Oxygen production over WO_3 in the presence of metal ions

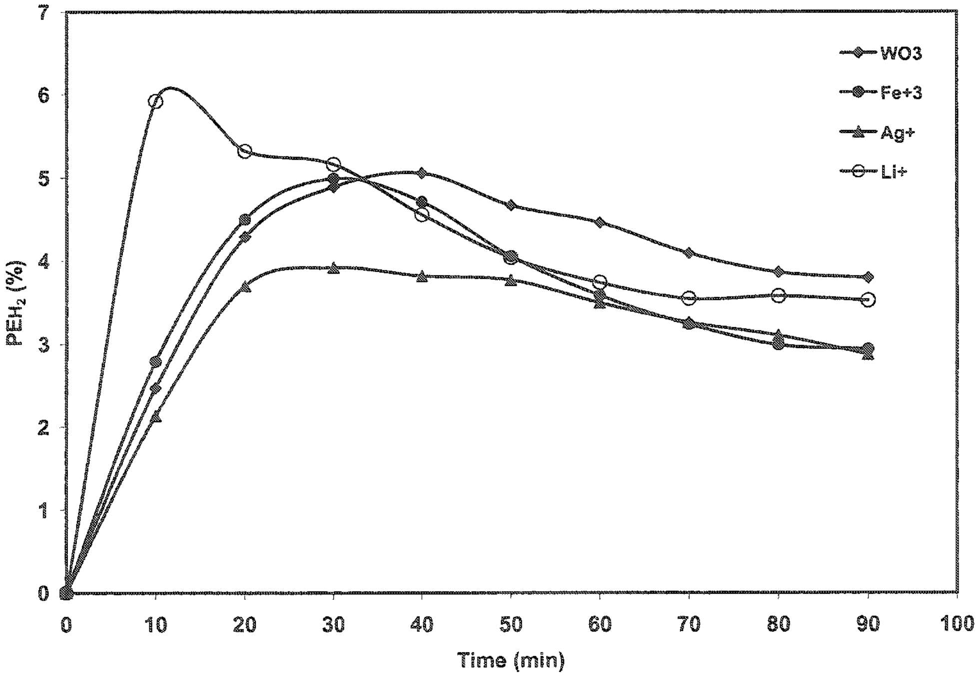

Figure 5.9 Photonic efficiency of hydrogen production over WO_3 in the presence of metal ions

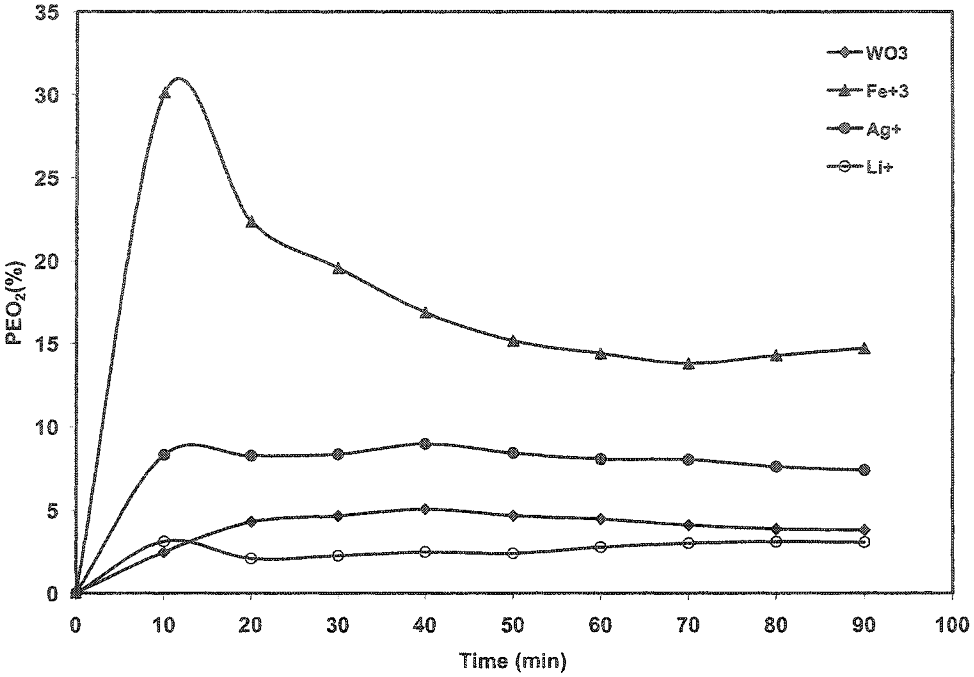

Figure 5.10 Photonic efficiency of oxygen production over WO_3 in the presence of metal ions

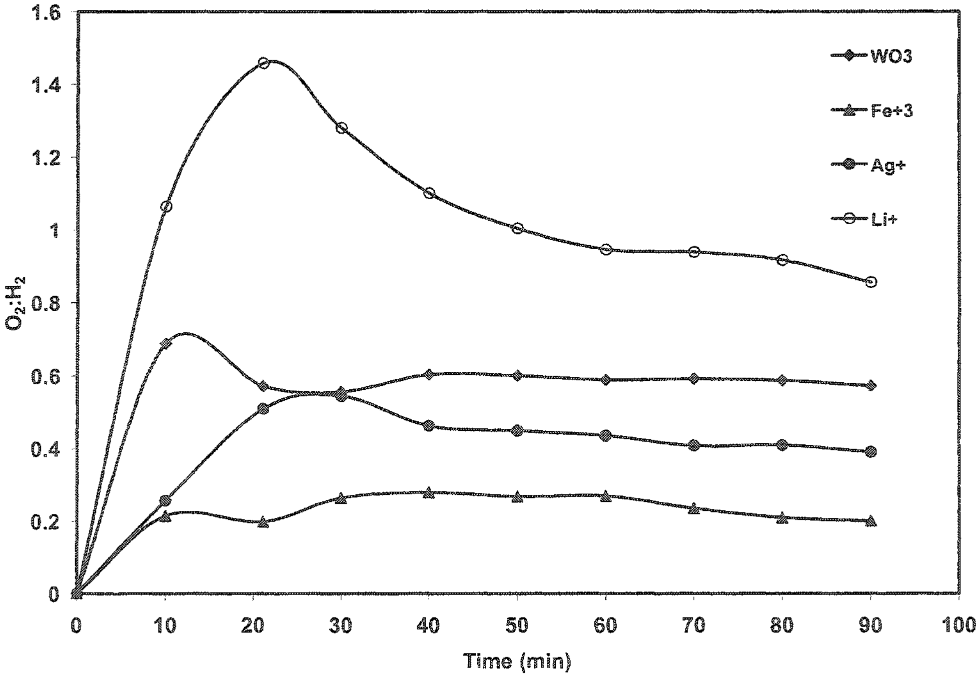

Figure 5.11 Comparison of oxygen to hydrogen ratio (O_2:H_2) over WO_3 in the presence of metal ions

5.3 Photocatalytic oxidation of water over TiO_2

The photocatalytic process over TiO_2 was studied by exposing the aqueous powder suspension to laser irradiation for 90 minutes and yield was recorded at 10 minute intervals. All other parameters were kept constant. With the increase in laser exposure time, it was observed that with the increase in laser exposure time the color of the catalyst changed from white to dark grey and the O_2 and H_2 evolved in non-stoichiometric amounts

The original color of the catalyst was not regenerated even when kept in the dark. The catalyst regained its original white color when heated at $450^{\circ}C$ in the presence of oxygen. This confirms the loss of lattice oxygen and the reduction of the catalyst under illumination. To check for H_2 and O_2 generation by multi photon photolysis of water a blank experiment (without TiO_2) under the same experimental conditions was performed. No hydrogen or oxygen was observed. The formation of hydrogen and oxygen in non-stoichiometric amounts was unexpected as the band edge positions i.e. valence (+2.72 V) and conduction bands (-0.48 V) at pH = 0 for TiO_2 [123] are highly suitable for this purpose.

TiO_2 (rutile) has a slightly distorted monoclinic structure and is well known for its photocatalytic properties. It consists of TiO_6 octahedra arranged in various corner-sharing or edge-sharing configurations [124]. In this configuration, each titanium atom exists as Ti^{4+}. In aqueous suspensions water is dissociatively adsorbed at the surface of TiO_2 in such a way that each Ti^{4+} bears one hydroxyl group. The nature of the bonding of hydroxyl ions with Ti^{4+} is not well understood [125].

Absorption of a photon of energy equal to or greater than the band gap energy ($E>E_g$) causes the transfer of an electron from the valence band of oxygen (2p) to the conduction band of Ti (3d) and the reduction of Ti^{4+} to Ti^{+3}. This electron transfer process weakens the titanium-oxygen bond and in turn drives out a lattice oxygen to create a "defect" or "tape" site.

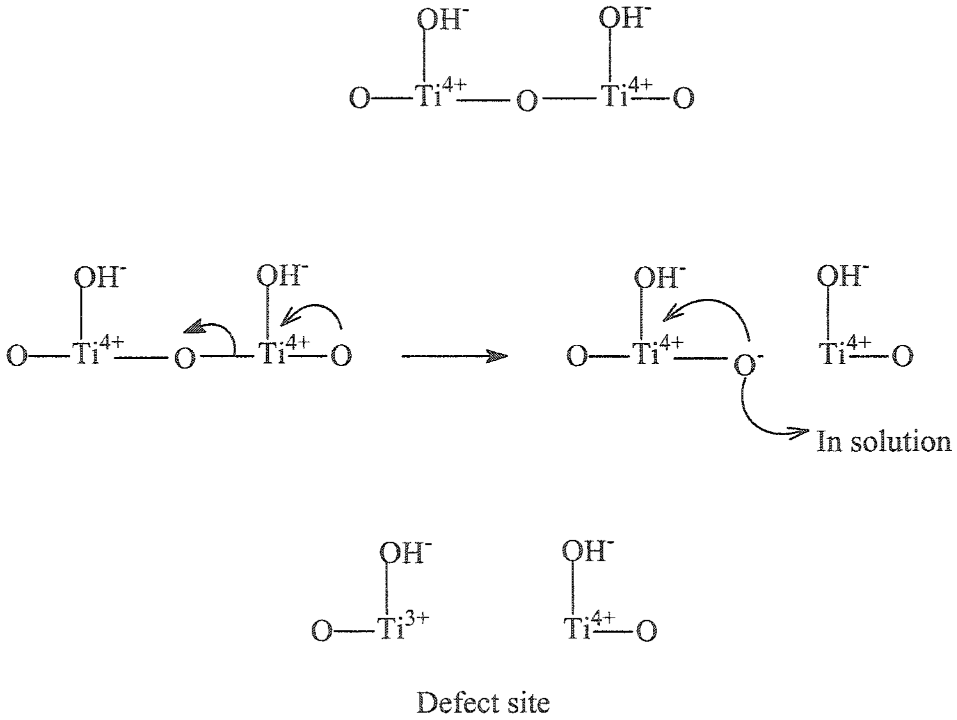

This light driven electron transfer leads to the formation of a hole in the valence band and a trapped electron at the defect site. The hole in the valence band oxidizes the adsorbed water molecule producing O_2 an H^+ ions in solution. The H^+ ion produced as a result of the photocatalytic oxidation of water captures the trapped electron from the defect sites to produce hydrogen (equations 5.1-5.4).

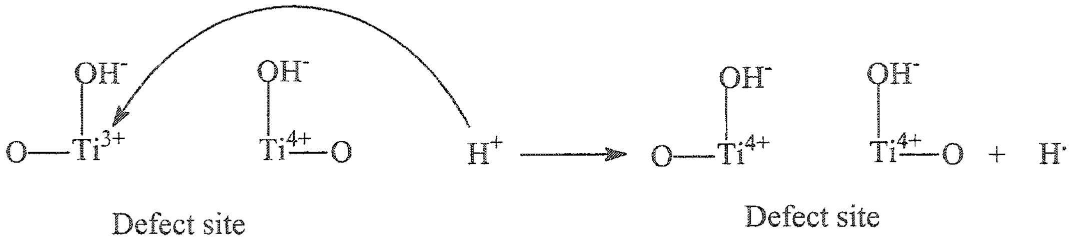

With this reduction process the stoichiometric rutile TiO_2 changes to non-stoichiometric TiO_{2-x} and a dark grey color is observed [126]. This process is reversible only at elevated temperatures in the oxidizing environment i.e. in presence of oxygen.

$$TiO_{2-x} + \tfrac{x}{2} O_2 \rightarrow TiO_2 \qquad 5.15$$

A plot of evolved gases (mmol) as a function of laser exposure time is presented in figure 5.12. Where it is observed that initially the amount of hydrogen produced is lower than that of oxygen formation but increases to exceed that of oxygen with the increase in the reduction of the catalyst or with the increase in bulk defect sites as these sites act as the trap and transfer sites for photoexcited electrons. This behavior indicates that oxygen is produced not only due to photocatalytic splitting of water but released from the lattice as well. The rates of production of hydrogen and oxygen as given in figure 5.13 where it is observed that the rate of hydrogen production increases with the increase in the number of defect sites (produced as a result of the reduction of catalyst) while the rate of oxygen production decreases very slightly over time. This slight decrease is oxygen production is attributed to the reduction of water (equation 5.16) which competes with the H^+ ions for conduction band electrons.

5.3.1 pH measurements

The role of produced O_2 on the photocatalytic process was studied by measuring the pH changes during the course of the reaction in an argon environment. As figure 5.14 shows, pH increases with laser exposure time. This pH increase is attributed to the reduction of produced oxygen through conduction band electron capture in the presence of water according to the equation,

$$O_2 + 2H_2O + 2e^- \rightarrow H_2O_2 + 2OH^- \qquad 5.16$$

Although the conduction band edge is suitable for hydrogen production, super oxide ($O_2^{\cdot-}$) formation through conduction band electron capture (equation 5.8) cannot be ignored. Super oxide radicals compete with H^+ ions for conduction band electrons. In addition, both the superoxide radicals and the hydroxyl ions (equation 5.16) act as scavengers for H^+ ions and negatively affect the formation of H_2 gas. In the presence of argon, the above-mentioned processes are activated when an appreciable amount of oxygen is produced by the photocatalytic splitting of water. In addition, the presence of argon atoms in the solution in higher concentration inhibits the adsorption of oxygen on TiO_2. It is also clear from figure 5.14 that the H^+ ions produced by the donation of electrons from water molecules to photogenerated holes either changes to hydrogen or react with hydroxyl ions or super oxide radicals ($O_2^{-\bullet}$) to form water (recombination) and HO_2 radicals.

$$H^+ + O_2^{-\bullet} \rightarrow H_2O^\bullet \qquad 5.17$$

The high oxygen yield promotes the production of hydroxyl ions through oxygen reduction by capture of photogenerated holes. Therefore, the reasons for low and non-stoichiometric evolution of H_2 are:

i. The formation of surface defects and release of lattice oxygen from TiO_2 lattice
ii. The recombination reaction of H^+ and OH^- ions
iii. The competition of H^+ ions with adsorbed oxygen for conduction band electrons

Another important feature associated with the reduction of water (equation 5.16) (that causes an increase in the pH of suspension) is the change in the positions of valence and conduction band edges. It is clear from figure 5.14, that the pH of the system sharply increases and reaches to a stable value of ~ 7.3. The positions of valence and conduction band edges at this pH can be approximated by using the relation [18].

$$E_{fb} = E_{fb}(pH = 0) - 0.059pH \qquad 5.18$$

Where E_{fb} is the flat band potential at the measured pH while $E_{fb}(pH = 0)$ is the flat band potential at zero pH. The calculated values for valence and conduction band edges are +2.29V and -0.9V respectively. These values indicate that with the reduction of the catalyst, the over potential associated with the formation of O_2 and H_2 from water decreases. The rate of H_2 and O_2 formation gradually increases with increase in the number of reduced catalyst particles.

5.3.2 Effect of metal ions

As mentioned in section 5.2, metal ions are used to enhance the efficiency of photocatalytic process by suppressing the non-productive electron-hole recombination [17,18,]. In this study, Fe^{3+} and Ag^{+} ions were selected as electron capture agents since their redox potentials are higher than the conduction band potential of WO_3. Although the redox potential of the Li^{+}/ Li^{o} couple is much negative than the conduction band potential of TiO_2, Li^{+} was selected to evaluate the effect of produced oxygen on the production of hydrogen through the mechanism described above. The reduction potentials of Fe^{3+}/ Fe^{2+}, Ag^{+}/ Ag^{0} and Li^{+}/ Li^{o} are +0.77 V, +0.80 V and -3.05 V respectively [122].

The effect of these metal ions on H_2 and O_2 production compared to that of pure TiO_2 is presented in figures 5.15 and 5.16 respectively. The drop in the production of H_2 (figure. 5.15) and the rise in the production of O_2 (figure. 5.16) in the presence of Fe^{3+} ions indicates the suitability of these ions as electron capture agents and the sustained increase indicates the regenerative behavior as given in equations 5.10 and 5.11. Also the deactivation of the catalyst by the deposition of $Fe(OH)_3$, in the presence of hydroxyl ions in the solution, cannot be neglected [17].

$$Fe^{3+} + 3OH^{-} \rightarrow Fe(OH)_3 \qquad 5.19$$

The favorable reduction potential of Ag^{+} (+0.80 V) makes it suitable as an electron scavenger however a weak effect of it relative to Fe^{3+} was observed in this study. The presence of Ag^{+} in aqueous suspension decreases the formation of H_2 (figure 5.15), increases O_2 (figure 5.16) initially, and starts decreasing gradually. The gradual decrease in O_2 yield over time suggests the disappearance of Ag^{+} in the solution with time as Ag_2O and as AgOH with an associated increase in the concentration of hydroxyl ions.

The reduction potential of Li^{+} is lower than the potential of conduction band electrons so the probability of capturing conduction band electrons is very low. A decrease in both H_2 and O_2 production in the presence of Li^{+} ions was observed owing to the deactivation of the catalyst by the formation and deposition of LiOH at the surface of the catalyst. This is again a confirmation of the presence of hydroxyl ions in the solution.

The efficiency of a photocatalytic process is measured on the basis of its ability to convert the photons in desired products. In this study, the photonic efficiency the photo-oxidation of water to H_2 and O_2 over pure TiO_2 and in the presence of metal ions was estimated. The plots of photonic efficiencies as a function of laser exposure time for H_2 and O_2 are presented in figures 5.17 and 5.18. It was observed that for pure TiO_2 the photonic efficiency for H_2 production increases sharply in the beginning and a slow rise was observed afterwards. This is due to the fact that in the beginning the photons are consumed more in the reduction of the catalyst than hydrogen production and once the catalyst is reduced fully, with the introduction of bulk defect sites, the photonic efficiency increase sharply. For O_2 production, the photonic efficiency initially increases rapidly, reaches to a maximum value and starts decreasing sharply before finally leveling out. The initial increase is due to the contribution from the lattice oxygen while the sharp decrease afterwards, indicates the depletion of the oxygen through reduction as mentioned above. An average photonic efficiency of ~25% was observed for pure TiO_2. In the presence of metal ions, an initial increase followed by a decrease in the photonic efficiency for H_2 production is due to the fact that these ions reduce the consumption of H^+ ions by hydroxyl ions. For O_2 production, the maximum photonic efficiency of 35% was observed for Ag^+ and the minimum photonic efficiency of less than 10% was observed for Li^+.

Another parameter to judge the efficiency of a photocatalytic water splitting process is O_2:H_2 ratio. Ideally, this ratio should be 1:2. In this study the O_2:H_2 ratio, for all the individual studies, was calculated and plotted in figure 5.19 as a function of time. For pure TiO_2, the O_2:H_2 ratio increases gradually with time indicating an increase in H_2 formation and decrease in O_2 formation with time. The maximum O_2:H_2 ratio was observed for Li^+ ions. This high O_2: H_2 ratio of 1:2.7 is due to the fact that Li^+ ions greatly effect the production of $O_2^{-\cdot}$ radicals by consuming O_2. For Fe^{3+} and Ag^+ ions, the initially higher followed by a lower O_2:H_2 ratio relative to pure TiO_2 confirms the - depletion of these ions with time.

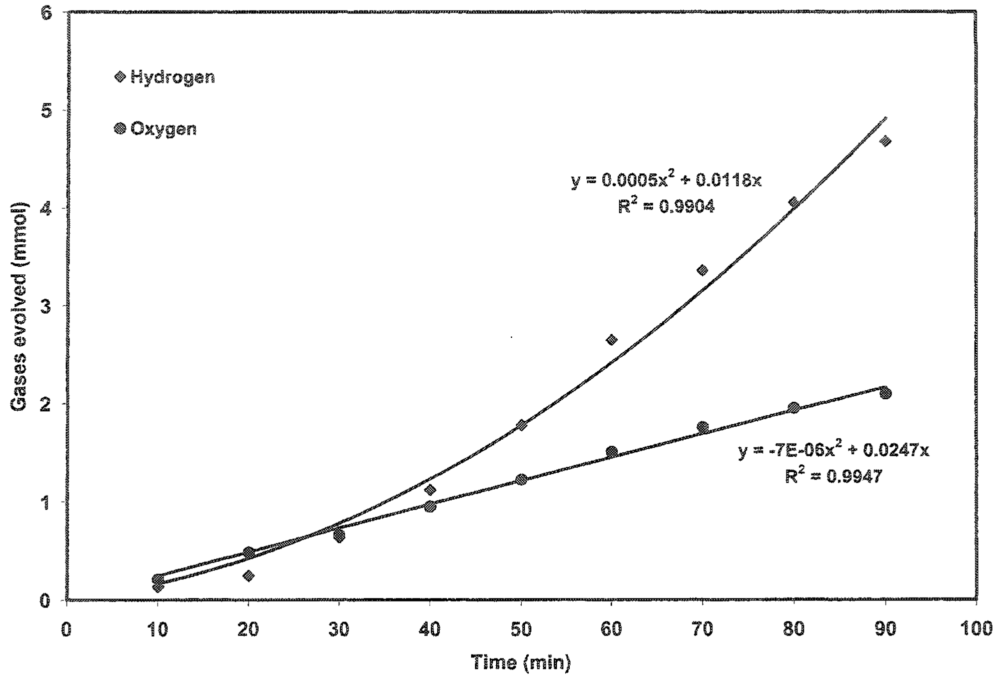

Figure 5.12 Hydrogen and oxygen production as a function of time over TiO_2

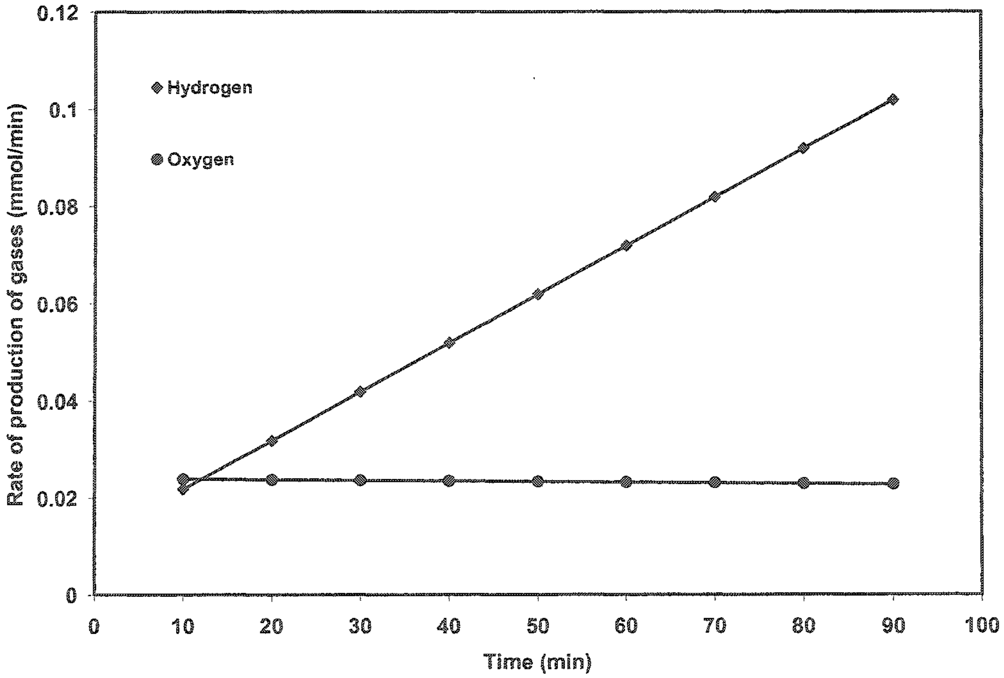

Figure 5.13 Rate of hydrogen and oxygen production over TiO_2

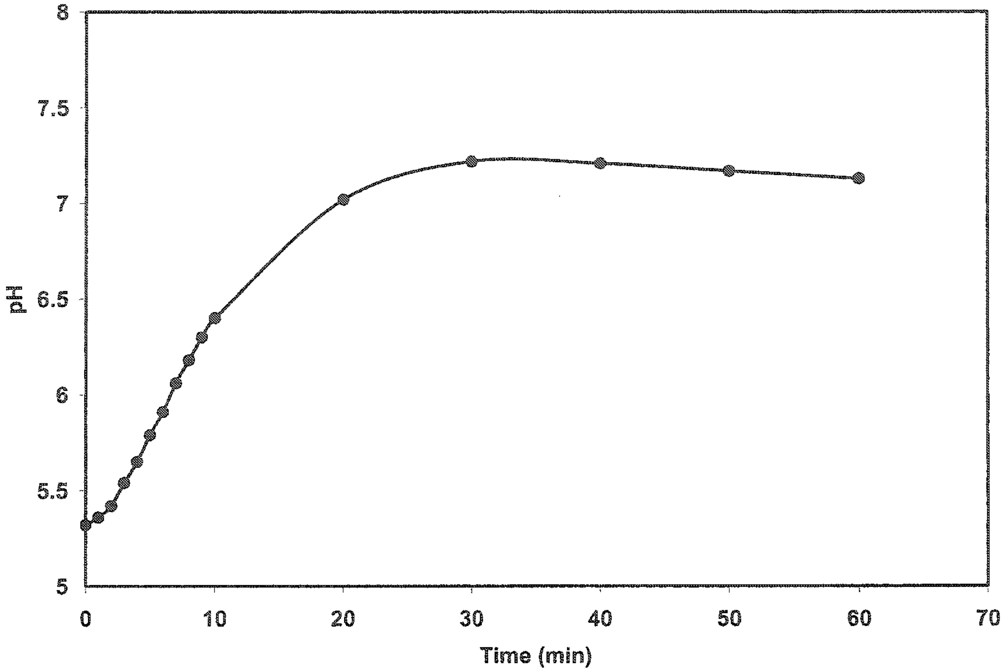

Figure 5.14 pH change during the course of photocatalytic splitting of water over TiO_2.

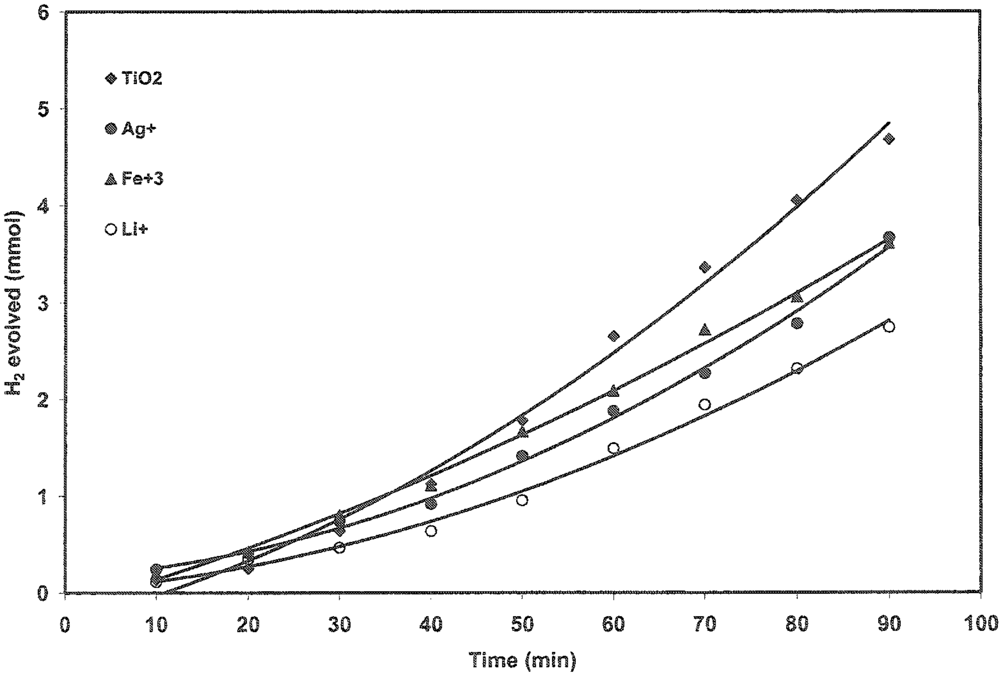

Figure 5.15 Hydrogen production over TiO_2 in the presence of metal ions

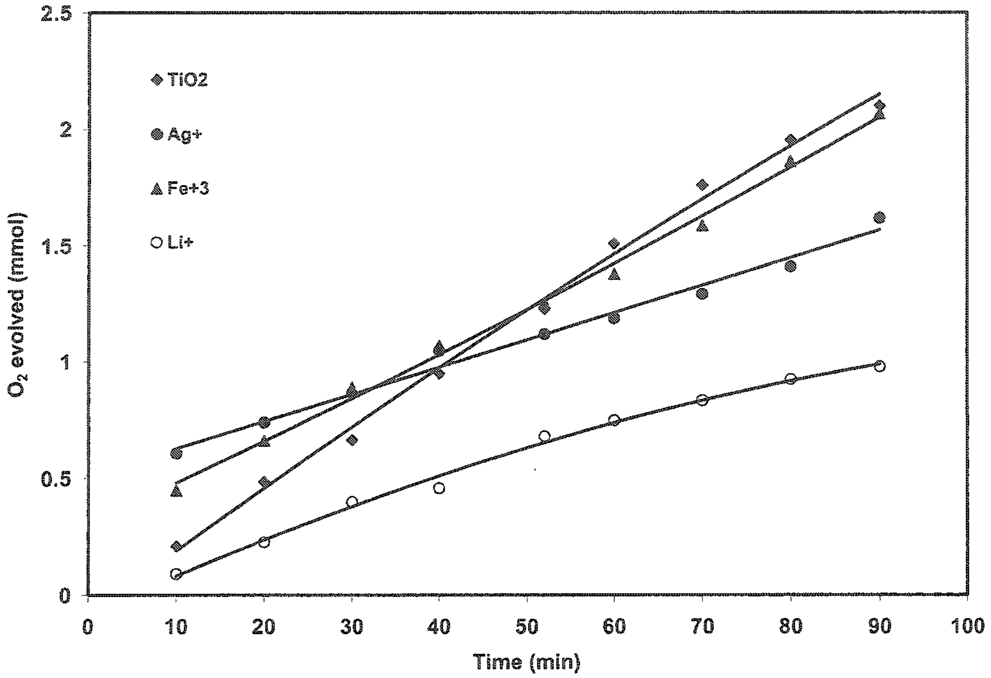

Figure 5.16 Oxygen production over TiO_2 in the presence of metal ions

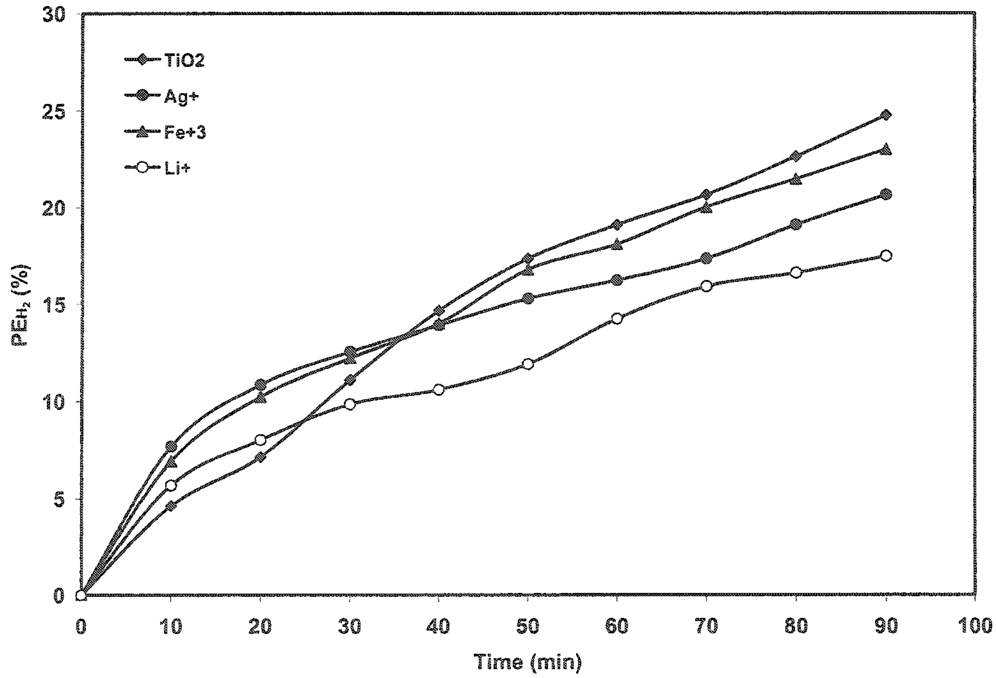

Figure 5.17 Photonic efficiency for hydrogen production over TiO_2 in the presence of metal ions

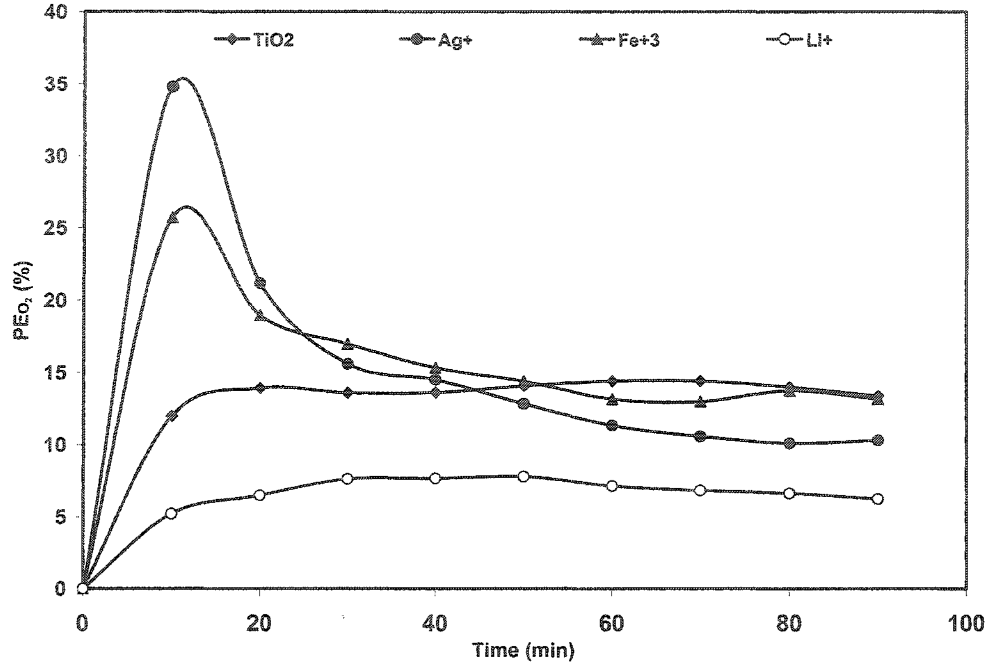

Figure 5.18 Photonic efficiency for oxygen production over TiO_2 in the presence of metal ions

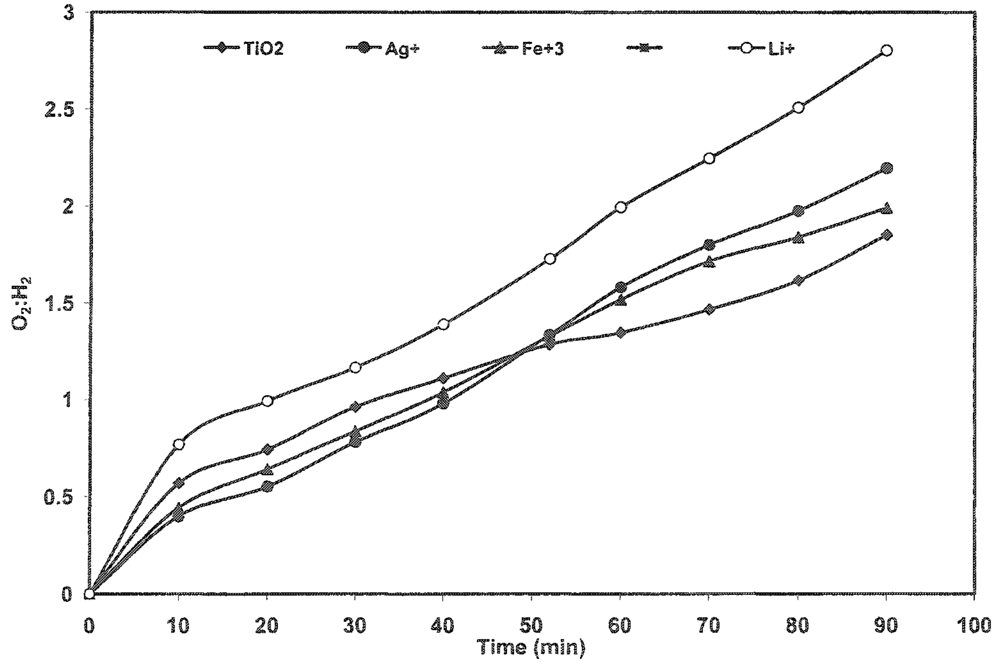

Figure 5.19 Comparison of oxygen to hydrogen ratio (O_2:H_2) over TiO_2 in the presence of metal ions

5.4 Photocatalytic splitting of water over NiO

The photocatalytic evolution of H_2 and O_2 as a function of time was studied by illuminating the colloidal suspension containing the optimized amount of NiO with a 355 nm laser, as light source, for a period of 90 minutes. The yield of the two gases was recorded at regular intervals of 10 minutes. The other parameters, i.e. stirring rate and beam diameter, were kept constant. The possibility of H_2 and O_2 generation by multi photon photolysis of water was ruled out by performing a blank experiment (without NiO) under the same experimental conditions. During the study, it was observed that with the increase in laser exposure time the color of the suspension changed from dark green to black and the formation of hydrogen compared to oxygen was non-stoichiometric. The original color of the catalyst was not regenerated even when the black NiO suspension was kept in dark for some time. In addition, NiO regained its original green color when heated at elevated temperatures in oxidizing environment confirming the release of lattice oxygen and reduction of the catalyst under illumination. The formation of H_2 in non-stoichiometric amounts was surprising as the band edge positions i.e. valence (+3.0 V) and conduction bands (-0.5 V) at pH 0, for NiO [127] are highly suitable for the photocatalytic splitting of water. Considering the changes mentioned above a close relation between the two was anticipated. The possible explanation of the above mentioned changes and the existing correlation between them is given below.

NiO is least studied for its photocatalytic properties but well studied as heterogeneous catalyst especially as hydrogenation catalyst [128]. In addition, it is well known for its photochromic properties. NiO has slightly distorted cubic rock salt structure and the non-polar (100) plane is the most stable surface. In this configuration, each Ni atom exists as Ni^{2+}.

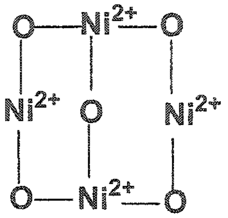

NiO (100) Surface

Absorption of a photon of energy equal to or greater than the band gap energy ($E>E_g$) causes the transfer of an electron from the valence band of oxygen (2p) to the conduction band of Ni (3d) atom and in turn the reduction of Ni^{2+} to Ni^{+}. This electron transfer process weakens the Ni^{+2}-O bond allowing lattice oxygen to be driven out creating a "defect" or "tape" site and leads to the formation of a hole in the valence band [129]. The hole in the valence band oxidizes the adsorbed water producing O_2 an H^+ ions in the solution. The H^+ ions produced as the result of photocatalytic oxidation of water are capable of capturing the conduction band electron, before diffusing to the bulk or getting trapped to create defect sites, to give $H^{\cdot}$ radicals or H_2 gas as shown in equations 5.1-5.4. The other possibilities are the reversible insertion of H^+ ions in the photogenerated defect sites (scheme I) to give H_xNiO_{1-x} type species or the hemolytic insertion of molecular hydrogen (H_2) (scheme II).

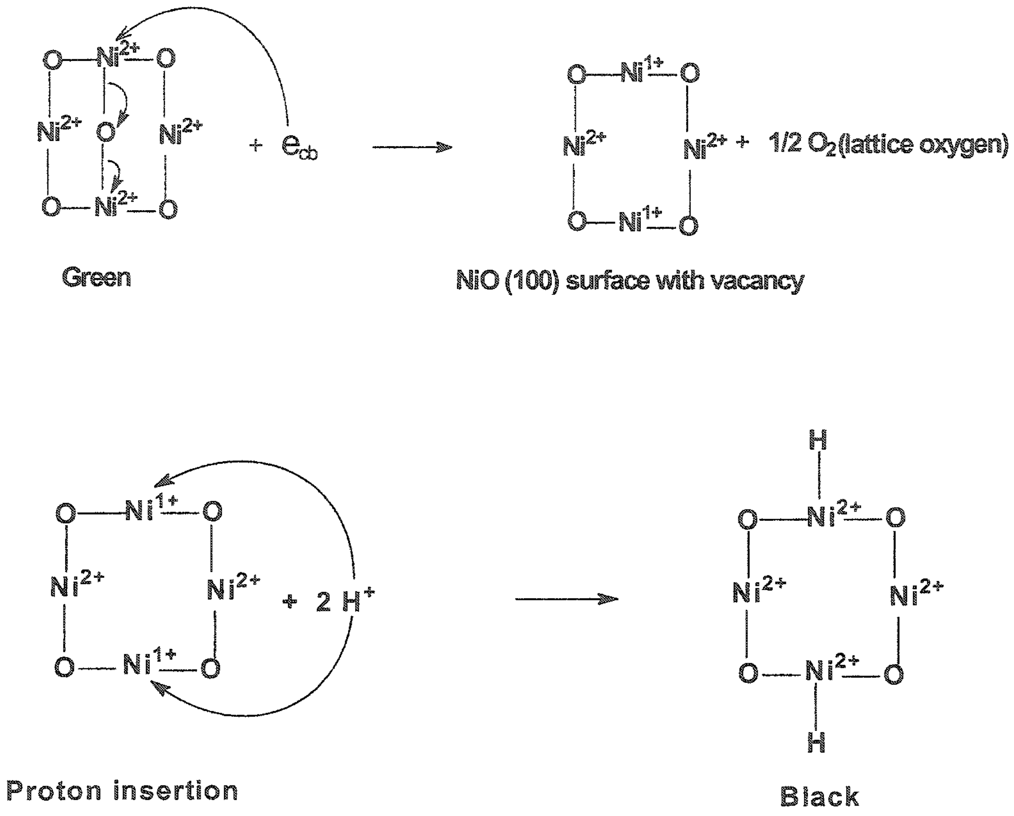

Scheme I

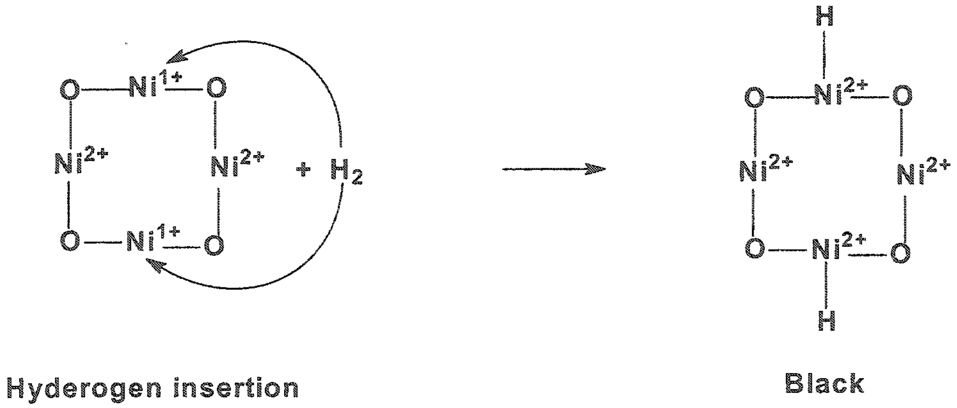

Scheme II

As mentioned earlier, this process is reversible only at elevated temperatures in the presence of oxygen.

$$H_xNiO_{1-x} + {}^{x}\!/_{2}O_2 \rightarrow NiO + {}^{x}\!/_{2}H_2 \qquad 5.20$$

According to the above-mentioned mechanism (scheme I) a measurable fraction of H^+ ions produced by photocatalytic splitting is consumed in the photoreduction of the catalyst causing an overall decrease in the yield of H_2 as given in figure 5.20. Another contributing factor in this regard is the possibility of hemolytic addition of molecular hydrogen to the defect sites (scheme II). The rate of H_2 formation decreases while the rate of formation of oxygen increases very slightly over time, as shown in figure 5.21. The decrease in the rate of hydrogen production is due to competition of H^+ ions and O_2 for conduction band electrons. The capture of conduction band electrons by the oxygen present in the system results in the formation of hydroxyl ions (equation 5.16) which serves as sink for H^+ ions. On the other hand, these hydroxyl ions serve as precursors for the production of additional hydroxyl radicals and cause an increase in the rate of production of oxygen.

5.4.1 pH measurements

To explore other factors which contribute to a decrease in the yield of H_2 the pH changes over time in an argon environment were studied. The changes in pH as a function of laser exposure time are presented in figure 5.22, where an increase in pH can be observed in an argon environment. In a period of 60 minutes the pH changes from ~5.2 to ~11.5. With the reduction of the NiO due to the large shift in the pH the valence and conduction band edges shift to +2.32 V and -1.18 V respectively. The value of +2.32 V for valence band edge shows a considerable decrease in the over potential associated with the oxidation of water by the valence band holes and suggests an appreciable increase in the rate of water oxidation with the reduction (or with the introduction of photo induced bulk defect sites) of the NiO. On the other hand, with the shifting of conduction band edge towards more negative value the suitability of the conduction band edge for water reduction through dissolved oxygen (equation 5.16) along with formation of hydrogen radicals from H^+ ions increases.

In the presence of argon, the above-mentioned process is activated immediately with the illumination of the suspended catalyst as indicated by a sharp rise in pH overtime at the out set (figure 5.22). A stable pH value afterwards reflects a steady state in the production and consumption of hydroxyl ions. It is also clear from figure 5.22 that a significant fraction of H^+ ions (that are produced by the donation of electrons from water molecules to photogenerated holes) reacts with hydroxyl ions to give water (recombination) and favor a low yield of hydrogen. The high oxygen yield due to the capture of the photo-generated holes by hydroxyl ions is an added advantage.

5.4.2 Effect of metal ions

The effect of dissolved metal ions was studied in the presence of three metal ions i.e. Fe^{3+}, Ag^+ and Li^+. Fe^{3+} and Ag^+ were selected as electron capture agents because their redox potentials are higher than the conduction band potential of NiO. The redox potential of Li^+/Li^o couple is much lower than the conduction band potential of NiO. Li^+ was selected because of the high reactivity of these ions with hydroxyl radicals and comparable activity to H^+ ions. The reduction potentials of Fe^{3+}/Fe^{2+}, Ag^+/Ag^o and Li^+/Li^o couples are +0.77 V, +0.80 V and -3.05 V respectively [122].

The effect of these metal ions on H_2 and O_2 yield is presented in figures 5.23 and 5.24 respectively. In the presence of Fe^{3+} ions, contrary to the expected decrease in hydrogen production a sustained increase was observed (figure. 5.23). This unusual behavior indicates that in the presence of high concentration of hydroxyl ions the metal ions (which were selected to work as electron capture agents) act as hydroxyl ion scavengers to form hydroxides and reduce the depletion of H^+ ions by the hydroxyl ions.

The unexpected decrease in oxygen production in the presence of both Fe^{3+} and Ag^+ compared to that of pure NiO, as shown in figure 5.24, indicates a decrease in the additional formation of oxygen with the decrease in the concentration of hydroxyl radicals. The initial increase in O_2 (figure. 5.24) formation and then a decrease afterwards indicate the depletion of Ag^+ with the time. This decrease is mainly due to the deposition of Ag^o at the surface and formation of oxides and hydroxides.

The reduction potential of Li^+ is much lower than the potential of conduction band electrons so the probability of capturing conduction band electrons is low. A decrease in both H_2 and O_2 production in the presence of Li^+ ions was observed owing to the deactivation of the catalyst by the formation and deposition of LiOH at the surface of the catalyst. This again is an indication of the presence of hydroxyl ions in the solution.

The photonic efficiency for the photocatalytic splitting of water to H_2 and O_2 over NiO in both the presence and absence of metal ions was measured. The plots of photonic efficiencies as a function of laser exposure time for H_2 and O_2 are presented in figures 5.25 and 5.26.

It was observed that for pure NiO, the photonic efficiency for H_2 production increases sharply and then slowly to a stable value indicating a low depletion of H^+ ions in the beginning and a steady state between generation and depletion of H^+ ions afterwards. The reasons for the low value of ~ 30% for H_2 production and ~ 23% for O_2 production have been discussed in the previous section. For all the metal ions, the photonic efficiency for H_2 generation was lower than pure NiO indicating that the metal ions also work as electron capture agents and follows the trend $Fe^{3+}>Ag^{+}>Li^{+}$. Approximately the same situation was observed for O_2 production but the observed trend was $Ag^{+}>Fe^{3+}> Li^{+}$.

In this study, the O_2:H_2 ratio for all the individual studies was calculated and plotted as a function of time in figure 5.27. The maximum O_2:H_2 ratio of ~1:2 was observed for Ag^+. For Ag^+ and Fe^{3+}, the calculated O_2:H_2 ratio was higher than that for pure NiO while for Li^+ even a ratio lower than pure NiO was observed. The main reasons for these observations are already discussed in the previous sections.

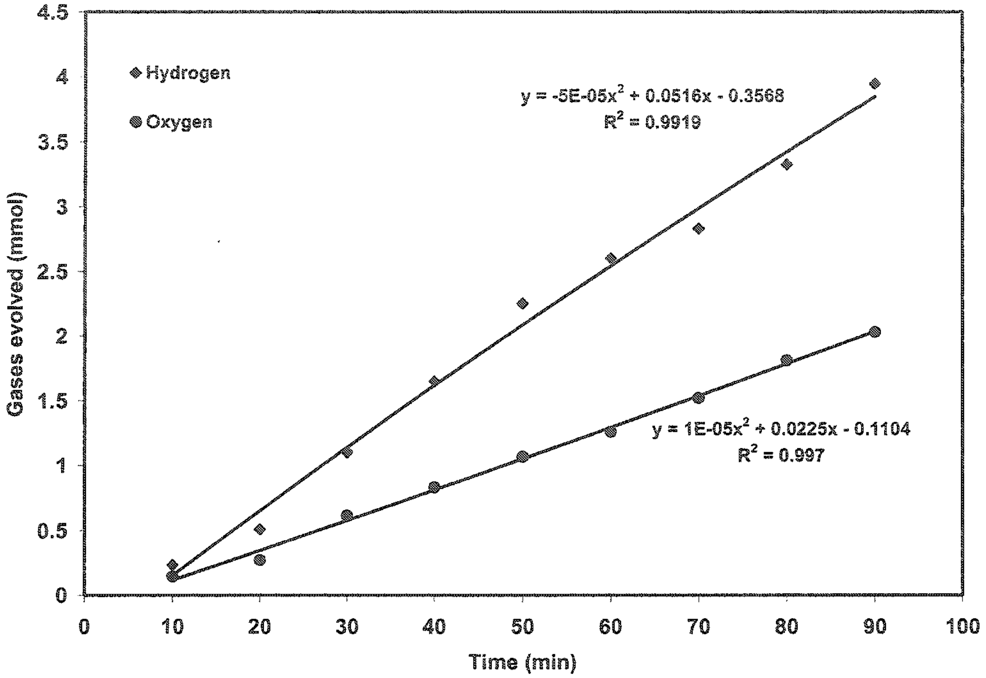

Figure 5.20 Hydrogen and oxygen production with time over NiO

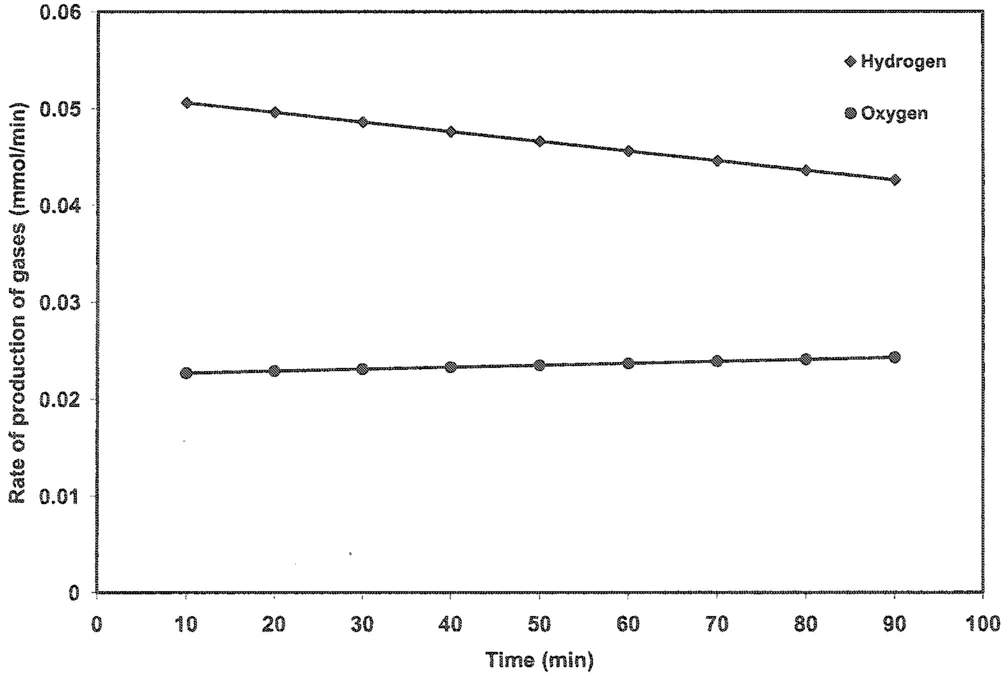

Figure 5.21 Rate of hydrogen and oxygen production over NiO

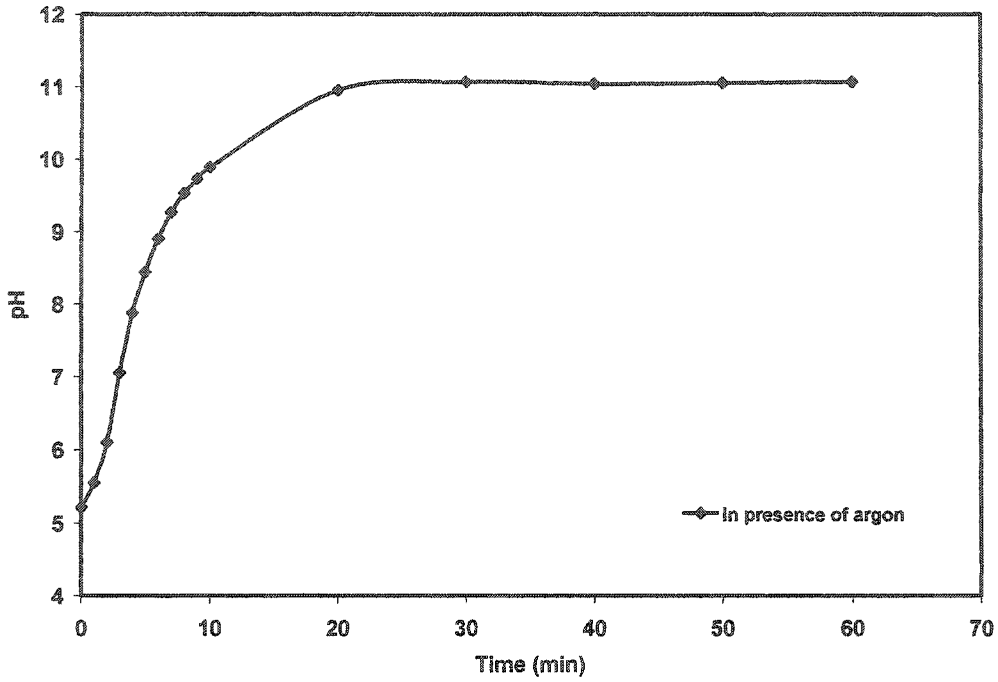

Figure 5.22 pH changes during the course of photocatalytic splitting of water over NiO

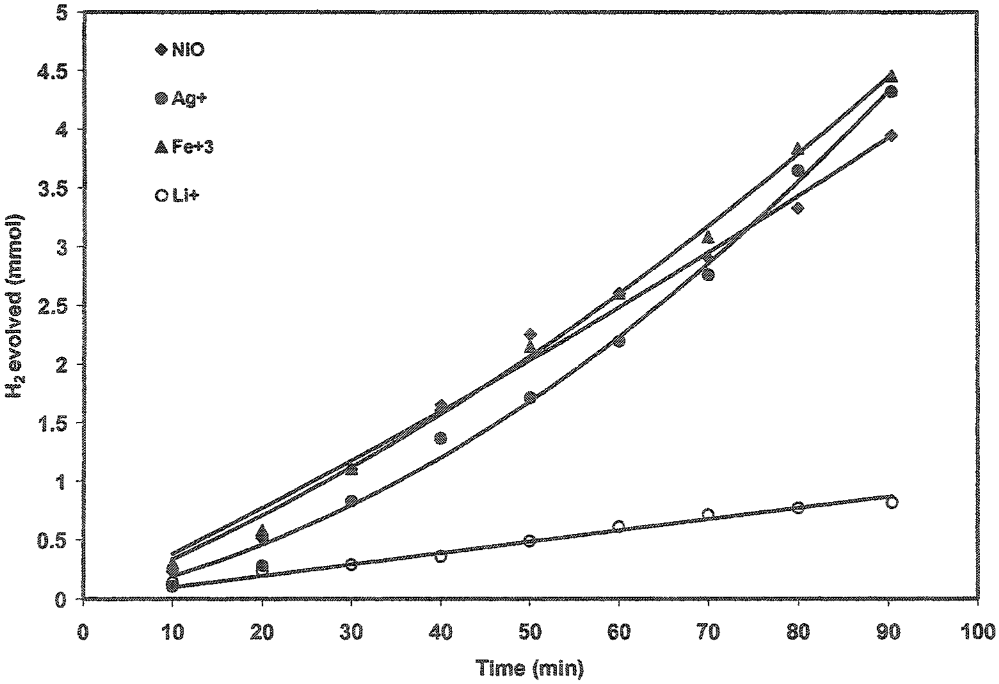

Figure 5.23 Hydrogen production over NiO in the presence of metal ions

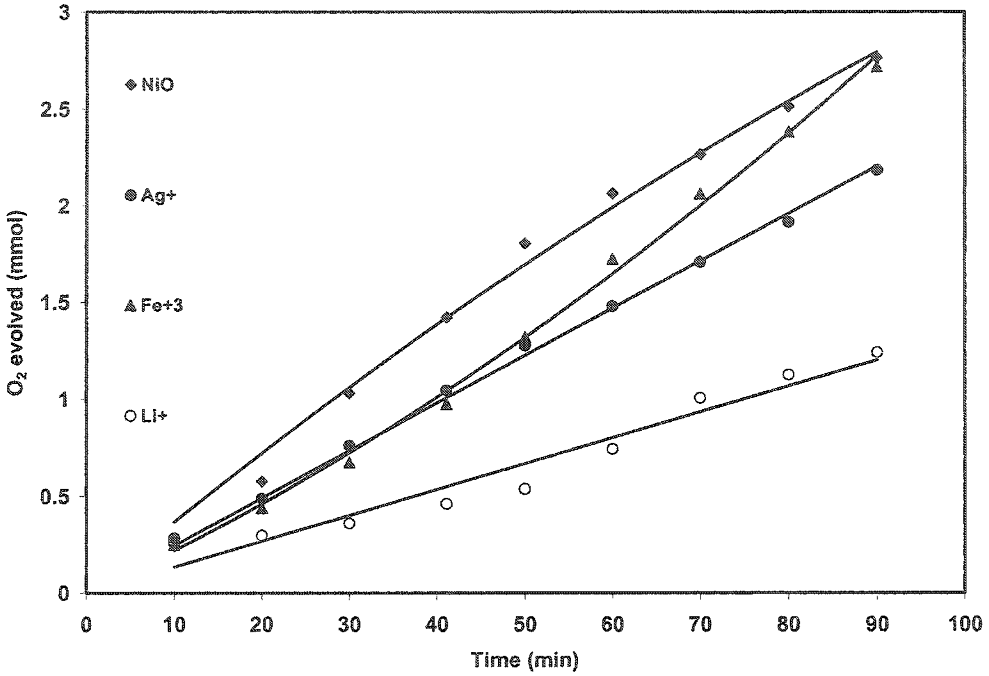

Figure 5.24 Oxygen production over NiO in the presence of metal ions

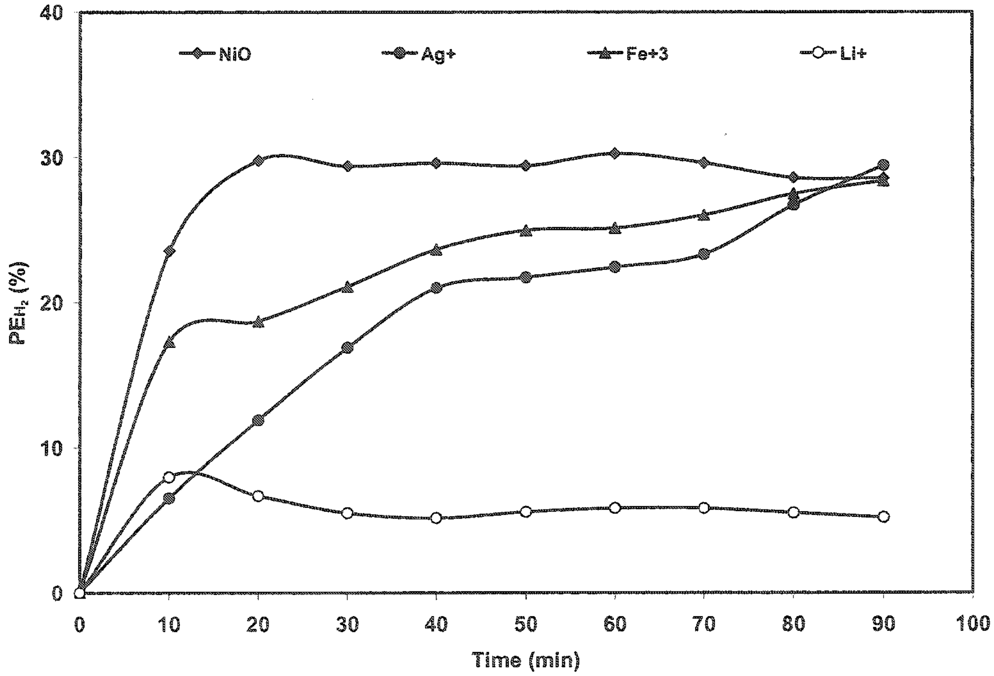

Figure 5.25 Photonic efficiency for hydrogen production over NiO in the presence of metal ions

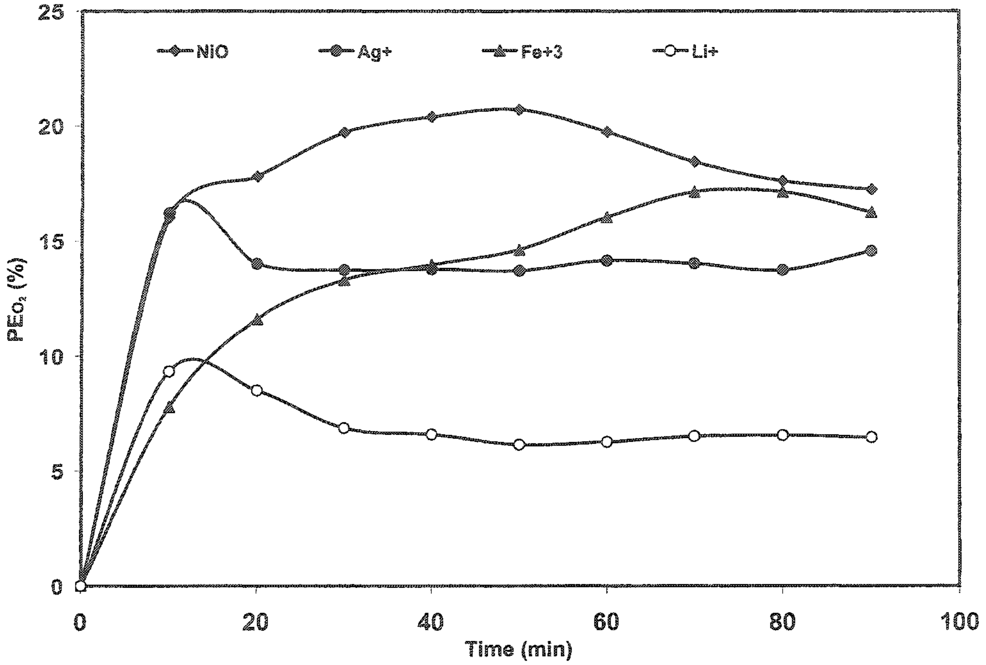

Figure 5.26 Photonic efficiency for oxygen production over NiO in the presence of metal ions

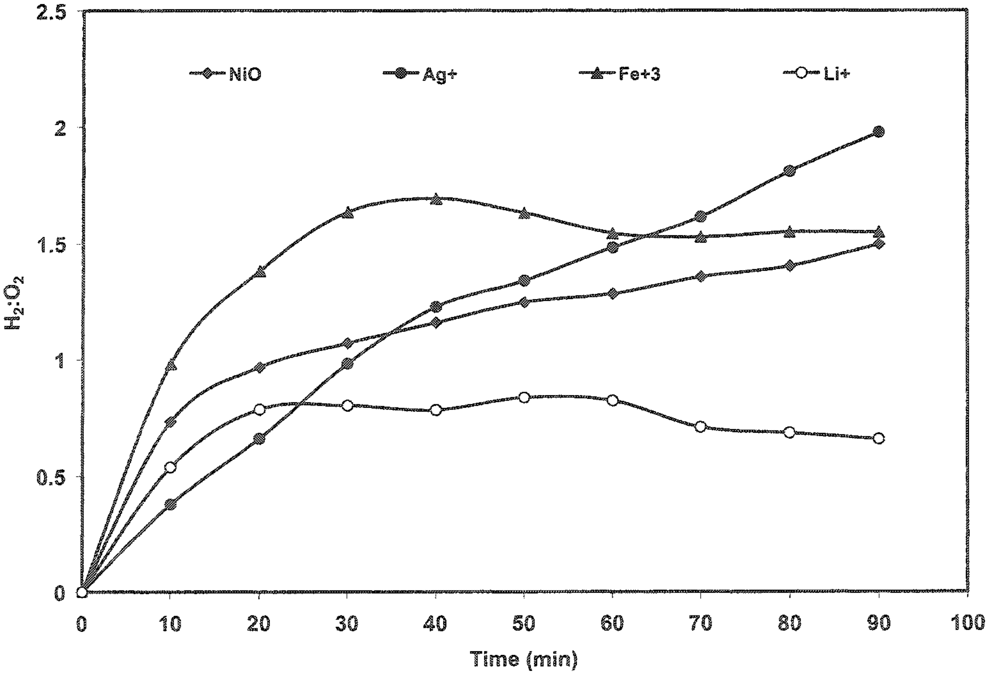

Figure 5.27 Comparison of oxygen to hydrogen ratio (O_2:H_2) over NiO in the presence of metal ions

5.5 Photocatalytic splitting of water over α-Fe_2O_3

The photocatalytic activity of Fe_2O_3 for the photocatalytic oxidation of water was studied by irradiating the aqueous suspension, containing the optimized amount of the catalyst, with a 355 nm laser beam. The experimental setup and the other parameters are discussed in detail in the previous sections.

Fe_2O_3 is n-type semiconductor commonly known as hematite. It has a band gap of 2.2 eV with a conduction band edge at +0.28 V and valence band edge at +2.4 V [130]. Although the valence band edge of Fe_2O_3 is highly suitable for water oxidation, the conduction band edge is highly unsuitable for photocatalytic hydrogen production. However, during the study, hydrogen in low yield and oxygen in very high yield were observed as shown in figure 5.28. The formation of hydrogen indicated the transformation of the catalyst into some other form suitable for hydrogen production through light absorption. The high yield of oxygen indicates an additional source of oxygen production alongside the photocatalytic splitting of water.

Absorption of 355 nm laser photon excites an electron from the valence band of oxygen (2p) to the conduction band of Fe^{3+} (3d), causing the reduction of Fe^{3+} to Fe^{2+}. This electron transfer process weakens the Fe^{3+}-O bond allowing lattice oxygen to be driven out creating two FeO molecules at the surface. The absorption of UV photons induces the generation of electrons and holes in α-Fe_2O_3. The photogenerated holes oxidize water and produce oxygen while the photogenerated electrons cause the photodecomposition of α-Fe_2O_3 creating FeO sites with the release of lattice oxygen as explained in the reaction below.

$$\alpha - Fe_2O_3 + e^- \rightarrow 2FeO + \tfrac{1}{2}O_2 \qquad 5.21$$

The divalent FeO is a p-type semiconductor having a band gap of 2.3 eV and the valence and conduction band edges at +2.13 V and -0.17 V respectively [131]. A photon generated FeO surface state behaves independently as a p-type semiconductor and serves as an electron trap and transfer site for hydrogen production.

Another likely reason for such a high yield of oxygen as compared to H_2 is the complete dissociation of the catalyst due to the photo-corrosion. In this process, the catalyst undergoes self-degradation under irradiation with a high photon flux of laser beam, contributing a large amount of O_2 as illustrated by the reaction below.

$$\alpha - Fe_2O_3 + 3h_{vb}^+ \rightarrow 2Fe^{3+} + \tfrac{3}{2}O_2 \qquad 5.22$$

It is clear from the above-mentioned mechanism that the anodic decomposition of Fe_2O_3 contributes significantly to the total oxygen produced during the photocatalytic oxidation process. In addition, Fe^{3+} serves as a precursor for the formation of Fe^{2+} which is capable of increasing the rate of water oxidation by homogeneous photo-Fenton type reactions (equation 5.12) [17].

The rates of hydrogen and oxygen production are presented in figure 5.29. The increase in the rate of production of hydrogen with time supports the formation of FeO through structural changes, as α-Fe_2O_3 cannot generate hydrogen by itself. Although the valence band edge of α-Fe_2O_3 is suitable for producing oxygen, the observed high rate of oxygen production indicates the photocorrosion of the catalyst, during photocatalytic process, as explained above.

5.5.1 pH measurements

The pH was measured at regular intervals during the course of reaction in an argon environment. These changes are plotted in figure 5.30, where a decrease in the pH can be noticed. The decrease in pH reveals that not all the H^+ ions that are produced in the photocatalytic process contribute towards hydrogen production and results in a low yield of hydrogen.

5.5.2 Effect of metal ions

In this study, three metal ions i.e. Fe^{3+}, Ag^+ and Li^+ were selected and there effect on the photocatalytic process of water oxidation over Fe_2O_3 was studied. The effect of these metal ions on hydrogen and oxygen yield is given in figures 5.31 and 5.32.

The expected increase and decrease in the yield of oxygen and hydrogen in presence of Fe^{3+} and Ag^+ reveals the suitability of the reduction potentials of these ions as electron capture agents. The sustained increase in O_2 production in the presence of Fe^{+3} (figure 5.31) suggests the regenerative behavior of the Fe^{3+}/Fe^{2+} couple through the reactions mentioned in equations 5.10 and 5.11.

Another pathway suggested in the literature [17] for the regeneration of Fe^{3+} is the homogeneous photo-Fenton-type reaction to produce additional OH radicals (equation 5.12).

Therefore, Fe^{3+} can be considered as a co-catalyst for the continuous production of hydroxyl radicals which serve as precursor for oxygen production and in turn enhance oxygen yield. On the other hand, the photo-Fenton-type reaction is also a cause for the depletion of H^+ ions causing a decrease in hydrogen yield. The decrease in the yield of oxygen with time is also due to the competition between H_2O and Fe^{2+} for valence band holes.

Ag^+ has also shown a high efficiency as an electron scavenger but the effect on the rate of O_2 formation is much lower than Fe^{3+} as illustrated in figure 5.32. The action mechanism of Ag^+ is the same as Fe^{3+} but Ag^o formed remains on the surface of the catalyst and is not regenerated back to Ag^+. The decrease in the yield of O_2 with time can also be attributed to the depletion of Ag^+ in the solution. Although the photo-deposited Ag^o, on the catalyst surface, improves the charge separation it does so less efficiently than Ag^+ [18]. In the presence of high concentration of oxygen in the solution, the formation of oxides cannot be neglected.

Li^+ ions have a lower reduction potential (-3.05 V) relative to the conduction band potentials of α-Fe_2O_3. The high negative value of the reduction potential shows the inability of Li^+ ions to capture conduction band electrons. A decrease in both oxygen and hydrogen production clearly indicates the formation and deposition of Li_2O at the surface of catalyst which results in the deactivation of the catalyst.

The comparison of photonic efficiencies as a function of exposure time for hydrogen and oxygen production in the presence of electron scavengers with that for pure Fe_2O_3 are depicted in figures 5.33 and 5.34.

A photonic efficiency of ~ 35% and ~ 17% for oxygen and hydrogen production respectively, was observed for pure Fe_2O_3. A notable decrease in photonic efficiency, in the presence of metal ions, was observed for hydrogen production. Such decrease in hydrogen production is probably due to the capture of conduction band electrons and other factors such as poisoning of the catalyst. An increase in photonic efficiency for oxygen production was observed in the presence of Fe^{3+} while a decrease was observed in the presence of Ag^+. This suggests the depletion of both Ag^+ and O_2 with the formation of Ag_2O in the presence of oxygen in the system.

The O_2:H_2 ratio for all the individual measurements were calculated and plotted as a function of time and are presented in figure 5.35. A low O_2:H_2 ratio less than 1 was observed for pure α-Fe_2O_3 as well as for the dissolved metal ions thereby supporting the argument on hydrogen production and the release of oxygen in larger amounts through photocorrosion.

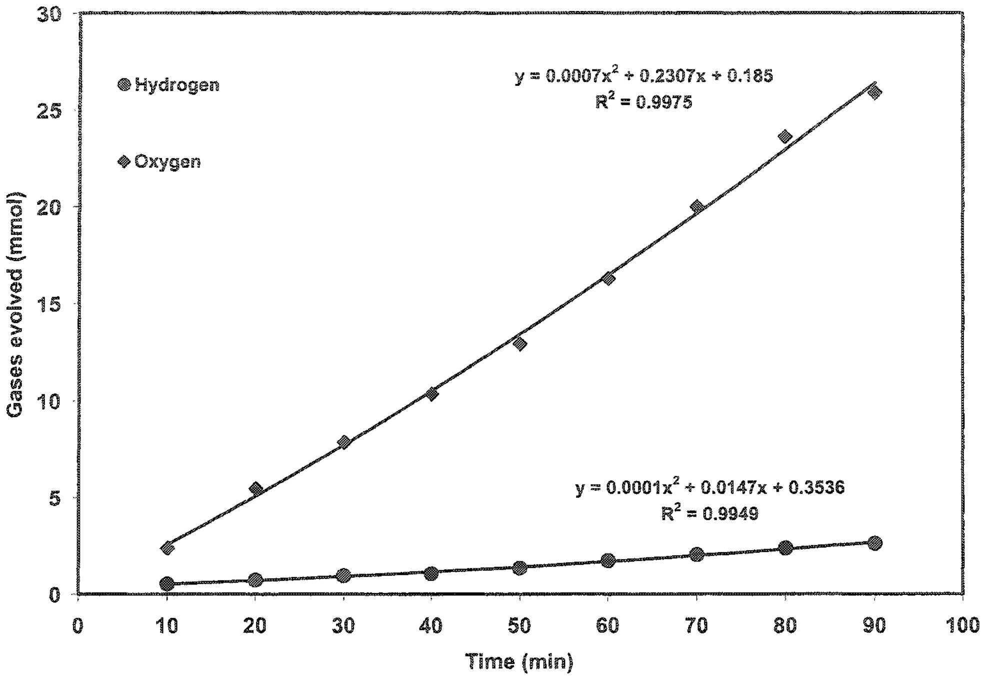

Figure 5.28 Hydrogen and oxygen production with time over α-Fe_2O_3

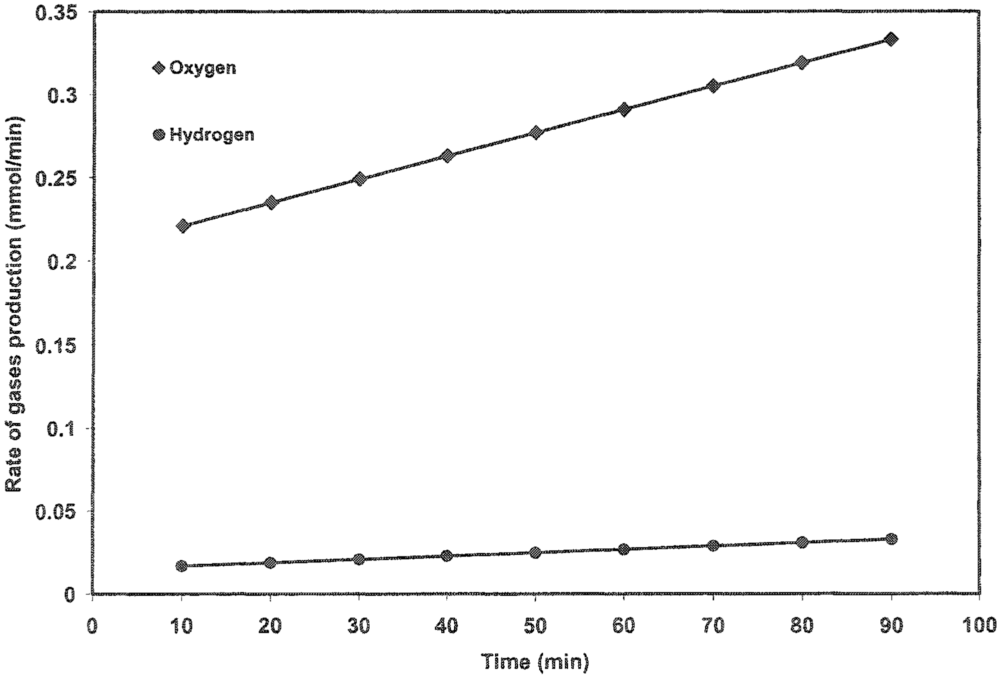

Figure 5.29 Rate of hydrogen and oxygen production over α-Fe_2O_3

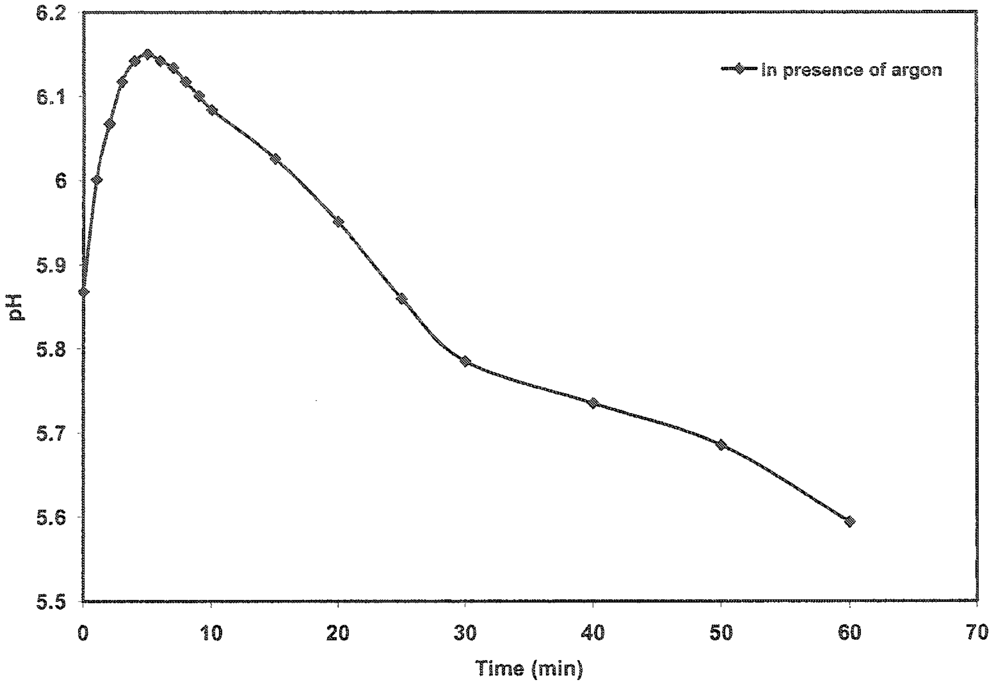

Figure 5.30 pH changes during the course of photocatalytic splitting of water over α-Fe_2O_3

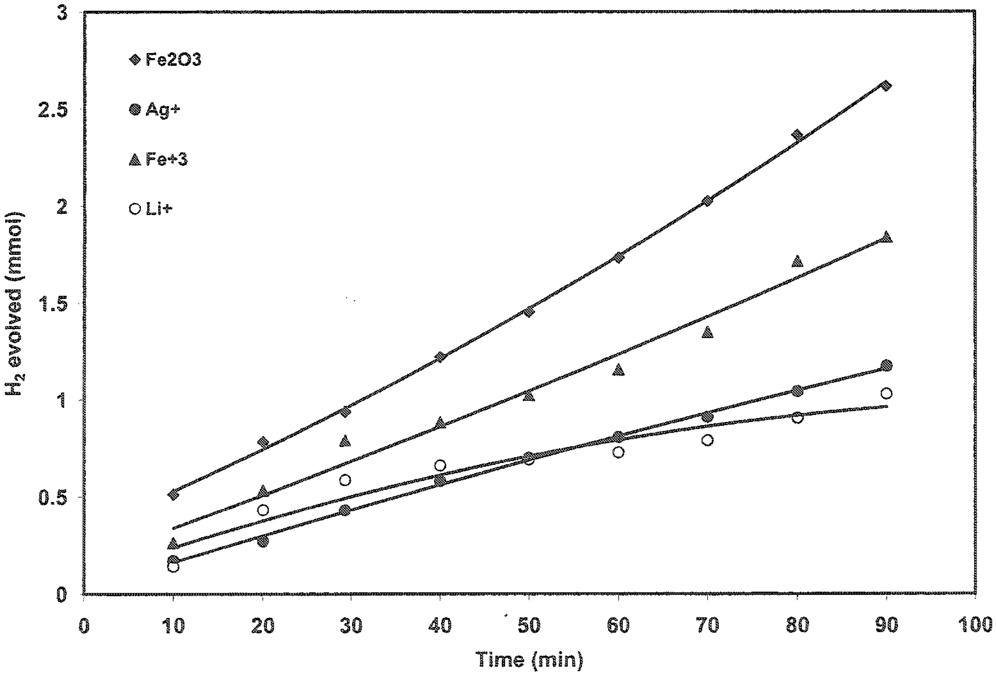

Figure 5.31 Hydrogen production in the presence of metal ions over α-Fe_2O_3

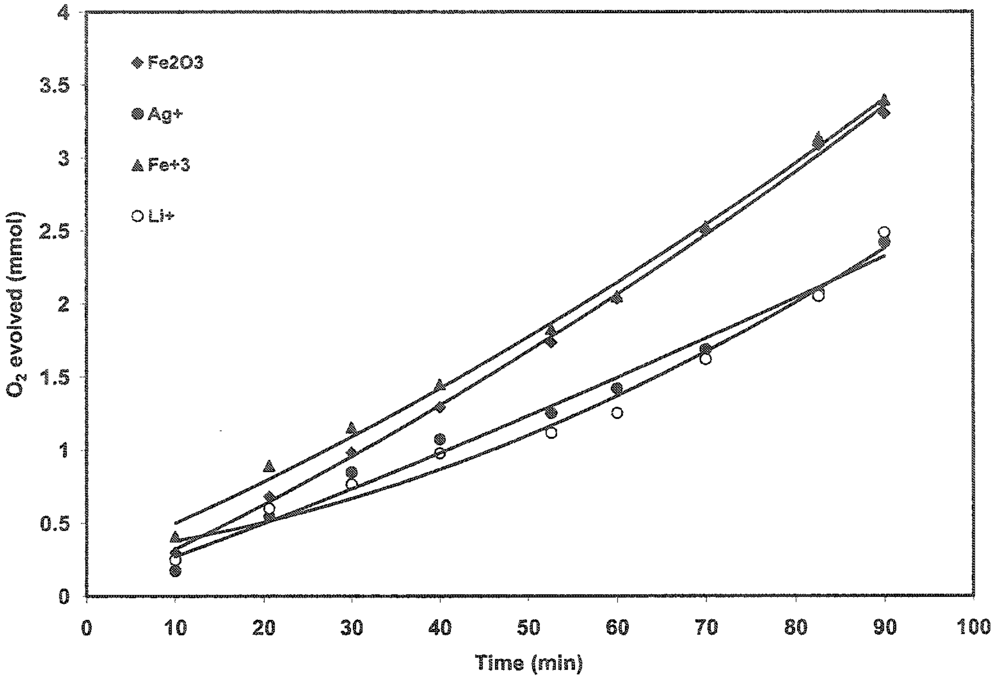

Figure 5.32 Oxygen production in the presence of metal ions over α-Fe_2O_3

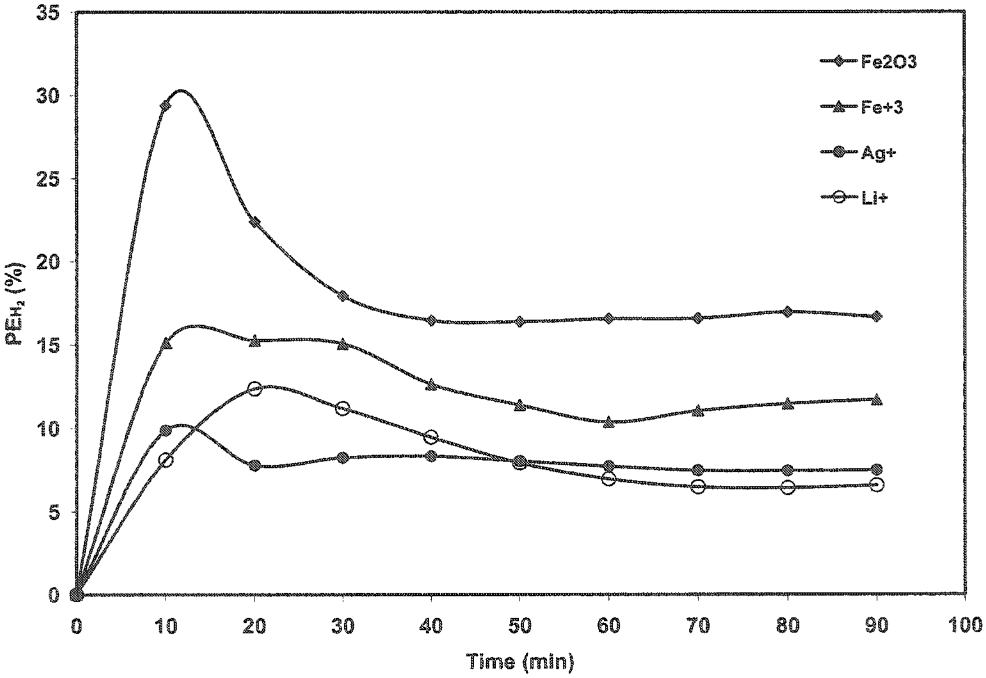

Figure 5.33 Photonic efficiency of hydrogen production in the presence of metal ions over α-Fe_2O_3

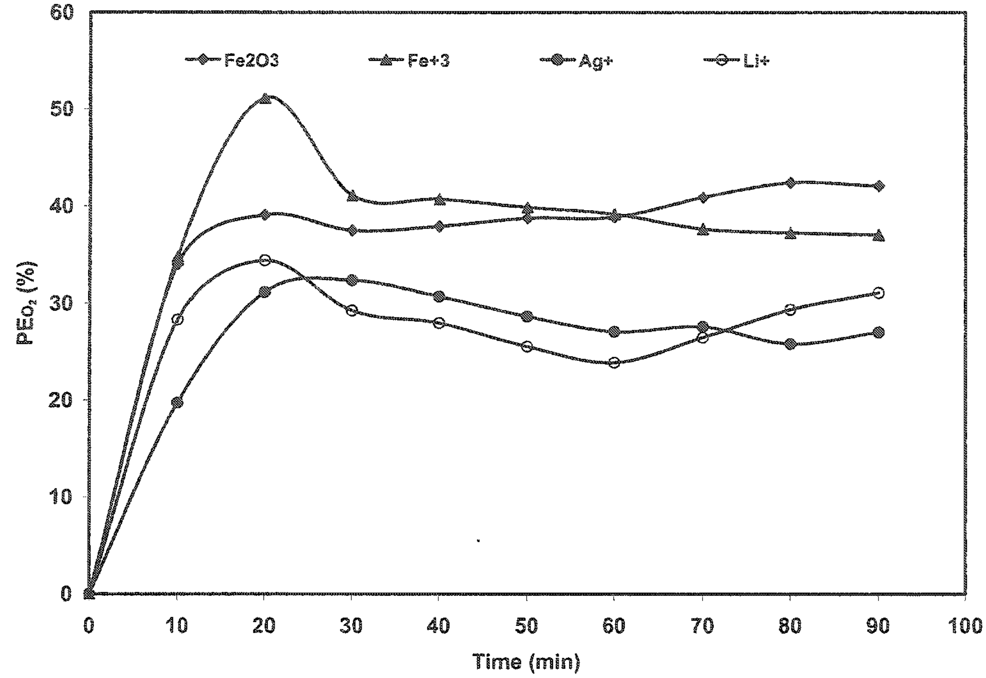

Figure 5.34 Photonic efficiency of oxygen production in the presence of metal ions over α-Fe_2O_3

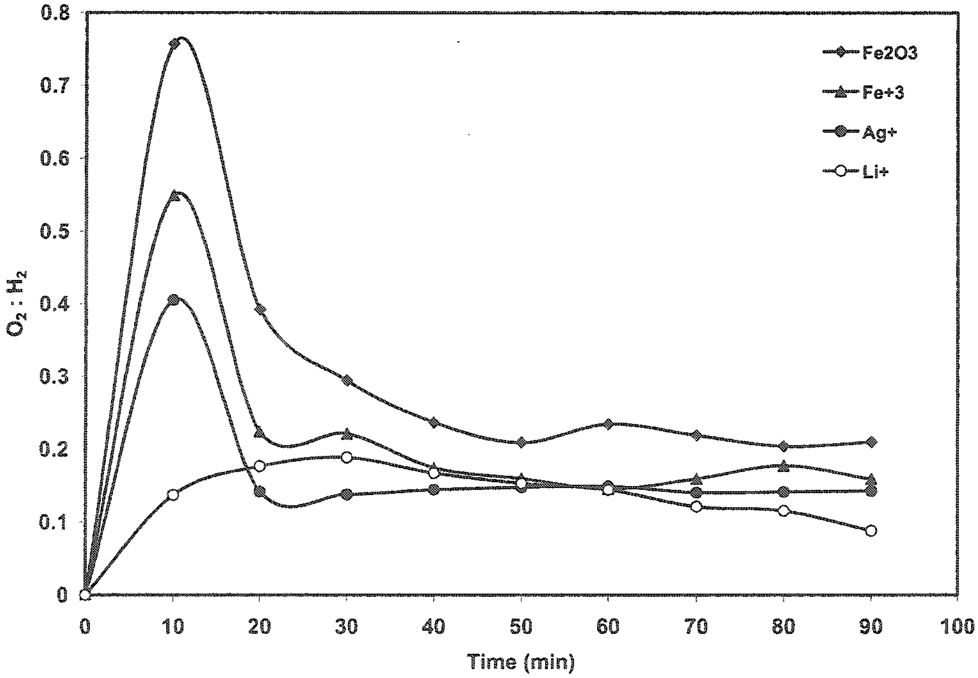

Figure 5.35 Comparison of oxygen to hydrogen ratio (O_2:H_2) in the presence of metal ions over α-Fe_2O_3

5.6 Comparison of water splitting over α-Fe_2O_3, WO_3, TiO_2 and NiO

The catalysts α-Fe_2O_3, WO_3, TiO_2 and NiO were subjected to the same experimental conditions and yields of oxygen and hydrogen were recorded at regular intervals. The common features observed are:

(i) All the catalysts undergo reduction with the absorption of 355 nm photons

(ii) The absorption of photons induces the release of lattice oxygen with the induction of bulk defects in all the catalysts

(iii) Non-stoichiometric release of oxygen and hydrogen was observed for all catalysts

On reduction of the catalyst by the absorption of high UV photon flux, the stoichiometry of hydrogen and oxygen production was lost yet the overall activity of the catalyst increased as observed in case of TiO_2 and NiO. In the case of WO_3, the light induced defects serve as the sites for hydrogen production. For α-Fe_2O_3 this is achieved by the photon generated FeO surface states. The only observed drawback of these structural changes was the release of additional oxygen. Despite the creation of defect sites, all the catalysts except α-Fe_2O_3 were found stable during the illumination and no photodecomposition either anodic or cathodic type was observed. The generation of defect sites was found valuable as an increase in the rate of photocatalytic splitting was observed with the increase in defect sites. The regeneration of the catalyst to its original form especially for WO_3 was observed in the dark while the same effect for TiO_2 and NiO was observed in the presence of excess oxygen at elevated temperatures.

The hydrogen production, for all the catalysts, given in figure 5.36 shows that the effectiveness of the catalysts follow the trend as NiO> TiO_2> α-Fe_2O_3> WO_3. This trend is consistent with the trend for the suitability of the conduction band edges of these catalysts for the production of hydrogen. Both NiO and TiO_2 have suitable conduction band edges for hydrogen production therefore the yield of hydrogen is high for these catalysts. The surface of α-Fe_2O_3 changes to FeO with the absorption of photons that serve as trapped site for the production of hydrogen as discussed in section 5.5. As the conduction band edge of WO_3 is not suitable for hydrogen production, a different mechanism was suggested which leads to the conversion of a fraction of H^+ ions to H_2. The detailed mechanism for hydrogen production is given in section 5.2.

The oxygen production for all the catalysts is given in figure 5.37 where the order of oxygen production can be observed as α-Fe_2O_3>WO_3> TiO_2>NiO. A high yield of oxygen was observed for α-Fe_2O_3 is attributed to the photocorrosion of the catalyst while the low yield of oxygen for NiO and TiO_2 relative to that of WO_3 is due to the suitability of the conduction band potential of these catalysts for oxygen reduction as well as for hydrogen production.

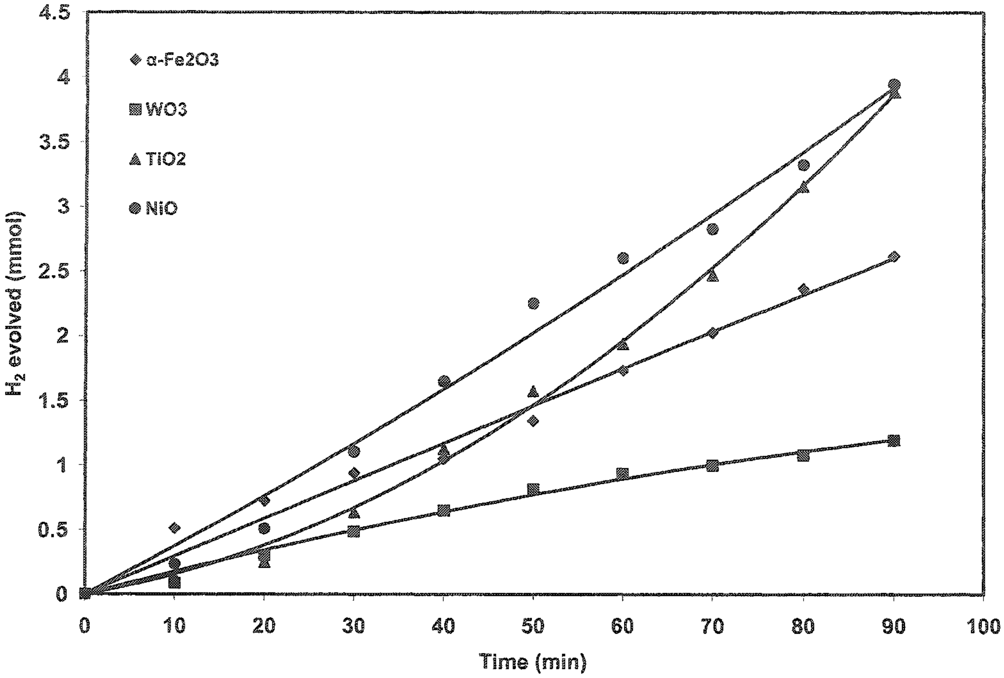

Figure 5.36 Comparison of hydrogen production over various photocatalysts

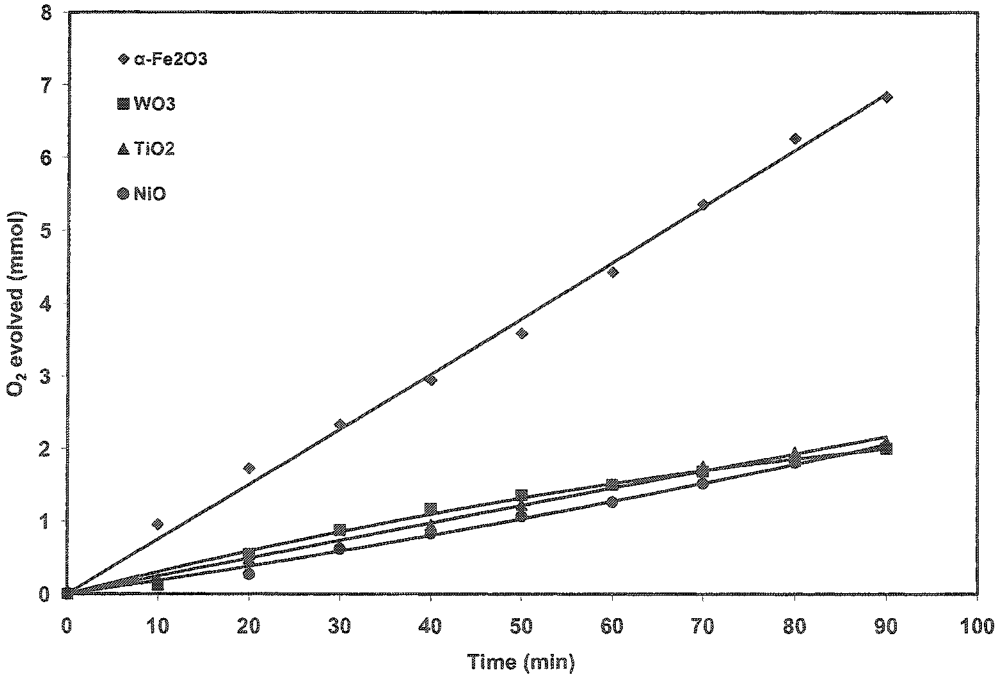

Figure 5.37 Comparison of oxygen production over various photocatalysts

5.7 Photocatalytic splitting of water over transition metal doped WO_3

As mentioned in introduction section, in heterogeneous photocatalytic systems, transition metals are used as dopants to enhance the spectral response and the photocatalytic activity of the photocatalyst by suppressing the unwanted electron-hole pair recombination [18]. These metals in ionic form bind with surface oxygen to form patches of doped metal oxides at the surface that act as electron capture and transfer sites under bandgap excitation. The presence of these metal ions at the surface of the semiconductor can influence the surface property and eventually the photocatalytic efficiency of the semiconductor by enhancing or retarding of desired reactions. The host absorbs the photons and generates the electron-hole pair. The photoexcited electron is transferred to the conduction band of the doped metal oxide. Therefore, the valence band of the host is used for the oxidation of water while the reduction of H^+ ions produced by the photocatalytic oxidation of the water occur at the doped metal oxide, present at the surface of the host. In a doped semiconductor powder under illumination the host behaves as a micro photoanode and the doped metal oxide work as micro photocathode [125]. The doped catalyst starts behaving as tandem or coupled catalyst. The host semiconductor work as an oxygen production site while the dopant serves as a hydrogen generator. For example, pure WO_3 is unable to produce hydrogen from the water directly by itself, as its band edges do not support the direct formation hydrogen. The metal oxide present at the surface of WO_3 can serve as hydrogen production centre. The formation of H^+ ions takes place at WO_3 through water oxidation while the formation of hydrogen from protons occurs at the metal oxide centre present at the surface of WO_3.

In this study, WO_3 was doped with Fe, Co, Ni, Cu, Zn and Ag in three different concentrations of 0.1, 1.0 and 10%. The oxidation states and chemical forms of these metals, at the surface of host WO_3, were identified by x-ray photoelectron spectroscopy and the procedure of these estimations is discussed in section 3.2.3. As predicted by XPS and given in table 4.4, the above mentioned metals were present in the form of Fe_2O_3, CoO, Ni_2O_3, Cu_2O, ZnO and Ag_2O respectively. The predicted oxidation states were +3, +2, +3, +1, +2 and +1 respectively. The purpose of selecting these three widely varying concentrations of doped metals was to study the effect of increasing concentration of dopant on the photocatalytic activity of WO_3 towards water splitting and the behavior of doped catalyst under illumination. It was observed that these metals affect the photocatalytic activity to varying degrees.

The photocatalysts loaded with various concentrations of transition metal oxides were studied under the same experimental conditions as unloaded WO_3. All the experiments were studied in an argon environment for 90 minutes. The evolved gases were analyzed and quantified by gas chromatography.

5.7.1 Photocatalytic splitting of water over Fe-loaded WO_3

Fe metal, in the form of Fe^{3+}, binds with the surface oxygen to give Fe_2O_3 (confirmed by XPS analysis). Fe_2O_3 is an n-type photocatalyst with a band gap of 2.2 eV and an unsuitable conduction band edge for the generation of hydrogen. Based on the potentials of the conduction band edges of WO_3 and Fe_2O_3, it can be concluded that there should not be any formation of hydrogen on Fe doped WO_3 yet an increase in yield with the increase in Fe concentration. As explained in section 5.2, the mechanism of hydrogen production for pure WO_3 is different from the photocatalytic production of hydrogen as observed for the catalysts with suitable potential of the conduction band edge for H_2 generation. The high UV flux, when aqueous colloidal suspension of WO_3 was irradiated with 355 nm laser, induces reversible reduction of the catalyst producing hydrogen gas and H_xWO_{3-x}. When Fe-WO_3 is subjected to the same experimental conditions, the high UV laser photon flux causes the cathodic decomposition of surface Fe_2O_3 to give FeO surface states with band potentials suitable for hydrogen production [131] as explained in section 5.5. The comparison of evolved H_2 and O_2 over Fe-doped WO_3 with that of pure WO_3 is presented in figures 5.38 and 5.39. For 0.1% Fe loading, the amount of dopant is probably not sufficient to produce any visible change in hydrogen and oxygen yield. A significant increase in the rate of production of both hydrogen and oxygen (figures 5.40 and 5.41) was observed for 1% and 10% Fe loadings compared to un-doped WO_3 while for 0.1% Fe loading no significant change in the rate was observed for both gases. For 1% and 10% Fe loading, the slow decrease in the rate of production of H_2 (figure 5.40) and O_2 (figure 5.41), with time, indicates the competition of H^+ ions and O_2 for conduction band electrons of FeO and the consumption in the formation of HO_2 radicals which finally leads to recombination reaction. The low yield of hydrogen for 0.1 and 1.0% loadings was found in agreement with the pH measurements during the course of reaction where it was observed that the number of H^+ ions in solution, produced by the oxidation of water through electron donation to photogenerated holes, decreases with the increase in metal loading suggesting an increase in hydrogen yield. In case of 10% Fe loading, the observed photonic efficiency for hydrogen production was ~ 45%. On the other hand, the photonic efficiency for oxygen production was ~ 77%. The comparison of the calculated photonic efficiencies, for H_2 and O_2, for various Fe loadings is plotted in figures 5.42 and 5.43 respectively. This high photonic efficiency for oxygen production indicates that all electrons transferred from WO_3 to Fe_2O_3, do not lead to the formation of H_2 but cause some structural changes in Fe_2O_3 releasing additional oxygen, which includes the formation of FeO and total decomposition of Fe_2O_3 as given in equations 5.21 and 5.22.

For 0.1 and 1.0% Fe loading, there was a decrease in pH while for 10% Fe loading there was a mild decrease followed by an increase in pH. The increase in pH is mainly due to the reduction of oxygen, produced during the photocatalytic process and the release of hydroxyl ions into the solution. This suggests that the conduction band edge of photogenerated FeO states is equally suitable for water reduction along with the generation of hydrogen. These hydroxyl ions serve as poison for H^+ ions and enhance the production of hydroxyl radicals which are the main precursors for oxygen formation.

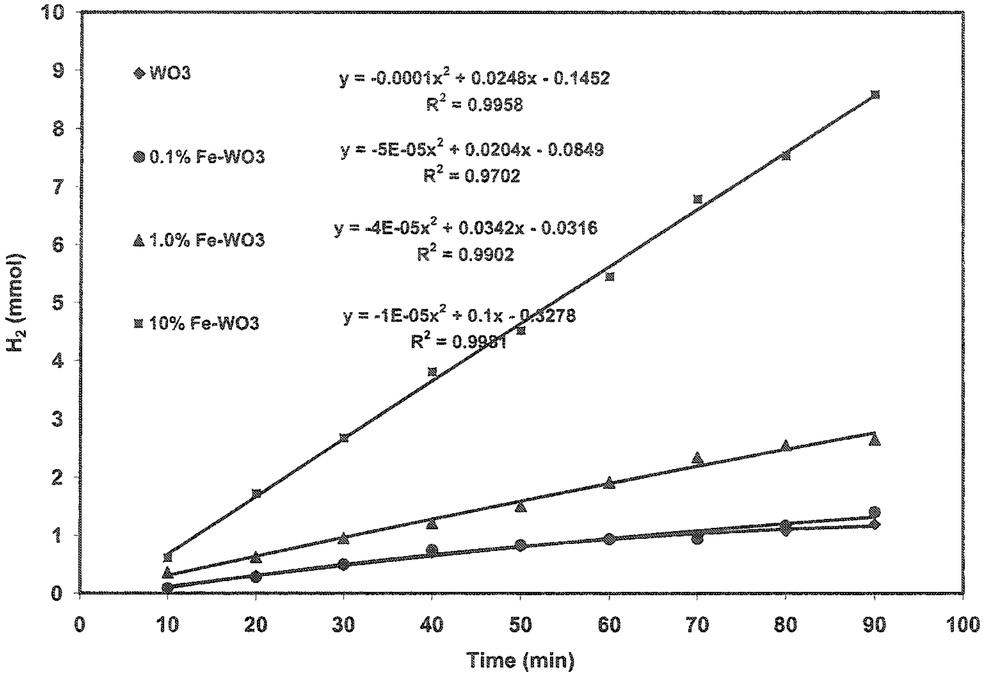

Figure 5.38 Comparison of H_2 yield for various Fe-loadings

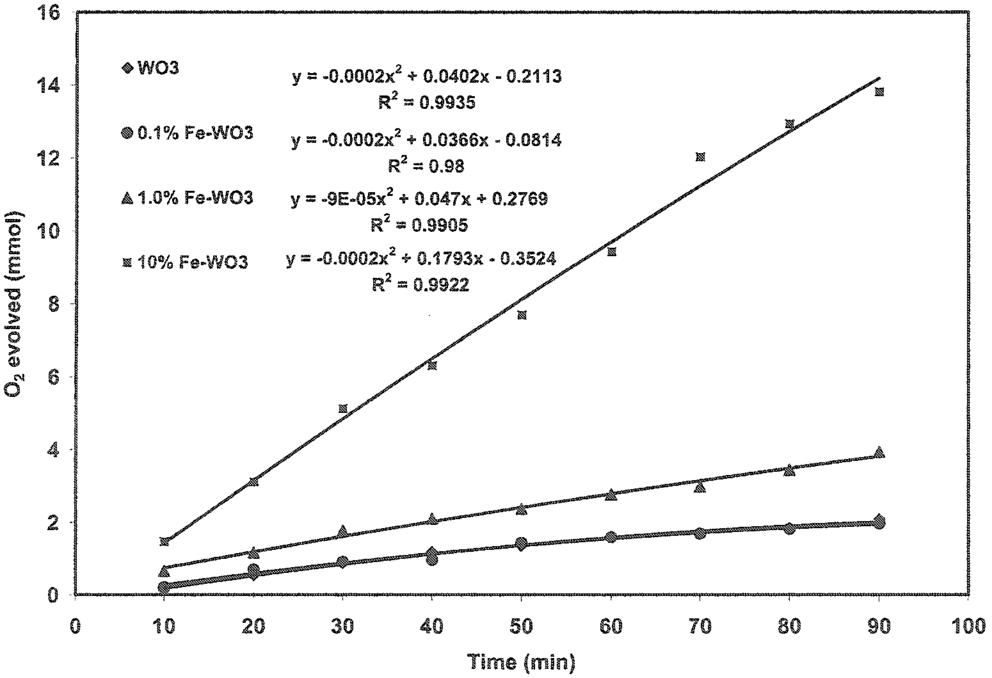

Figure 5.39 Comparison of O_2 yield for various Fe-loadings

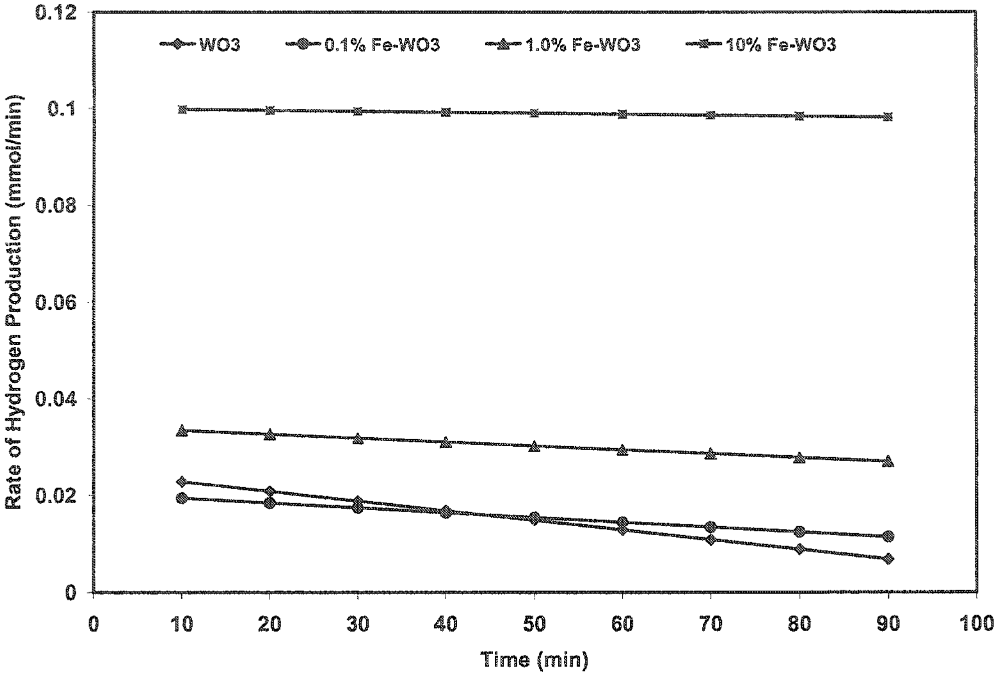

Figure 5.40 Comparison of the rate of H_2 formation for various Fe-loadings

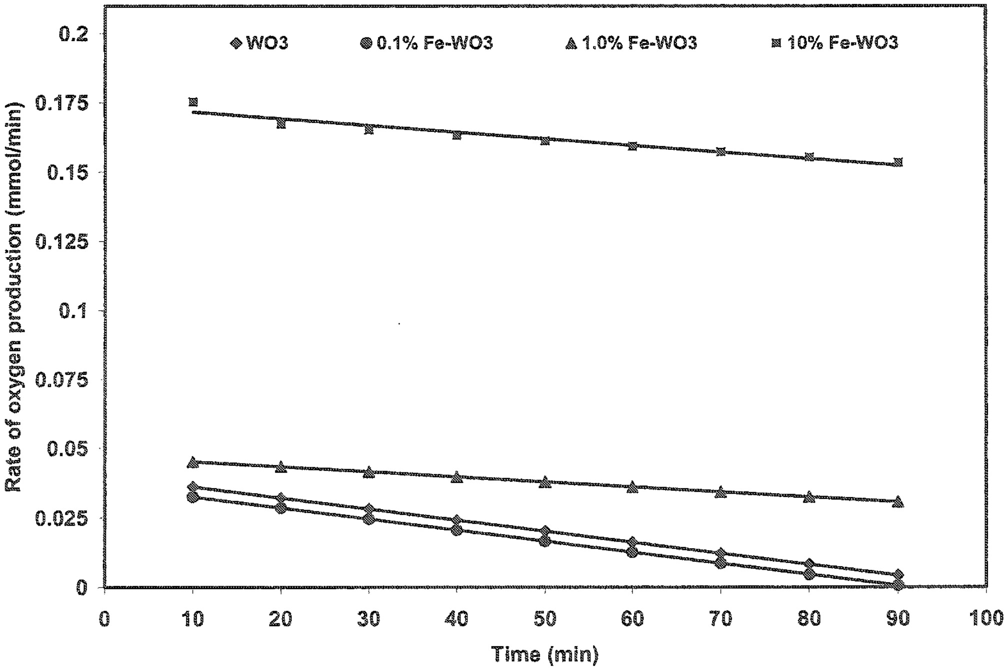

Figure 5.41 Comparison of the rate of O_2 formation for various Fe-loadings

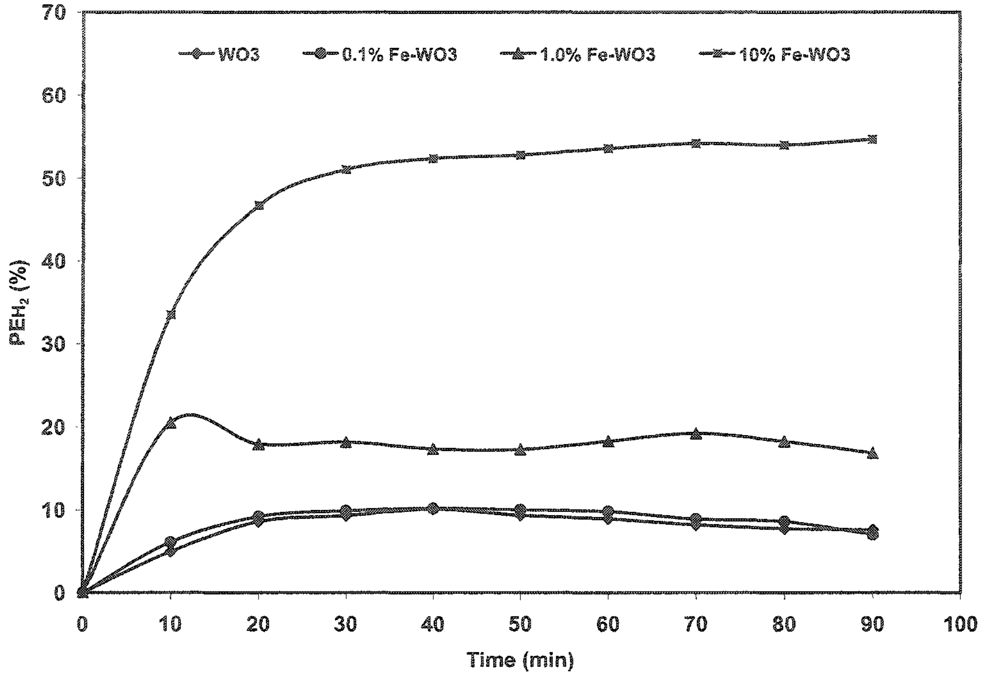

Figure 5.42 Comparison of photonic efficiency for H_2 formation for various Fe-loadings

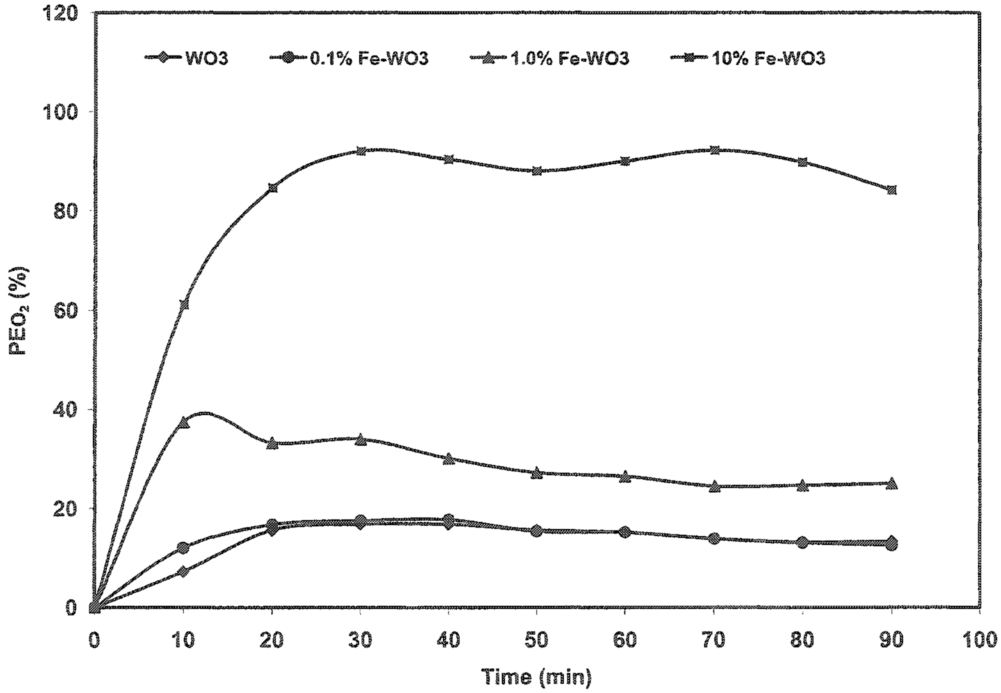

Figure 5.43 Comparison of photonic efficiency for O_2 formation for various Fe-loadings

5.7.2 Photocatalytic splitting of water over Co-loaded WO_3

The XPS analysis indicated the presence of Co, as Co^{2+} ions, in the form of CoO at the surface of WO_3. The comparison of evolved H_2 and O_2 for Co-loaded WO_3 with pure WO_3 is presented in figures 5.44 and 5.45. An increase in the production of both H_2 and O_2 was observed with the increase in metal loading. A sharp decrease in the rate of production of hydrogen overtime for 10% Co loading while a gradual decrease was observed for 1.0% and 0.1% Co loadings (figure 5.46). Similarly, a decrease in the rate of production of oxygen (figure 5.47) was observed for all Co loadings. Bases on these observations it can be inferred that with the increase in Co loading, the extent of the opposing reactions i.e. the formation of hydroxyl ions through water reduction, increases causing a decrease in the yield of both the gases. The increase in the Co loading enhances the yield of both oxygen and hydrogen but simultaneously enhances the rates of undesired reactions. The pH changes follow the same pattern as discussed in case of Fe-loading. The high yield of oxygen for 0.1, 1.0% and 10% Co loadings indicates the contribution of lattice oxygen, released from WO_3, which contributes in the overall yield of oxygen. A maximum photonic efficiency of ~ 77% for hydrogen production was observed for 10% Co loading which was 10 times higher than that of WO_3, indicating the suitability of surface CoO as micro-cathode. The surface adsorbed CoO is itself a p-type semiconductor with the band edge positions suitable for the production of hydrogen and oxygen through water splitting in the aqueous medium [131]. The high overall photonic efficiency of 60% for oxygen production and the overall O_2:H_2 ratio of ~1.3 indicates the contribution of self-reduction of CoO through anodic mechanism under UV illumination as explained below [17].

$$CoO + 2h^{+} \rightarrow Co^{2+} + \tfrac{1}{2}O_2 \qquad 5.23$$

The presence of Co^{2+} was confirmed by the presence of purple color in the solution. A comparison of calculated photonic efficiencies for H_2 and O_2 production for various concentrations of Co loading is presented in figure 5.48 and 5.49. The initial increase in the photonic efficiency followed by decrease overtime for both H_2 and O_2 indicates the depletion of H^+ ions and O_2 through reduction with the formation of hydroxyl radicals. This confirms the suitability of conduction band edge of CoO (E_{cb} = -0.11 V) for the reduction of oxygen (equation 5.16) as well as for hydrogen production. When the concentration of oxygen reaches to an appreciable limit in the solution, it starts competing with H^+ ions for conduction band electrons to produce hydroxyl ions in the solution. This serves as poison for H^+ ions causing a decrease in hydrogen yield with time.

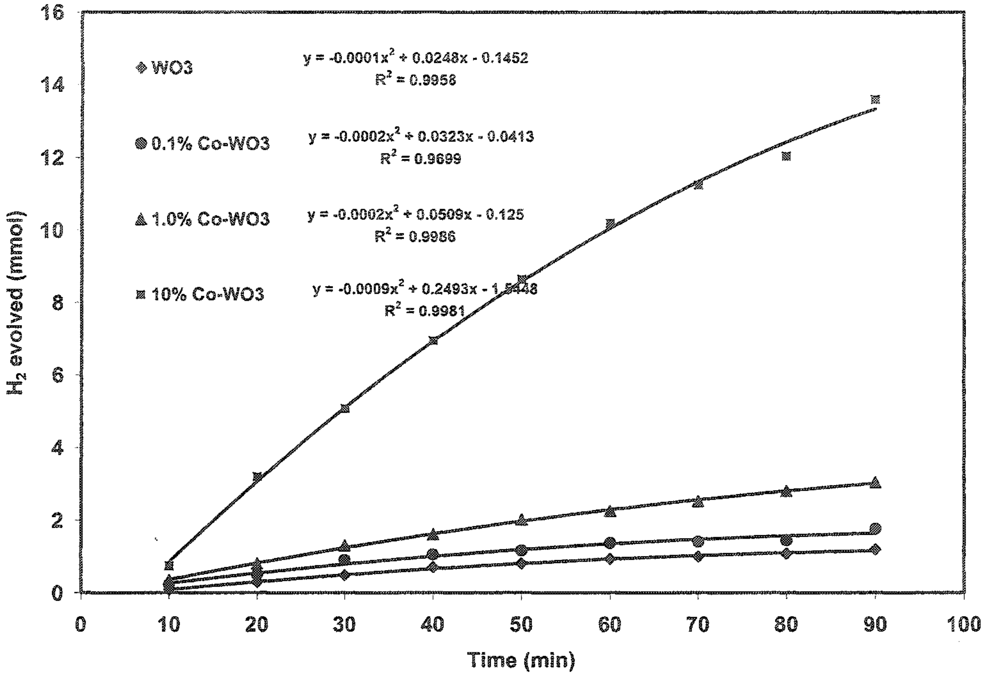

Figure 5.44 Comparison of H_2 yield for various Co-loadings

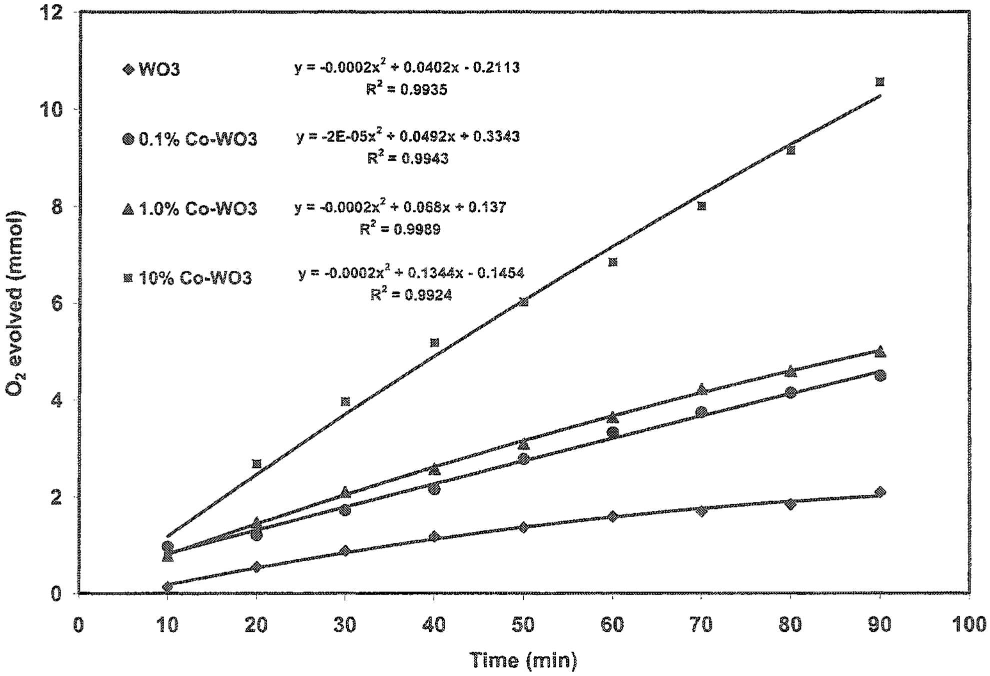

Figure 5.45 Comparison of O_2 yield for various Co-loadings

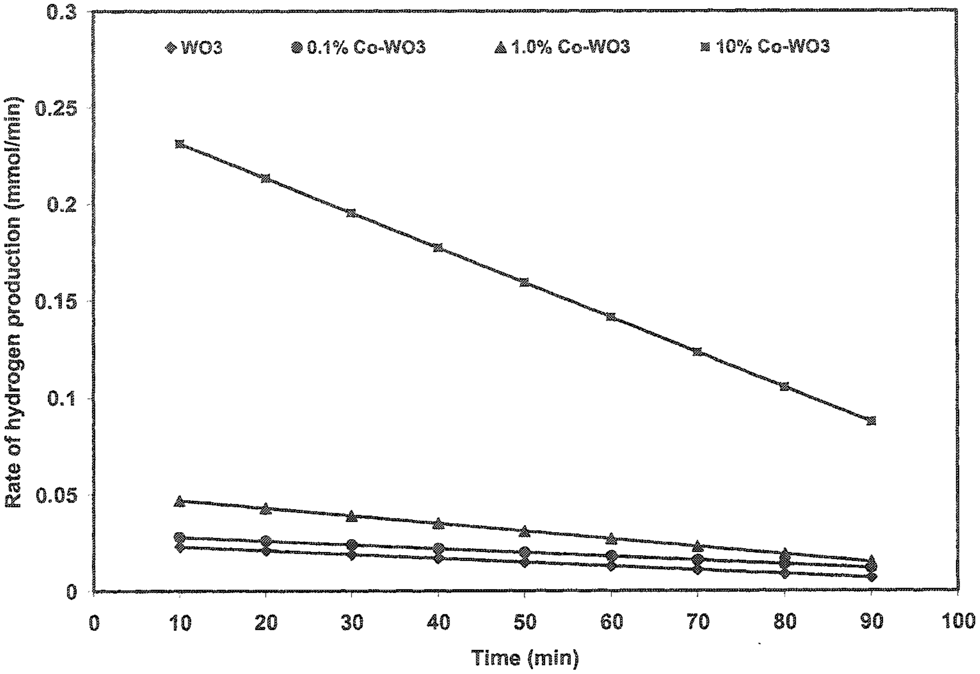

Figure 5.46 Comparison of the rate of H_2 formation for various Co-loadings

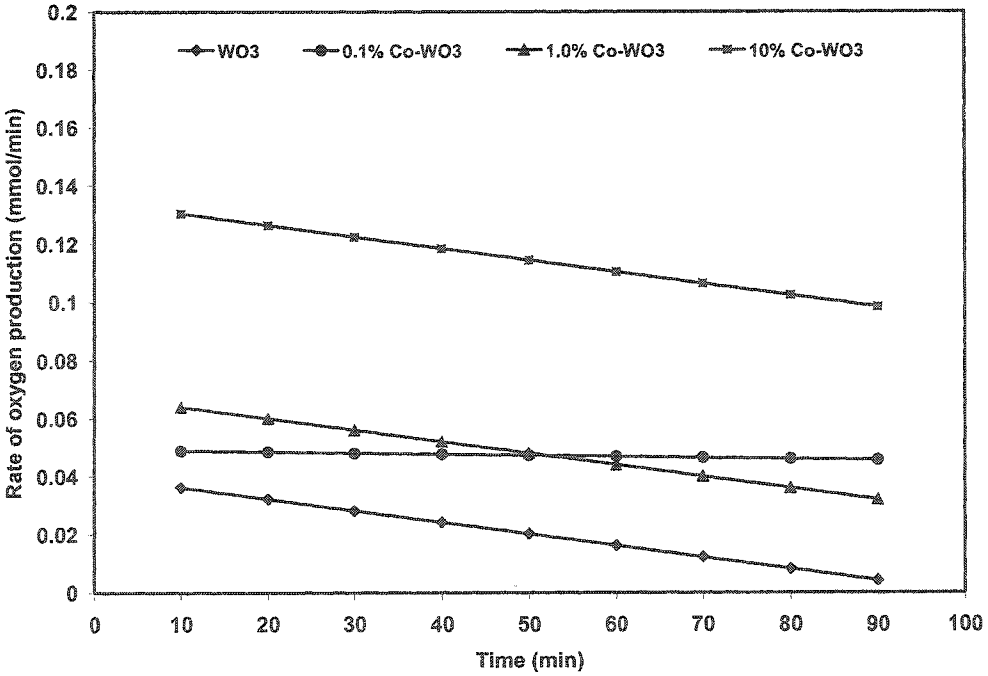

Figure 5.47 Comparison of the rate of O_2 formation for various Co-loadings

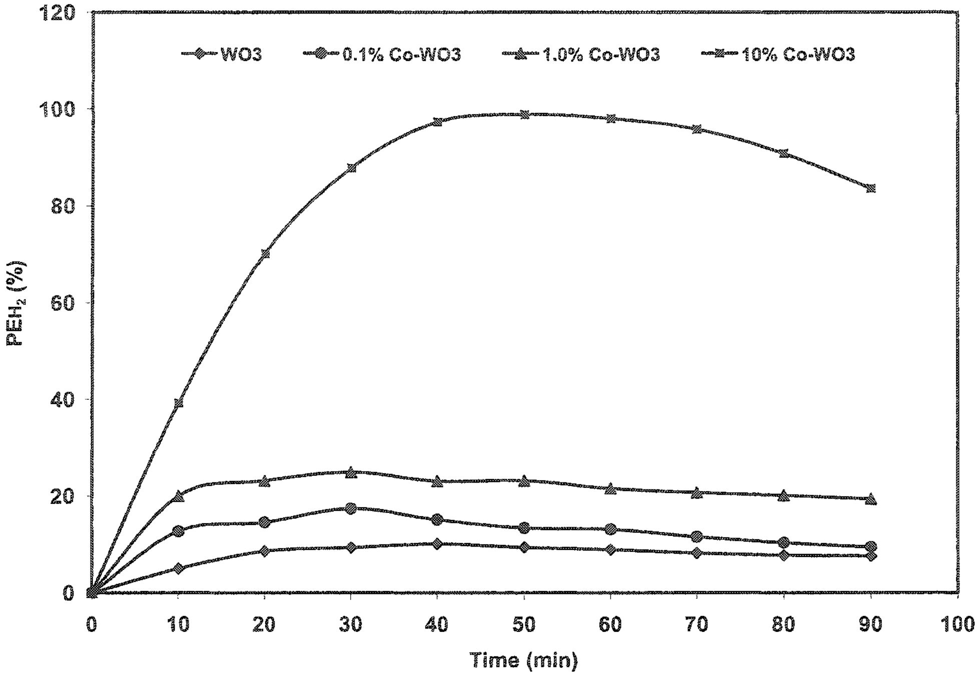

Figure 5.48 Comparison of photonic efficiency for H_2 formation for various Co-loadings

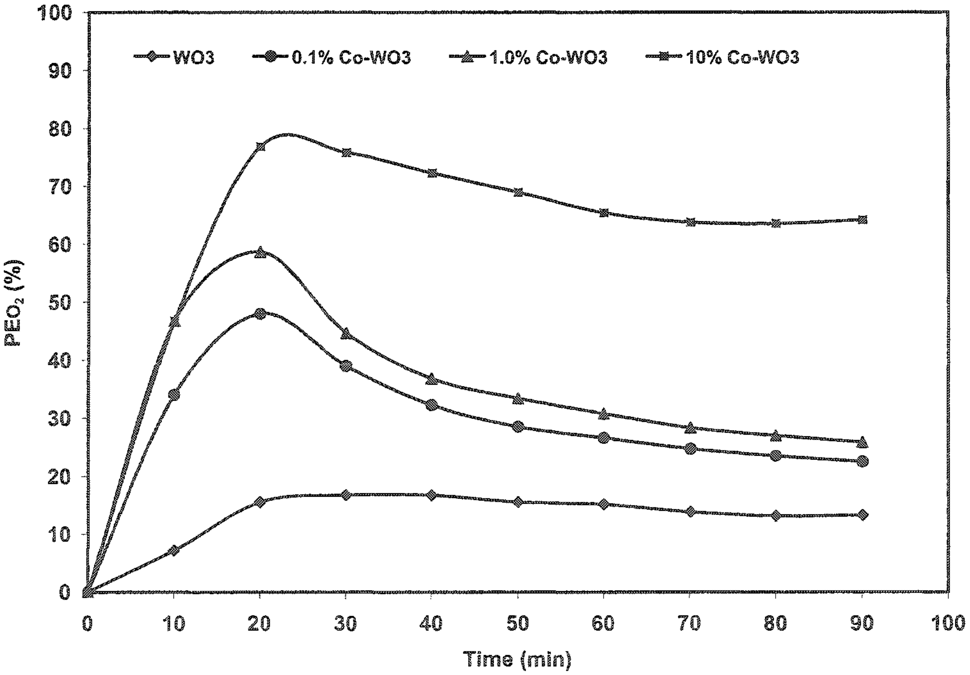

Figure 5.49 Comparison of photonic efficiency for O_2 formation for various Co-loadings

5.7.3 Photocatalytic splitting of water over Ni loaded WO_3

XPS analysis predicted the presence of Ni as Ni_2O_3 at the surface of WO_3 as described in chapter 4. The comparison of evolved H_2 and O_2 over WO_3 doped with various concentrations of Ni with that of pure WO_3 is presented in figures 5.50 and 5.51. An increase in the production of both H_2 and O_2 with the increase in metal loading indicates the suitability of Ni as dopants for photocatalytic splitting of water. A significant decrease in the rate of production of hydrogen (figure 5.52) was observed for 10% Ni doping which is due to the competition between the H^+ ions and oxygen for conduction band electron and the depletion of H^+ ions by the hydroxyl ions produced as a result of the water reduction reaction. For the rate of oxygen production (figure 5.53), the decrease is not as sharp as in case of hydrogen production because the reduction of water affects the yield of hydrogen by capturing the conduction band electron and producing the hydroxyl radicals which serve as a sink for H^+ ions. The pH measurements follow the same pattern as in the cases of Fe and Co loadings. The non-stoichiometric release of oxygen for 0.1 and 1.0% Ni loadings indicates the contribution of lattice oxygen from WO_3 and the reduction of Ni_2O_3 to NiO as given below [126].

$$Ni_2O_3 + 2e^- \rightarrow 2NiO + \frac{1}{2}O_2 \qquad 5.24$$

The improvement of the oxygen to hydrogen ratio for the 10% Ni loading is indicative of the decrease in the release of lattice oxygen from WO_3 and suggests that the reduction of Ni_2O_3 to NiO contributes to the enhanced yield of oxygen. The reduced form of Ni_2O_3 i.e. NiO, is itself a p-type semiconductor with a conduction band edge at -0.5V

[127,131] which is highly suitable for H^+/H_2 and oxygen reduction process. The overall photonic efficiency of ~ 81% for hydrogen production is 11 times higher than that of WO_3. The overall photonic efficiency of oxygen production is 60% which is 19% higher than the photonic efficiency for the production of H_2 and O_2 as shown in figures 5.54 and 5.55. This deviation from the ideal 1:2 oxygen to hydrogen ratio suggests the release of oxygen from NiO itself under a high UV photon flux and the creation of defect sites in the bulk of the catalyst. The photonic efficiency for both H_2 and O_2 increases initially with time and reaches a stable value afterwards. This trend indicates that most H^+ ions produced by photocatalytic splitting of water over WO_3 compete with adsorbed oxygen and capture the electrons from the conduction band of NiO and change to hydrogen. On the other hand, the increase in pH for 10% metal loading suggests the depletion of H^+ ions by hydroxyl ions.

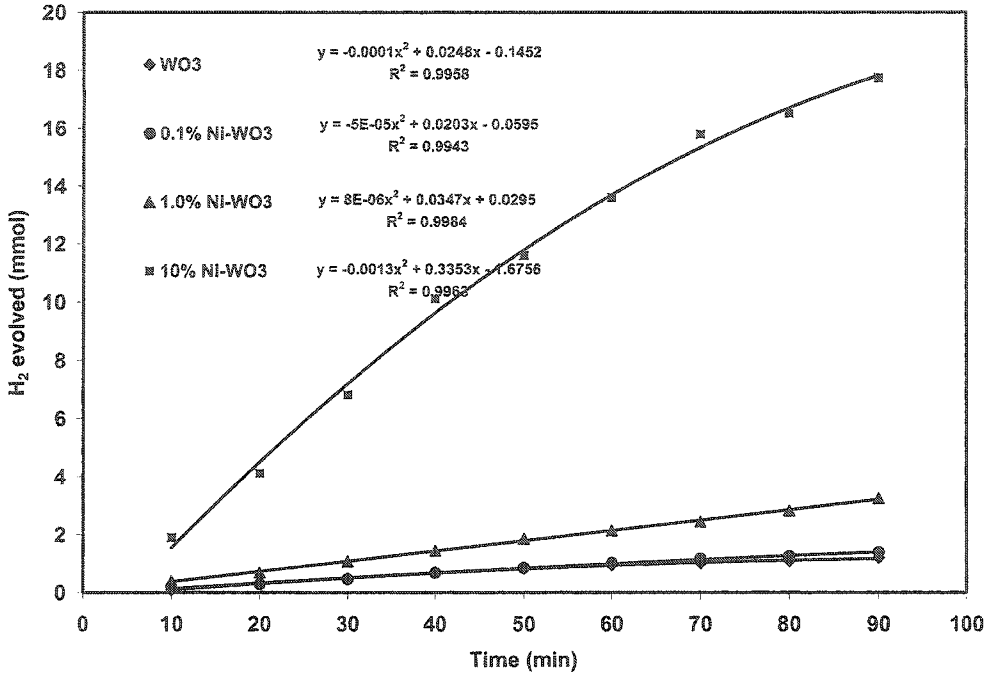

Figure 5.50 Comparison of H_2 yield for various Ni-loading

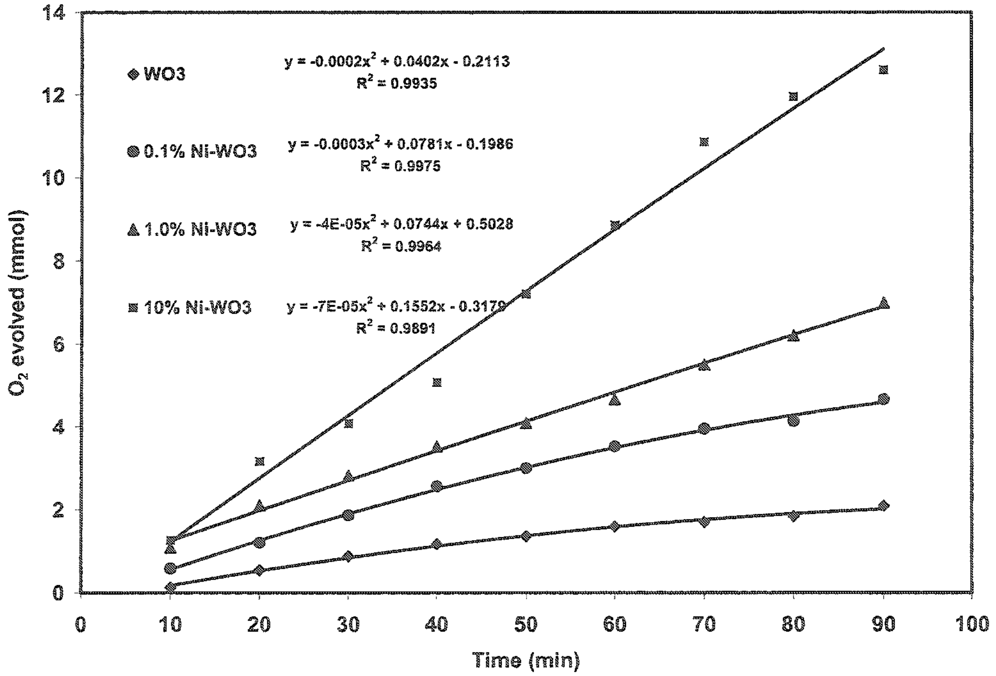

Figure 5.51 Comparison of O_2 yield for various Ni-loading

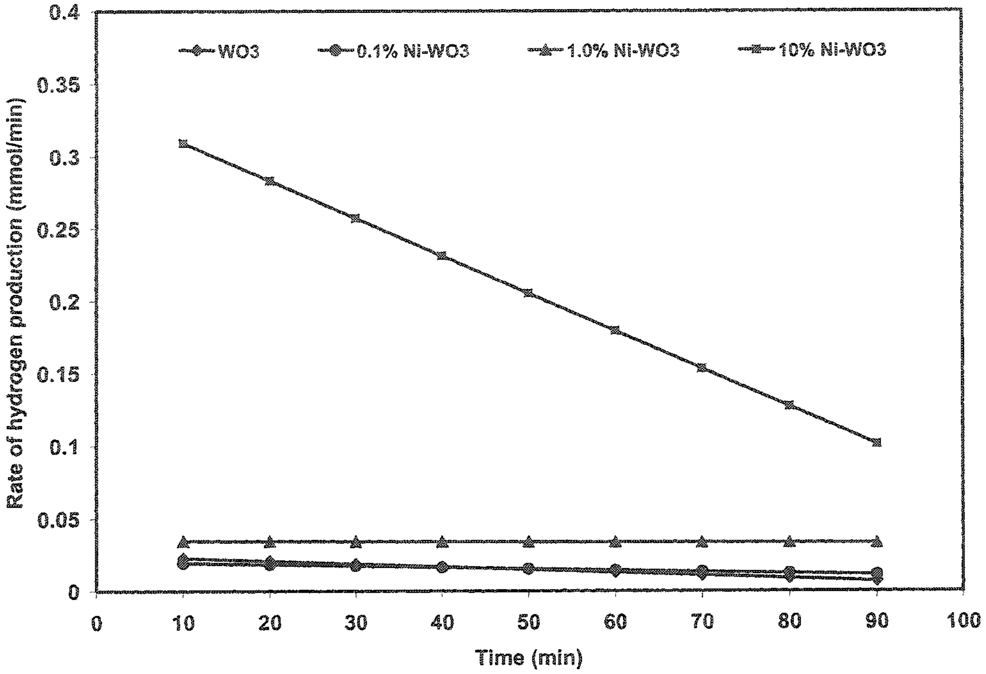

Figure 5.52 Comparison of the rate of H_2 formation for various Ni-loading

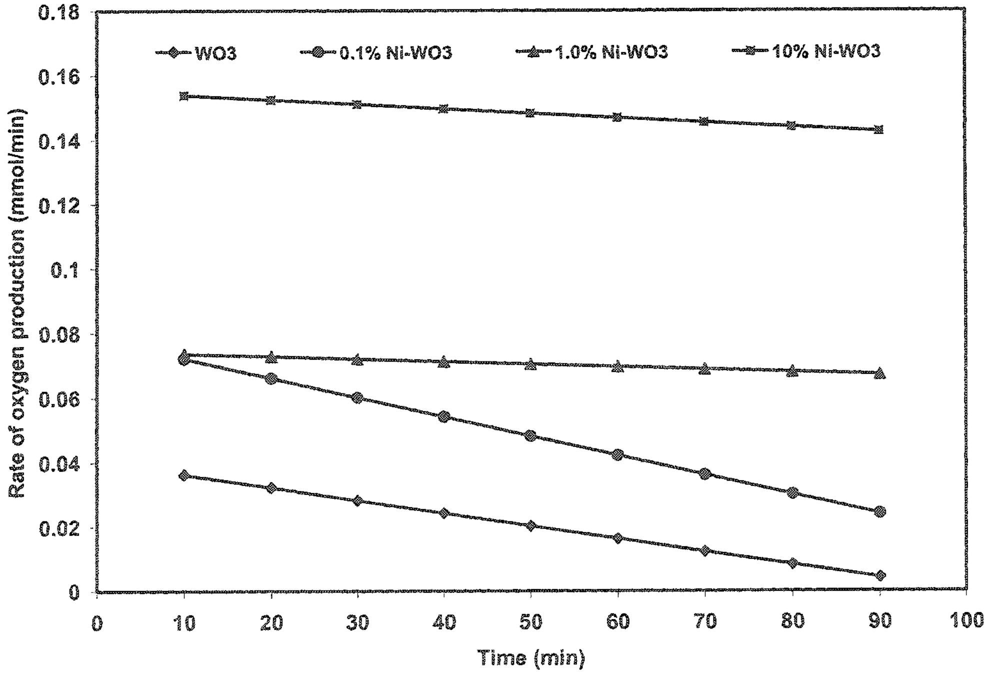

Figure 5.53 Comparison of the rate of O_2 formation for various Ni-loading

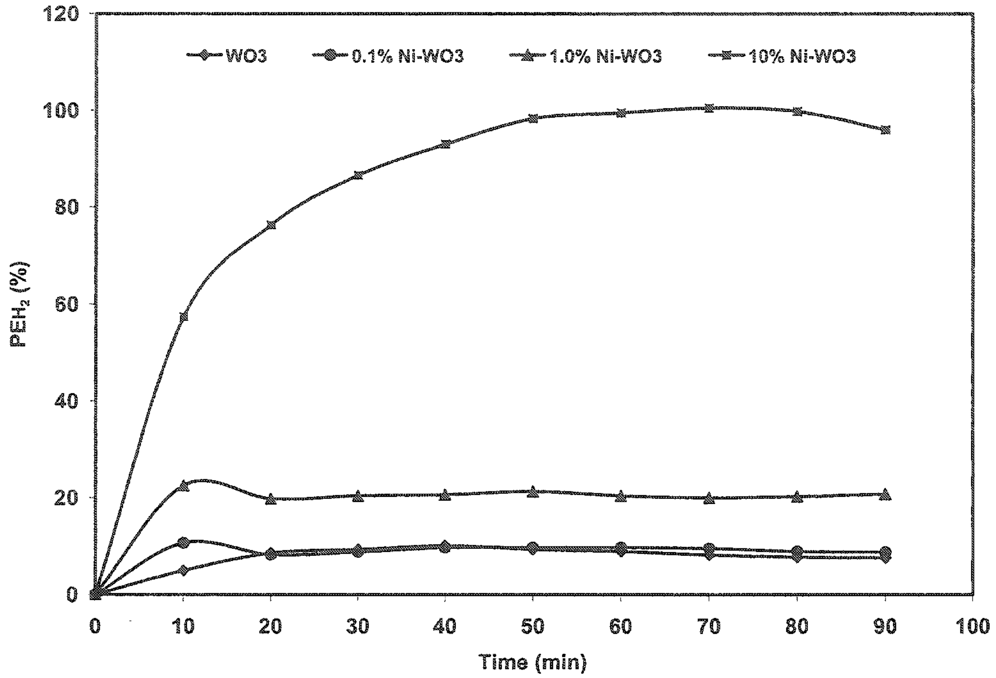

Figure 5.54 Comparison of photonic efficiency for H_2 formation for various Ni-loading

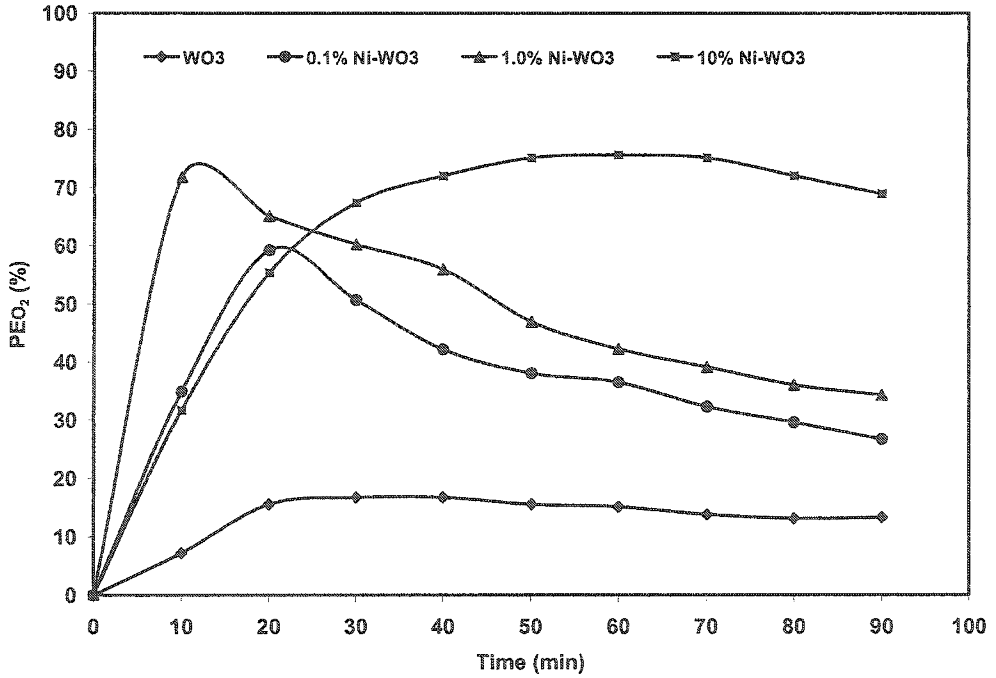

Figure 5.55 Comparison of photonic efficiency for O_2 formation for various Ni-loading

5.7.4 Photocatalytic splitting of water over Cu loaded WO_3

The XPS studies indicated the presence of Cu as Cu_2O at the surface of WO_3 host as described earlier. A gradual increase in the production of both H_2 and O_2 was observed and is presented in figures 5.56 and 5.57. The rates of hydrogen and oxygen production are presented in figures 5.58 and 5.59. For 0.1 and 1.0% Cu loading, a sharp increase followed by a gradual decrease in the rate of formation of H_2 suggests the depletion of surface Cu_2O with time through cathodic decomposition mechanism i.e. through the trapping of conduction band electron to leave metallic Cu at the surface [132].

$$Cu_2O + H_2O + 2e^- \rightarrow 2Cu + 2OH^- \qquad 5.25$$

A higher rate of hydrogen production compared to un-doped WO_3 was observed for increased Cu loading. A decreasing trend was observed in the rate of hydrogen and oxygen production for all Cu loadings. For 10% Cu loading, a sharp decrease in the rate of both gases. This decrease in the rat of production is sharper for H_2. It seems that the electron capture process changes the doped metal oxide to a form that is unsuitable for hydrogen production and enhances the unwanted electron-hole pair recombination, which in turn decreases the rate of formation of oxygen as well. In addition, the production of hydroxyl radicals by the decomposition of Cu_2O (equation 5.25), serve as additional cause for the decrease in the rate of hydrogen.

The formation of hydroxyl ions in the solution initiates the formation of CuO at the surface through anodic pathway [133].

$$Cu_2O + 2OH^- + h_{vb}^+ \rightarrow 2CuO + H_2O \qquad 5.26$$

In case of Cu doping Cu_2O is a p-type semiconductor with a direct band gap of 2.2 eV and has suitable band edges for water oxidation [132-133]. It was also noticed that this oxide is unstable in aqueous suspensions and undergoes both oxidation and reduction, with the formation of metallic copper and CuO, under illumination. This is a serious problem that restricts its use as photocatalyst [134]. For 10% Cu-loading the rate of hydrogen production (figure 5.58) and photonic efficiency (figure 5.60) gradually increases, reaches a stable value, and then starts to decrease. The decrease in rate and photonic efficiency with time is mainly due to the reduction of Cu_2O to metallic Cu through the above- mentioned reaction and due to the competition between the produced oxygen and H^+ ions for conduction band electrons. Another contributing factor is the formation of hydroxyl ions through water reduction in the system and their role as scavengers for H^+ ions. The pH measurements during the illumination also support this hypothesis. In addition, a sharp decrease in the rate of oxygen production (figure 5.59) and photonic efficiency (figure 5.61) is due to the reduction of O_2.

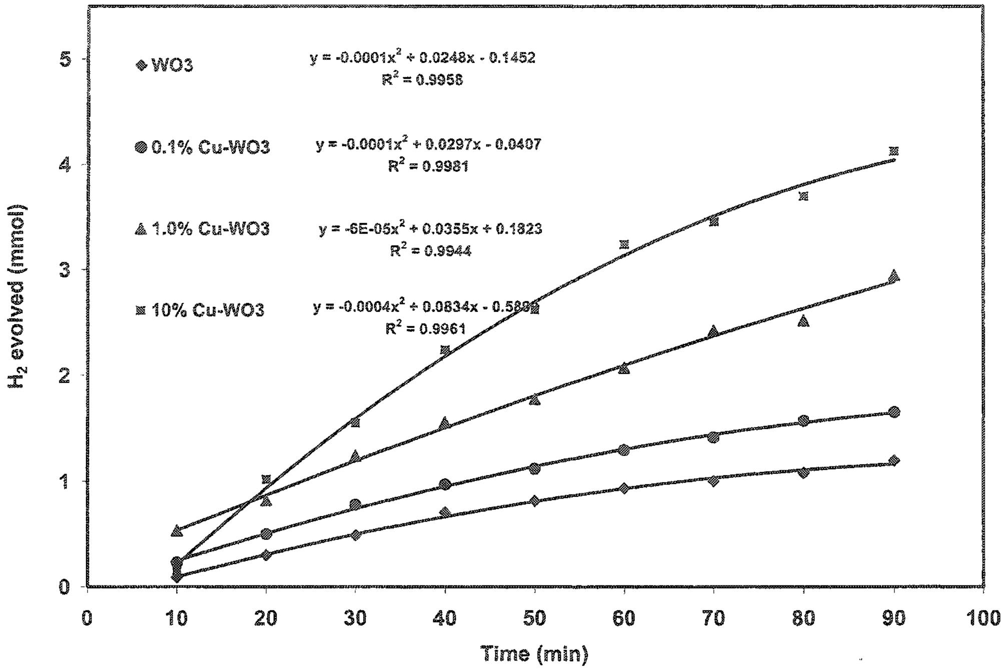

Figure 5.56 Comparison of H_2 yield for various Cu-loading

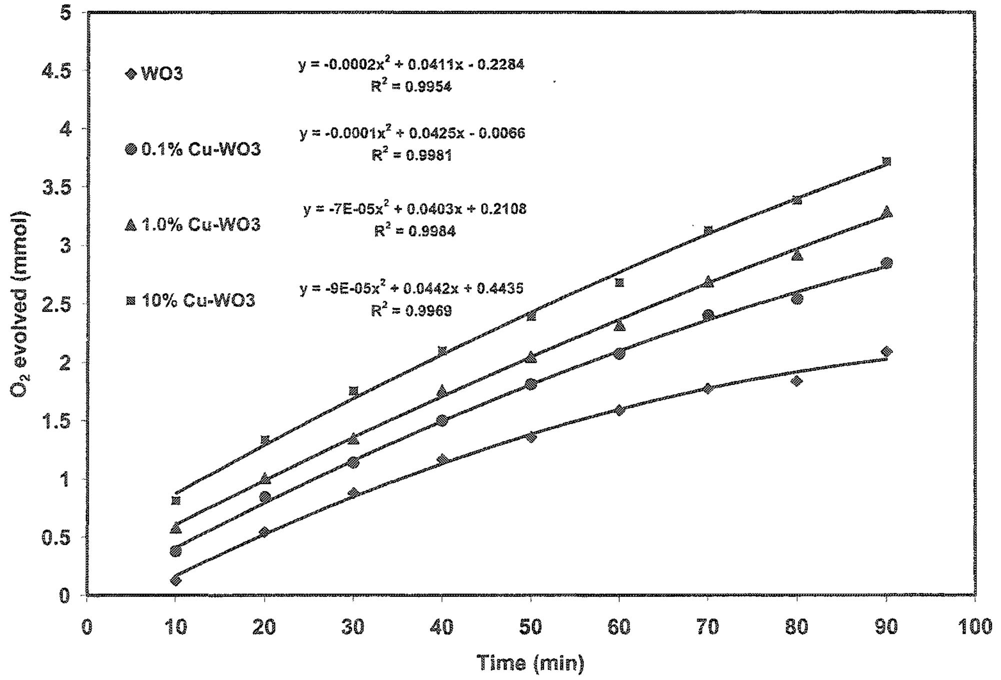

Figure 5.57 Comparison of O_2 yield for various Cu-loading

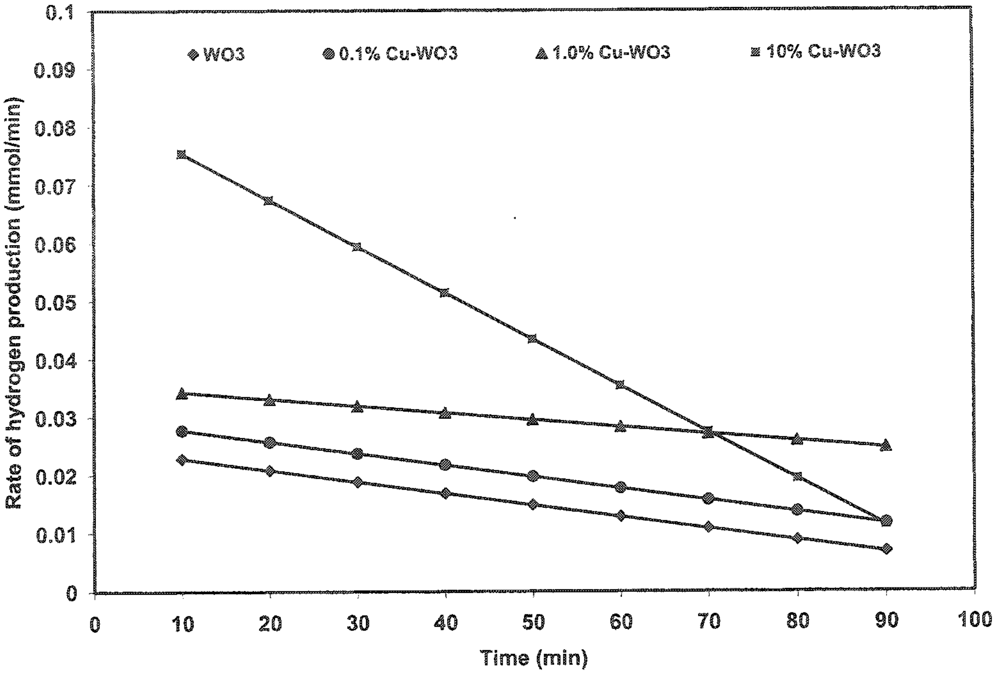

Figure 5.58 Comparison of the rate of H_2 formation for various Cu-loading

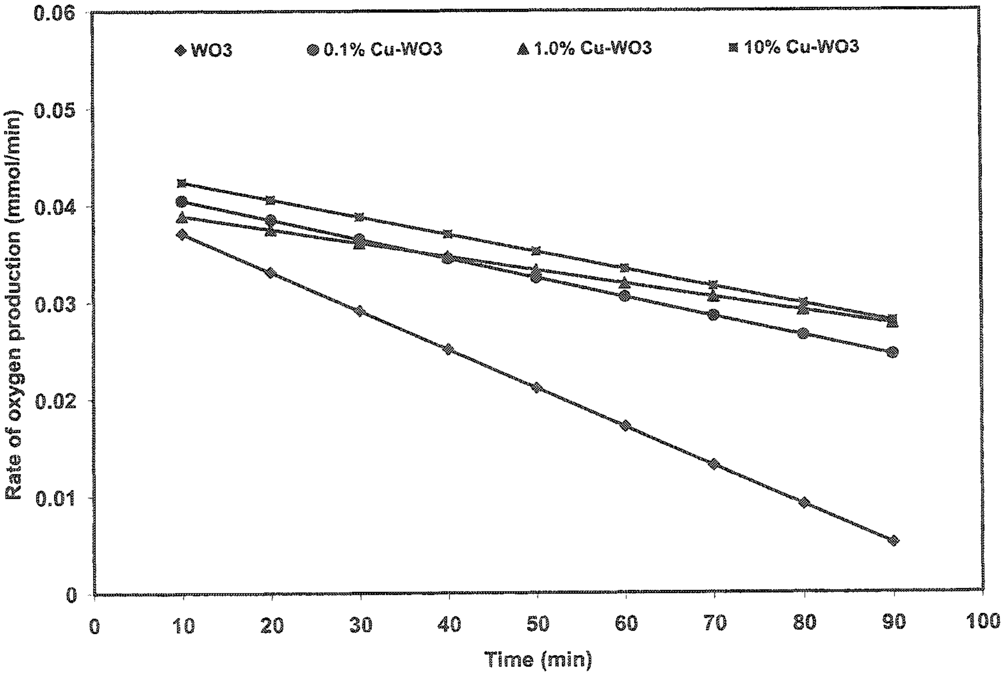

Figure 5.59 Comparison of the rate of O_2 formation for various Cu-loading

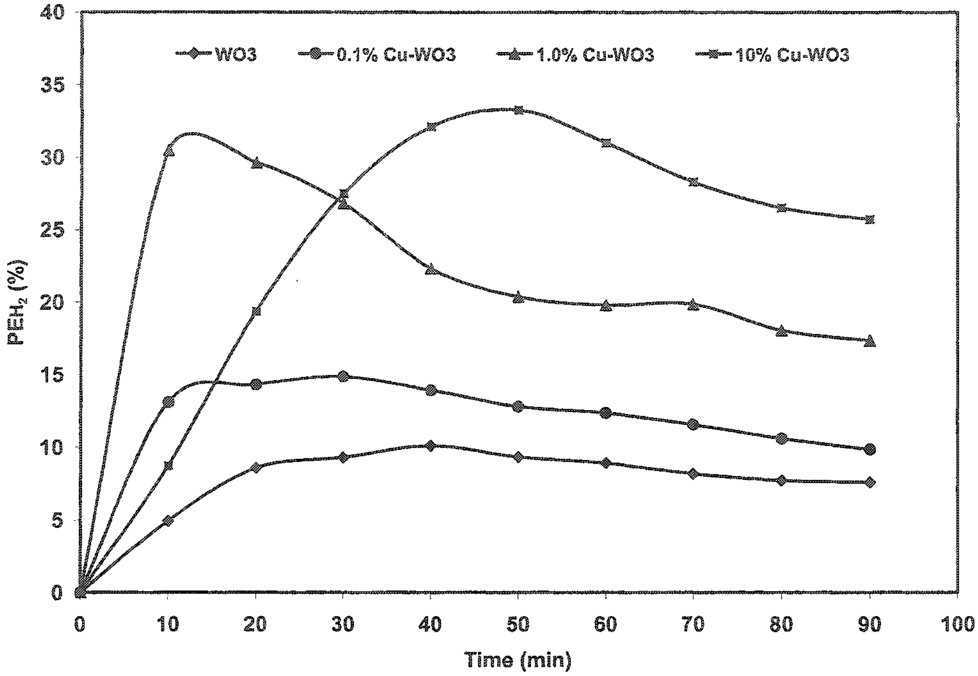

Figure 5.60 Comparison of photonic efficiency for H_2 formation for various Cu-loadings

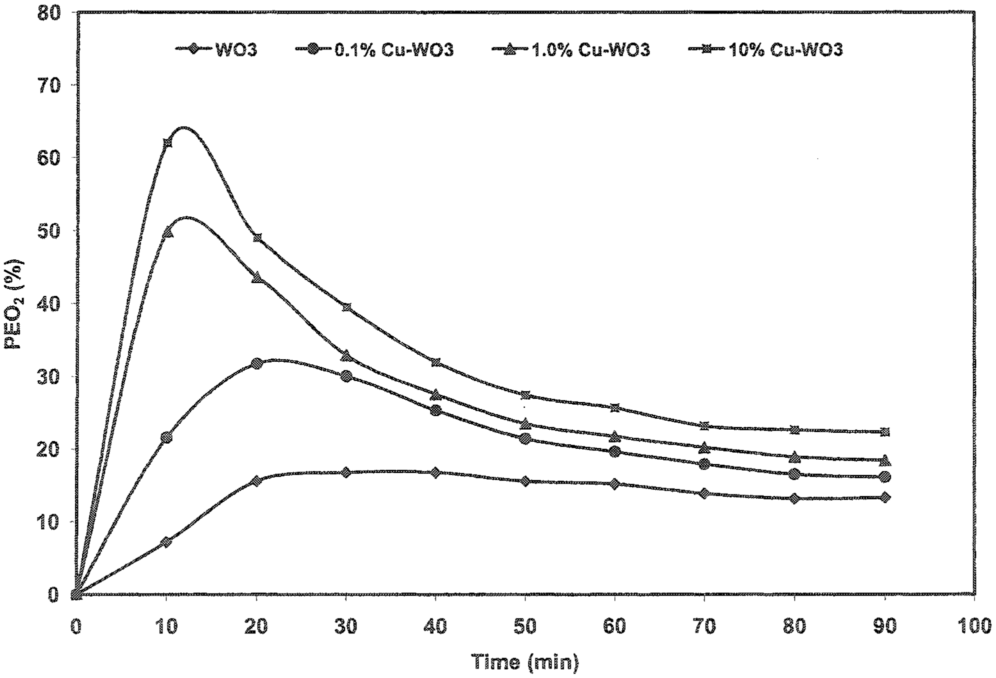

Figure 5.61 Comparison of photonic efficiency for O_2 formation for various Cu-loadings

5.7.5 Photocatalytic splitting of water over Zn loaded WO_3

A very different trend for H_2 and O_2 production was observed in photocatalytic splitting of water over the WO_3 based catalysts loaded with different concentrations of Zinc. Relative to the un-doped WO_3, an increase in hydrogen production (figure 5.62) was observed for the 0.1 and 1.0% Zn loading while a decrease in hydrogen production was observed for the 10% Zn loading. Relative to the un-doped WO_3, an increase in oxygen production (figure 5.63) for 0.1% Zn loaded catalyst and a substantial decrease in oxygen production with further increase in metal loading were observed. In addition, a significant drop in photonic efficiency for both hydrogen and oxygen production (figure 5.66 and 5.67) as compared to other transition metals was observed. ZnO (confirmed by XPS) possesses a bandgap of 3.2 eV and has a suitable conduction band edge of -0.31 V [131]. The low photonic efficiency, especially for 10% Zn loading, for both H_2 and O_2 production indicates the increased rate of surface recombination due to the inefficient electron trapping by the metal loading. In ZnO, the Zn metal exists in +2 oxidation state with $3d^{10}$ configurations. The presence of completely filled "d" orbitals shows the inability of ZnO towards efficient capture of photoexcited conduction band electrons thus causing an increase in electron-hole recombination and a decrease in the rate of hydrogen and oxygen (figure 5.64 and 5.65). The increasing concentration of Zn also suppresses the creation of surface defects in the WO_3 host causing a decrease in H_2 and O_2 yield even lower than un-doped WO_3. All the above-mentioned observations suggest that even in the presence of suitable conduction band edge, Zn-loadings are not suitable for capturing the photoexcited electrons.

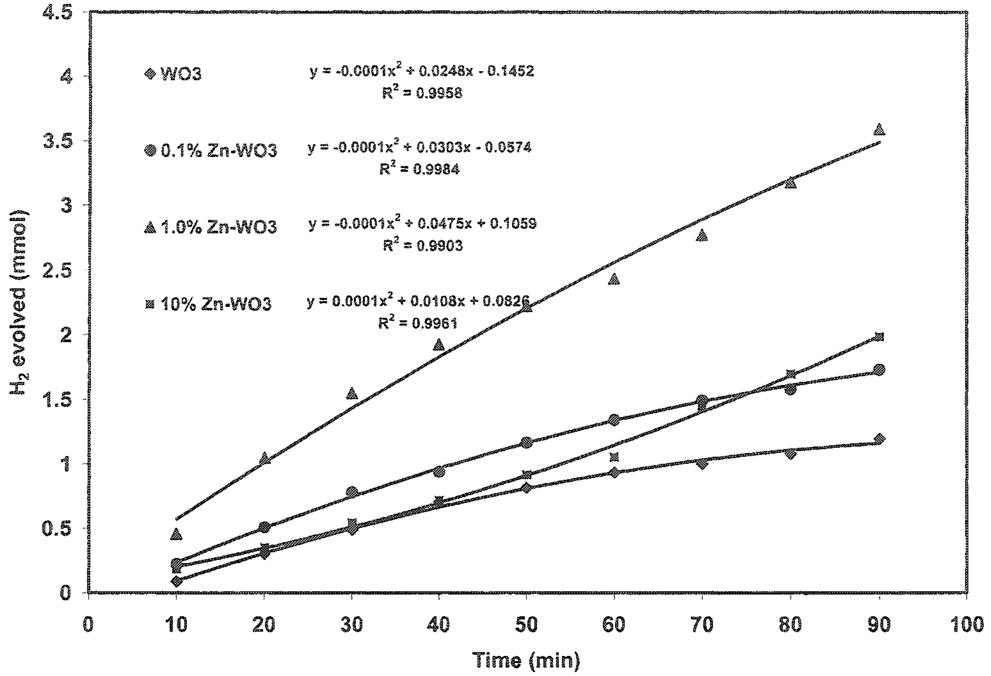

Figure 5.62 Comparison of H_2 yield for various Zn-loading

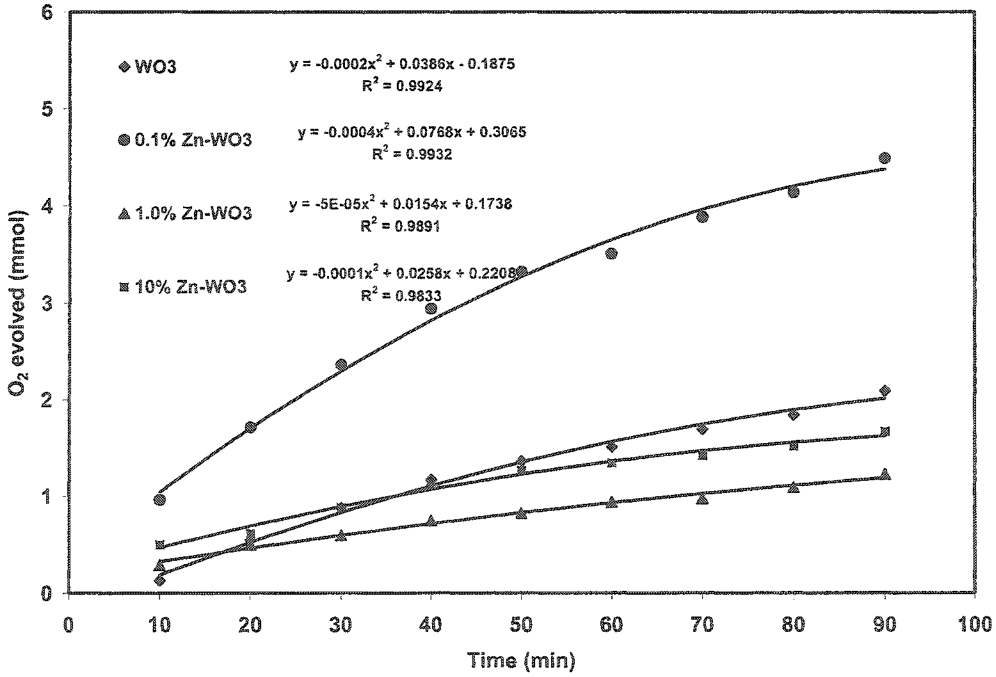

Figure 5.63 Comparison of O_2 yield for various Zn-loading

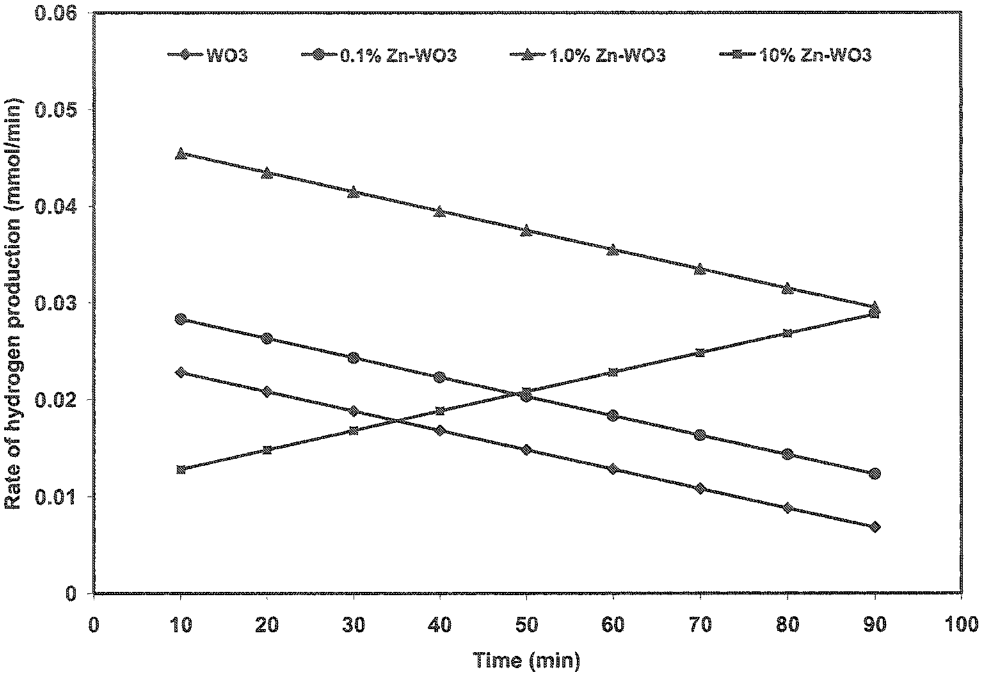

Figure 5.64 Comparison of the rate of H_2 formation for various Zn-loading

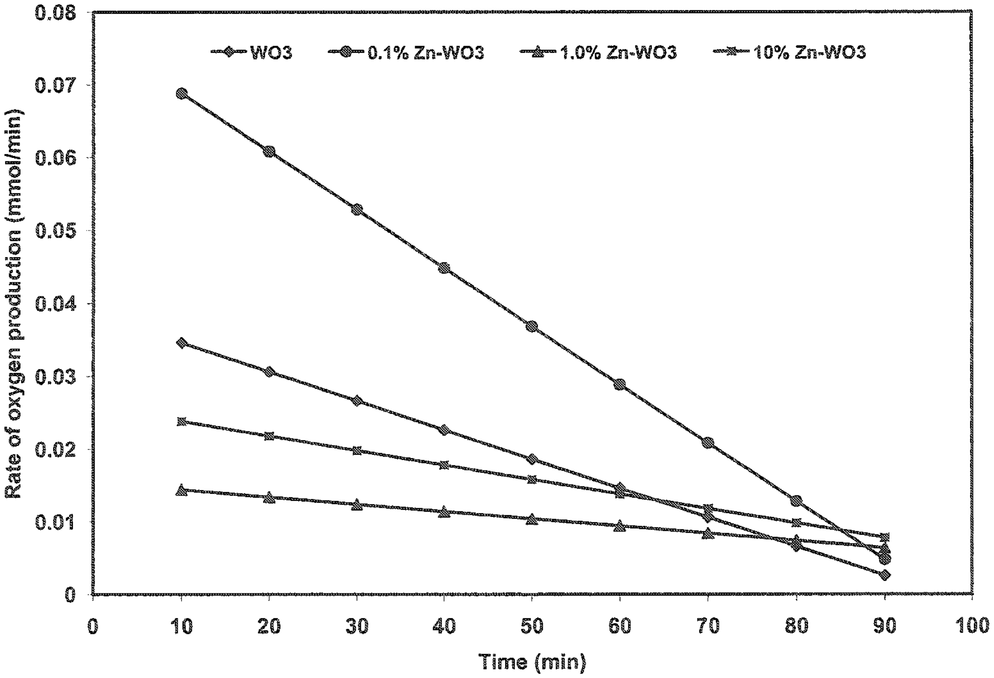

Figure 5.65 Comparison of the rate for O_2 formation for various Zn-loading

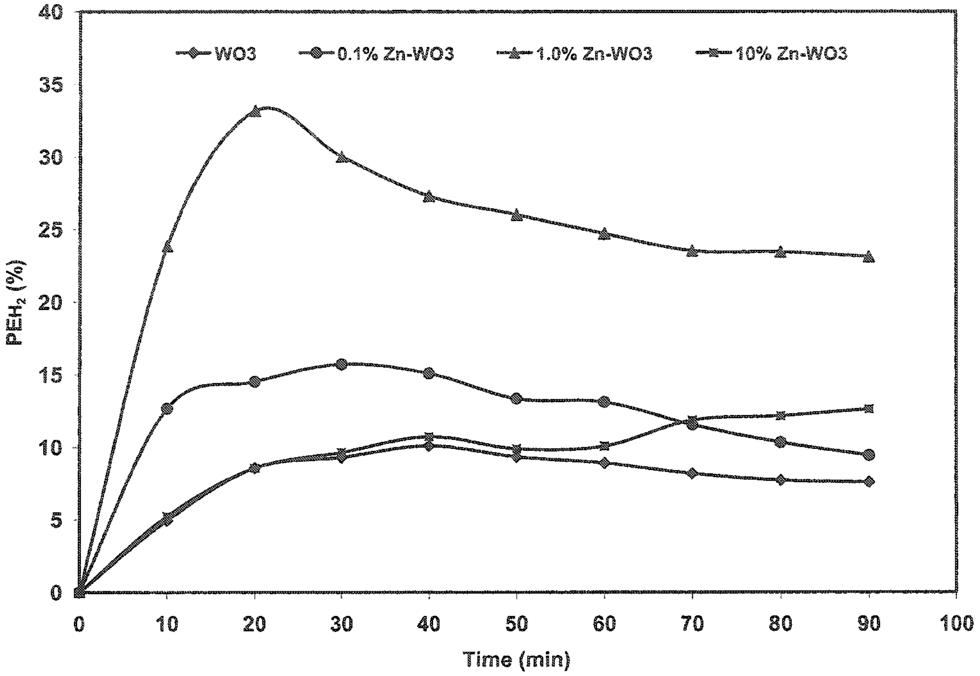

Figure 5.66 Comparison of photonic efficiency for H_2 formation for various Zn-loading

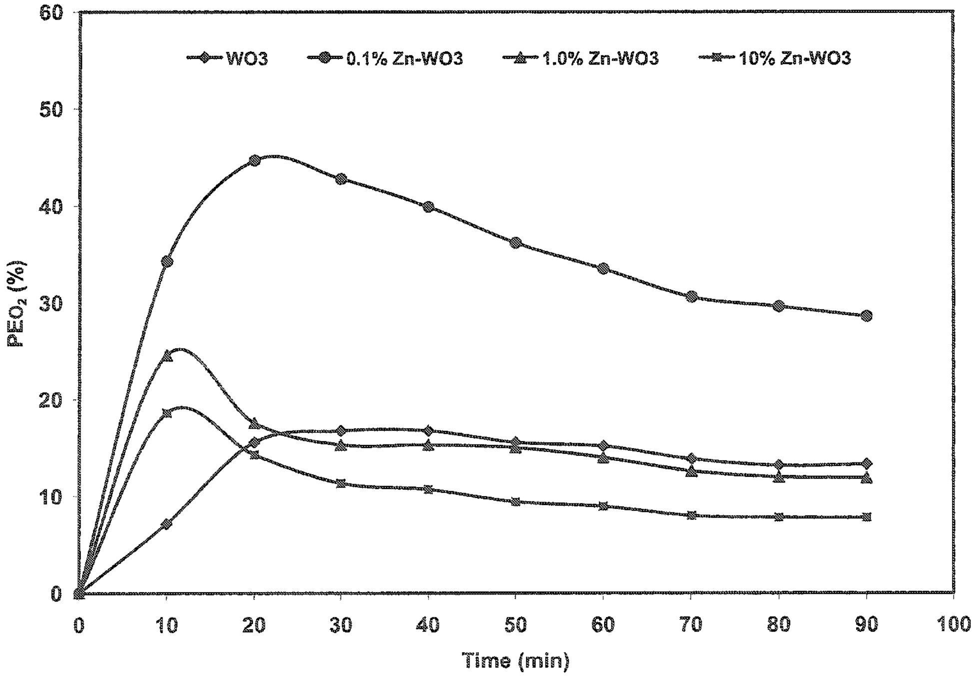

Figure 5.67 Comparison of photonic efficiency for O_2 formation for various Zn-loading

5.7.6 Photocatalytic splitting of water over Ag loaded WO_3

Since no significant change regarding water splitting was observed for 0.1% metal loaded catalysts in the cases discussed earlier, only the water splitting over 1.0 and 10% Ag loaded catalysts is reported and discussed here. XPS studies predicted the presence of Ag, as Ag_2O, at the surface of WO_3. The yield of H_2 (figure 5.68) and O_2 (figure 5.69) are higher for 1.0% metal loading than the 10% loading which in turn is comparable to un-doped WO_3 or slightly above it. A sharp decrease in the rate of production of both hydrogen and oxygen (figures 5.70 and 5.71) predicts an enhanced electron-hole pair recombination with increasing Ag loading. The initial increase followed by a sharp decrease in photonic efficiency (figures 5.72 and 5.73) for the 1.0% Ag loading which indicates an initial charge separation followed by the depletion of Ag_2O and the formation of metallic silver through a cathodic decomposition mechanism.

$$Ag_2O + e^- \rightarrow AgO + Ag^{\circ} \qquad 5.27$$

In the case of 10% Ag loading, the absorption of UV photons causes the decomposition of Ag_2O to give AgO and metallic Ag at the surface favored by the bandgap of 1.20 eV [131]. In addition the conduction band edge of surface formed AgO is not suitable to deliver electrons to the H^+ ions generated by the oxidation of water over WO_3 leading to the formation of hydrogen. The formation and deposition of metallic silver on the walls of the reaction cell was also observed during the study.

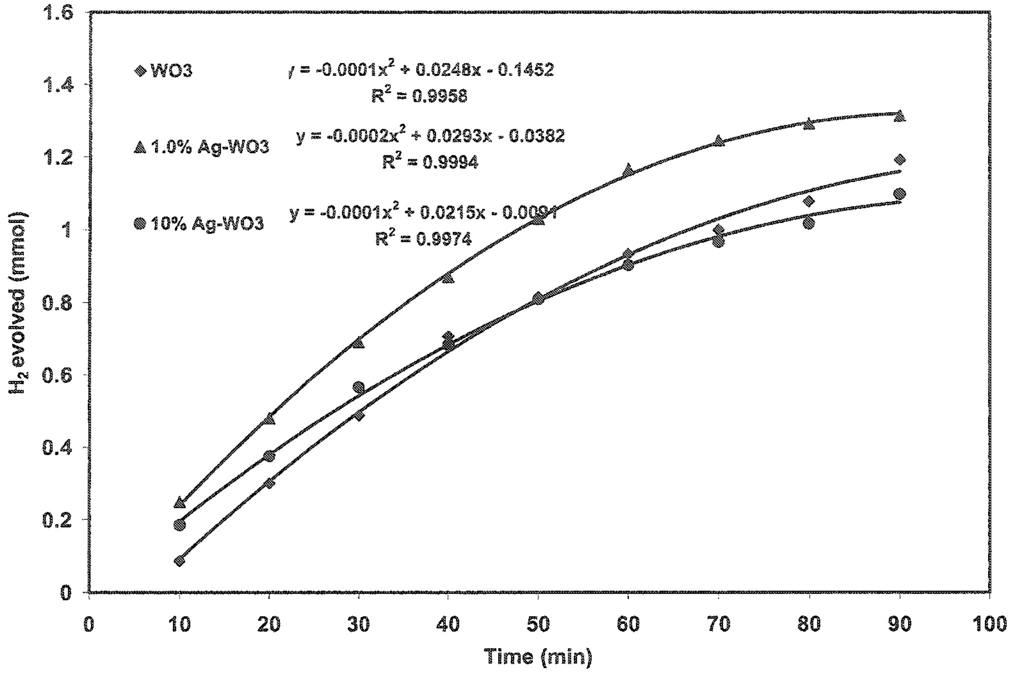

Figure 5.68 Comparison of H_2 yield for various Ag-loadings

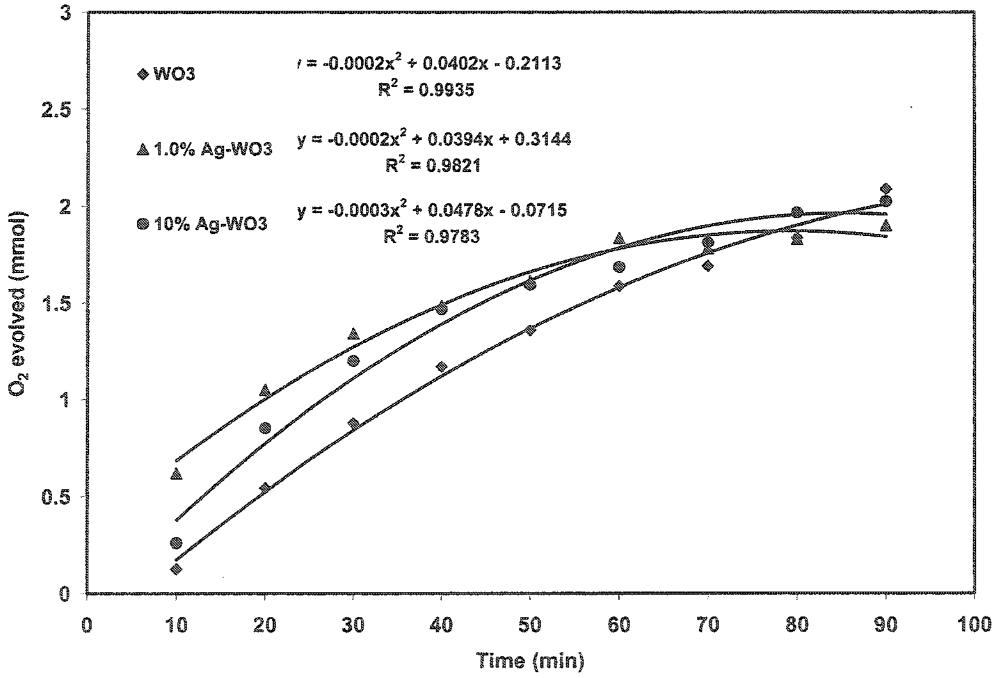

Figure 5.69 Comparison of O_2 yield for various Ag-loadings

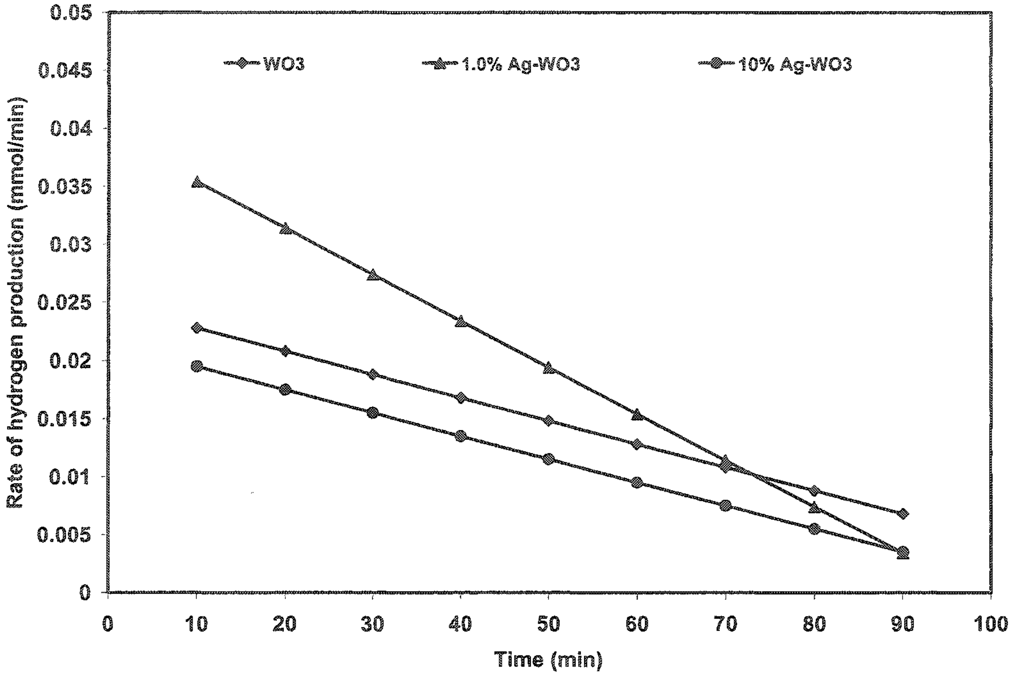

Figure 5.70 Comparison of the rate of H_2 formation for various Ag-loadings

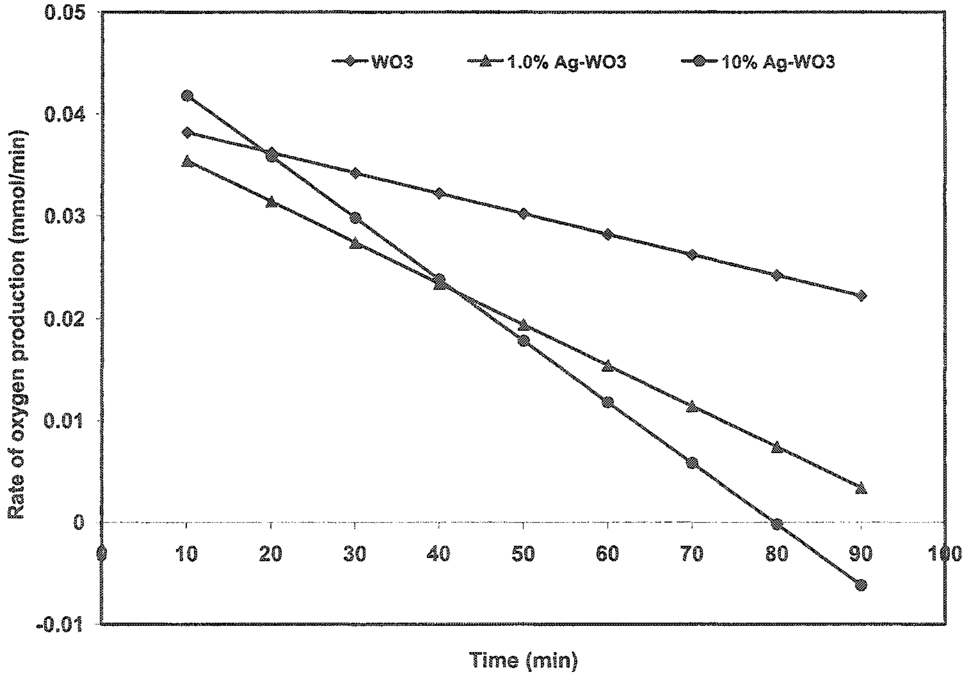

Figure 5.71 Comparison of the rate of O_2 formation for various Ag-loadings

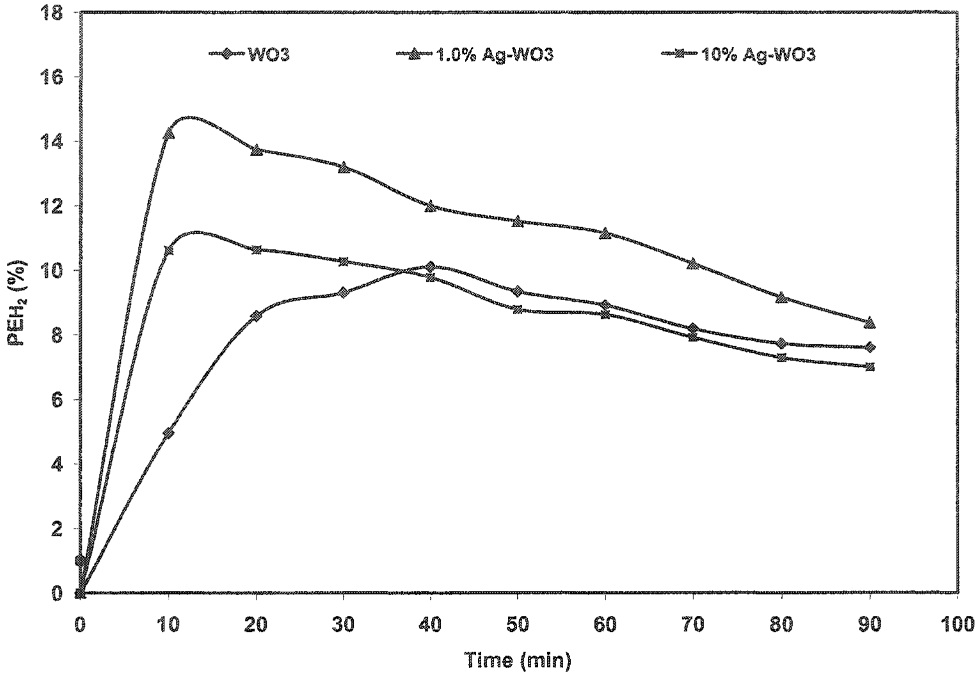

Figure 5.72 Comparison of photonic efficiency for H_2 formation for various Ag-loadings

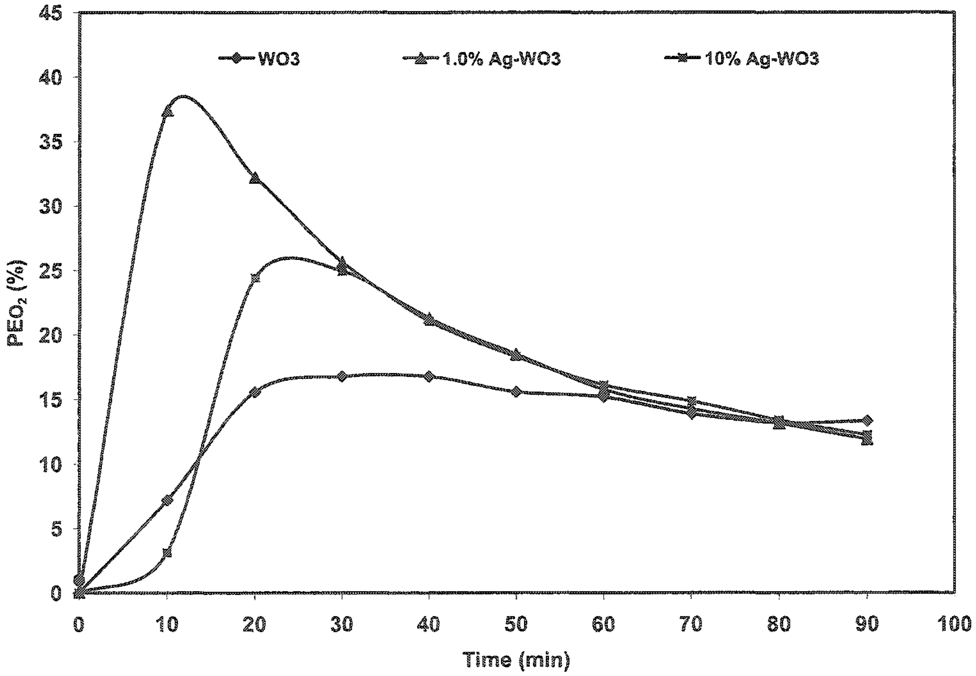

Figure 5.73 Comparison of photonic efficiency for O_2 formation for various Ag-loadings

5.8 Comparison of photocatalytic water splitting over transition metal doped WO_3

A significant change in photocatalytic activity of WO_3 towards hydrogen generation was observed in the presence of transition metals as dopants. The comparison of hydrogen and oxygen yield for 1% and 10% transition metal dopants is given in figures 5.74-5.77 respectively. The excited electrons are trapped in the conduction band of the doped metal oxides formed by the "3d" orbitals of transition metal dopants. Therefore, that is the configuration of "3d" orbitals, which actually predicts the electron capture ability of a dopant. An increase in the hydrogen production was observed for $3d^5$, $3d^7$, and $3d^8$ metals i.e. Fe^{3+}, Co^{2+} and Ni^{2+} respectively. In case of Fe^{3+} ($3d^5$), it was predicted that first it changes to Fe^{2+} ($3d^6$) and than hydrogen production occurs as the conduction band edge of +3 oxidation state (Fe_2O_3) is not suitable for hydrogen production while the +2 oxidation state (FeO) has the required suitability. The $3d^9$ and $4d^9$ metals i.e. Cu^+ and Ag^+ present as Cu_2O and Ag_2O shows the similar behavior with the capture of excited electron giving M^o (nd^{10}) and M^{2+} (nd^8) states at the surface. The +2 states of both Cu and Ag i.e. CuO and AgO capture the photoexcited electrons however in the absence of a suitable conduction band edge, fail to deliver it to photogenerated protons, thus enhancing electron-hole pair recombination. The "$3d^{10}$" configuration Zn^{2+} does not show any ability for capturing the conduction band electrons deactivates the surface and reduces the rate of formation of products.

The observed trends for hydrogen and oxygen yield over 1% and 10% transition metal dopants respectively, are given below.

Hydrogen production for 1% M-WO_3 where M = Fe, Co, Ni, Cu, Zn and Ag

WO_3 < Ag-WO_3 < Zn-WO_3 < Fe-WO_3 < Cu-WO_3 < Co-WO_3 < Ni-WO_3

Hydrogen production for 10% M-WO_3 where M = Fe, Co, Ni, Cu, Zn and Ag

WO_3 = Ag-WO_3 = Zn-WO_3 < Cu-WO_3 < Fe-WO_3 < Co-WO_3 < Ni-WO_3

Oxygen production for 1% M-WO_3 where M = Fe, Co, Ni, Cu, Zn and Ag

Zn-WO_3 < WO_3 < Ag-WO_3 < Cu-WO_3 < Fe-WO_3 < Co-WO_3 < Ni-WO_3

Oxygen production for 10% M-WO_3 where M = Fe, Co, Ni, Cu, Zn and Ag

Zn-WO_3 < WO_3 < Ag-WO_3 < Cu-WO_3 < Fe-WO_3 < Co-WO_3 < Ni-WO_3

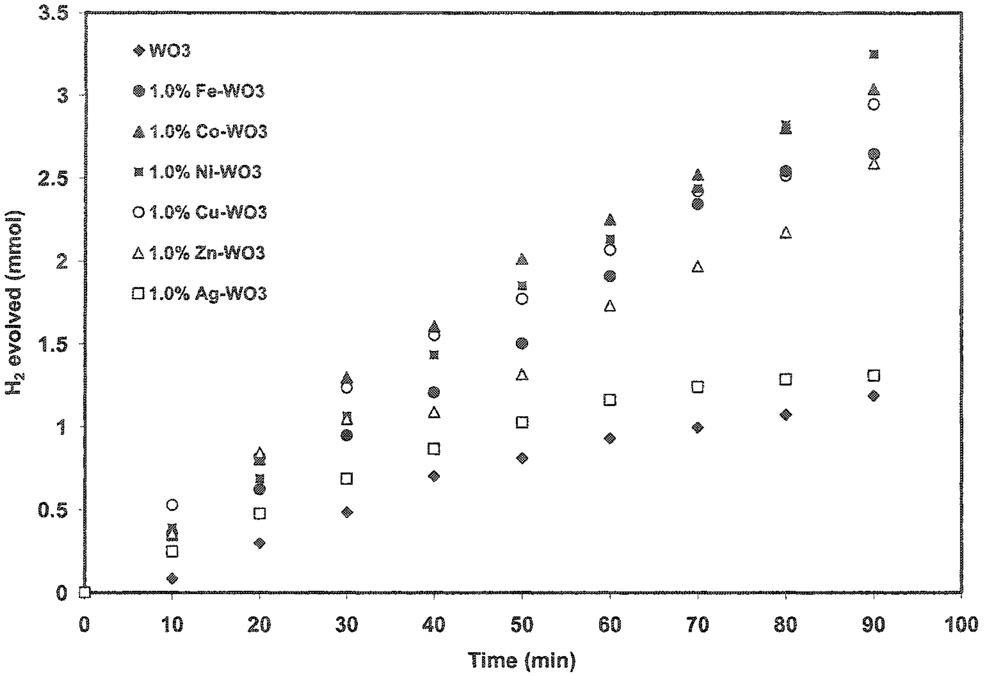

Figure 5.74 comparison of evolved hydrogen over 1% transition metal doped WO_3

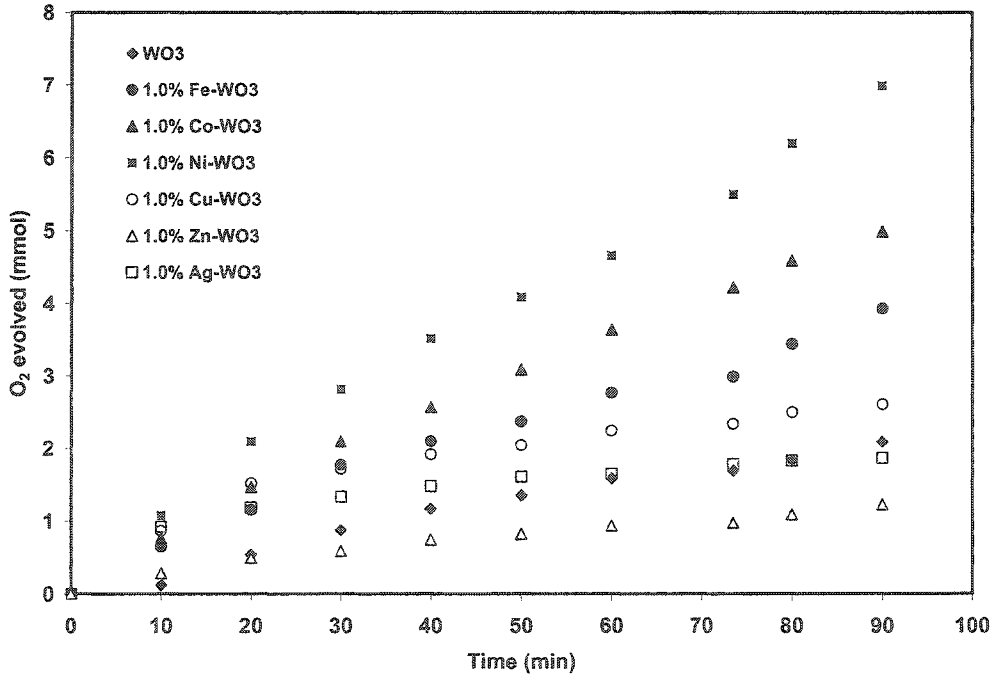

Figure 5.75 comparison of evolved Oxygen over 1% transition metal doped WO_3

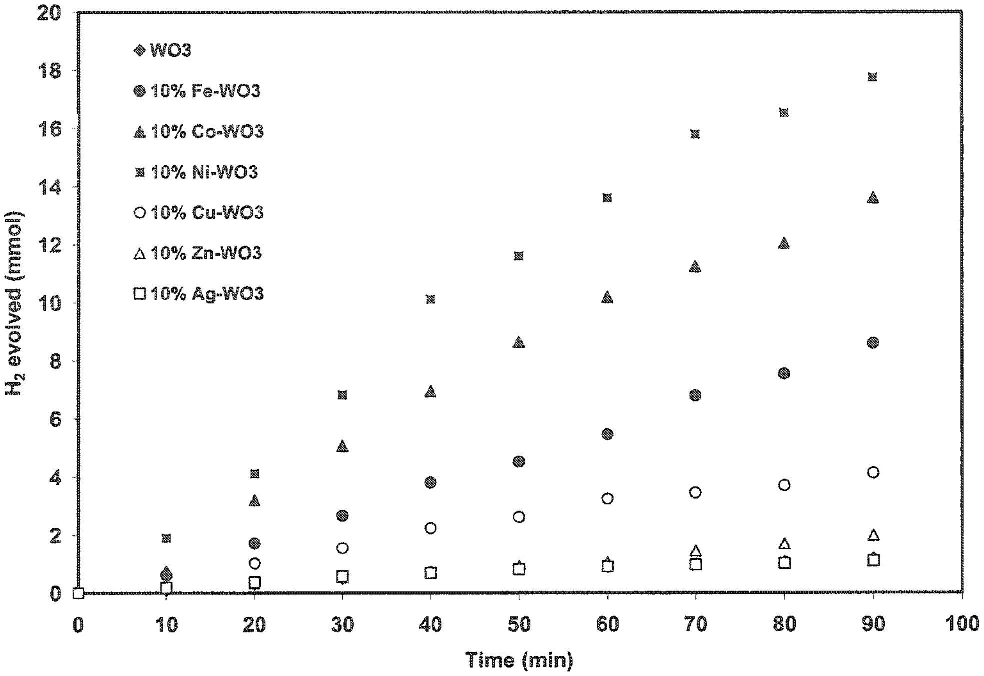

Figure 5.76 comparison of evolved hydrogen over 10% transition metal doped WO_3

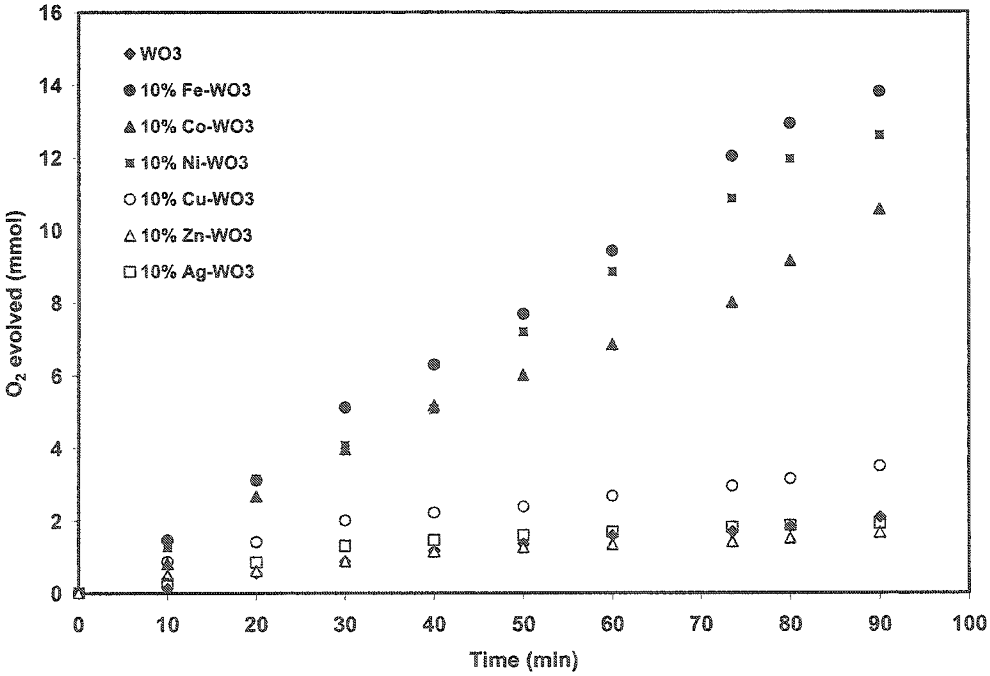

Figure 5.77 comparison of evolved Oxygen over 10% transition metal doped WO_3

CHAPTER SIX

PHOTOCATALYTIC CONVERSION OF METHANE INTO METHANOL

The photocatalytic conversion of methane into methanol over various pure photocatalysts i.e. α-Fe_2O_3, WO_3, TiO_2 & NiO, and transition metal doped WO_3 is discussed in this chapter. The photocatalytic conversion of methane into methanol was studied by suspending the optimized amount of the catalyst in 60 ml of water. The process on each catalyst was studied as batch process. The colloidal suspension was saturated with methane by passing the gas at a high flow rate for a period of 15 minutes then sealing the reactor at atmospheric pressure. The saturated suspension was then illuminated with a 355nm laser light source. The change in the concentration of methanol was monitored by analyzing the samples from the reactor at regular intervals. The mechanism of the conversion process is discussed below.

The absorption of photons initiates the formation of hydroxyl radicals through bandgap excitation. In the presence of methane, the hydroxyl radicals produced as a result of photocatalytic process can undergo one of the following possible processes.

(i) Combine with each other to generate H_2O_2 and finally oxygen

$$OH^{\bullet} + OH^{\bullet} \rightarrow H_2O_2 \rightarrow H_2O + \tfrac{1}{2}O_2 \qquad 6.1$$

(ii) Combine with methane molecules to generate methanol

$$OH^{\bullet} + CH_4 \rightarrow CH_3OH + H^{\bullet} \qquad 6.2$$

(iii) Recombine with hydrogen radical to generate water

$$OH^{\bullet} + H^{\bullet} \rightarrow H_2O \tag{6.3}$$

Based on the reactions mentioned above, it can be inferred that the basic requirement for photocatalytic conversion of methane into methanol is the generation of hydroxyl radicals. The basic requirement for a semiconductor to convert methane into methanol is its ability to oxidize the solvent i.e. water to produce hydroxyl radicals. The higher the rate of production of hydroxyl radicals, the higher will be the conversion of methane into methanol. The detailed proposed pathway of methane conversion into methanol is given below.

$$SC + h\upsilon \rightarrow SC(h_{vb}^{+}, e_{cb}^{-}) \rightarrow \mathrm{Re}combination \tag{6.4}$$

$$H_2O + h_{vb}^{+} \rightarrow H_2O^{+} \rightarrow OH^{\bullet} + H^{+} \tag{6.5}$$

$$HO^{\bullet} + CH_4 \rightarrow CH_3OH + H^{\bullet} \tag{6.6}$$

$$OH^{\bullet} + OH^{\bullet} \rightarrow H_2O_2 \rightarrow H_2O + \tfrac{1}{2}O_2 \tag{6.7}$$

$$OH^{\bullet} + H^{\bullet} \rightarrow H_2O(\mathrm{Re}combination) \tag{6.8}$$

$$H^{+} + e_{cb}^{-} \rightarrow H^{\bullet} \tag{6.9}$$

$$H^{\bullet} + H^{\bullet} \rightarrow H_2 \tag{6.10}$$

The production of hydroxyl radicals can be enhanced using metal ions as electron capture agents.

The above mentioned mechanism shows that along with the formation of methanol additional hydrogen is produced in the methane conversion process. As all the reactions were performed at the room temperature, the methanol that is produced remain in the solution and when its concentration reaches to an appreciable value, it starts competing with water for valence band holes. The transfer of electrons to holes led to the transformation of methanol in other compounds such as formaldehyde which, as shown below, leads to formation of additional hydrogen.

$$CH_3OH + h_{vb}^+ \rightarrow CH_3OH^+ \rightarrow H_2CO + H^\bullet + H^+ \qquad 6.11$$

$$H_2CO + h_{vb}^+ \rightarrow CO + H^\bullet + H^+ \qquad 6.12$$

The oxygen produced by the combination of hydroxyl radicals, competes with the H^+ ions (if the band edges of the semiconductor are suitable for oxygen reduction), for conduction band electrons to produce highly reactive oxidizing species termed as "super oxide radicals" ($O_2^{-\bullet}$). Because of their strong oxidizing nature super oxide radicals oxidize both the methane produced and methane.

$$O_2 + e_{cb}^- \rightarrow O_2^{\bullet -} \qquad 6.13$$

$$CH_3OH + O_2^{\bullet -} \rightarrow CO_2 + H_2O + e^- \qquad 6.14$$

$$CH_4 + 2O_2^{\bullet -} \rightarrow CO_2 + 2H_2O + 2e^- \qquad 6.15$$

Therefore, the factors, which can influence the yield of methanol in the photocatalytic process, are:

(i) The production of hydroxyl radicals

(ii) The degradation of produced methanol by valence band holes

(iii) The formation of super oxide radicals

In the next sections, the photocatalytic conversion of methane in the aqueous solution, studied on different pure catalysts (WO_3, TiO_2, α-Fe_2O_3 and NiO) and on transition metal-doped WO_3 is discussed.

6.1 Photocatalytic conversion of methane over WO_3

The properties of WO_3 and its behavior, under illumination, in the aqueous environment have already been discussed in detail in section 5.2. WO_3 was subjected to the same experimental conditions used for studying water splitting except that methane was used as purge gas instead of argon. The progress of methanol formation was monitored by analyzing liquid samples at regular intervals. The methanol yield and the rate of methanol production as a function of time are plotted in figures 6.1 & 6.2. It can be observed that initially the methanol yield increases rapidly with the time, reaches to a maximum value and starts decreasing afterwards. As the formation and degradation of methanol occur simultaneously the two rates i.e. the rate of formation and rate of degradation, tend to equalize each other. After about 55 minutes, the rate of degradation overcomes the rate of formation. As discussed earlier, in the aqueous environment at room temperature there are two possible pathways for the degradation of methanol i.e. either through oxidation by super oxide radical or by the direct donation of electrons to photogenerated holes. For WO_3, the methanol degradation through super oxide radical is less probable as the conduction band edge of WO_3 is not suitable for the formation of the super oxide radical ($O_2^{\cdot -}$), which requires a potential of -0.28V [131]. The other mechanism is through the donation of electrons to the photogenerated holes in competition with that of adsorbed water to give formaldehyde or any other oxygen containing intermediate and additional hydrogen precursors i.e. hydrogen radicals, as given in equation 6.11. The high yield of hydrogen in the presence of methane, as presented in figure 6.3, predicts that the formaldehyde produced by the methanol produces additional amount of hydrogen. Additionally, the trapping of a photogenerated hole, by either methanol or any other oxygen containing intermediate, enhances the lifetime of photogenerated electrons, which in turns enhances the production of hydrogen through electron transfer at defect sites.

Along with the formation of additional amounts of hydrogen, these free radicals can initiate a number of reactions leading to a variety of other products such as acetone, acetic acid, acetaldehyde, dimethyl ether etc. Some of these products were identified during the analysis of samples but their concentrations were too low to be identified. All these free radical reactions contribute to additional hydrogen yield.

In this study, two metal ions i.e. Fe^{3+} and Ag^{+} were used as electron capture agents and their effect on methanol was studied as a function of time. Both Fe^{3+} and Ag^{+}, with suitable redox potentials for conduction band electron capture, qualify as electron capture agents. In the presence of both ions, an increase in methanol yield was observed which is presented in figure 6.4. For Fe^{3+}, methanol yield increase sharply in the beginning and then reaches a steady state. The stable value of methanol yield indicates the establishment of a steady state between the rate of production and rate of degradation. Fe^{3+} ions enhances the rate of production by capturing conduction band electrons to give

Fe^{2+} which competes with both methanol and water molecules for valence band holes to give Fe^{3+}. This regenerative behavior enhances the yield of methanol, reduces the extent of methanol degradation, and leads to a stable methanol yield. For Ag^+ an initial increase and then a gradual decrease in methanol yield compared to that of WO_3 indicates the depletion of Ag^+ ions in the system. The deposition of Ag^+ ions as Ag^o at the surface of the catalyst after capturing conduction band electrons can be considered as the most probable cause.

The photonic efficiency of a photocatalytic process is actually a measure of its ability to produce the desired product compared to the incident photons. In this study the photonic efficiencies of methanol conversion, in the presence of electron capture agents, were calculated with respect to the methanol yield only. The photonic efficiencies of less than 10% were observed for all the systems and plotted in figure 6.5. The basic reasons for the low photonic efficiencies are:

- Simultaneous production and degradation of methanol
- Low solubility of methane in water

Another parameter, which measures the efficiency of any catalytic system, is the estimation of percentage conversion of reactant into desired product. In this study the percentage conversion of methane into methanol was evaluated on the basis of maximum solubility of methane in water at 25°C (24 ppm/100 ml). An overall percentage conversion of ~21% for pure WO_3 and ~ 27% for Fe^{3+} was observed. While a maximum conversion of 23% was observed for Ag^+.

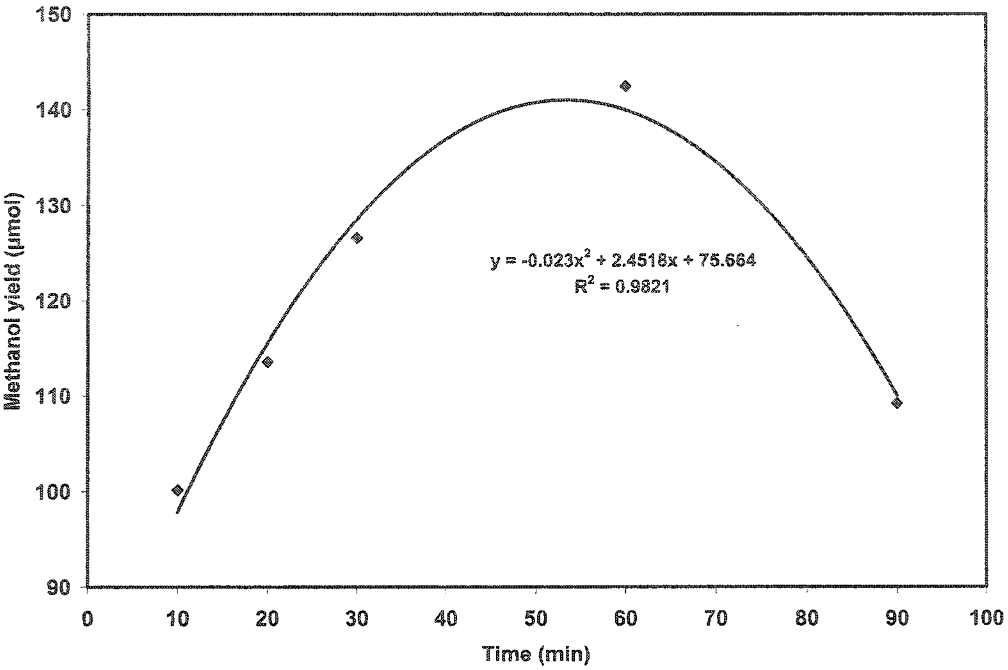

Figure 6.1 Methanol yield as a function of time over WO_3

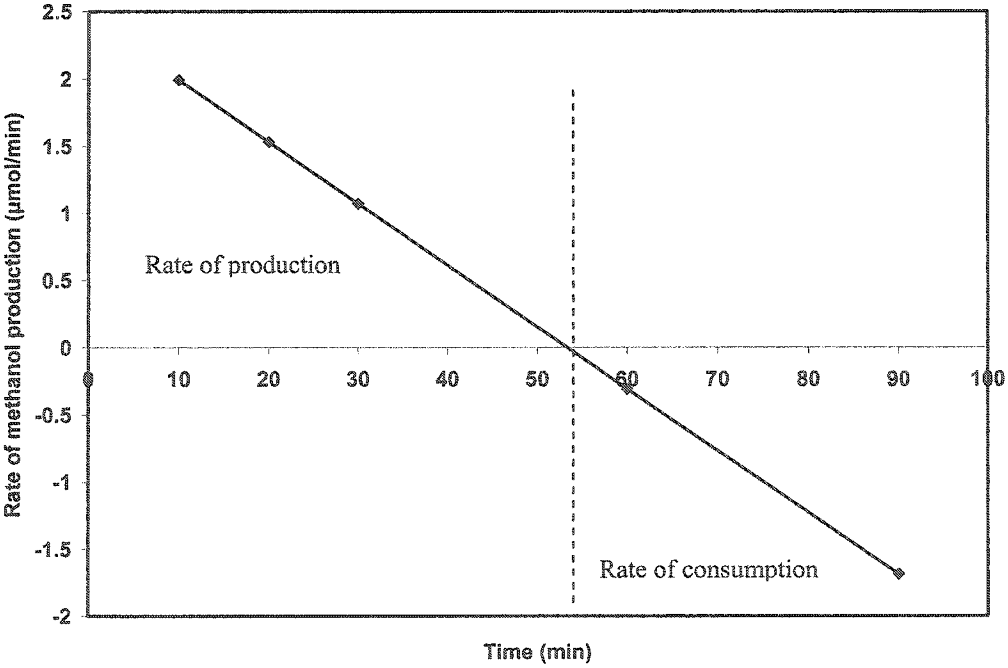

Figure 6.2 Change in the rate of methanol production with time over WO_3

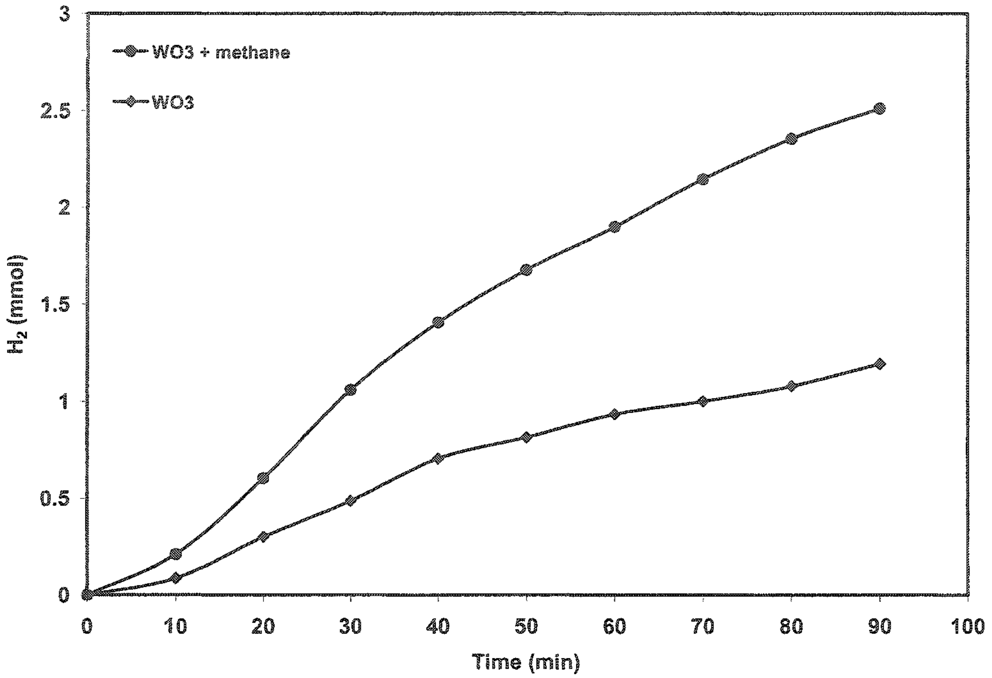

Figure 6.3 Hydrogen production in the presence and absence of methane over WO_3

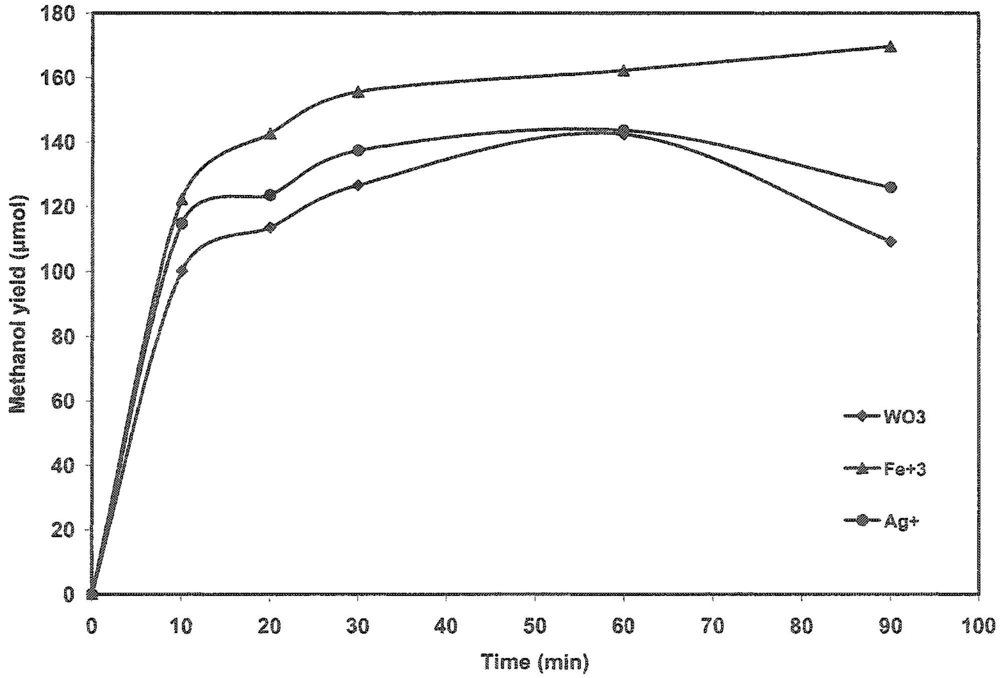

Figure 6.4 Effect of electron capture agents on methanol yield over WO_3

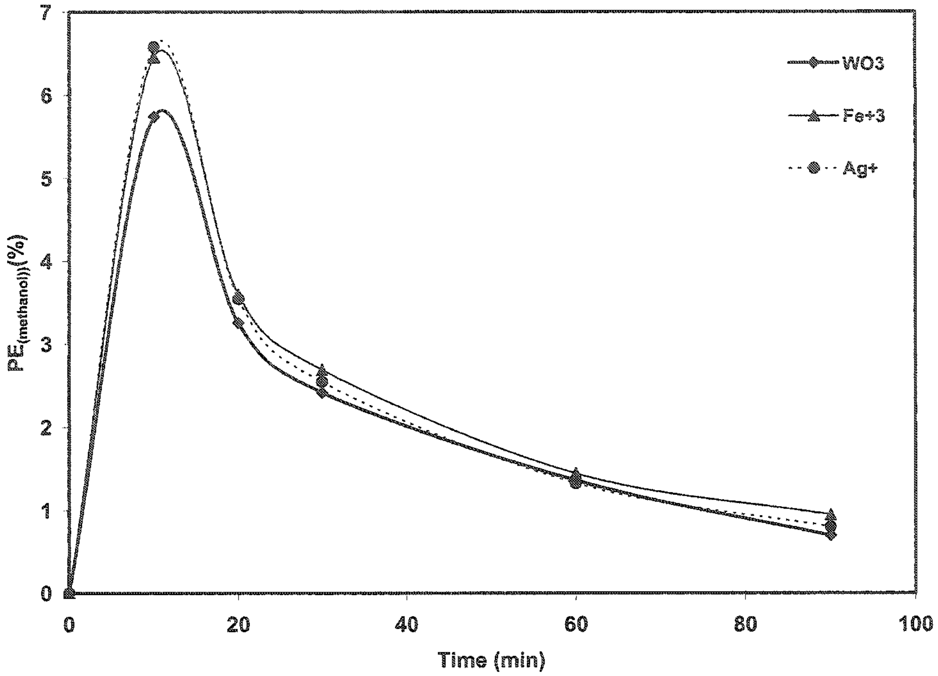

Figure 6.5 Photonic efficiency of methanol production in the presence of electron capture agents over WO_3

6.2 Photocatalytic conversion of methane over TiO_2

The behavior of TiO_2, in aqueous suspensions under illumination, is already discussed in detail in section 5.3. In this section, the activity of TiO_2 towards methane conversion will be discussed. The methanol yield measured at different times is presented in figure 6.6 where an increase in the yield can be noticed with time. As discussed in section 5.3, the absorption of UV photons introduces defect sites by removing the lattice hydrogen and the activity of the catalyst increases with the increase in the number of defect sites over time. These defect sites serve as electron transfer and trap sites and enhance the generation of hydroxyl radicals through water oxidation. The same behavior was observed for methanol which shows an increase in yield with the increase of defect sites over time. The rate of methanol formation as a function of time is presented in figure 6.7 where a slight decrease in the rate of methanol formation can be observed. This behavior indicates that the formation of methanol occurs at a higher rate compared to degradation. The degradation process does not override methanol formation thus the net methanol formation remains almost constant.

As mentioned earlier that in an aqueous photocatalytic system methanol can degrade either by the donation of electrons to photogenerated holes or by reacting with super oxide radicals if the conduction band edge of the semiconductor is suitable for oxygen reduction (+0.03 V) in the aqueous medium. If the conduction band edge is suitable for oxygen reduction, the probability of methanol degradation by super oxide oxidation increases.

As the conduction band edge of TiO_2 is suitable for the formation of super oxide radical so it is expected that the extent of methanol degradation through super oxide radicals will be higher compared to valence band hole donation process. The contribution of each mode in the degradation of produced methanol was evaluated by measuring the yield of hydrogen in the presence of methane and without methane. A comparison of hydrogen yield is presented in figure 6.8. The initial increase in hydrogen yield in the presence and absence of methane suggests that a fraction of produced methanol degrades through valence band hole mode as most of the excited electrons are consumed in the reduction of the catalyst and do not remain accessible to the oxygen produced in the system. With the passage of time, the reduction of the catalyst as well as the concentration of oxygen increases in the system and the mode of degradation of the produced methanol switches to super oxide oxidation causing a decrease in hydrogen yield.

The effect of dissolved metal ions on methane conversion was studied by performing the reaction in the presence of Fe^{+3} and Ag^{+} ions. Based on the redox potentials, these ions have the capability to scavenge the conduction band electrons to enhance the rate of methane conversion through an increased rate of water oxidation. The scavenging ability of these ions also helps in reducing the production of super oxide radicals. A comparison of the yield of methanol in the presence of Fe^{3+} and Ag^{+} with that of a pure system is presented in figure 6.9. The positive effect of both ions on the methanol yield suggests that these ions enhance the yield by suppressing the unwanted formation of super oxide radicals through conduction band electron transfer which in turns increases the production of more hydroxyl radicals. The sustained increase in the presence of Fe^{3+} predicts the regenerative behavior of these ions while for Ag^{+} a sharp increase followed by rapid decrease indicates the deposition of these ions as Ag^{o} on the catalyst. In addition, the deactivation of the catalyst by the deposition of Ag_2O in the presence of oxygen and conduction band electrons cannot be neglected.

A comparison of photonic efficiencies, for methane conversion, calculated in the presence of metal ions with that for pure TiO_2, as a function of time is given in figure 6.10. A low photonic efficiency of less than 4.5% was observed for all the systems. The low photonic efficiency is mainly due to the suitable band edges for super oxide radical formation that act as sink for produced methanol molecules. The increase in the photonic efficiency in the presence of Fe^{3+} and Ag^{+} ions reveals that both ions enhance the yield of methanol by suppressing the formation of super oxide radicals.

A gradual increase in percentage of methane conversion for pure TiO_2 percentage conversion of methane to methanol was observed. The same trend was observed for Fe^{3+} ions while for Ag^{+} ions, an initial increase followed by a gradual decrease in percentage conversion owing to the deposition of Ag^{o} and Ag_2O at the surface of the catalyst, as discussed earlier, was observed. An overall conversion of less than 25% was observed for all the systems.

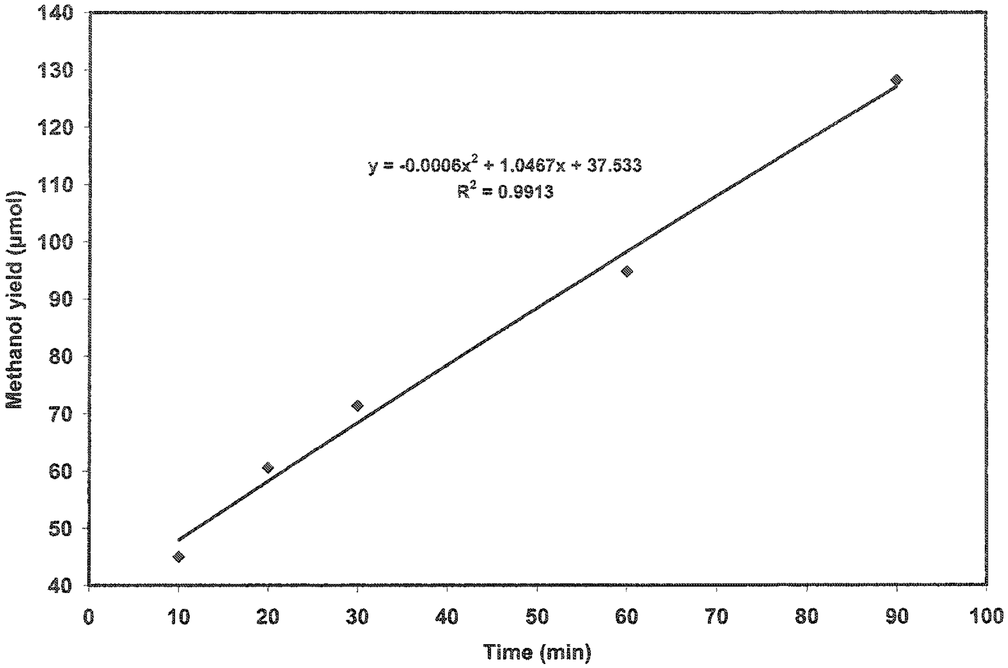

Figure 6.6 Methanol yield as a function of time over TiO_2

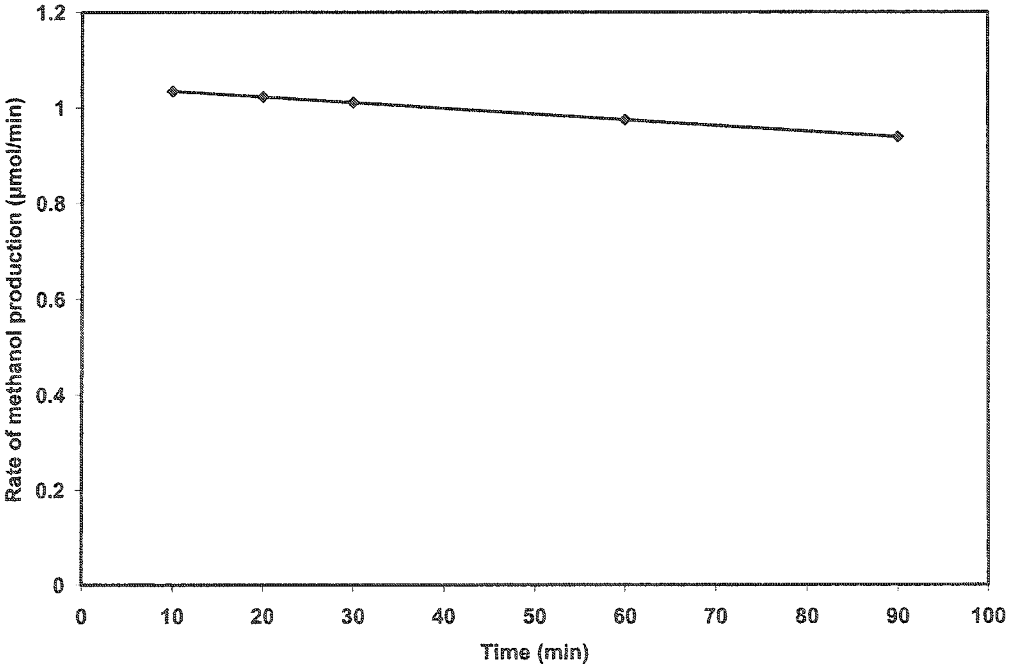

Figure 6.7 Change in the rate of methanol production with time over TiO_2

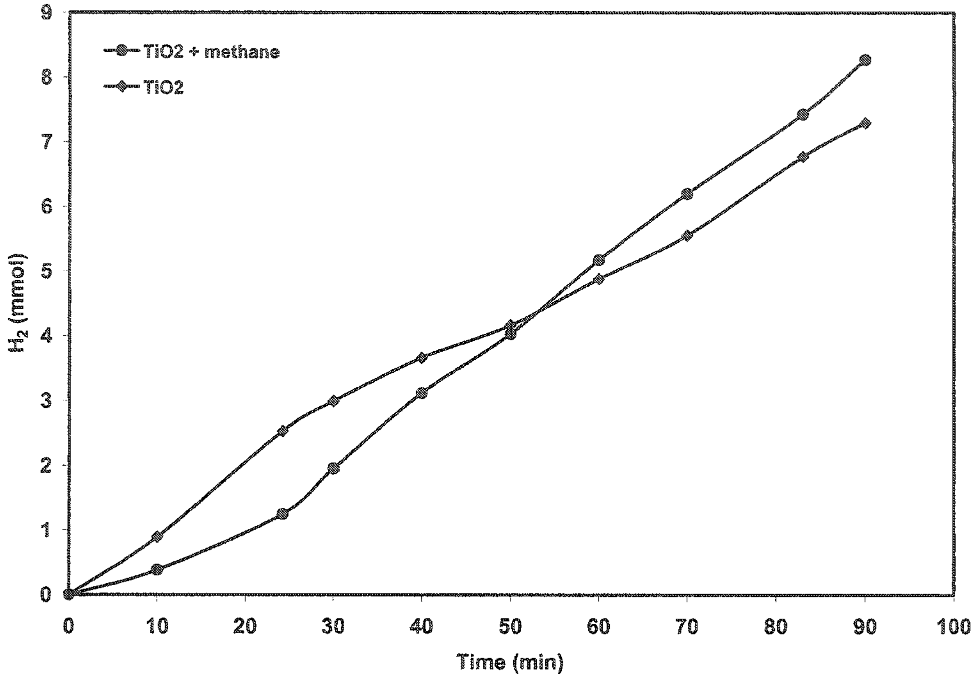

Figure 6.8 Hydrogen production in the presence and absence of methane over TiO_2

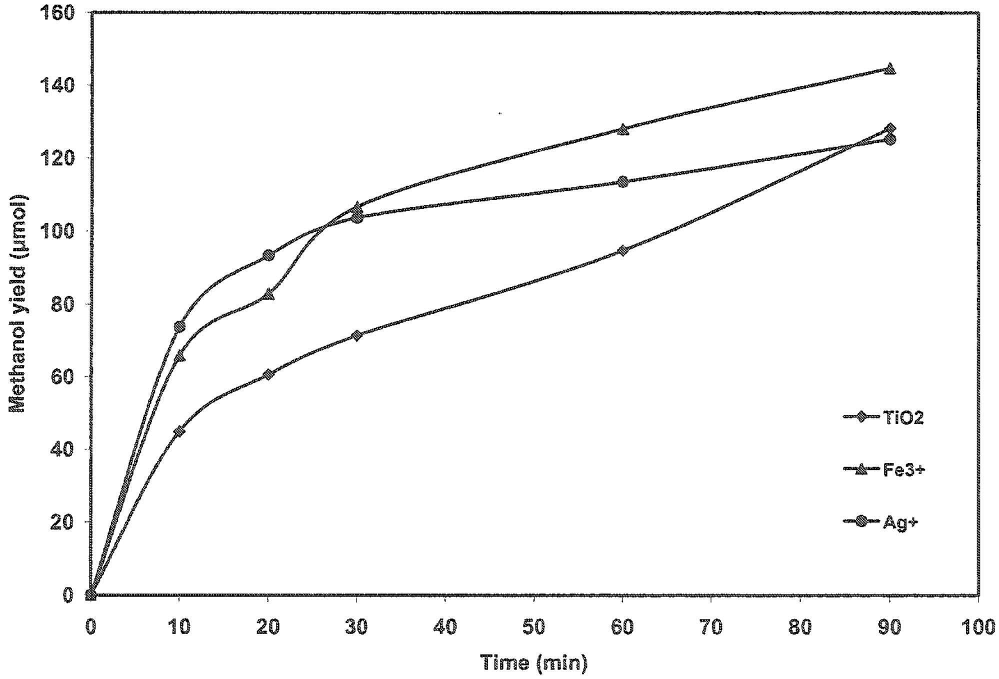

Figure 6.9 Effect of electron capture agents on methanol yield over TiO_2

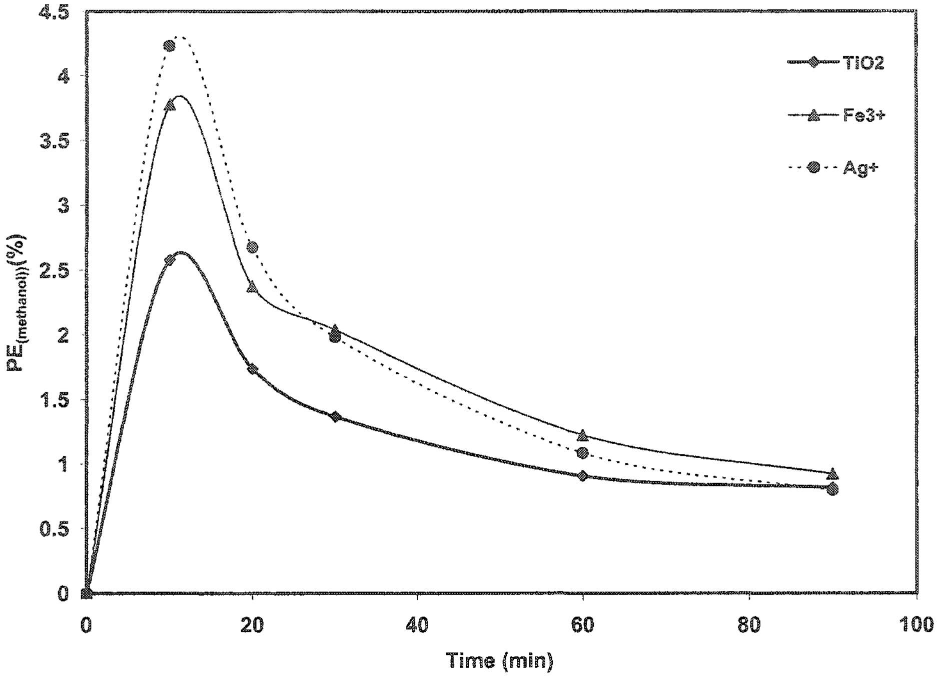

Figure 6.10 Photonic efficiency for methanol production in the presence of electron capture agents over TiO_2

6.3 Photocatalytic conversion of methane over NiO

In this section, the activity of NiO towards methane conversion to methanol based on its activity in aqueous suspension under illumination is discussed. The activity of NiO towards water splitting is already discussed in section 5.4. The methanol yield as a function of time is plotted in figure 6.11 where an initial increase than a decrease in the amount of methanol produced over time is observed. A decrease was observed in the rate of methanol formation as presented in figure 6.12. Although the conduction band edge of NiO is highly suitable for oxygen reduction, the initial increase in the yield of methanol production predicts that initially the majority of photogenerated electrons are consumed in the reduction of the catalyst after being trapped at the defect sites and only a small fraction of these electrons cause the reduction of photo-produced oxygen as explained in the section 5.4. Once the catalyst is fully reduced, the rate of oxygen reduction increases rapidly causing a sharp decrease in the yield and rate of methanol production. It is clear from the figure 6.14 that after 30 minutes the rate of degradation of methanol becomes much higher than its rate of production resulting in a net rate of consumption. The comparison of evolved hydrogen in the presence of methane, with that over pure NiO in argon environment is plotted and presented in figure 6.13. It can be inferred from the study that the basic mode of methanol degradation is through a super oxide radical oxidation. The rate of methanol degradation is high compared with the rate of conversion. Super oxide radicals simultaneously oxidize the methanol, which is produced through methane conversion.

Because the redox potentials of Fe^{3+} and Ag^{+} match with the conduction band edge of NiO and qualify as electron capture agents, a slight or even no decrease in the methanol yield was observed in the presence of these ions as presented in figure 6.14. This slight decrease may be due the deactivation of NiO with the deposition of some $Fe(OH)_3$ and AgOH at the surface of the catalyst. The sharp change in pH i.e. from 5.5 to 11.0 in a short span of time also supports the formation of metal hydroxides. In the presence of very high concentration of hydroxyl ions, the metal ions fail to act as electron scavengers.

A decrease in the photonic efficiency in the presence of metal ions compared to that of pure NiO was observed. A photonic efficiency of less than 6% was observed for all the systems. The main reason for this low photonic efficiency is the enhanced formation of super oxide radicals, which act as poison for photo produced methanol, over pure NiO and the possible deactivation of the catalyst in the presence of metal ions. The calculated photonic efficiencies for NiO in presence and absence of electron capture agents are plotted as a function of time are presented in figure 6.15.

The percentage conversions were calculated on the basis of the maximum solubility of methane. A decrease in percentage conversion in the presence of metal ions was noticed indicating a high rate of degradation compared to formation of methanol from methane. The factors, which lead to this observation, are already discussed. An overall percentage conversion of less than 17% was observed for all the systems.

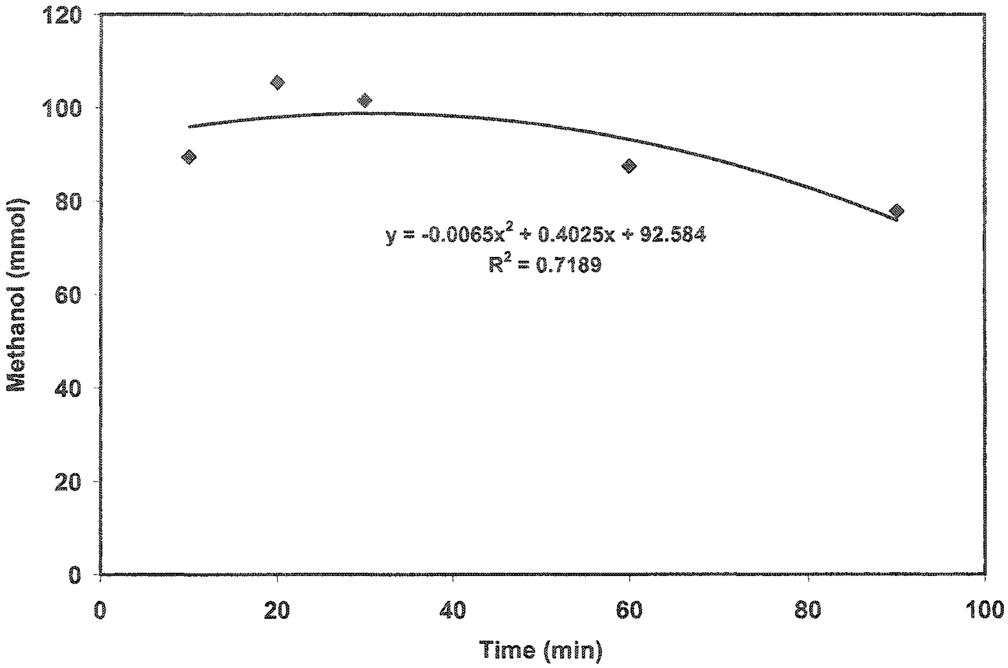

Figure 6.11 Methanol yield as a function of time over NiO

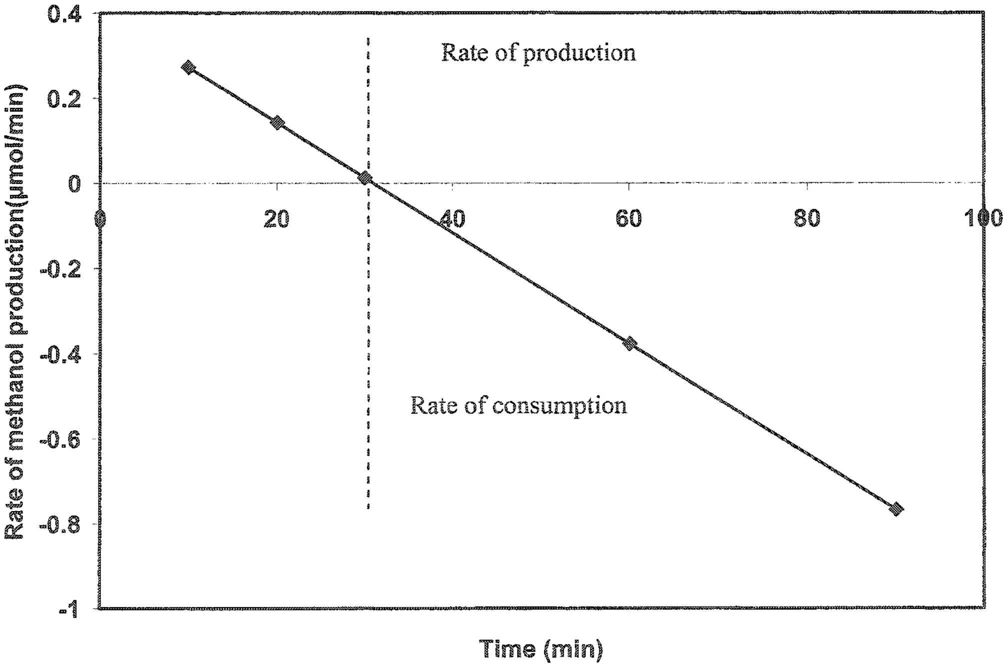

Figure 6.12 Change in the rate of methanol production with time over NiO

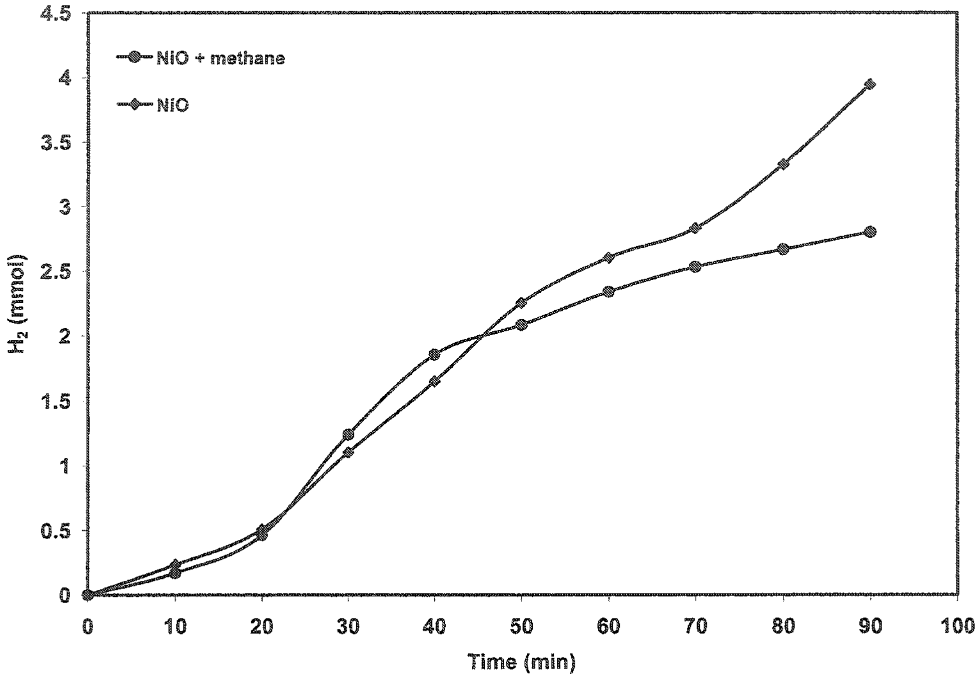

Figure 6.13 Hydrogen production in the presence and absence of methane over NiO

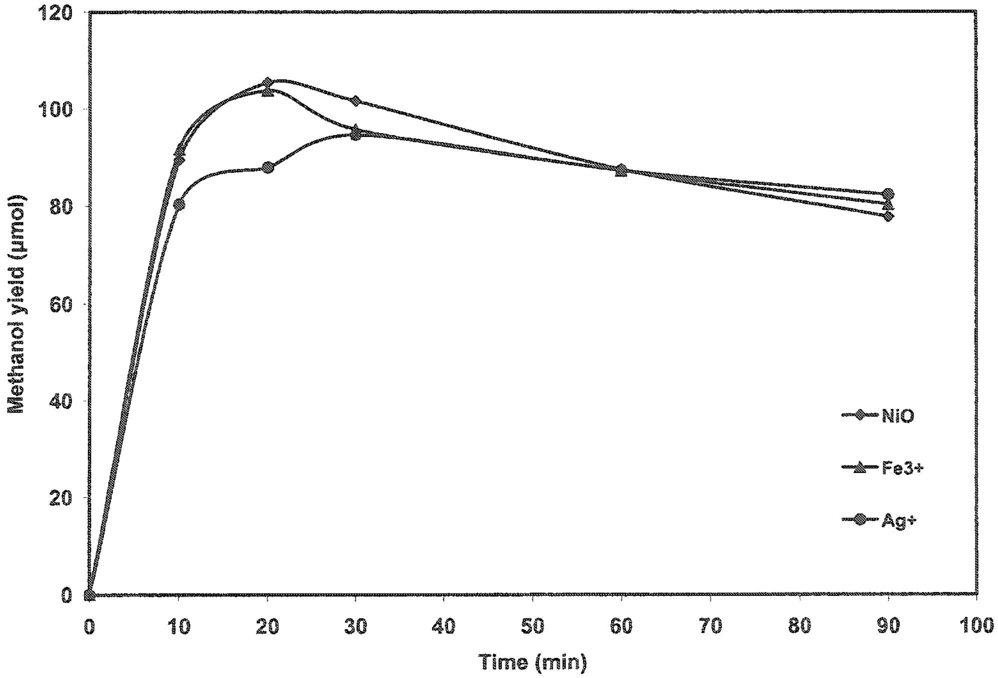

Figure 6.14 Effect of electron capture agents on methanol yield over NiO

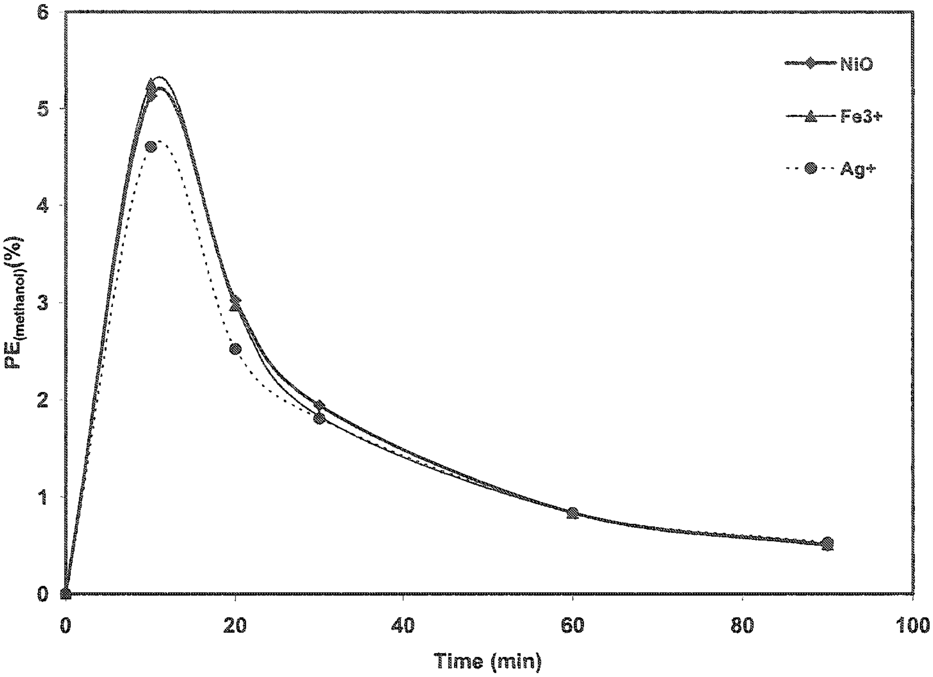

Figure 6.15 Photonic efficiency for methanol production in the presence of electron capture agents over NiO

6.4 Photocatalytic conversion of methane over α-Fe_2O_3

The photocatalytic conversion of methane into methanol was studied by illuminating the methane saturated aqueous suspension of α-Fe_2O_3 with 355 nm laser photons. The change in the yield of methanol produced because of photocatalytic process is plotted in figure 6.16. It shows a gradual decrease in the amount of methanol produced over time, after the first measurement at 10 minutes. Beyond this time the rate of methanol production, as presented in figure 6.17, decreases sharply with the passage of time. This indicates that the rate of methanol degradation overrides its formation as the time passes. The above-mentioned observations about the methanol yield and the rate of methanol formation suggest the transformation of α-Fe_2O_3 to a form suitable for the generation of super oxide radicals in the system. The structural changes in α-Fe_2O_3 under illumination in aqueous solution have already been discussed in section 5.5 where the formation of FeO surface states was discussed. The sharp decrease in the rate of methanol formation with time also supports the formation of FeO surface states, as the conduction band edge of α-Fe_2O_3 is not suitable for super oxide generation. To establish the mechanism of methanol formation and degradation, the hydrogen changes in the presence and absence of methane, are plotted in figure 6.18. It was noticed that both the mechanisms i.e. degradation through hole donation or through super-oxide radicals, contribute to the methanol degradation to varying degrees. Initially the mechanism via valence band hole dominates the degradation process while with the establishment of FeO surface states the contribution of the super oxide mechanism increases. This is again an evidence for surface structural changes with time.

An increase in the methanol yield, as expected, was observed in the presence of Fe^{3+} and Ag^{+} which establishes the role of these metal ions as electron capture agents. The change in methanol production in the presence of metal ions is plotted in figure 6.19. The methanol yield in the presence of Fe^{3+} initially increases and reaches to a stable value afterwards which indicates a steady state in the rate of formation and degradation of methanol and a non-depleting behavior with respect to Fe^{3+} ions. For Ag^{+} ions, the methanol yield increases sharply and decreases afterwards reflecting the consumption of these ions with time.

An overall photonic efficiency of less than 7% was observed for all cases as presented in figure 6.20. An increase in photonic efficiency was noticed for Fe^{3+} and Ag^{+} ions. An increase of 2% was observed for Ag^{+} ions for a short span of time. The reasons for the increase and than decrease in the photonic efficiency are the same as discussed earlier.

An overall percentage of methane conversion of ~ 13% was observed for pure α-Fe_2O_3. A stable increase of ~ 7% in methane conversion was observed in the presence of Fe^{3+} ions while for Ag^{+} ions this increase was only ~ 4% indicating the regeneration of Fe^{3+} ions and depletion of Ag^{+} ions with time. The increase in percentage yield is mainly due to the increased production of hydroxyl ions in the presence of Fe^{3+} and Ag^{+} ions.

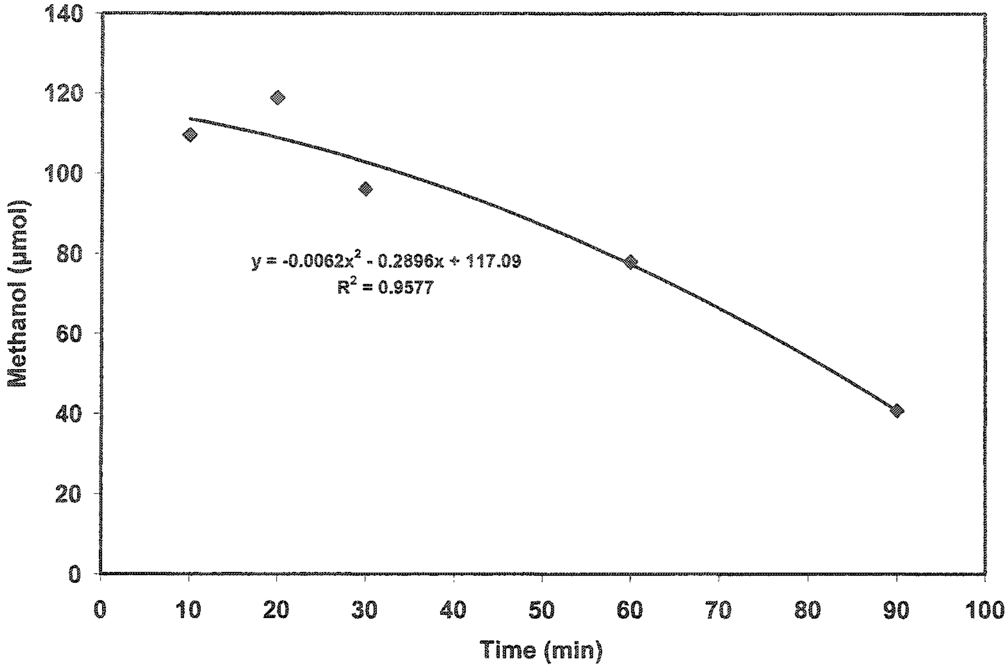

Figure 6.16 Methanol yield as a function of time over α-Fe_2O_3

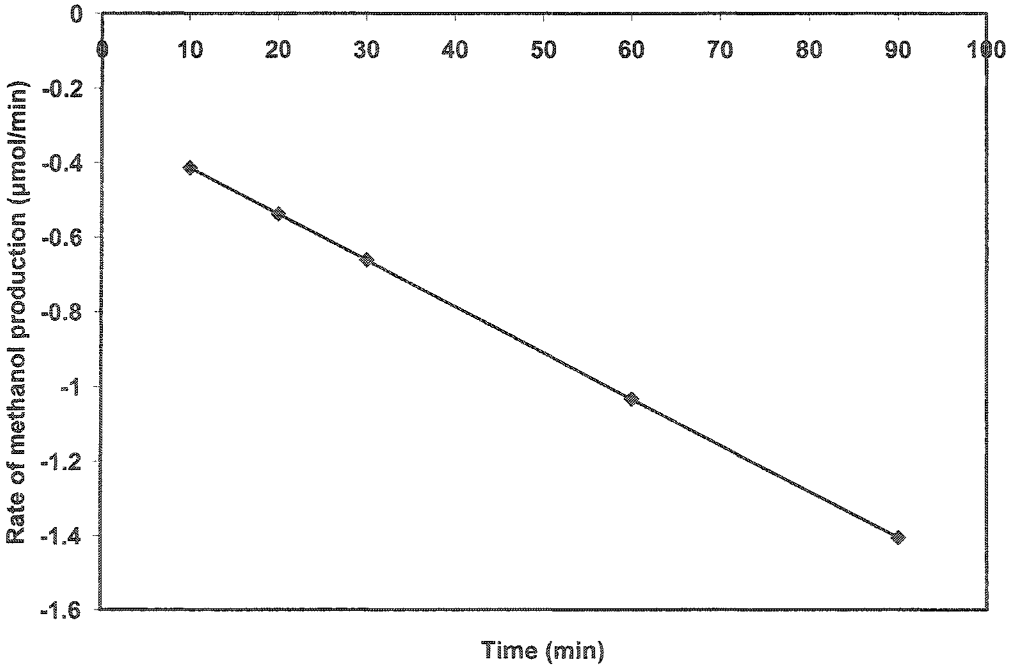

Figure 6.17 Change in the rate of methanol production with time over α-Fe_2O_3

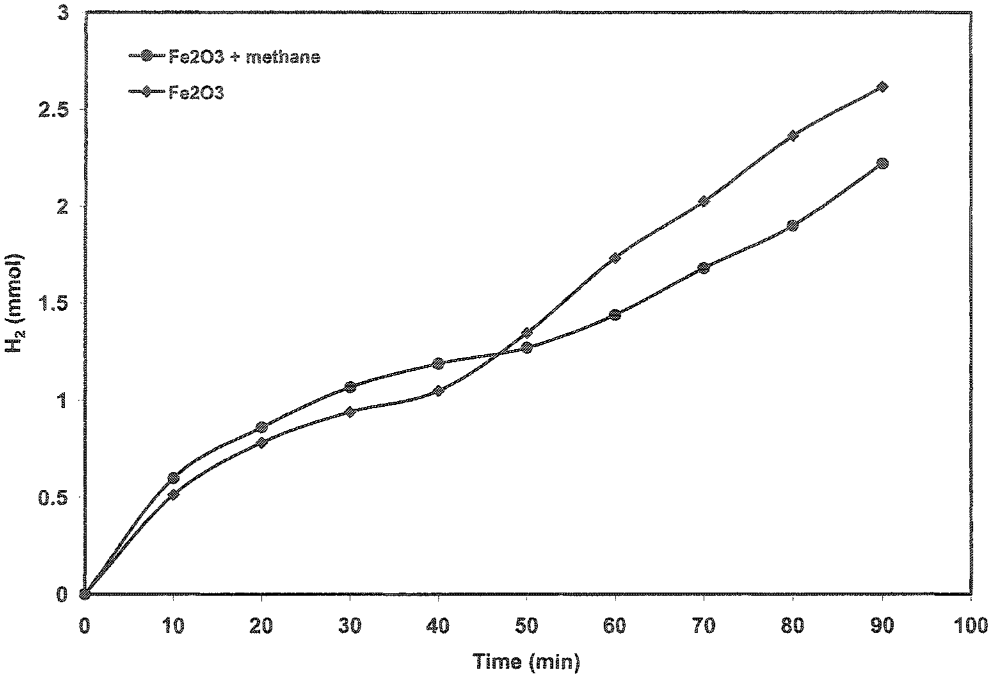

Figure 6.18 Hydrogen production in the presence and absence of methane over α-Fe_2O_3

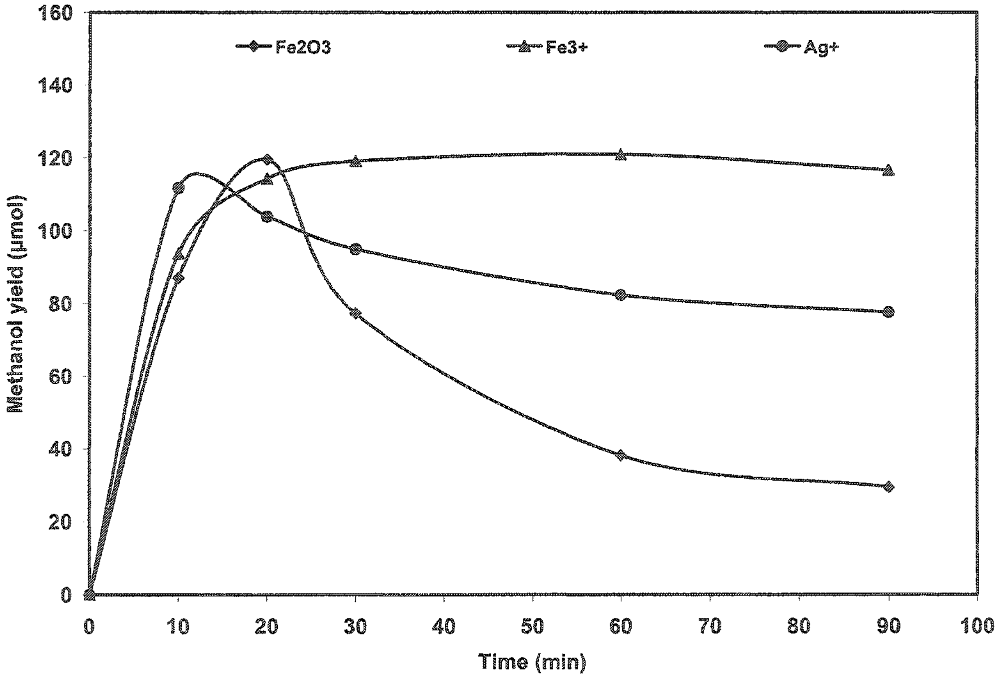

Figure 6.19 Effect of electron capture agents on methanol yield over α-Fe_2O_3

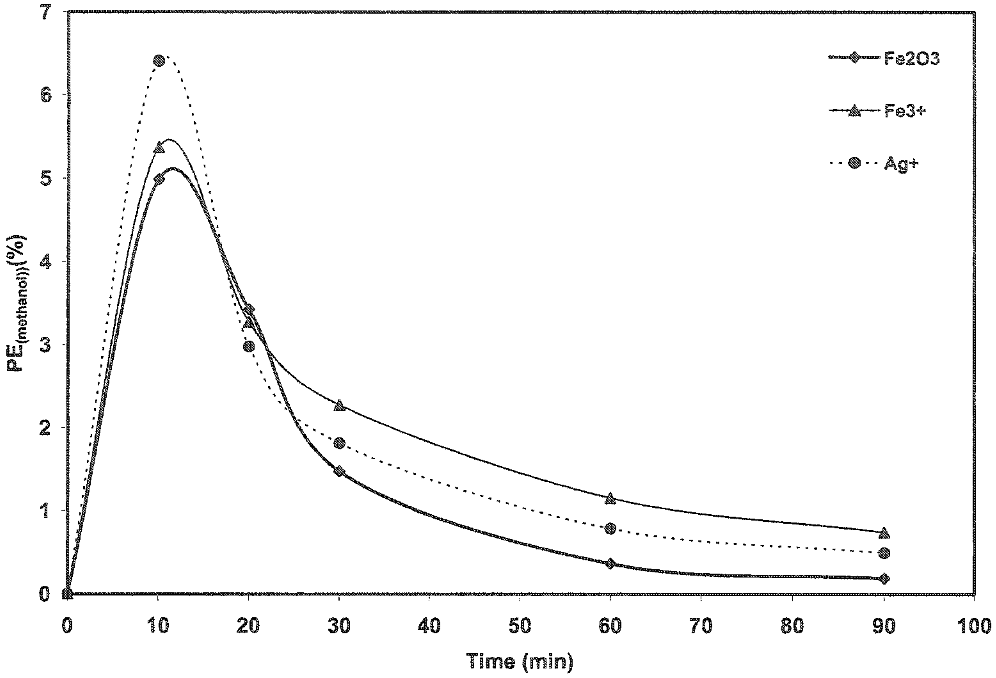

Figure 6.20 Photonic efficiency for methanol production in the presence of electron capture agents over α-Fe_2O_3

6.5 Comparison of methanol production over WO_3, TiO_2, NiO and α-Fe_2O_3

The comparison of methanol yield over WO_3, TiO_2, NiO and α-Fe_2O_3 is presented in figure 6.21. All the catalysts behaved in different fashions and no systematic trend was noticed for methanol production. A maximum methanol yield (followed by a slight) decrease was obtained for WO_3 while for TiO_2 an increasing trend was observed. A sharp increase for α-Fe_2O_3 and NiO was followed by a gradual decrease and a sharp decrease respectively. From the discussion of the results in the previous sections, it can be inferred that all the catalysts are capable of producing hydroxyl radicals at varying rates through water oxidation. These hydroxyl radicals serve as precursor for methane conversion into methanol. The main factor which controls the yield of methanol is the degradation of methanol after its formation. On the basis of the degrading nature of each catalyst, it can be generalized that for the catalyst whose conduction band edge is not suitable for the reduction of oxygen or for the formation of super oxide radical, such as WO_3, methanol degradation occurs through electron donation to valence band holes in competition with water. For the catalyst that has the suitable conduction band edges, such as TiO_2 and NiO, for oxygen reduction the methanol degradation occurs by either electron donation to valence band hole or through super oxide oxidation or both. The degradation of methanol via valence band hole leads to the additional formation of hydrogen while oxidation through super oxide radicals decreases the production of hydrogen through conduction band electron capture and complete mineralization of methanol. Based on hydrogen measurements, it was observed that for WO_3 the dominating methanol degradation mechanism is through valence band hole while for TiO_2 and NiO the dominating mechanism is via a super oxide mechanism. For α-Fe_2O_3

initially the valence band hole mechanism dominates but with the formation of FeO states the mechanism switches to super oxide oxidation.

The comparison of photonic efficiency for all the catalysts is presented in figure 6.22. The photonic efficiency of methane conversion for all the catalysts was less than 10%. The maximum photonic efficiency of 5.8% and a minimum of 2.5% were observed for WO_3 and TiO_2 respectively. The low photonic efficiency of methane conversion indicates the suitability of TiO_2 for degradation rather than synthesis purposes. Approximately the same pattern of photonic efficiency was observed for NiO and α-Fe_2O_3. Here it can be inferred that the photocatalyst (either n-type or p-type) which has the suitable conduction band edge for super oxide radical formation cannot be used efficiently for synthesis purposes unless a suitable electron capture agent is used. The efficiency of a photocatalyst towards photocatalytic synthesis, with unsuitable conduction band edge for super oxide formation, can be enhanced by using a suitable electron capture agent.

The overall percentage conversions of 22%, 15%, 17% and 13% were observed for WO_3, TiO_2, NiO and α-Fe_2O_3 respectively. The basic reason for such low conversions is the same as discussed in the previous sections i.e. the simultaneous formation and degradation of methanol. The low solubility of methane also contributes to low conversion.

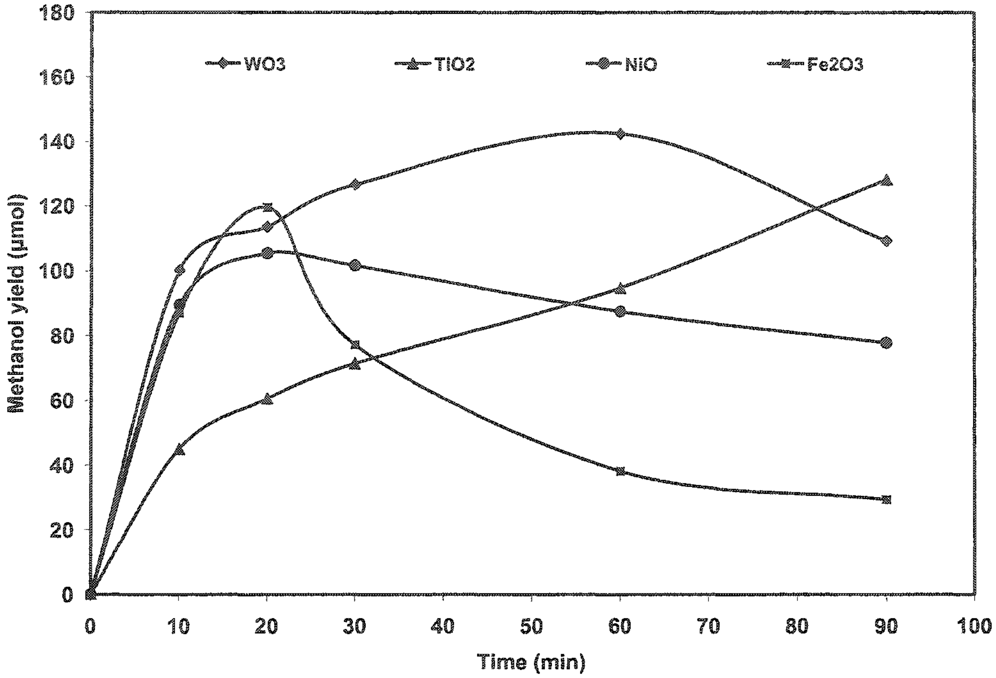

Figure 6.21 Comparison of methanol yield as a function of time over WO_3, TiO_2, NiO and α-Fe_2O_3

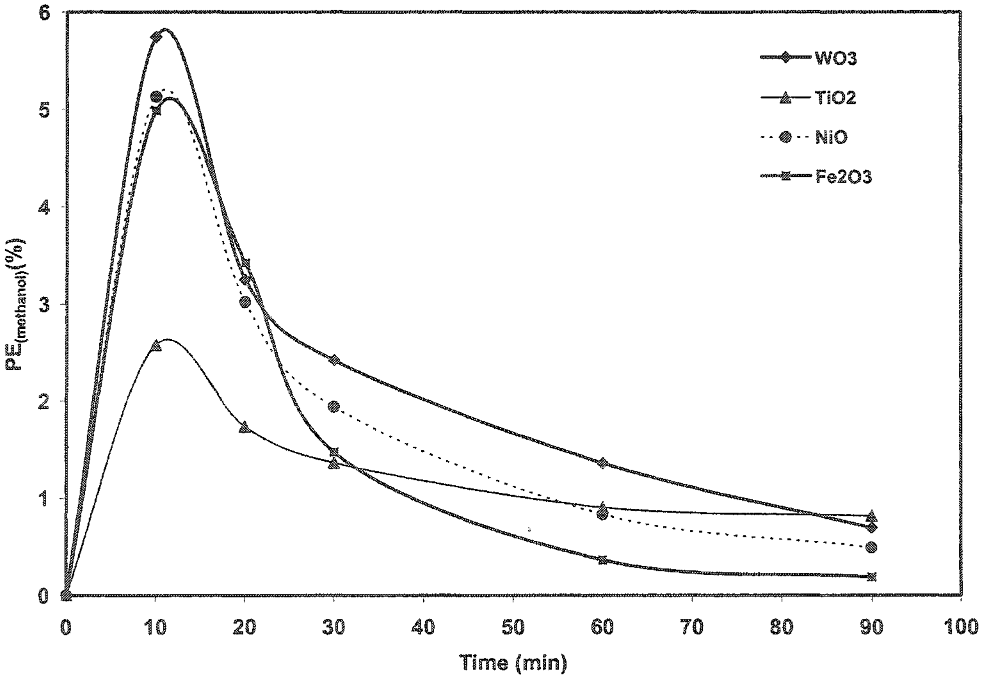

Figure 6.22 Comparison of photonic efficiency of methanol production over WO_3, TiO_2, NiO and α-Fe_2O_3

6.6 Photocatalytic conversion of methane into methanol over transition metal doped WO_3

In photocatalytic conversion of methane into methanol in an aqueous system, the light absorption by the host semiconductor creates an electron-hole pair. The photoexcited hole serves as an oxidant and generates hydroxyl radicals required to convert methane into methanol while the photoexcited electrons are first transferred to the metal of the host and then to the low vacant orbitals of the doped transition metal. The doped metal site (usually oxides of transition metals) act as reducing site and can transfer the electrons to photogenerated protons to give hydrogen or to other adsorbed species, such as oxygen to give super oxide radicals ($O_2^{\cdot-}$).

Based on the mechanism of methane conversion, it can be inferred that the conversion of methane into methanol is a free radical process and the rate of methanol formation increases with the increase in hydroxyl radicals. On the other hand, the increase in the formation of hydroxyl radicals enhances the production of oxygen that in turns enhances the formation of super oxide radicals ($O_2^{\cdot-}$).

As the methanol is soluble in water at room temperature therefore, it remains in the aqueous suspension after its formation along with other reactants and can under go decay through the various processes mentioned below.

The structural similarity of methanol molecules to water molecules make them compete with water molecules for valence band hole causing a decrease in overall methanol yield and the release of additional hydrogen. The super oxide radicals produced by the reduction of oxygen can mineralize the produced methanol through oxidation. The mode of decay of the produced methanol can be predicted on the basis of the knowledge of the conduction band edge and the comparison of evolved hydrogen in the presence of methane with that in the absence of methane in aqueous suspension. In a photocatalytic aqueous system for methane conversion the major sources of hydrogen are:

(i) The reduction of H^+ ions produced from water splitting
(ii) The hydroxylation of methane
(iii) The oxidation of methanol to some intermediate
(iv) The oxidation of intermediate to CO or to some other appropriate intermediates

In order to study the above mentioned processes in detail, WO_3 was doped with Fe, Co, Ni, Cu, Zn and Ag in varying concentrations and their effect on its photocatalytic activity towards methane conversion was explored. The results are discussed in detail in the next sections.

6.6.1 Photocatalytic conversion of methane into methanol over Fe doped WO_3

To study the photocatalytic activity for methane conversion WO_3 doped with varying concentrations of Fe i.e. 0.1%, 1.0% and 10%, was studied under the same experimental conditions as for water splitting. Instead of argon, the aqueous suspension was saturated with methane. The effect of increasing concentration of Fe on the yield of methanol and its comparison with that of un-doped WO_3 is presented in figure 6.23. An increase in the methanol yield was observed for 0.1% and 1.0% Fe concentration while a detrimental effect of further increase in yield i.e. 10% Fe was observed. With the increase in the concentration of Fe, the charge trapping increases leading to the enhanced yield of hydroxyl radicals thus enhances the yield of methanol. As 0.1 and 1% Fe present at the surface as Fe_2O_3 is not enough to produce sufficient FeO surface states therefore, the produced methanol is degraded only through hole oxidation. With 10% Fe doping, although the rate of methanol formation increase but with the formation of FeO surface states the band edges becomes suitable enough to oxidize the methanol simultaneously and causes a substantial decrease in methanol yield.

Comparisons of hydrogen production over 0.1%, 1.0% and 10% Fe doped WO_3 in the presence and absence of methane are presented in figures 6.24, 6.25 and 6.26. Here an increase in hydrogen production can be observed for 0.1% and 1.0% Fe loading clearly suggesting that hole oxidation is the dominating route for methanol degradation. For 10% Fe loading, an initially higher hydrogen yield followed by lower hydrogen yield relative to the system without methane is due to methane conversion and the depletion of both methane and methanol though reduction by the super oxide radicals.

A comparison of the photonic efficiencies of Fe-doped WO_3 with that of un-doped WO_3 is presented in figure 6.27. A low photonic efficiency of less than 7% was observed for all the systems. An increase in the photonic efficiency was observed for 0.1% and 1.0% Fe loading while a substantial decrease in the photonic efficiency was observed for 10% Fe loading. An initial increase followed by a sharp decrease in the photonic efficiencies clearly predicts that the rate of methanol degradation is higher than the rate of formation.

An overall increase in percentage conversion of methane was observed for 0.1% and 1.0% Fe loading while a decrease in the same was observed for 10% Fe loading. An increase of 7% in overall methane conversion was observed for 1.0% Fe-WO_3 while a decrease of 8% was observed for 10% Fe-WO_3.

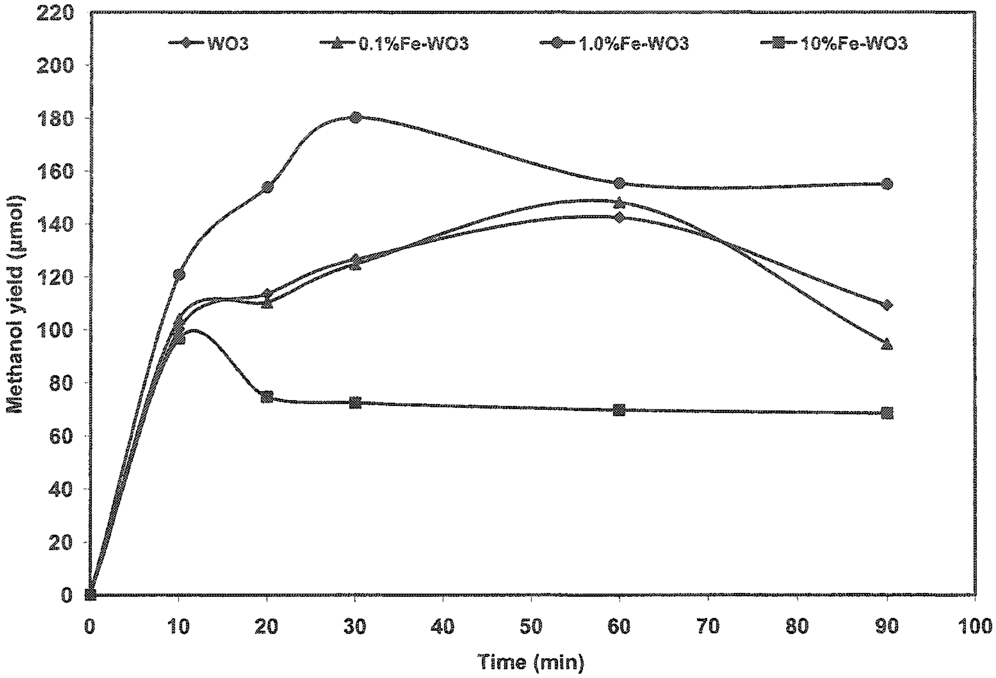

Figure 6.23 Comparison of methanol yield over Fe doped WO_3

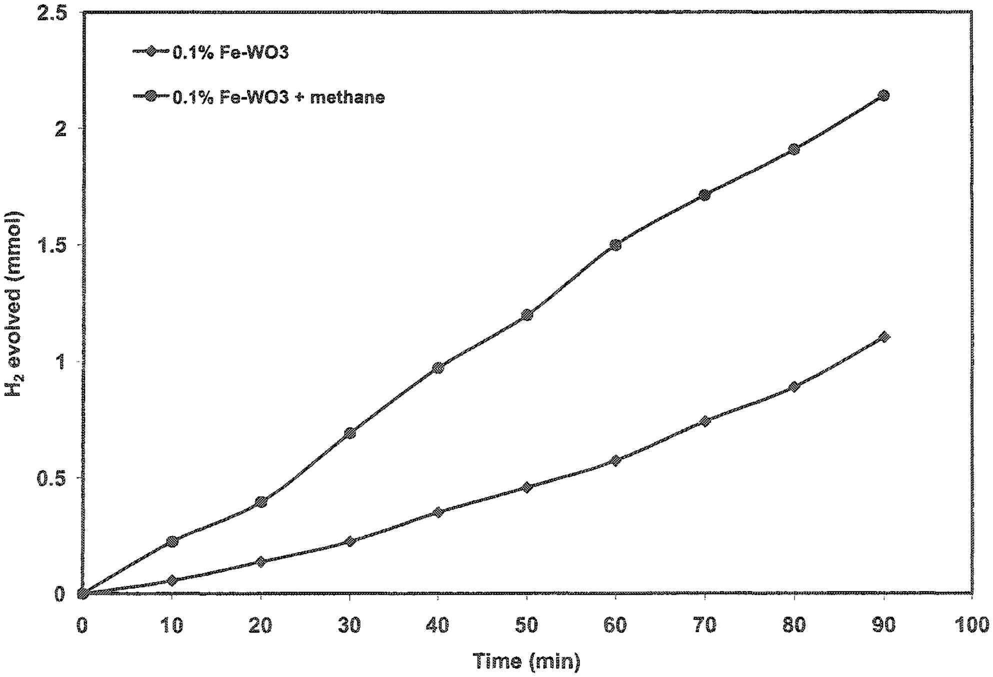

Figure 6.24 Comparison of hydrogen production in the presence of methane over 0.1% Fe-WO_3

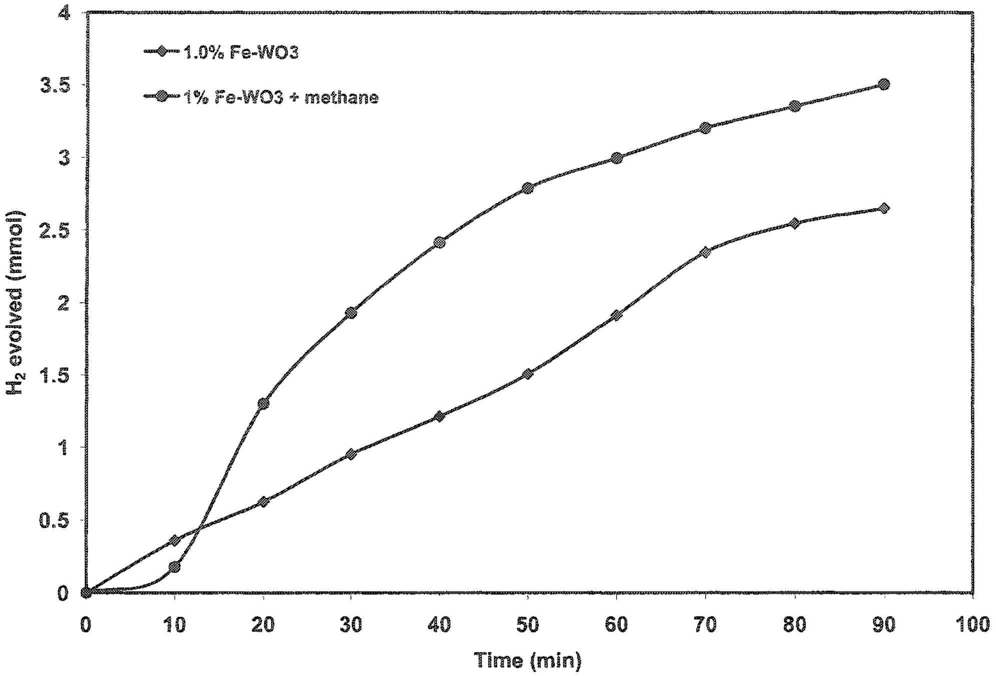

Figure 6.25 Comparison of hydrogen production in the presence of methane over 1.0% Fe-WO_3

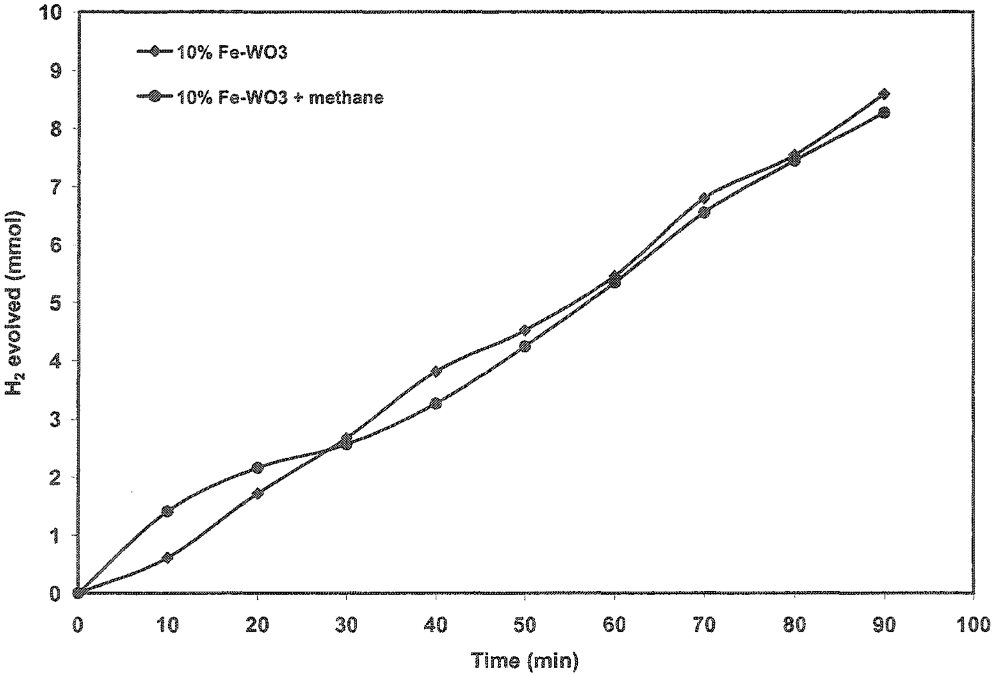

Figure 6.26 Comparison of hydrogen production in the presence of methane over 10% Fe-WO_3

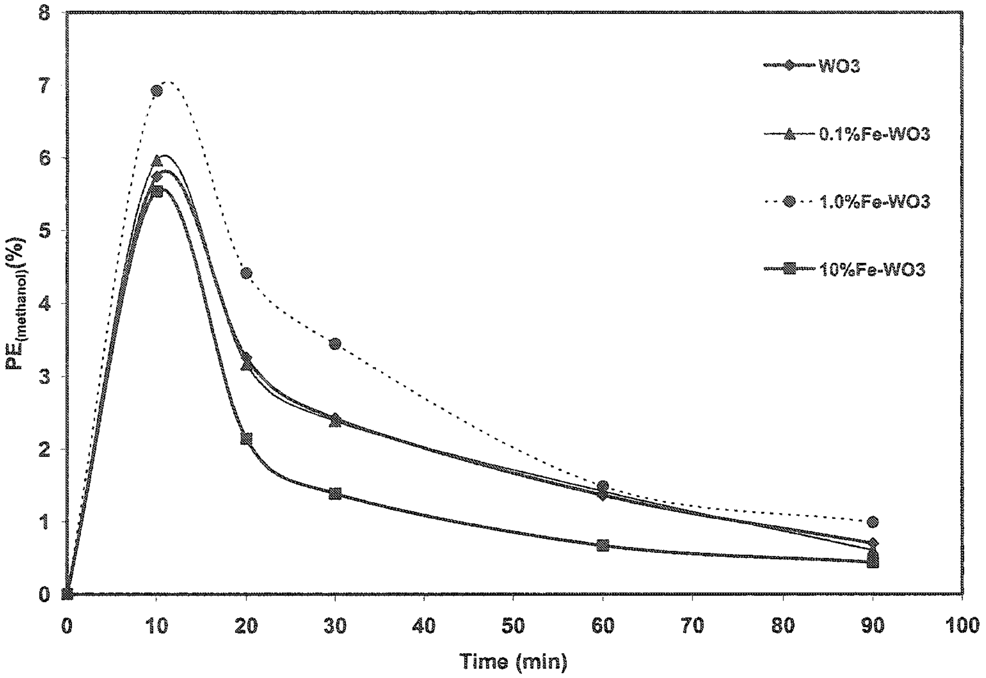

Figure 6.27 Comparison of photonic efficiency for methanol production over Fe-doped WO_3

6.6.2 Photocatalytic conversion of methane into methanol over Co-doped WO_3

A comparison of methanol yield for the photocatalytic conversion of methane over Co-doped WO_3 with that of un-doped WO_3 is presented in figure 6.28. An increase in the methanol yield for 0.1% and 1.0% Co loading and a decrease was observed for 10% Co loading. The increase in the yield of methanol with the increase in Co loading up to 1% reflects an increased yield of hydroxyl radicals through effective charge separation. The production of hydroxyl radicals also increases for 10% Co loading as observed in water splitting on the basis of oxygen yield but simultaneously the extent of the oxygen reduction, due to the suitability of the conduction band edge of the metal oxide present at the surface, also increases with the formation of highly reactive super oxide radicals. These super oxide radicals act as a sink to both methanol and methane causing an unwanted decrease in the methanol yield.

The mode of methanol decay after its formation was estimated by measuring the hydrogen produced on the doped catalysts in the presence of methane. A comparison of evolved hydrogen over various concentrations of Co-doped WO_3 in the presence and absence of methane is presented in figures 6.29-6.31. An increase in the hydrogen yield was observed for 0.1% and 1.0% Co loading reflecting a possible decrease in methanol concentration, after its formation, through valence band hole oxidation. While for 10% Co loading an initial increase in both methanol and hydrogen yield suggests the possible decay of methanol and the un-reacted methane through super oxide oxidation mechanism.

A maximum photonic efficiency of over 7% was observed for 1.0% Co loading while a minimum photonic efficiency of less than 5% was observed for 10% Co loading and a plot of photonic efficiency is presented in figure 6.32. The causes of observed increase and decrease in photonic efficiencies compared to that un-doped WO_3 are discussed in detail above.

An improved methane conversion was observed in the presence 0.1% and 1.0% Co loading. An increasing trend observed for 1.0% Co loading, indicates the suitability of Co loading for charge separation. A noticeable decrease in methane conversion was observed for 10% Co loading.

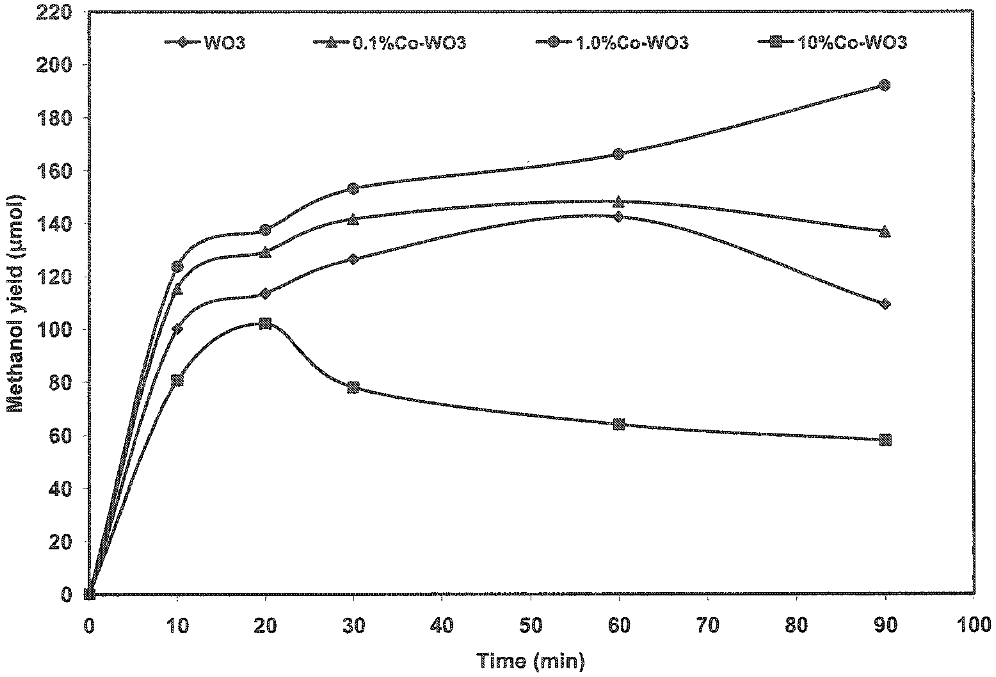

Figure 6.28 Comparison of methanol yield over Co-doped WO_3

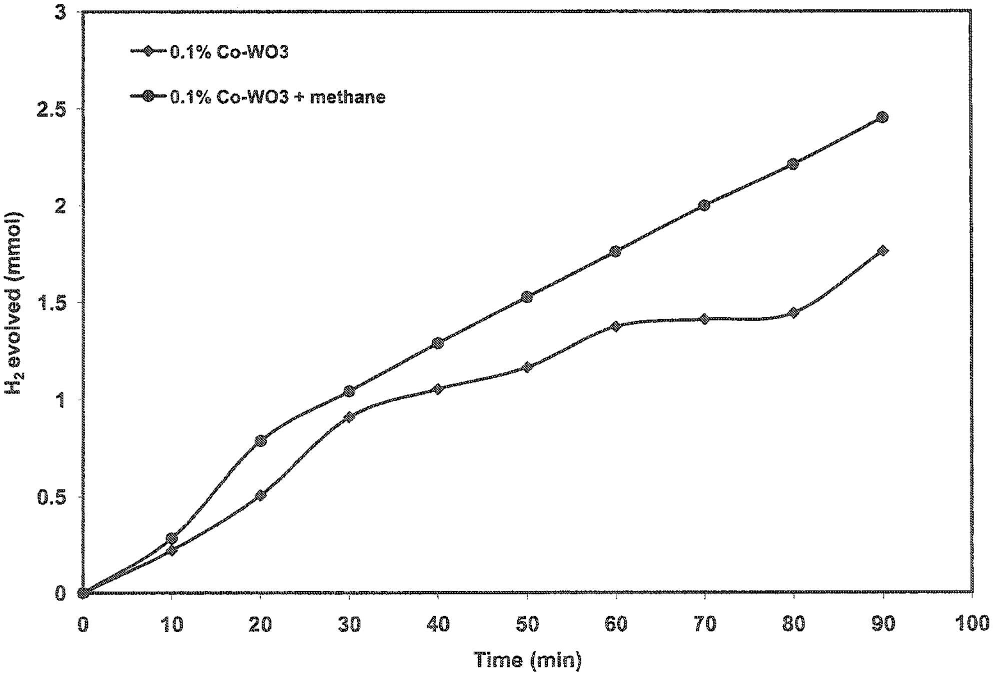

Figure 6.29 Comparison of hydrogen production in the presence of methane over 0.1% Co-WO_3

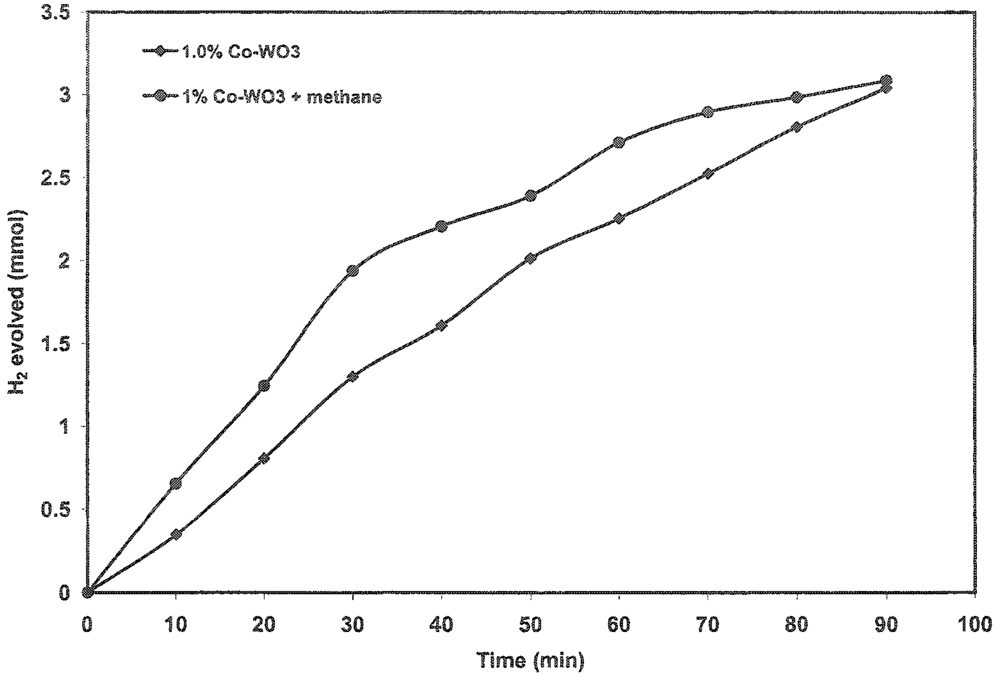

Figure 6.30 Comparison of hydrogen production in the presence of methane over 1.0% Co-WO_3

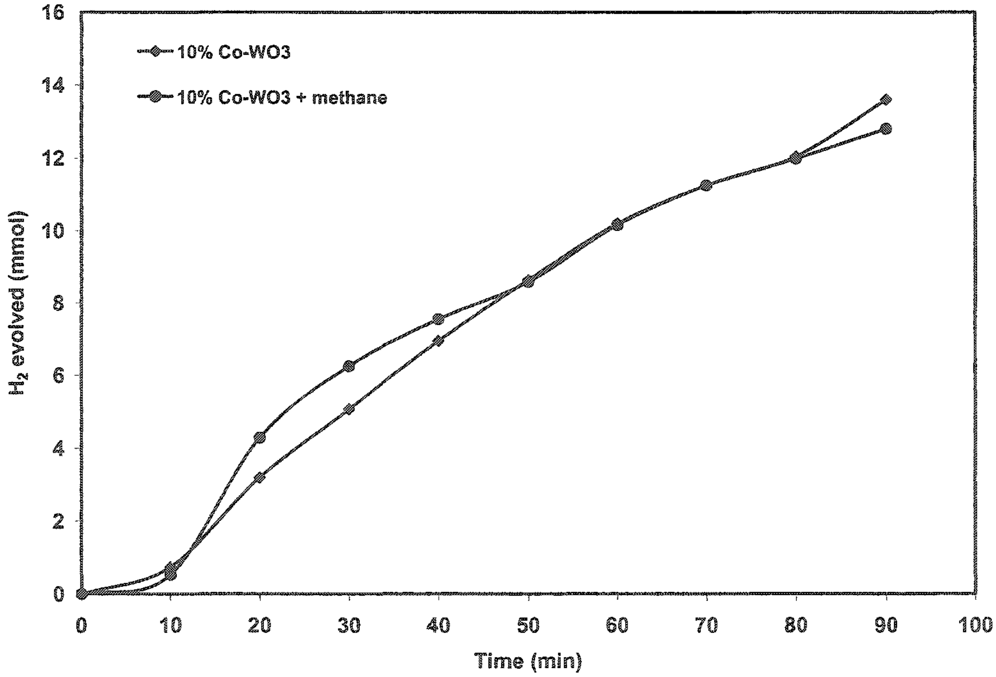

Figure 6.31 Comparison of hydrogen production in the presence of methane over 10% Co-WO_3

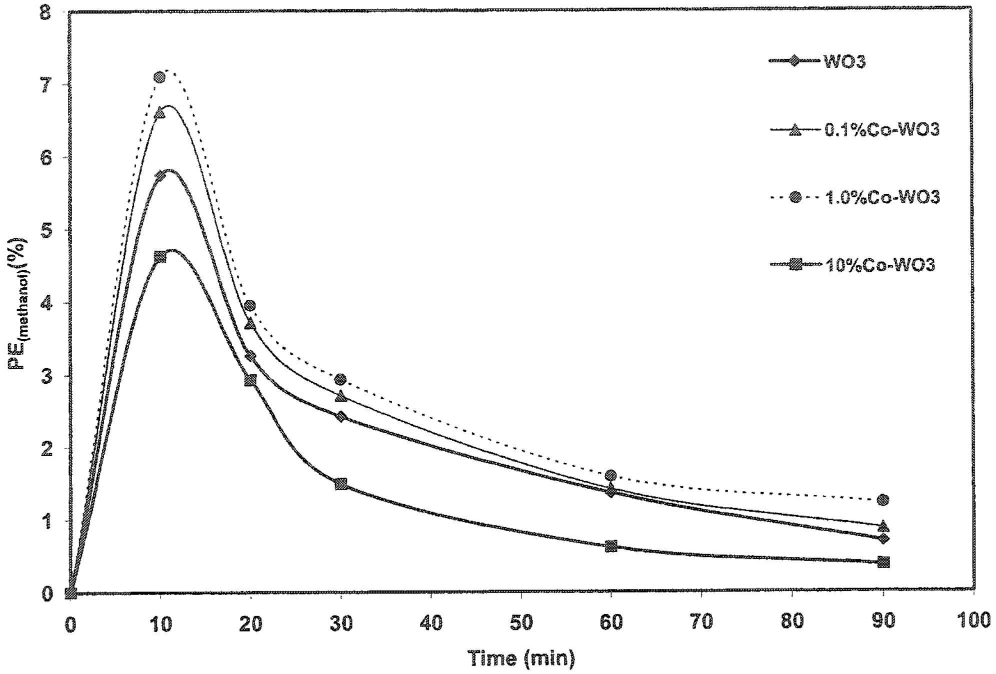

Figure 6.32 Comparison of photonic efficiency for methanol production over Co-doped WO_3

6.6.3 Photocatalytic conversion of methane into methanol over Ni-doped WO_3

The behavior of Ni-doped WO_3 in aqueous suspension under illumination is already discussed in detail in water splitting section. In this section, the activity of these catalysts towards methane conversion is discussed. A comparison of the methanol yield over WO_3 doped with various concentrations of Ni with that of un-doped WO_3 is presented in figure 6.33. Approximately a behavior similar to Fe and Co-doped WO_3 was observed. An initial increase with approximately stable value was observed for 0.1% and 1.0% Ni loading. For 10% Ni loading, a sharp increase followed by a sharp decrease was observed. As already discussed in the previous sections the basic reason for the decrease in the yield of methanol is its degradation immediately after its formation. The two mechanisms of methanol degradation were already discussed.

The comparison of the hydrogen evolved in the presence of methane to that without methane over catalysts doped with various concentrations of Ni is presented in figures 6.34-6.36. This study reveals that for 0.1% and 1.0% Ni doping, the principle mechanism of methanol decay after its formation is through hole oxidation with a minor contribution from the super oxide oxidation. While for 10% Ni doping the main oxidation route is through conduction band oxidation.

An initial increase followed by a sharp decrease in the photonic efficiency was observed for all Ni loadings as presented in figure 6.37. A maximum photonic efficiency of about 7% was observed for 1.0% Ni loading. After 90 minutes, a photonic efficiency of less than 1% was observed for all the catalysts.

An increase in the methane conversion, compared to un-doped WO_3, was observed for 0.1% and 1% Ni loading while a decrease was noticed for 10% Ni loading.

An overall percentage conversion of 23%, 26% and 17% compared to 21% for un-doped WO_3, was observed for 0.1%, 1.0% and 10% Ni loading respectively.

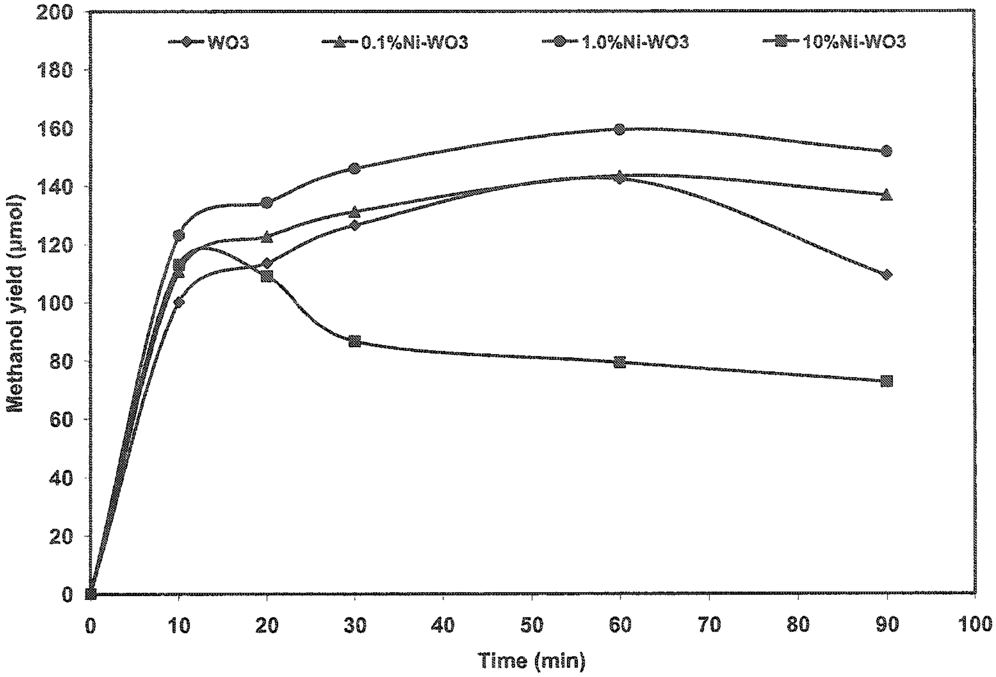

Figure 6.33 Comparison of methanol yield over Ni-doped WO_3

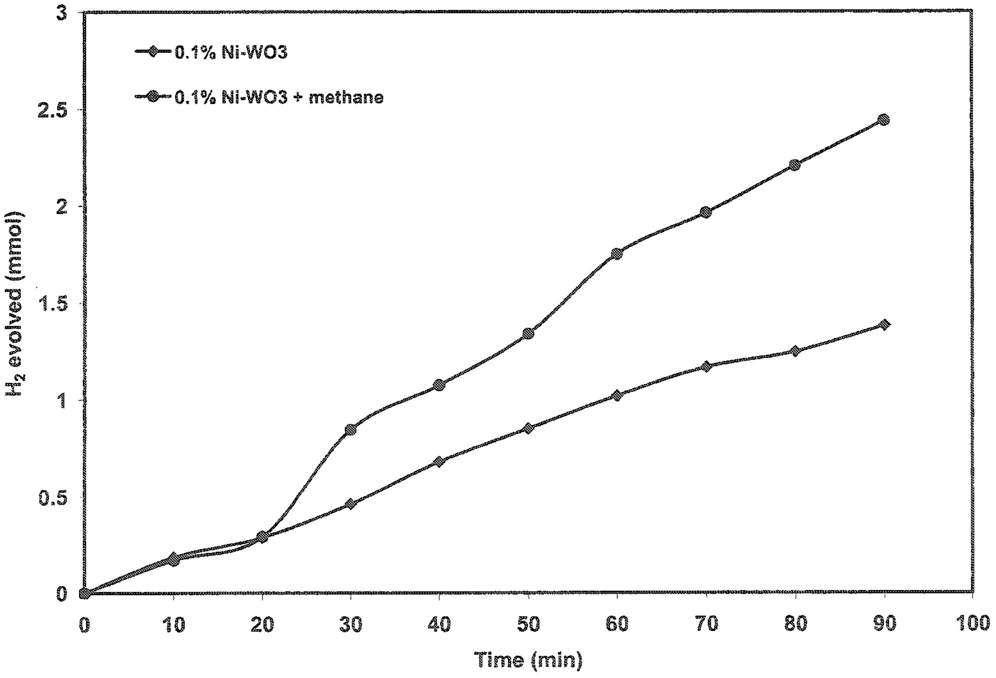

Figure 6.34 Comparison of hydrogen production in the presence of methane over 0.1% Ni-WO_3

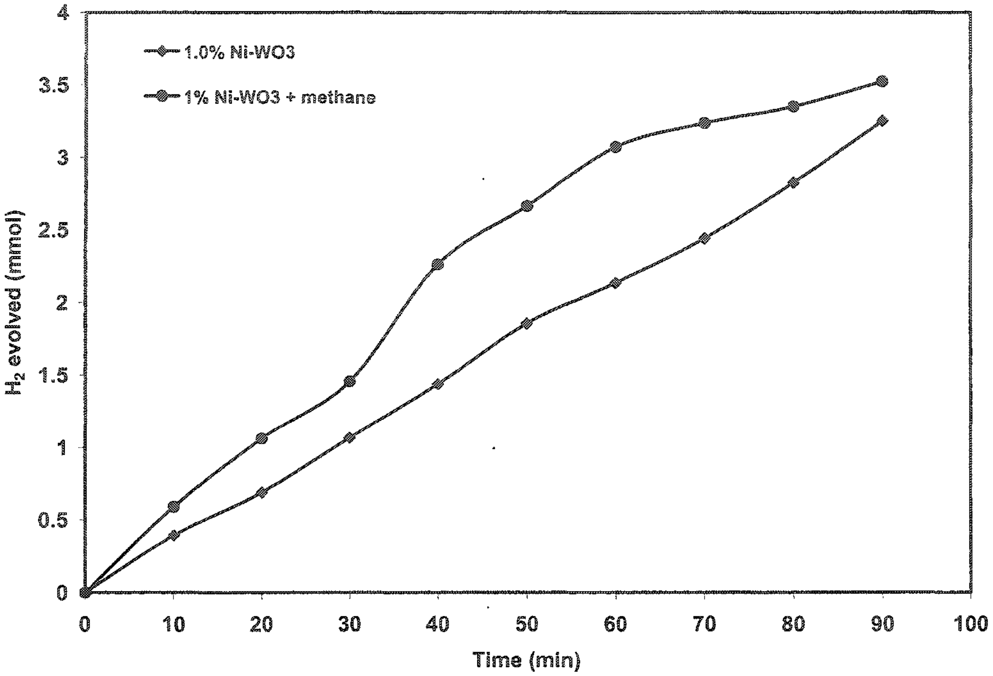

Figure 6.35 Comparison of hydrogen production in the presence of methane over 1.0% Ni-WO_3

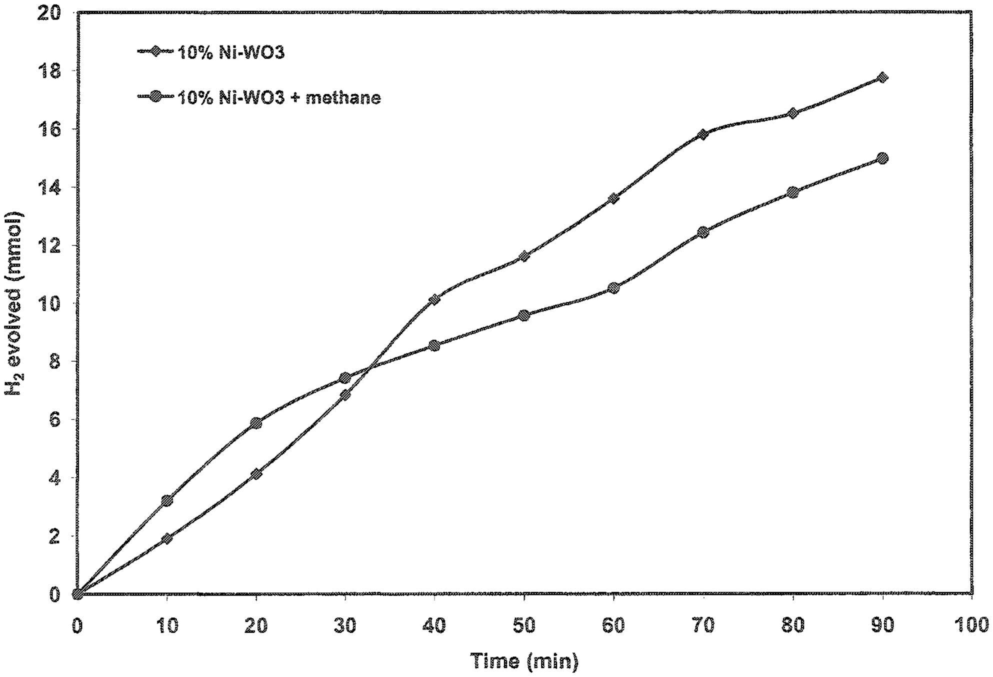

Figure 6.36 Comparison of hydrogen production in the presence of methane over 10% Ni-WO_3

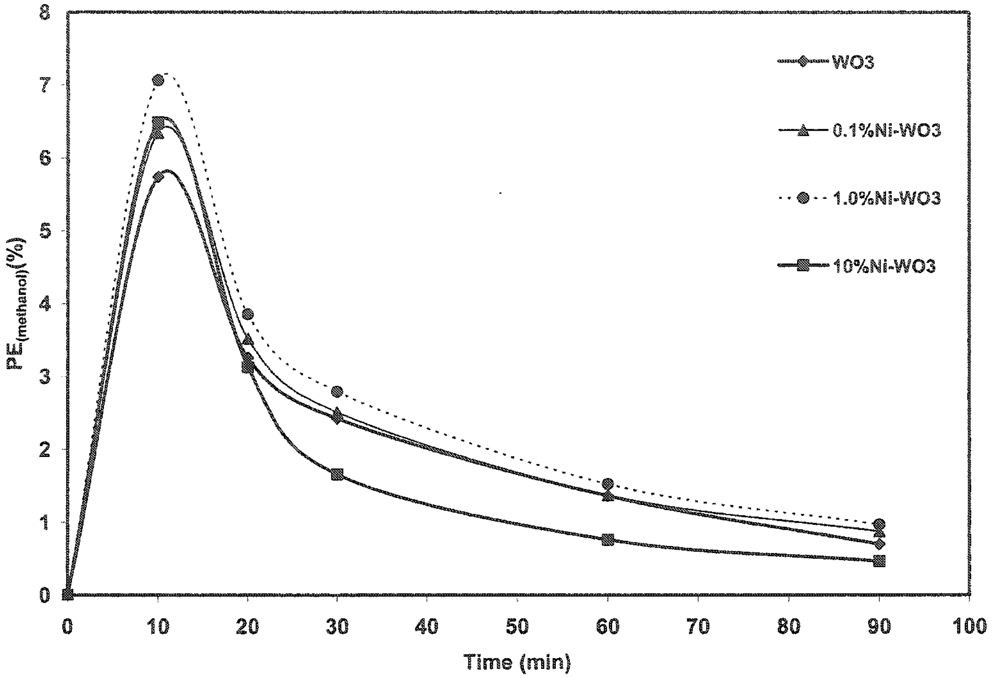

Figure 6.37 Comparison of photonic efficiency for methanol production over Ni-doped WO_3

6.6.4 Photocatalytic conversion of methane into methanol over Cu-doped WO_3

The comparison of the yield of methanol for various concentrations of Cu loading is presented in figure 6.38. An increase in methanol yield with increase in Cu loading was observed between 10 to 50 minutes followed by a decrease for 0.1 and 10% loadings. An increasing methanol yield was observed for 1.0% Cu loading throughout. The sharp decreasing trend as observed in the previous cases was not observed. A different behavior compared to that of Fe, Co Ni towards methane conversion for various Cu loading was observed. An increase in the Cu loading caused an increase in the yield of methanol. On the other hand, slow rates of methanol decay were also observed after about 50 minutes of exposure time. Based on the above observations it can be inferred that

(i) The presence of Cu at the surface enhances the yield of hydroxyl radicals

(ii) The formation of super oxide radical is negligible in the presence of Cu at the surface of WO_3

(iii) The main route of methanol decay after formation is through photogenerated valence band oxidation

As mentioned in the water splitting section, Cu binds with the surface of WO_3 host as Cu_2O. The absorption of laser light by WO_3 causes the transfer of an electron from the 2p orbital of oxygen to 4f orbital of W, which is than transferred to low laying 3d-orbitals of Cu. This transfer of an electron, in aqueous suspension, causes the photocathodic deposition of Cu at the surface of the catalyst. In other words, this process may be termed as trapping of photogenerated electrons. With the increase in Cu loading, the extent of photocathodic deposition of Cu increases which in turns enhances the yield of hydroxyl radicals which in turn enhance the yield of methanol. With the mechanism described above, the photo-generated electrons are fully trapped and the chance for the capture of electrons by the oxygen produced during the process tends to be negligible. With the increase in the number of hydroxyl radicals by the trapping of photoexcited electrons and the formation of more methanol the extent of methanol decay through valence band hole oxidation is increased.

As discussed in the previous sections, the mode of decay of the methanol produced during the process can be estimated by measuring the yield of hydrogen in the presence of methane. In case of Cu loading, an increase in hydrogen yield was observed in the presence of methane predicting the decay of methanol by hole oxidation. A comparison of hydrogen yield in the presence of methane WO_3 doped with various concentrations of Cu loading are presented in figures 6.39-6.41.

An increase in the photonic efficiency was observed for various concentrations of Cu. The order of increase was observed to be 1.0%Cu>10%Cu>0.1%Cu. A maximum photonic efficiency of less than 7% was observed for all catalysts as presented in figure 6.42.

An increase in the methane conversion with the increase in Cu loading relative to un-doped WO_3 was observed. A maximum overall percentage conversion of 26% was observed for 1.0% Cu loading. An overall percentage conversion of 24%, and 25% was observed for 0.1% and 10% Cu loading respectively.

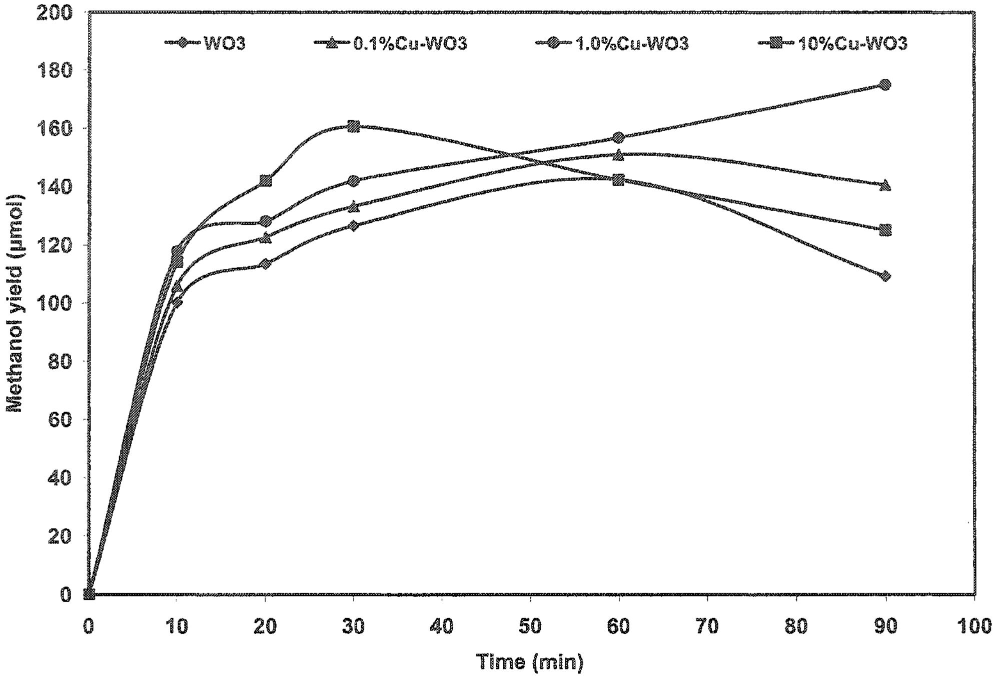

Figure 6.38 Comparison of methanol yield over Cu-doped WO_3

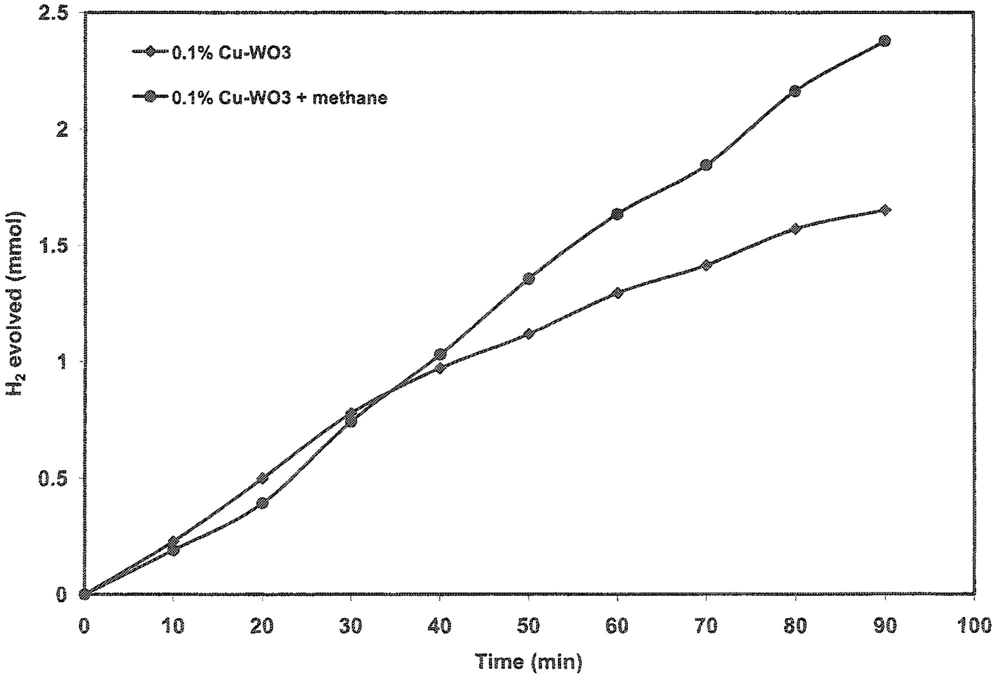

Figure 6.39 Comparison of hydrogen production in the presence of methane over 0.1% Cu-WO_3

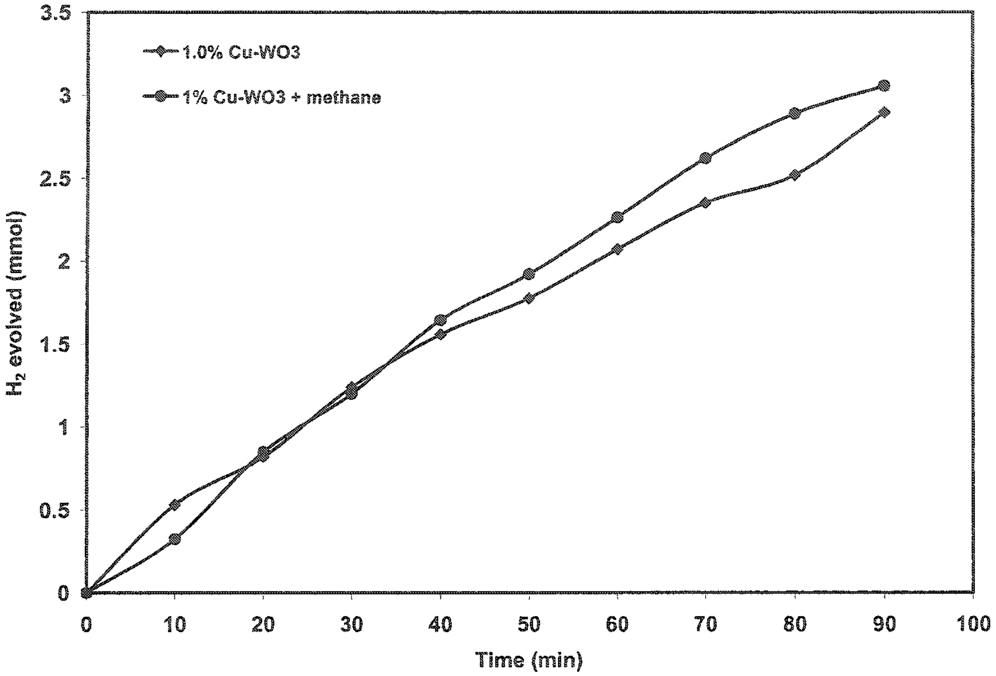

Figure 6.40 Comparison of hydrogen production in the presence of methane over 1.0% $Cu\text{-}WO_3$

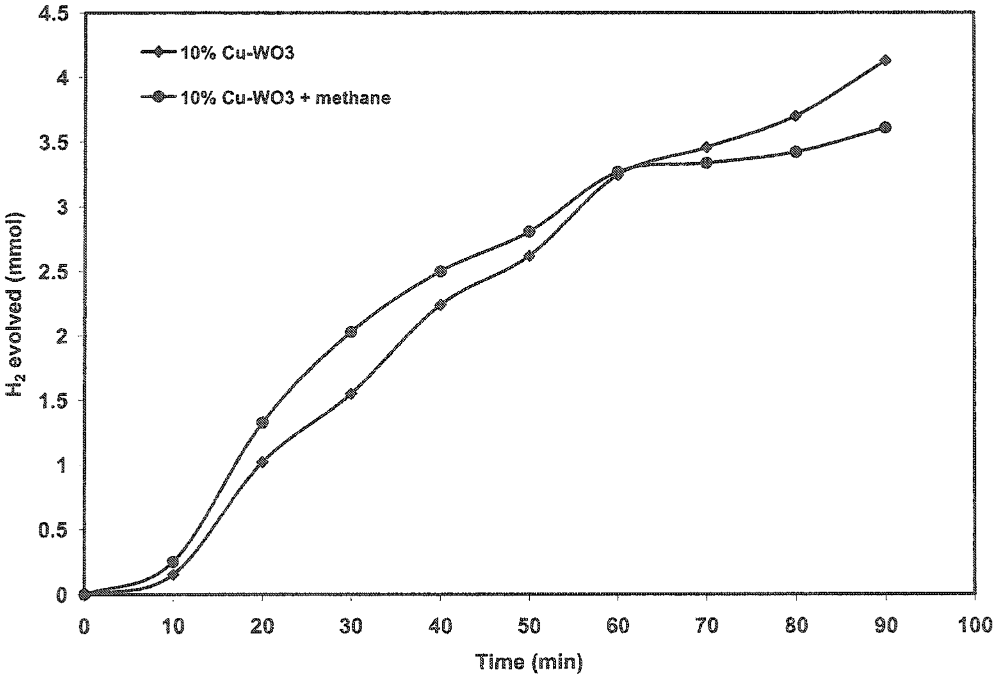

Figure 6.41 Comparison of hydrogen production in the presence of methane over 10% $Cu\text{-}WO_3$

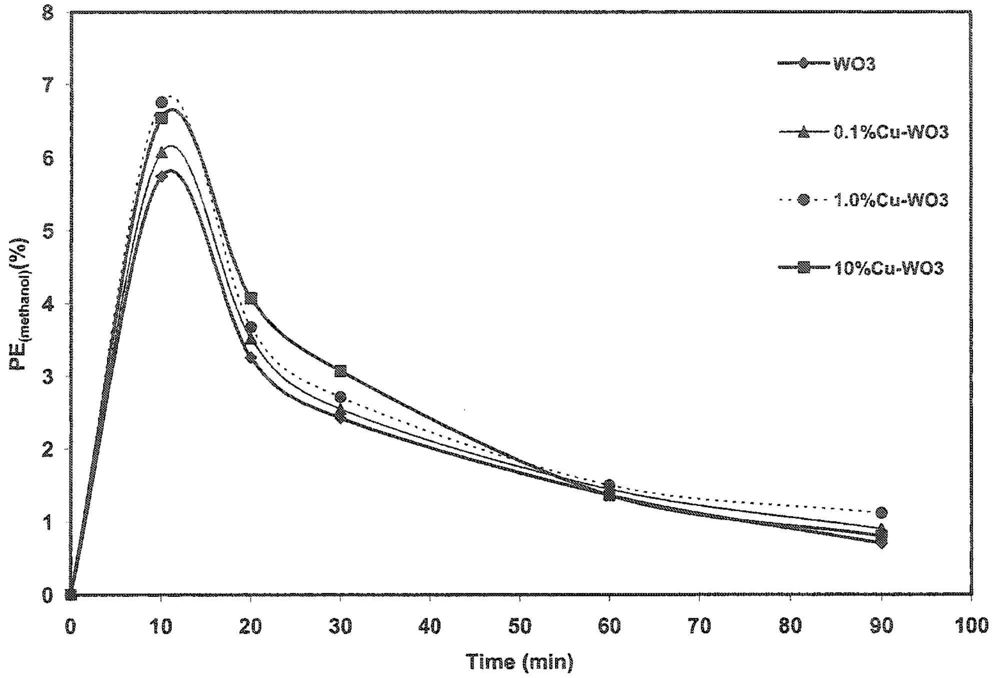

Figure 6.42 Comparison of photonic efficiency for methanol production over Cu-doped WO_3

6.6.5 Photocatalytic conversion of methane into methanol over Zn-doped WO_3

A comparison of the methanol yield over WO_3 doped with various concentrations of Zn with that of un-doped WO_3 is presented in figure 6.43. No significant change in the photocatalytic activity toward methane conversion was observed for any concentration of Zn. A mild increase in methanol yield was observed at the initial stages. This behavior may be attributed to the inability of Zn to induce charge separation through conduction band electron capture. The basic reason for this inability is the d^{10} configuration of Zn in ZnO (as predicted by XPS). In the presence of filled 3d-orbital Zn fails to capture the electron delivered by WO_3 after photo-excitation which leads to higher recombination rate and low yield hydroxyl radicals as for un-doped WO_3.

The comparison of the hydrogen evolved in the presence of methane to that of in the absence over catalysts doped with various concentrations of Zn, as presented in figures 6.44-6.46, reveals again no significant change. No significant increase in hydrogen yield was observed for doped catalyst compared to un-doped WO_3.

An initial increase followed by a sharp decrease in the photonic efficiency was observed for all Zn loadings as presented in figure 6.47. A maximum photonic efficiency of about 6.5% was observed for 10% Ni loading. After 90 minutes, a photonic efficiency of less than 1% was observed for all catalysts.

An increase in the methane conversion was observed for 0.1%, 1% and 10%Zn loading. An overall percentage conversion of 24%, 24% and 22% for 0.1%, 1.0% and 10% Zn loading respectively compared to a percentage conversion of 21% for un-doped WO_3 was observed.

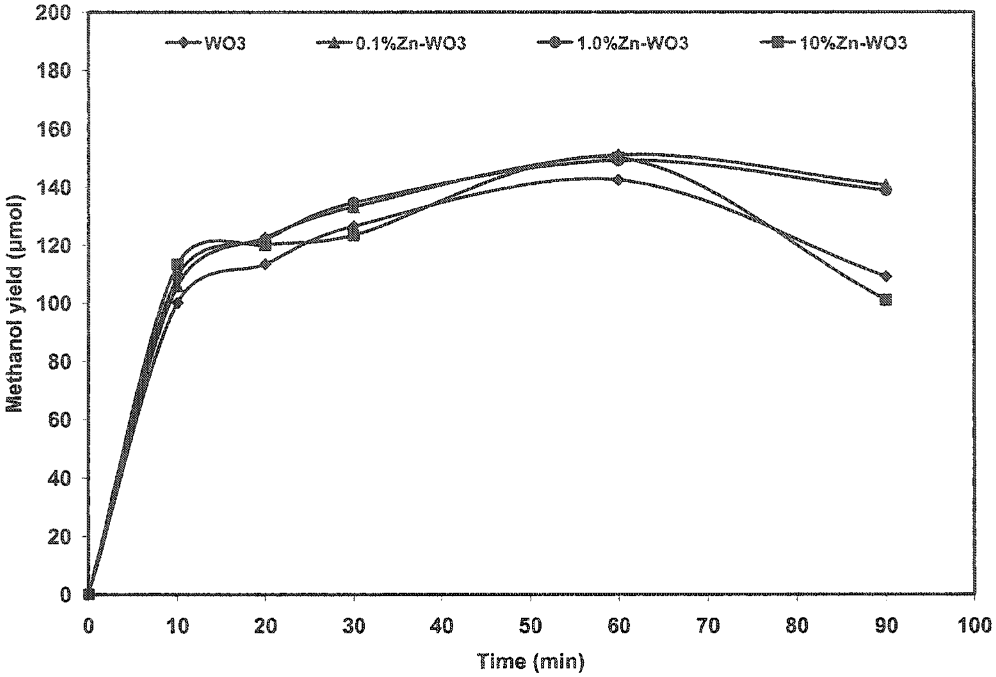

Figure 6.43 Comparison of methanol yield over Zn-doped WO_3

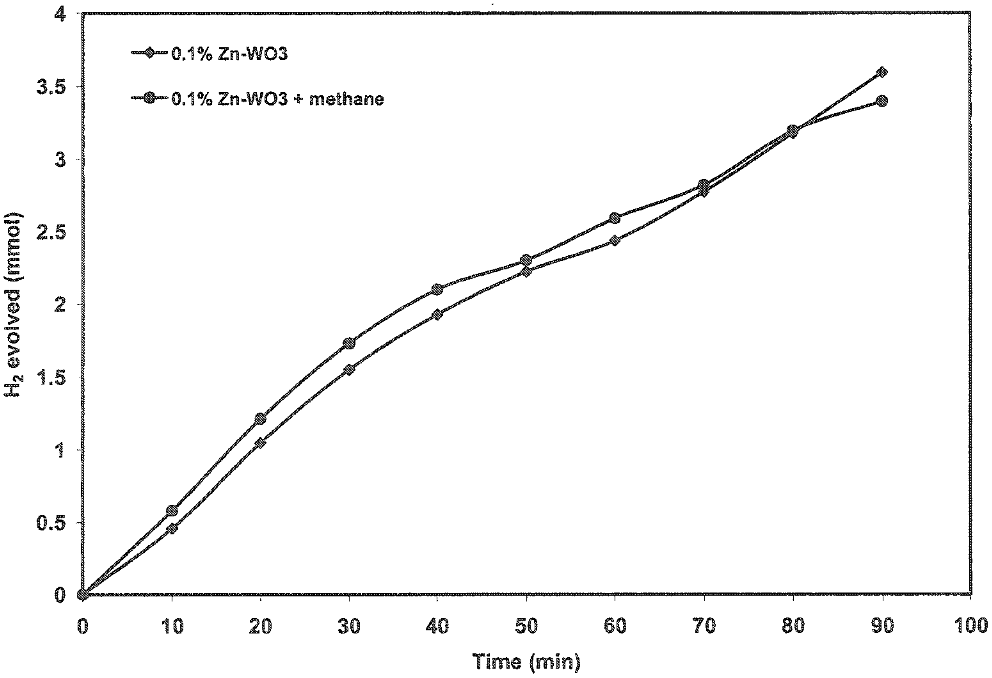

Figure 6.44 Comparison of hydrogen production in the presence of methane over 0.1% Zn-WO_3

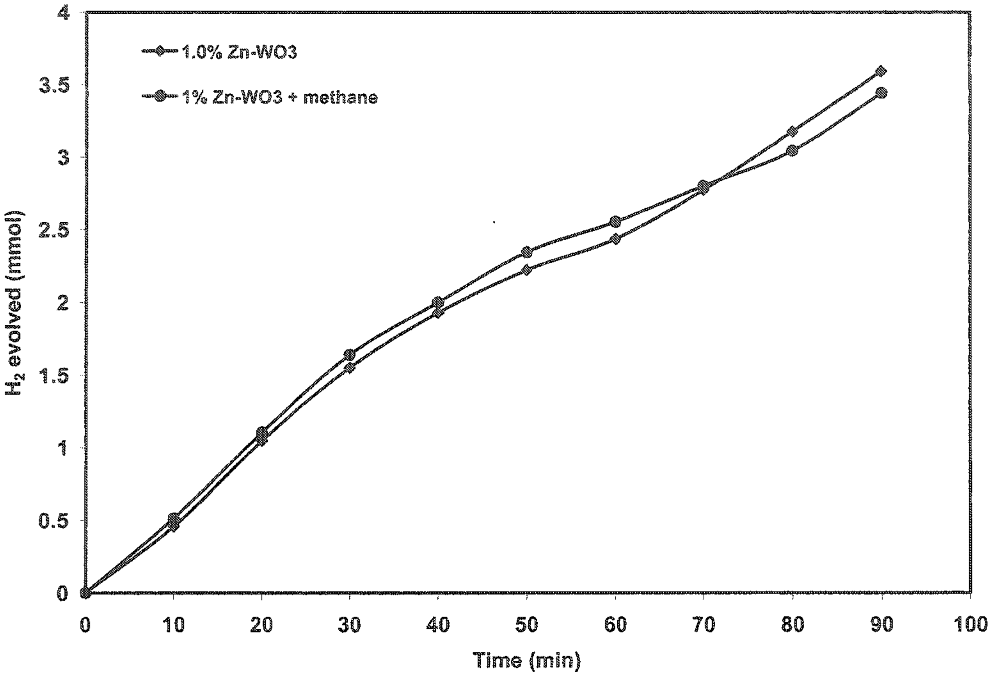

Figure 6.45 Comparison of hydrogen production in the presence of methane over 1.0% $Zn-WO_3$

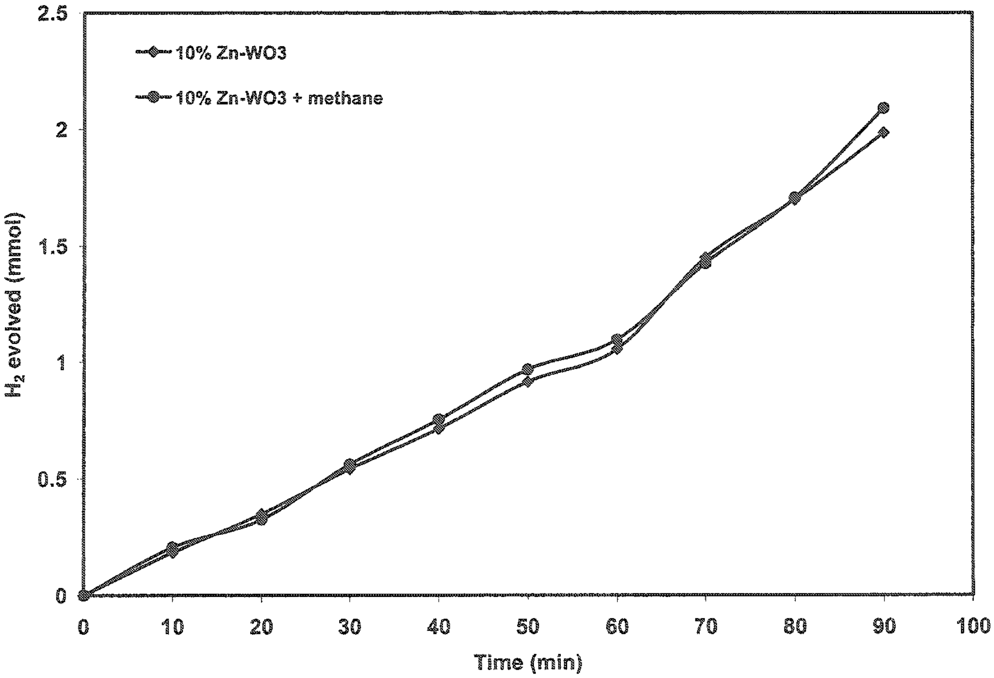

Figure 6.46 Comparison of hydrogen production in the presence of methane over 10% $Zn-WO_3$

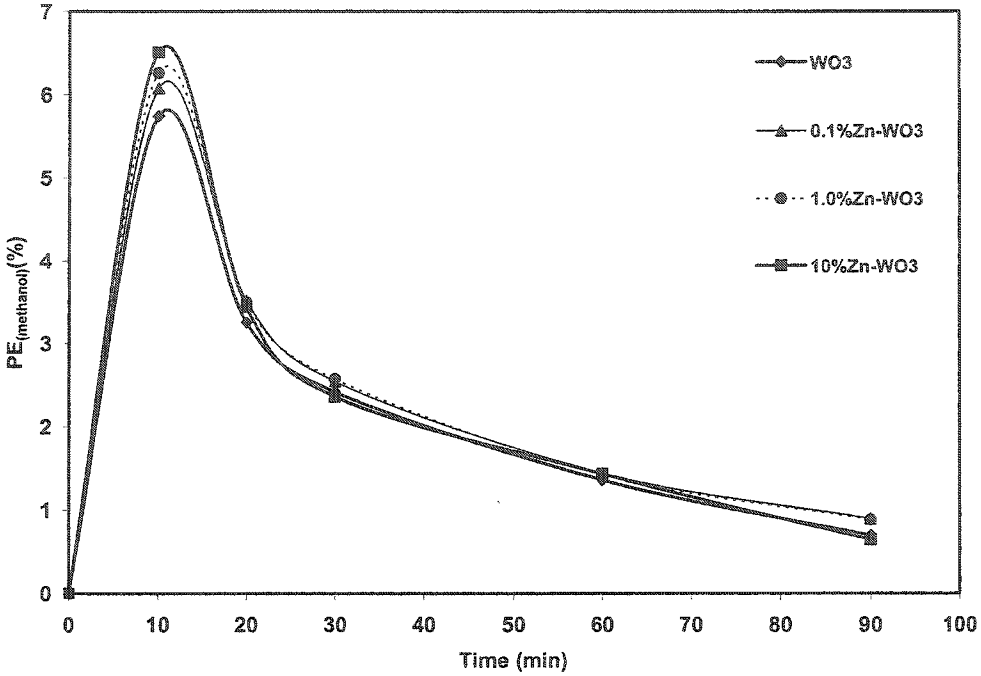

Figure 6.47 Comparison of photonic efficiency for methanol production over Zn-doped WO_3

6.6.6 Photocatalytic conversion of methane into methanol over Ag-doped WO_3

The case of Ag loading is similar to that of Cu. An increase in methanol yield was observed with increasing concentration of Ag between 10 to 50 minutes followed by a decrease afterward except for 10% Ag loading where an increase in the methanol yield was observed throughout the experiment. Like Cu, a slow rate of methanol decay was observed for Ag loading. These observations suggest that the presence of Ag at the surface enhances the yield of hydroxyl radicals.

Ag binds with the surface oxygen and forms Ag_2O at the surface As predicted by XPS. The absorption of light by WO_3 causes the transfer of an electron from the 2p orbital of oxygen to 4f orbital of W, which is then transferred to low laying 4f-orbitals of Ag. This electron transfer, in aqueous suspension, causes the photocathodic deposition of Ag at the surface of the catalyst leaving metallic Ag at the surface. With the increase in Ag, loading the extent of photocathodic deposition increases which causes an increase in the yield of hydroxyl radicals required to boost the yield of methanol. The formation of metallic silver leads to the complete trapping of electrons, which become inaccessible to the oxygen produced during the process. With the increase in the number of hydroxyl radicals by the trapping of photoexcited electrons along with the formation of more methanol the extent of methanol decay through valence band hole oxidation is increased. The comparison of the yield of methanol for various concentrations of Ag loading is presented in figure 6.48 where an increase in methanol yield with the increase in Ag loading is observed.

As discussed in the previous sections, the mode of decay of the methanol produced during the process can be estimated by measuring the yield of hydrogen in the presence of methane. In case of Ag an increase in hydrogen yield was observed in the presence of methane predicting the decay of methanol by hole oxidation. A comparison of hydrogen yield in the presence of methane WO_3 doped with various concentrations of Ag loading are presented in figures 6.49-6.51.

An increase in the photonic efficiency was observed for various concentrations of Ag. The order of increase was observed to be 10%Ag>1.0%Ag>0.1%Ag. A maximum photonic efficiency of more than 7% was observed for 1.0%Ag and 10%Ag catalysts as presented in figure 6.52.

An increase in the methane conversion with the increase in Ag loading was observed. A maximum overall percentage conversion of 29% was observed for 10% Ag loading. An overall percentage conversion of 21%, and 27% was observed for 0.1% and 1.0% Ag loading respectively.

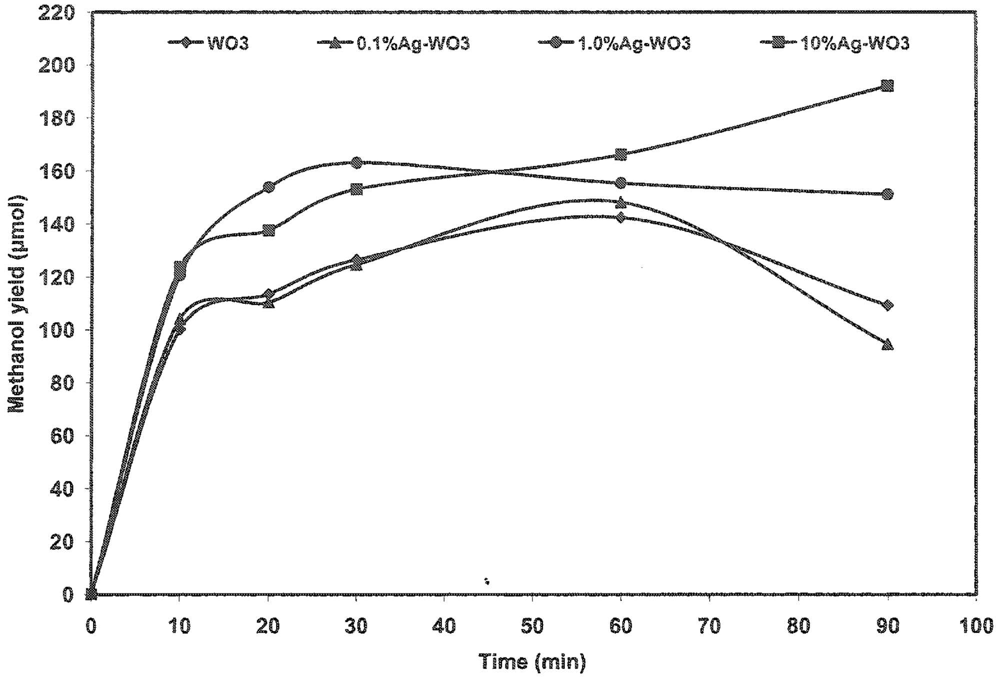

Figure 6.48 Comparison of methanol yield over Ag-doped WO_3

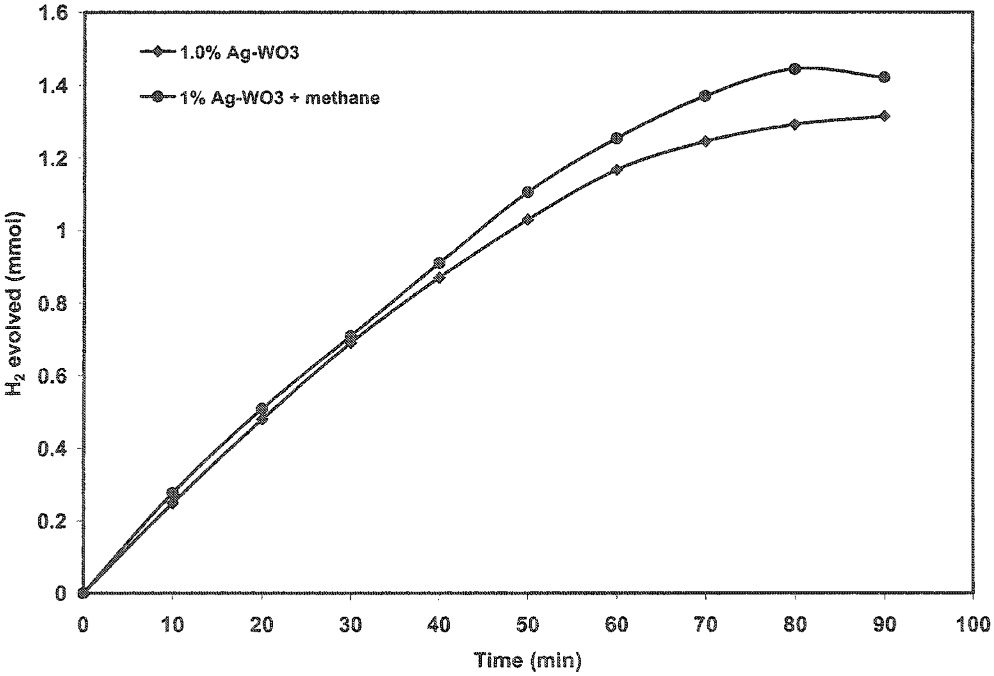

Figure 6.49 Comparison of hydrogen production in the presence of methane over 0.1% Ag-WO_3

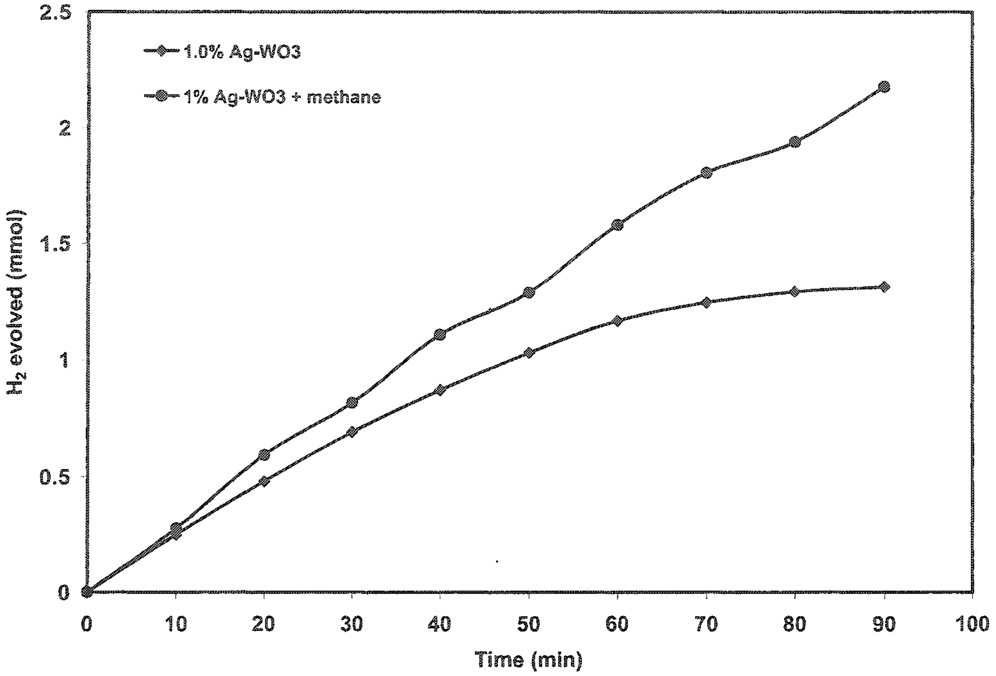

Figure 6.50 Comparison of hydrogen production in the presence of methane over 1.0% Ag-WO_3

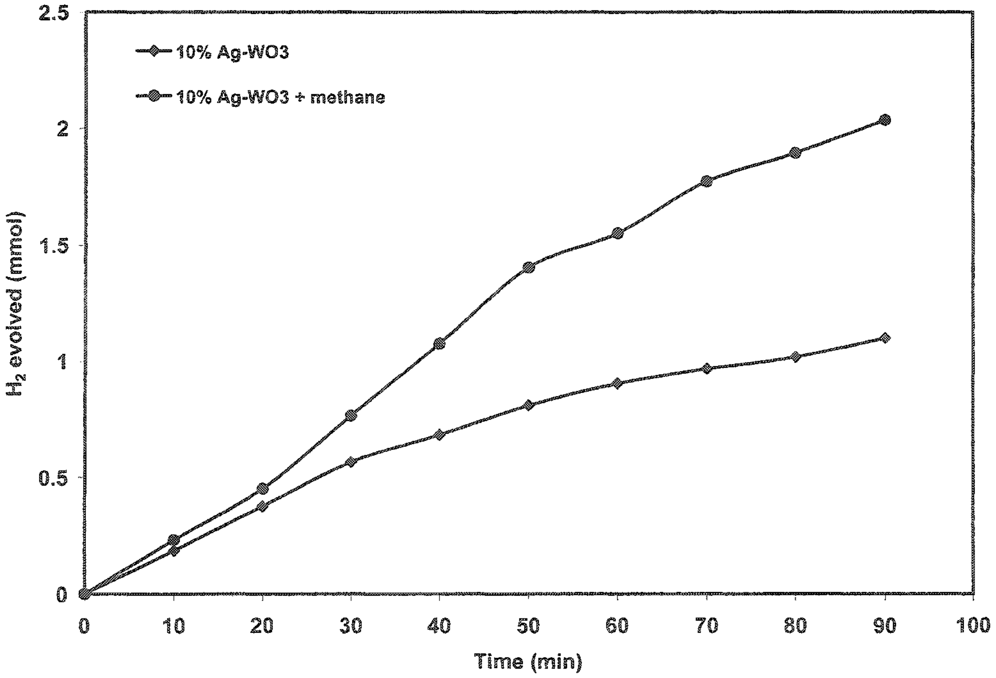

Figure 6.51 Comparison of hydrogen production in the presence of methane over 10% Ag-WO_3

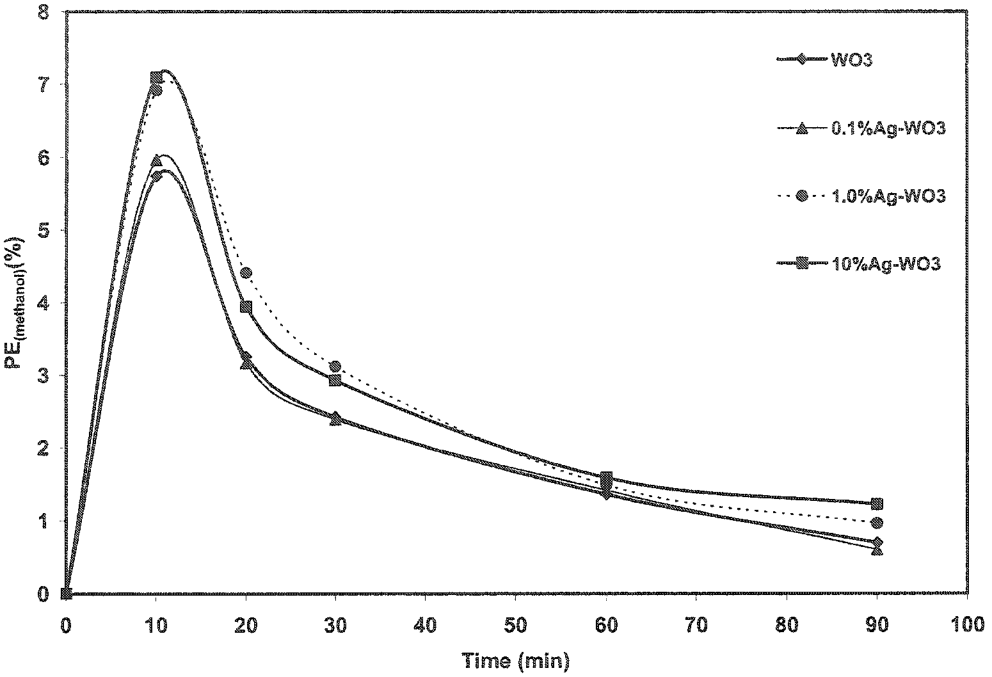

Figure 6.52 Comparison of photonic efficiency for methanol production over Ag-doped WO_3

6.7 Comparison of photocatalytic conversion of methane into methanol over transition metal doped WO_3

The comparison of methanol yield for the photocatalytic conversion of methane over 1.0 and 10% transition metal doped WO_3 is presented in figures 6.53 & 6.54 respectively. As shown in figure 6.53, the methanol yield is higher, for all 1% transition metal-doped WO_3, than un-doped. The reasons for this increase are discussed in detail in previous sections. To summarize, the presence of 1% transition metals induces a better charge separation compared to un-doped WO_3, which enhances the yield of hydroxyl radicals, thus causing an increase in methanol yield. Moreover, the presence of transition metals in low concentration inhibits the reduction of oxygen and suppresses the formation of super oxide radicals that reduces the rate of methanol degradation.

Although the increase in the concentration of doped metals i.e. from 1% to 10%, causes an increase in the production of hydroxyl radicals but on the other hand, increases the production of super oxide radicals also increases due to the suitability of conduction band edges, as discussed in section 6.2, causing an increase in the rate of methanol degradation. So an overall decrease was observed in methanol yield for 10% transition metal doped WO_3 compared to un-doped WO_3 as presented in figure 6.54.

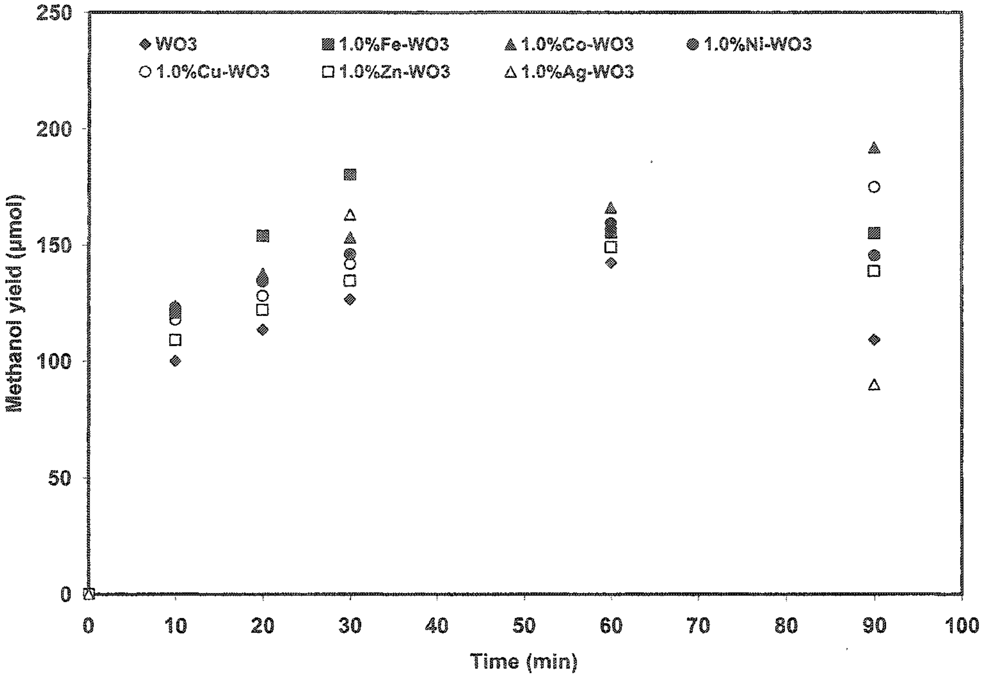

Figure 6.53 Comparison of methanol over 1% transition metal doped WO_3

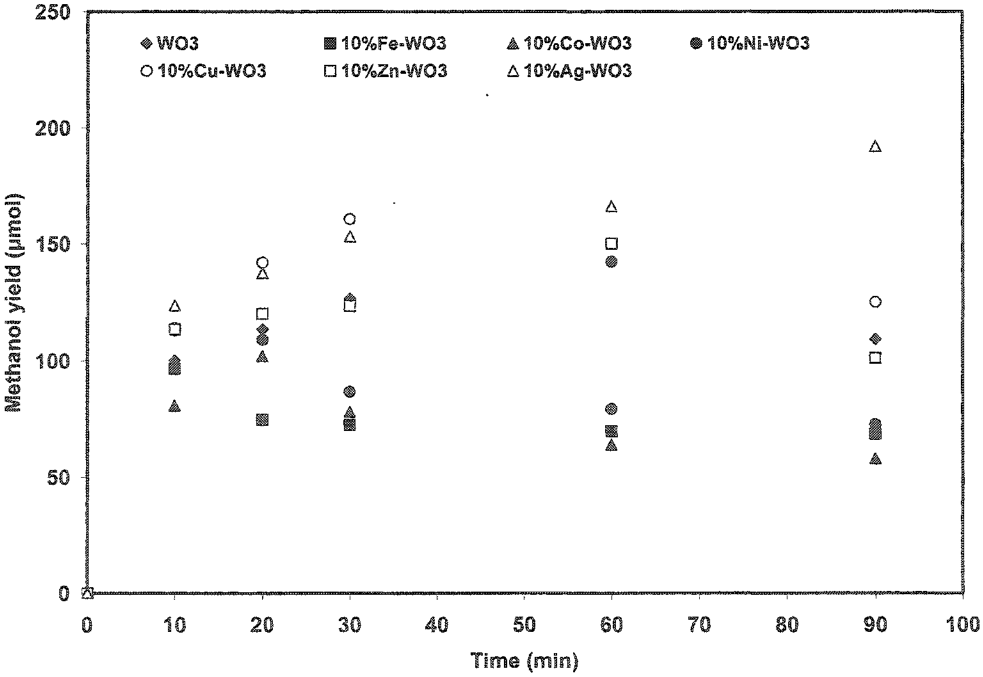

Figure 6.54 Comparison of methanol over 10% transition metal doped WO_3

CHAPTER SEVEN

CONCLUSIONS AND FUTURE PROSPECTS

7.1 Conclusions

The main conclusions of this research work are:

1. Laser induced photocatalytic process for water splitting and methane conversion is superior to conventional photocatalysis using broad spectral lamps, which is indicated by the high photonic efficiency in a short span of time.
2. The structural changes in the photocatalysts can be observed only with an intense light source such as a laser.
3. Transition metal doping shifted the spectral response of catalysts towards the visible region as a clear red shift was observed in λ_{max} for transition metal doped WO_3.
4. Photonic efficiencies of 5%, 25%, 30% and 29% were achieved over WO_3, TiO_2, NiO, α-Fe_2O_3 photocatalysts for hydrogen production.
5. Photonic efficiencies of 30, 35, 20 and 50% were attained over WO_3, TiO_2, NiO, α-Fe_2O_3 photocatalysts for oxygen production.
6. The high oxygen yield observed as a result of water splitting over α-Fe_2O_3 indicated the photocorrosion of catalyst due to the absorption of strong UV laser radiations.

7. A substantial increase in oxygen production was observed in the presence of Fe^{3+} and Ag^{+} for WO_3, TiO_2 and α-Fe_2O_3 while a decrease was observed for NiO.

8. The electron capture performance of Fe^{3+} was found to be better than that of Ag^{+} due to its higher oxidation state.

9. Metal in higher oxidation states are better electron capture agents than metals in lower oxidation states.

10. pH measurement during the photocatalytic processes is useful in explaining the possible reaction mechanism.

11. A decrease in the pH was observed for the catalysts whose conduction band edge position is un-suitable for hydrogen production and in the presence of electron capture agents.

12. A significant change in the photocatalytic activity of WO_3 towards hydrogen production was observed in the presence of transition metals as dopants. The transition metals with d^7 and d^8 configuration were found highly suitable, as dopants, for hydrogen production through water splitting.

13. High overall photonic efficiencies of 77% and 81% for hydrogen production were observed for WO_3 with 10% Co and 10% Ni respectively.

14. Overall percent conversions of 22%, 15%, 17% and 13% were observed for the photocatalytic conversion of methane into methanol over WO_3, TiO_2, NiO and α-Fe_2O_3 respectively.

15. An overall percentage conversion of ~22% was found for pure WO_3 while ~ 27% and 23% percent conversions were observed for Fe^{3+} and Ag^{+} ions in aqueous solution.

16. For TiO_2, an overall methane conversion of less than 20% was observed for all the systems.

17. For NiO, an overall methane percent conversion of less than 17% was observed for all the systems.

18. An overall percent of methane conversion of ~ 13% was observed for pure α-Fe_2O_3. A stable increase of ~ 7% and ~ 4% in methane conversion was observed in the presence of Fe^{3+} and Ag^{+} ions respectively.

19. A photonic efficiency of less than 10% was observed for all cases for methane conversion.

20. An increase of 7% in overall methane conversion was observed for 1.0% Fe-WO_3 while a decrease of 8% was observed for 10% Fe-WO_3. Similarly an increase in the methane conversion was observed for 0.1% and 1.0% Co-doped WO_3 while a decrease was observed 10% Co loading.

21. An overall methane conversion of 23%, 26% and 17% was observed for 0.1%, 1.0% and 10% Ni loading respectively.

22. An overall methane conversion of 24%, 26% and 25% was observed for 0.1% , 1.0% and 10% Cu loading respectively.

23. Overall percent conversions of 24%, 24% and 22% for 0.1%, 1.0% and 10% Zn loading respectively were observed, compared to 22% for un-doped WO_3.

24. A maximum overall percent conversion of 29% was observed for 10% Ag loading and 21%, and 27% were observed for 0.1% and 1.0% Ag loading respectively.

7.2 Future prospects

The photocatalysis is still in the development stage and several hidden aspects of this technology are yet to be explored. The main focus of research in this area is to use sunlight as a light source for clean fuel production and to reduce environmental contamination. Unfortunately, at present TiO_2 is in commercial use, as photocatalytic agent, for water and air purification. The other commercial applications of the TiO_2 photocatalyst are as an anti-fogging and an anti-microbial agent. Extensive research efforts are needed for the development of new photocatalysts of high activity for commercial uses.

Although the ultimate goal is to use sunlight as a light source for above-mentioned purposes, in this study, it was demonstrated that other light sources such as lasers could be used to trigger photocatalytic processes at much higher rates and efficiencies. These sources can be used for practical application of photocatalysis especially at the locations where enough sun light is not available such as indoor applications.

In this dissertation, the activity of the pure and synthesized catalysts was studied in the UV region i.e. 355 nm. The shifting of the bandgap of transition metal doped WO_3 towards higher wavelength with the change in doping level clearly indicates that the doped catalysts will show a good spectral response and photocatalytic activity in the visible region as well. Therefore, It is recommended that the activity of these catalysts especially for transition metal doped WO_3, should be studied in the visible region i.e. 400-600 nm so that sunlight can be applied in future for commercial applications. In addition, the high photonic efficiencies achieved in this work requires that this laser based technique, developed in this dissertation, should not be limited only to water splitting or methane conversion but should be extended in future to other potential areas of research in photocatalysis as mentioned below.

- Reduction of carbon dioxide to useful organic compounds
- Reduction of nitrogen to ammonia
- Photocatalytic desulphurization of crude oil
- Photocatalytic removal of toxic metals
- Photocatalytic degradation of carcinogenic organic compounds
- Recovery of precious metals such as platinum, gold etc. from aqueous solutions

REFERENCES

1. A. Fujishima, K. Honda, Nature, **238** (1972) 37.
2. M.R. Hoffmann, S.T. Martin, W. Choi, D.M. Bahnemann, Chem. Rev., **95** (1995) 69.
3. J. Peral, X. Domenech, D.F. Ollis, J. Chem. Tech. Biotech., **70** (1997) 117.
4. G.D. Surender, G.P. Fotou, S.E. Pratsinis, Trends Chem.Eng., **4** (1998) 145.
5. P.V. Kamat, Chem. Rev., **93** (1993) 267.
6. O.M. Alfano, D. Bahnemann, A.E. Cassano, R. Dillert, R. Goslich, R. Cat. Today, **58** (2000) 199.
7. M. Ashokkumar, P. Maruthamuthu, P. Int. J. Hydrogen Energy, **16** (1991) 591.
8. B. Pal, M. Sharon, J. Chem. Technol. Biotechnol., **73** (1998) 269.
9. P.E. de Jongh, D. Vanmaekelbergh, J.J. Kelly, Chem. Comm., (1999) 1069.
10. P. Maruthamuthu, K. Gurunathan, E. Subramanian, M.V.C. Sastri, Int. J. Hydr. Energy, **19** (1994) 889.
11. S.K. Poznyak, A.N. Golubev, A.I. Kulak, A.I., Surf. Sci., **454** (2000) 396.
12. K. Tennakone, J. Bandara, App. Catal. A , **208** (2001) 335.
13. T. Sivakumar, K. Shanthi, T.N. Samuel, Bioproc. Eng., **23** (2000) 579.
14. J.A. Navio, M.C. Hidalgo, G. Colon, S.G. Botta, M.I. Litter, Langmuir, **7** (2001) 202.
15. R.F. Khairutdinov, Colloid J., **59** (1997) 535.
16. C.S. Turchi, D.F. Ollis. D.F., J. Cat., **122** (1990) 178.
17. M.I. Litter, App. Catal. B, **23** (1999) 89.

18. M.A. Fox, M.T. Dulay, Chem. Rev., **93** (1993) 341.

19. K. Rajashwer, J. Appl. Electrochem., **25** (1995) 1067.

20. O. Legrini, E. Oliveros, A.M. Braun, Chem. Rev., **93** (1993) 671.

21. N. Serpone, J. Photoche. Photobiol. A: Chemistry, **104** (1997) 1

22. N. Serpone, E. Pelizzetti (Eds.), Photocatalysis, Fundamentals & Applications, Wiley, New York, 1989 p. 169 & p. 369.

23. R.W. Matthews, J. Chem. Soc. Faraday Trans., **80** (1984) 457.

24. R.F. Howe, M. Gräzel, J. Phys. Chem., **91** (1987) 3906.

25. M.A. Fox, C.C. Chen, J. Am. Chem. Soc., **103** (1981) 6757.

26. H. Greischer, A. Heller, A. J. Electrochem. Soc., **139** (1992) 113.

27. S.F. Nelsen, M.F. Teasely, P.L. Kapp, J. Am. Chem. Soc., **108** (1986) 5503.

28. M.A. Fox, Abdel-Wahab, A. A., Kim, Y. S., M.T. Dulay, J. Catal., **126** (1990) 693.

29. J. Cunninghum, S. Srijaranai, J. Photoche. Photobiol. A: Chemistry, **43** (1988) 329.

30. J. Peral, J. Casado, J. Domenech, J. Photoche. Photobiol. A: Chemistry, **44** (1988) 209.

31. C.S. Turchi, D.F. Ollis, J. Catal., **122** (1990) 178.

32. K. Tanaka, T. Hisanaga, K. Harada, J. Photoche. Photobiol. A: Chemistry, **48** (1989) 155.

33. R.W. Matthews, J. Catal., **113** (1988) 549.

34. B. Jenny, P. Pichat, P., Langmuir, **7** (1991) 947.

35. B. Siffert, J.M. Metzger, Colloids Surf., **53** (1991) 79.

36. J. Augustinski, Struct. Bonding, **69** (1988) 1.

37. B. Ohtani, Y. Okugawa, S. Nishimoto, T. Kagiya, J. Phys. Chem., **91**(1987) 3550.

38. N.R. Blake, G.L. Griffin, J. Phys. Chem., **92** (1988) 5697.

39. T. Y. Wei, Y. Y. Wang, C. C. Wan J. Photochem. Photobiol. A: Chemistry, **55** (1990) 115.

40. B. Bahnemann, D. Bockelmann, R. Goslich, R., Sol. Energy. Mater., **24** (1991) 564.

41. J. A. Turner, Science, **285** (1999) 687.

42. A. J. Nozik, R. Memming, J. Phys. Chem., **100** (1996) 13061.

43. M. Grätzel, Cattech, **3** (1999) 4.

44. D. A. Tryk, A. Fujishima, K. Honda, Electrochimica Acta, **45** (2000) 2363.

45. J. R. Bolton, Sol. Energy Mat. Sol. Cells, **38** (1995) 543.

46. M. Yagi, M. Kaneko, Chem. Rev., **101** (2001) 21.

47. M. Ashokkumar, Int. J. Hydrogen Energy, **23** (1998) 427.

48. A. J. Bard, M. A. Fox, Accounts Chem. Res., **28** (1995) 28.

49. T. Takata, A. Tanaka, M. Hara, J.N. Kondo, K. Domen, Catalysis Today, **44** (1998) 17.

50. E. Amouyal, Sol. Energy Mat. Sol. Cells, **38** (1995) 249.

51. A. Kumar, P. G. Santangelo, N. S. Lewis, J. Phys. Chem., **96** (1992) 834.

52. S. Licht, J. Phys. Chem., **105** (2001) 6281.

53. M. P. Dare-Edwards, J. B. Goodenough, A. Hamnett, P. R. Trevellick, J. Chem.Soc., Faraday Trans., **79** (1983) 2027.

54. K. Gurunathan, P. Maruthamuthu, Int. J. Hydrogen Energy, **20** (1995) 287.

55. S. Licht, B. Wang, S. Mukerji, T. Soga, M. Umeno, H. Tributsch, J. Phys. Chem. B, **104** (2000) 8920.

56. M. A. Green, Solar Cells: Operation Principles, Technology and System Applications, University of New South Wales, Kensington, 1992.

57. M. Fujihara, Y. Satoh, T. Osa, Chem. Lett. (Chem. Soc. Jpn.), (1981) 1053.

58. U. Björksten, J. Moser, M. Grätzel, Chem. Mater., **6** (1994) 858.

59. S. U. M. Khan, Z. Y. Zhou, J. Electroanal.Chem., **357** (1993) 407.

60. C. Santato, M. Ulmann, J. Augustynski, Conference Abstract, IPS-2000, July 30-August 4-2000, Snowmass, Colorado, USA, 2000.

61. G.R. Bamwenda, K. Sayama, H. Arkawa, Chem. Lett., (1999) 1051.

62. T. Ohno, D. Haga, K. Fujihara, K. Kaizaki, M. Matsumura, J. Photochem. Photobiol. A: Chemistry, **118** (1998) 41.

63. G.R. Bamwenda, H. Arkawa, Sol. Energy Mat. & Sol. Cells, **70** (2000) 1.

64. C. Santato, M. Ulmann, J. Augustynski, J. Phys. Chem. B, **105** (2001) 936.

65. A. Heller, R. G. Vadimsky, Phys. Rev. Letters, **46** (1981) 1153.

66. J. E. Turner, M. Hendewerk, G.A. Somorjai, Chem. Phys. Letters, **105** (1984) 581.

67. J. E. Turner, M. Hendewerk, J. Parmeter, D. Neiman, G. A. Somorjai, J. Electrochem. Soc., **131** (1984) 1777.

68. O. Khaselev, J. A. Turner, Science, **280** (1998) 425.

69. J. Augustynski, G. Calzaferri, J. C. Courvoisier, M. Grätzel, M. Ulmann, Proc. 10th International Conference Photochem. Stor. Sol. Energy, Interlaken, Switzerland, 1994. 229.

70. S. Licht, B. Wang, S. Mukerji, T. Soga, M. Umeno, H. Tributsch, Int. J. Hydrogen Energy, **26** (2001) 653.

71. M. Hara, C. C. Waraksa, J. T. Lean, B. A. Lewis, T. E. Mallouk, J. Phys. Chem. A, **104** (2000) 5275.

72. H. Harada, C. Hosoki, A. Kudo, Ultrasonic Sonochemistry, **8** (2001) 55.

73. K. Sayama, H. Arakawa, J. Chem. Soc. Faraday Trans, **93** (1997) 1647.

74. M. Lanz, D. Schurch, G. Calzaferri, J. of Photochem. Photobiol. A: Chemistry, **120** (1999) 105.

75. M. Hara, M. Komoda, H. Hasei, M. Yashima, S. Ikeda, T. Takata, J.N. Kondo, K.Domen, J. Phys. Chem. B, **104** (2000) 780.

76. C.E. Taylor, R.P. Noceti, Catal. Today, **55** (2000) 259.

77. K. Ogura, M. Kataoka, J. Mol. Catal., **43** (1988) 371.

78. K. Ogura, C.T. Migita, M. Fujita, Ind. Eng. Chem. Res., **27** (1988) 1387.

79. P. Maruthamuthu, M. Ashokkomar, K. Gurunathan, E. Subramanian, M.V.C. Shastri, Int. J. Hydrogen energy, **14(8)** (1989) 525.

80. P. Maruthamuthu, M. Ashokkomar, Int. J. Hydrogen energy, **14(4)** (1989) 275.

81. M.A. Gondal, A. Hameed, A. Suwaiyan, Appl. Catal. A, **243** (2003) 165.

82. A. Sclafani, L. Palmiano, Schiavello, Res. Chem. Intermed., **18** (1992) 211.

83. H. Reiche, W.W. Dunn, A.J. Bard, J. Phys.Chem., **83** (1979) 2248.

84. J. R. Darwent, A. Mills, J. Chem. Soc., Faraday Trans., **78(2)** (1982) 359.

85. G.R.Bamwenda, T. Uesigi, Y. Abe, K. Sayama, H. Arkawa, Appl. Catal. A, **205** (2001)117.

86. G.R.Bamwenda, H. Arkawa, Appl. Catal. A, **210** (2001)181.

87. G.R. Bamwenda, K. Sayama, H. Arkawa, J. Photochem. Photobiol. A: Chem., **122** (1999) 175.

88. M. S. Wrighton, P. T. Wolczanski, A. B. Ellis, J. Solid State Chem., **22** (1977) 17.

89. T. Ohno, D. Haga, K. Fujihara, M. Matsumura, J. Phys. Chem. B, **101** (1997) 6415

90. Okamoto, K., Yamamoto, Y., Tanaka, H., Itaya, A., Bull. Chem. Soc. Jpn., **58** (1985) 2023.

91. L. Zang, C. Y. Liu, X. M.Ren, J. Chem. Soc., Farady Trans., **91** (1995) 917.

92. M. Fujihara, Y. Satoh, T. Osa, Nature (London) ,**293** (1981) 206.

93. E. Baciocchi, G. C. Rosato, C. Rol, G. V. Sebastiani, J. Chem. Soc., Chem. Commun., (1992) 59.

94. E. Baciocchi, G. C. Rosato, C. Rol, G. V. Sebastiani, Tetrahedron Lett., **33** (1992) 5437.

95. T. Saketa, T. Kawai, K. Hashimoto, J. Phys. Chem., **88** (1984) 2344.

96. V. Brezova, A. Blazkova, E. Borsova, M. Ceppan, R. Fiala, J. Mol. Catal., **98** (1995) 109.

97. D.F.Ollis, H. Al-Ekabi (Eds), Photocatalytic Purification and Treatment of Water and Air, Elsevier, Amsterdam, 1993.

98. L.X. Chen, T. Rajh, Z. Wang, M.C. Thurnauer, J. Phys. Chem. B, **101** (1997) 10688.

99. M.R. Dhananjeyan, R. Annapoorani, R. Renganathan, J. Photochem. Photobiol. A: Chemistry, **109** (1997) 147.

100. W.S. Rader, L. Solujic, E.B. Milosavljevic, J.L. Handrix, J.H. Nelson, J. Solar Energy Eng., **116** (1994) 125.

101. J. Domenech, A. Prieto, Electrochim. Acta., **31** (1986) 1317.

102. R.P. Noceti, C.E. Taylor, J.R. D'Este, Catal. Today, **33** (1997) 199.

103. T.R.N. Kutty, K. Avudaithai, Chem. Phys. Lett., **163** (1989) 93.

104. W.K. Wong, M.A. Malati, Sol. Energy, **36** (1986) 163.

105. C. Morterra, A. Zecchina, G. Costa, (Eds), Structure and Reactivity of Surfaces, Elsevier, Amsterdam, 1989, 307p.

106. J. Soria, J.C. Conesa, V. Auguliaro, L. Palmisano, M. Schiavello, A. Sclafani, J. Phys. Chem., **95** (1991) 274.

107. J.A. Navio, F.J. Marchena, M. Roncel, M.A. de la Rosa, J. Photochem. Photobiol. A: Chemistry, **55** (1991) 319.

108. Z. Luo, Q.H. Gao, J. Photochem. Photobiol. A: Chemistry, **63** (1992) 367

109. J. Peral, J. Casado, J. Domenech, J. Photochem. Photobiol. A: Chemistry, **44** (1988) 209.

110. H.P. Maruska, A.K. Ghosh, Sol. Energy Mater., **1**(1979) 237.

111. V.W. Day, W.G. Klemperer, D.J. Main, J. Inorg. Chem., **29** (1990) 2345.

112. Sclafani, L. Palmisano, E. Davi, J. Photochem. Photobiol. A: Chemistry, **56** (1991) 113.

113. T. Cassagneau, J.H. Fendler, T.E. Mallouk, Langmuir, **16** (2000) 241

114. M. Fox, Optical Properties of Solids, Oxford University Press Inc. New York, 2001.

115. J.F. Moulder, W.F. Stickle, P.E. Sobol, K. Bomben, Handbook of X-ray Photoelectron Spectroscopy, Perkin–Elmer, Eden Praire, 1995.

116. D.C. Frost, C.A. McDowell, I.S. Woolsey, I. S., Molecular Physics, **27** (1974) 1473.

117. A. Calafat, J. Laine, J. Catal., **147** (1994) 88.

118. A. Hjelm, C.G. Granqvist, J.M. Wills, Physical Review B, **54** (1996) 2436.

119. C.G. Granqvist, Sol. Energy Mat. & Sol. Cells, **60** (2000) 201.

120. L. Se-Hee, M. Hyeonsik, C. Cheong, T. Edwin, M. Angelo, K.B. David, D.K. Satyen, Electrochimica Acta, **44** (1999) 3111.

121. A. Kuzmin, J. Purans, E. Cazzanelli, C. Vinegoni,G. Mariotto, J. Appl. Phys., **84** (1998) 5515.

122. A.J. Bard, R. Pearsons, J. Jordan, Editors, Standard Potentials in Aqueous Solutions. IUPAC, New York (1985).

123. A. Fujishima, T.N. Rao, D.A. Tryk. J. of Photochem. Photobiol. C, **1** (2000) 1.

124. U. Diebold, Appl. Phys. A, **76** (2002) 1.

125. A.L. Linsebigler, G. Lu, J.T. Yates, Chem. Rev., **95** (1995) 735.

126. O.T. SØrensen, Nonstoichiometric Oxides, Academic Press, New York, 1981.

127. F. Quarto, C. Sunseri, S. Piazza, M. Romano, M. J. Phys. Chem., **396** (1997) 2519.

128. V.R. Choudhary, A.M. Rajput, A.S. Mamman, J. Catal., **178** (1998) 576.

129. S. Hüfner, Adv. Phys., **43** (1994) 183.

130. U. Björksten, J. Moser, M. Grätzel, Chem. Mater., **6** (1994) 858.

131. Y. Xu, M.A.A. Schoonen, American Mineralogist, **85** (2000) 543

132. P. E. de Jongh, D. Vanmaekelbergh, J. J. Kelly, J. Electrochem. Soc., **147** (2) (2000) 486.

133. J. Li and L. M. Peter, J. Electroanal. Chem., **182** (1985) 399.

134. T. D. Golden, M. G. Shumsky,Y. Zhou, R. A. Vanderwerf, R. A.van Leeuwen, J. A. Switzer, Chem. Mater., **8** (1996) 2499.

Curriculum vitae

Personal Data

Full Name : ABDUL HAMEED
Date of Birth : 15th March, 1966
Nationality : Pakistani

Permanent Address
: House No. 497, Street No. 9
Sector G-10/1, Islamabad
Pakistan
Present Address : P.O. Box No. 1112,
King Fahd University Of Petroleum & Minerals,
Dhahran, Kingdom of Saudi Arabia
Marital Status : Married (Two daughters)
Contact No. : Tel. (Off) +966-3-8604104, (Res) +966-3-8606157
E-Mail : hameedch@kfupm.edu.sa/ hameedch@yahoo.com
Languages : English, Urdu & Punjabi

Education

1999 – 2003 **Doctor of Philosophy (Ph.D) in Chemistry**

"Laser induced photocatalytic conversion of methane into methanol"

King Fahd University of Petroleum & Minerals, Dhahran, Saudi Arabia

- Major in Physical Chemistry
- Minor in Inorganic Chemistry

1991 – 1993 **Master of Philosophy (M.Phil) in Chemistry**

"Adsorption studies of dyes on alumina and silica gel"

Quaid-e-Azam University, Islamabad, Pakistan

- Major in Physical Chemistry

1987 – 1990 **Master of Science (M.Sc) in Chemistry**

"Preparation of MMSA-Sn-Tc^{99m} complex by using $SnSO_4$ and its polarographic studies"

Institute of chemistry, University of the Punjab, Lahore, Pakistan

- Major in Physical Chemistry

Publications

Patent

A patent on the invention **entitled "A Method for the Production of Hydrogen from Methanol using Laser Photocatalytic Process"** has been prepared and submitted to US patent office

Journals

1. **A. Hameed**, Gondal, M. A. and A. Al-Suwaiyan **(2003)**, Effect Of Dissolved Metal Ions On Laser Induced Photocatalytic Splitting Of Water Over WO_3, **Energy Sources** (accepted and in press).

2. Gondal, M. A., **A. Hameed**, Z.H. Yamani and A. Al-Suwaiyan **(2003)**, Laser Induced Photocatalytic Oxidation/Splitting of Water over α-Fe_2O_3, WO_3, TiO_2 and NiO Catalysts: Activity Comparison, **Chemical Physics Letters** Vol. 385, pp 111-115.

3. Gondal, M. A., **A. Hameed** and A. Al-Suwaiyan **(2003)**, Photocatalytic conversion of methane into methanol using visible laser, **Applied Catalysis** Vol 243, pp 165 – 174.

4. M. Saleem, M. Afzal, F. Mahmood and **A. Hameed (1994)**. Thermodynamics of adsorption of Rhodamine B and Nile blue sulfate on alumina from aqueous solutions, **J. Chem. Soc. Pak.** Vol 2, pp 16-19.

5. Gondal, M. A., **A. Hameed**, Z.H. Yamani, and A. Al-Suwaiyan **(2003)**, Production of Hydrogen and Oxygen by Water Splitting

Using Laser Photo-catalysis over Fe_2O_3 , **Applied Catalysis** (accepted).

6. **A. Hameed**, Gondal, M. A. and A. Al-Suwaiyan **(2004)**, Photocatalytic Splitting of water over NiO and Its comparison with TiO_2 (rutile), **J. Mol. Catal.** (Submitted).

Conferences

1. Gondal, M. A., **A. Hameed**, Z. H. Yamani, A. Suwaiyan and A. Arfaj **(2004)**, Activity of WO_3 , NiO and Fe_2O_3 Catalysts for Hydrogen Production under UV Laser Irradiation, Chemistry in industry (CHEMINDIX 2004), Manama, Bhahrain (September 27-29, 2004).
2. M. A. Gondal, **A. Hameed**, Z. H. Yamani, A. Suwaiyan and A. Arfaj (2004), Laser photocatalytic conversion of methanol into hydrogen, Second Saudi Science Conference, Jeddah (Saudi Arabia).
3. M. A. Gondal, **A. Hameed,** Z. H Yamani and A. Al-Suwaiyan (2003) Photocatalytic Splitting of Water into Hydrogen and Oxygen Using Laser, The 4th Middle East Refinery & Petrochemical Conference (Petrotech), Manama, Bahrain (30th September -1st October, 2003).
4. Gondal, M. A., **A. Hameed** and A. Al-Suwaiyan (2002), Laser photocatalytic conversion of methane using WO_3 and water, 5th International conference on Chemistry in Industry, Manama (Oct 14-16) Bahrain.
5. Gondal, M. **A., Hameed**, A., and Suwaiyan, A., 11th Saudi-Japanese Symposium on Catalysis in Petroleum Refining & Petrochemicals, Dhahran (11-12 November, 2001).